MANCHESTER 1824
The University of Manchester

Ion transport properties of atomically-thin crystals: Novel proton transport, ion-exchange and selectivity properties.

A thesis submitted to the University of Manchester for the degree of
Doctor of Philosophy
in the Faculty of Science and Engineering

2021

Lucas Mogg
Department of Physics and Astronomy

Contents

Word Count: 67,270

List of Figures

List of Tables

List of Publications

Mogg, L., Hao, G.P., Zhang, S., Bacaksiz, C., Zou, Y.C., Haigh, S.J., Peeters, F.M., Geim, A.K. and Lozada-Hidalgo, M., 2019. Atomically thin micas as proton-conducting membranes. Nature nanotechnology, 14(10), pp.962-966.

Mogg, L., Zhang, S., Hao, G.P., Gopinadhan, K., Barry, D., Liu, B.L., Cheng, H.M., Geim, A.K. and Lozada-Hidalgo, M., 2019. Perfect proton selectivity in ion transport through two-dimensional crystals. Nature communications, 10(1), pp.1-5.

Griffin, E., Mogg, L., Hao, G.P., Kalon, G., Bacaksiz, C., Lopez-Polin, G., Zhou, T.Y., Guarochico, V., Cai, J., Neumann, C. and Winter, A., 2020. Proton and Li-ion permeation through graphene with eight-atom-ring defects. Acs Nano, 14(6), pp.7280-7286.

Abstract

Dedication in this thesis has been made to the study of ion transport both through (and within) atomically-thin crystals. We explore how protons over chloride ions selectively passage through 2D materials such as hexagonal boron nitride (hBN). Next, we reveal how protons can permeate through 5 Å-wide channels in proton-exchanged muscovite mica and vermiculite. Finally, we report an enhanced ion-exchange rate in few-layer clays, as well as imaging of their ion distribution to high levels of detail. An introduction to the topics and research conducted is first presented. Next, three background sections that equip the reader with sufficient knowledge to understand the results presented are given. The first background section introduces the topic of ion transport in a broad sense, covering the fundamental driving forces, as well as more focused areas including mechanisms of ion-selectivity. Next, the second background chapter provides an overview and literature review of the nascent field of proton-transport through 2D materials, both from an experimental and a theoretical perspective. The final two background chapters present an overview of ion-exchange and then experimental techniques are provided. The next three chapters contain results of work in journal format as either accepted publications or as a submitted manuscript. The first results chapter contains work on proton-selectivity through 2D materials. The second results chapter is that of a study regarding proton-transport through ion-exchanged mica. In the last results chapter, we present an ion-exchange study of few layer mica and clay. We then finally conclude the thesis and discuss future directions and outlooks.

The implications and significance of our findings presented in this thesis are as follows. We anticipate that we have contributed to the debate on how protons permeate through the lattice of 2D materials. We ascribe the proton-selective nature of hBN and graphene to that of permeation through the intrinsic lattice. Secondly, we have reported a new class of proton-conducting membrane, that of proton-exchanged few-layer mica. This membrane can be operated at high (>200 °C) temperatures at an areal conductivity exceeding 10 Scm^{-2}. We anticipate that scaling of these membranes may be possible, in the same fashion that CVD graphene is scalable. Lastly, we have reported enhanced ion-exchange rates for few layer clays and their ion-distribution in unprecedented detail. This opens up a new avenue for researchers to explore ion-exchange effects in clays and other 2D exchanging materials from both a fundamental and applications perspective.

Declaration of Originality

I hereby confirm that no portion of the work referred to in the thesis has been submitted in support of an application for another degree or qualification of this or any other university or other institute of learning.

Copyright Statement

i The author of this thesis (including any appendices and/or schedules to this thesis) owns certain copyright or related rights in it (the "Copyright") and s/he has given The University of Manchester certain rights to use such Copyright, including for administrative purposes.

ii Copies of this thesis, either in full or in extracts and whether in hard or electronic copy, may be made *only* in accordance with the Copyright, Designs and Patents Act 1988 (as amended) and regulations issued under it or, where appropriate, in accordance with licensing agreements which the University has from time to time. This page must form part of any such copies made.

iii The ownership of certain Copyright, patents, designs, trademarks and other intellectual property (the "Intellectual Property") and any reproductions of copyright works in the thesis, for example graphs and tables ("Reproductions"), which may be described in this thesis, may not be owned by the author and may be owned by third parties. Such Intellectual Property and Reproductions cannot and must not be made available for use without the prior written permission of the owner(s) of the relevant Intellectual Property and/or Reproductions.

iv Further information on the conditions under which disclosure, publication and commercialisation of this thesis, the Copyright and any Intellectual Property and/or Reproductions described in it may take place is available in the University IP Policy (see `http://documents.manchester.ac.uk/DocuInfo.aspx?DocID=24420`), in any relevant Thesis restriction declarations deposited in the University Library, The University Library's regulations (see `http://www.library.manchester.ac.uk/about/regulations/`) and in The University's policy on Presentation of Theses.

Acknowledgements

Firstly, I would like to thank Prof Robert Young of Lancaster University for introducing me to 2D material and nanotechnology research. He kindly helped organise an undergraduate placement for me that set in motion many things that have altered the course of my career, I think for the better.

I would like to especially thank Prof Sheng Zhang of Tianjin University, who while at Manchester, patiently taught me many aspects of Physical- and Electro-Chemistry. I would also like to thank Prof Guang-Ping Hao for his support and help fabricating and the measurement of devices as well as our discussions. I will not forget the time a hot air gun came to our rescue during a measurement. Your humility, integrity and sense of humour have made an impression on me. I also thank Mr Eoin Griffin, Dr Victor Guarochico Moreira and Mr Donnchadh Barry for their help measuring and making devices as well as our discussions about their interpretation. I am particularly grateful to Prof Sheng Hu and Dr Marcelo Lozada-Hidalgo for sharing their device fabrication knowledge at an early stage of the PhD, allowing me to use the clean room effectively thereafter. I would further like to thank Prof Yichao Zhou and Prof Sarah Haigh for the S/TEM work performed. Thank you Yichao for your dedication and our effective collaboration imaging few-layer clays.

I am indebted to Prof Andre Geim, Prof Irina Griogrieva and Dr Marcelo Lozada-Hidalgo for initiating and helping guide the projects that I embarked upon during this PhD. While the project certainly evolved during the work, I nonetheless found it stimulating enough to see it through. I am incredibly grateful to all the NGI clean room staff for making it such a great and effective research facility. I could not have undertaken the work without your help. Special thanks to Dr Lee Hague, Dr Maddison Coke and Dr Andrew Brook for their assistance. To the friends I met, lived and studied with at Manchester, you made the experience one of the best of my life and I will always look back on our times together fondly. Especially to my friends Dr Harry Waring and Dr Servet Ozdemir, I shall miss our fun times in Manchester together. I thank my grandparents and mother who have helped support my studies. Elliott, for your help whilst I wrote this thesis and interest over the years. Lastly, Dr Meena Nayagam, words cannot express how grateful I am for your kindness, love and care that have kept me going during the PhD.

Studying the nanoscale systems presented in this thesis, in such a hands on experimental way, has easily been the most rewarding yet also difficult task of my life. I feel privileged to have worked in such an incredible facility and research group. I thank the EPSRC and NOWNANO for funding projects like mine.

Chapter 1

Introduction

Controlling matter at the atomic scale using 2D materials is an extremely active area of research. The discovery of graphene, a single atomic layer of carbon, and now the wider 2D material family, has ignited a new field of research within condensed matter physics as well as many other areas of science and engineering. Many unexpected discoveries have been revealed, too many to start discussing in detail here. The work presented in this thesis is a direct consequence of such an unexpected experimental discovery that 2D materials such as graphene and hexagonal boron nitride (hBN) can enable protons to permeate through their lattices, intrinsically. That they do is certainly not self-evident, the electron density surrounding 2D membranes should exclude, if not severely impair, passage through the lattice. How then could protons pass through such a membrane? This question has sparked a debate among academics, continuing to the present day. Given the experimental evidence that graphene and monolayer hBN permit proton transport, we can consider, is it possible for 2D material membranes to allow other ions to pass through the lattice? A simple way to approach this question is to measure the selective behaviour of protons over chloride ions using HCl as an electrolyte, with a 2D membrane barrier. This is the topic of the first results chapter of this thesis, presented in journal format, within Chapter 6. In this study, we do indeed observe total proton selective behaviour through 2D material membranes, lending support to the view that protons pass through the intrinsic lattice of these materials.

We next explore another group of 2D materials (mica silicate minerals), which arguably have more a priori reasoning to be proton conductive than graphene. Indeed, other related silicate structures (zeolites) contain one-, two- or three-dimensional channel systems with cation- exchange abilities and are known to be fast ionic conductors. Micas contain structural similarities to zeolites. They possess 5 Å-wide channels, containing OH groups, with exchangeable cations on their surface and interlayer. We exploit this property and turn micas into proton-conducting membranes by exchanging native ions for protons, unblocking pathways through the lattice. This is the topic of Chapter 7, which is also presented in journal submission format.

Having demonstrated the impact that proton exchange can have on the proton transport properties of mica, a logical continuation of Chapter 7 is to investigate the phenomena of ion-exchange in few-layer micas and clays (weathered micas) more broadly. These minerals are abundant within soils worldwide, where the studies of which go back as far as the time of Ancient Greece. A significant experimental effort to characterise the ion-exchange properties

of these minerals was undertaken in the 19th and 20th centuries. However, even to this day, the kinetics and dynamics of ion-exchange in these minerals, are still an active area of research. We undertook a scanning transmission electron microscopy (S/TEM) study where we desired to investigate whether the exchange rate or mechanisms diverge as clays approach their fundamental atomic unit. We discovered that the exchange rate is indeed orders of magnitude faster in few-layer vermiculite when measured via a novel S/TEM 'snapshot' method. Along with this discovery, we were able to image the ion distribution on the clay and mica surface to very high levels of precision, identifying the binding sites via S/TEM imaging. We also report new moiré superlattices for restacked twisted layers. These are the topics of results in Chapter 8.

We finally conclude this thesis and provide an outlook for further research in Chapter 9. The full nature and extent of this author's contribution, and that of co-authors and the other collaborators to the publications, are fully provided in the introductory sections of each respective result chapter. Presenting this thesis in journal format was appropriate given that the author's contribution to the work involved all aspects of the production of the papers, including data acquisition, analysis and writing. Further, all the researched materials were derived from original research undertaken after the date initially registered with this university. This work was carried out in the Physics Department and National Graphene Institute, University of Manchester, between 2016 and 2021.

Chapter 2

Ion Transport

2.1 Introduction

Ions and their movement impact all aspects of life. From ion transport in batteries powering ever more demanding electrical devices to ion motion through few nanometre-thin biological membranes, a ubiquitous hallmark of life, ion transport underpins such phenomena. Our brains rely upon regulated ion transport to operate, where cell membranes perform exquisite ion-selective transport, both in a transient and permanent fashion. This is a crucial component to regulate cellular behaviour [1]. Most, if not all, living cells rely upon the controlled passage of ions such as sodium, potassium, calcium and chloride through biological pores, channels, pumps and other intricate systems. One particularly celebrated process, is that of the ion-transporting enzyme Na+/K+ ATPase [2] which transports ions against their concentration gradients, the discovery of which garnered a Nobel Prize in Chemistry to Jens C. Skou, John E. Walker and Paul D. Boyer. The mechanisms of ion selectivity in nature are marvels of evolution, where intricate channels can distinguish ions by their atomic composition and stereo-chemistry [3]. A further Nobel Prize in Chemistry was awarded to R. MacKinnon for insights into the selectivity of potassium channels in biological membranes.

Synthetic ion-selective membranes and ion-transport-restricted pores are also of importance to industry and researchers. Areas of application and research include: reverse osmosis through semi-permeable membranes for desalinisation, using nanopores for DNA and RNA sequencing[1][4], membrane-based processes for power generation from salinity gradients [5], [6], fuel cell technologies [7], [8] and vanadium redox flow batteries [9]. Chapters 6 and 7 relate to 2D materials as separation barriers and novel proton transport membranes respectively. The key underlying principles, presented in this chapter, almost certainly apply to these atomically-thin membranes. Fundamental properties of ionic flux are introduced to the reader, where, as we shall see, the gradient of electrochemical potential determines transport. Ion selectivity and ionic mobility are introduced, with the key underlying equations presented. Other ionic interactions including ion hydration, the unique case of the proton, chloride ion and transport through crystalline/quasi-crystalline phases are provided. Ion transport is a vast topic. Therefore care has been paid here to restrict topics covered to those which are useful as background knowledge for this thesis. Let us now discuss these.

[1] As of 2021, Oxford Nanopore Technologies Ltd has received over £600m of fundraising capital and has successfully implemented nanopore sequencing technology.

2.2 Fundamentals of Ion Transport

Firstly, let us provide a working definition of ion transport. It is the motion of mass and its associated charge through a media[2], via diffusion, migration and convection. Diffusion and migration of ions occur when there is a gradient in the electrochemical potential μ [10]. The electrochemical potential of a given ion (μ_i) at an absolute temperature (T) and pressure (P) is given, as is customary, as

$$\mu_i = \mu_i^0 + \mathrm{RTln}(a_i) + (P - P_0)V_i + z_i\mathrm{F}\psi \tag{2.1}$$

where R is the ideal gas constant, a_i is the activity of the ion species, P_0 is the standard pressure (1 atm), V_i is the partial molar volume, z_i is the charge number of ion i, F is the Faraday constant and ψ is the electric potential. The convective transport of ions arises from any imbalance of forces acting upon the ionic solution, creating motion. These three components are what drive ionic flux $\boldsymbol{J_i}$. Where convective influences on ion flux can be neglected, a given ion species' i motion, is governed solely by the gradient of its electrochemical potential. In this case, ions will move from the direction of higher to lower chemical potential.

$$\boldsymbol{J_i} = \frac{C_i D_i}{\mathrm{RT}} \nabla \mu_i \tag{2.2}$$

where C_i is the ion concentration, D_i diffusion constant and ∇ is the gradient operator. Therefore, it follows, for linear mass transfer, and if we replace the activity of a chemical species with its concentration (setting the activity coefficient γ to unity, where $a_i = \gamma_i C_i$) and assume pressure changes are negligible, then we arrive at the Nernst–Planck equation (intermediate steps provided in Appendix A), as

$$\boldsymbol{J_i} = -D_i \nabla C_i - \frac{z_i \mathrm{F}}{\mathrm{RT}} D_i C_i \nabla \psi + C_i \boldsymbol{v_i} \tag{2.3}$$

where $\boldsymbol{v_i}$ is the ion velocity and D_i is the diffusion coefficient, originating from the constant of proportionality in Equation 2.1. Moreover, it is possible to couple the Nernst–Planck equation to Poisson's equation for electrostatics in combination, yielding the nonlinear Poisson–Nernst–Planck (PNP) equations 2.3 and 2.4

$$\nabla \cdot (-\nabla \psi) = \frac{ze\rho}{\epsilon} \tag{2.4}$$

where ρ is charge density (which we can relate to C_i) and ϵ being the permittivity of the medium. The PNP equations are an excellent tool with which to describe the essentials of coupled transport of several kinds of ions through bulk and nanoscale systems [11]. Further, if only ion flux as a function of concentration gradient is considered, we arrive at the well-known Fick's law of diffusion

$$\bar{J} = -D_i \nabla C_i. \tag{2.5}$$

[2]Typically, a solute.

which is intuitively understandable from the fact that concentrated solutions tend to disperse within a dilute phase. At this stage, we should also introduce Fick's second law of diffusion which we can derive from the requirement of conservation of mass and Fick's first law, Equation 2.5. Fick's second law is

$$\frac{dC_i}{dt} = -D_i \nabla^2 C_i. \tag{2.6}$$

which is an important relationship for describing the kinetics of ion/mass transfer.

Ion transport systems can be experimentally characterised using electrochemical current-voltage measurements. Either DC or AC measurements will encapsulate ion transport phenomena. Assuming quiescent solution conditions and if the concentration gradient is constant across a region for each ion species i and the potential gradient is constant at V, then the total ion current can be measured as

$$I = GV + C_{\Delta C} \tag{2.7}$$

where G is the conductance of the system, V the potential and $C_{\Delta C}$ is a constant offset due to a concentration gradient effect. The two effects of potential and gradients in concentration on ion transport are depicted visually in figure 2.1 b. If concentration gradients are negligible or well characterised and assumptions about voltage changes can be made, then we can extract diffusion coefficients, and therefore mobilities, from current-voltage data (see Appendix A for clarification). Now, diffusion coefficients are governed by the underlying ion transport mechanism(s). In an aqueous solution, this is typically given via the Einstein-Smoluchowski equation [10] as

$$D_i = \frac{\mathrm{RT}}{z_i \mathrm{F}} \mu_i \tag{2.8}$$

where μ_i, in this case, is the ionic mobility. In the solid state, diffusion constants can often, but not always, be described by an Arrhenius expression, as shown in equation 2.9 [12]. This can be extracted when measurements of the temperature dependence on ion conductivity are performed, where the diffusion constant can be given as

$$D_i = D \cdot \exp\left(-\frac{E_A}{k_b \mathrm{T}}\right) \tag{2.9}$$

Where D is the frequency factor (units m^2/s) and E_a is the activation energy of the underlying ion transport mechanism. Equation 2.9 is a type of Arrhenius relation, applying to many thermally dependent processes in electrochemistry. Equation 2.9 is typically a facile description of ion transport, encapsulating complex underlying ion transport mechanisms in a single expression. However, it is a useful measure to characterise and attempt to match with theoretical modelling. Figure 2.1 a shows how we can visualise the activation energy of a system. It can be considered to be the barrier between two local energy minima, and an ion can diffuse forward (or backward) along a reaction pathway. The expression also describes how the diffusion rate will relate to temperature (depending on the activation energy). Negative activation energies can also exist, for example, the proton conductivity of ice can be described using an activation energy value of approximately -0.15 eV [13]. We shall use

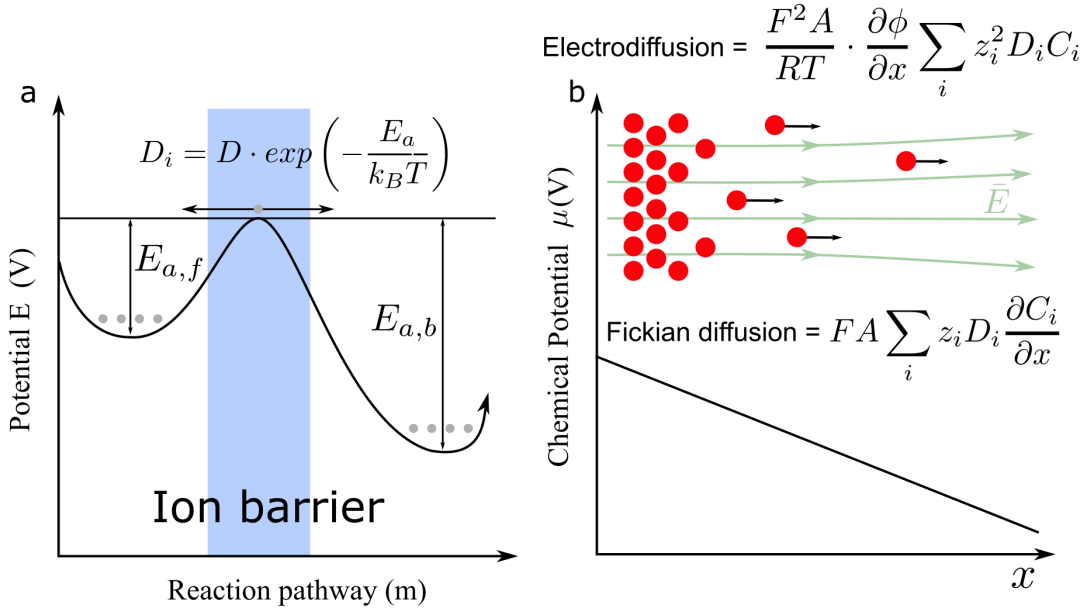

Figure 2.1: (**a**) Potential profile for a given reaction pathway showing both a forward ($E_{a,f}$) and a backward ($E_{a,b}$) activation energy for a thermally-activated diffusion process which can be characterised by the Arhennius expression. (**b**) Migration and diffusion terms governing ion transport due to a concentration gradient and electric field. The chemical potential gradient is shown underneath the stylisation of these processes.

measured activation energies in interpreting temperature dependent measurements presented in Chapter 7.

Let us review. We now know the driving forces behind ion transport. It is the gradient of electrochemical potential and convective forces, the former involving two distinct processes: diffusion and migration. Diffusive transport from gradients in concentration, migration from a gradient in electrical potential and convection arising from the motion of ions from imbalanced forces, causing solution flow. These are the underlying driving forces behind ion transport in any system.

2.2.1 Convective and Steady State Transport

For completeness, let us look at the dynamic (time–dependent) case of ion transport. From the continuity equation and assuming incomprehensibility of solution, the time dependent case of ion concentration profiles can be expressed as [10]

$$\frac{\partial C_i}{\partial t} = -\boldsymbol{\nabla} \cdot \boldsymbol{J_i} = D_i \nabla^2 C_i - \frac{z_i \mathrm{F}}{\mathrm{RT}} D_i C_i \nabla^2 \psi - \boldsymbol{v} \cdot \nabla C_i, \tag{2.10}$$

where we can determine the velocity profile, $\boldsymbol{v}$, from the Navier–Stokes equation (presented in Appendix A, equation A.6). Solving this equation provides solutions to dynamic ion transport properties and are known as the Poisson–Nernst–Planck–Navier–Stokes (PNP–NS) equations. Let us now turn our attention to ion-selective systems. How can we describe the

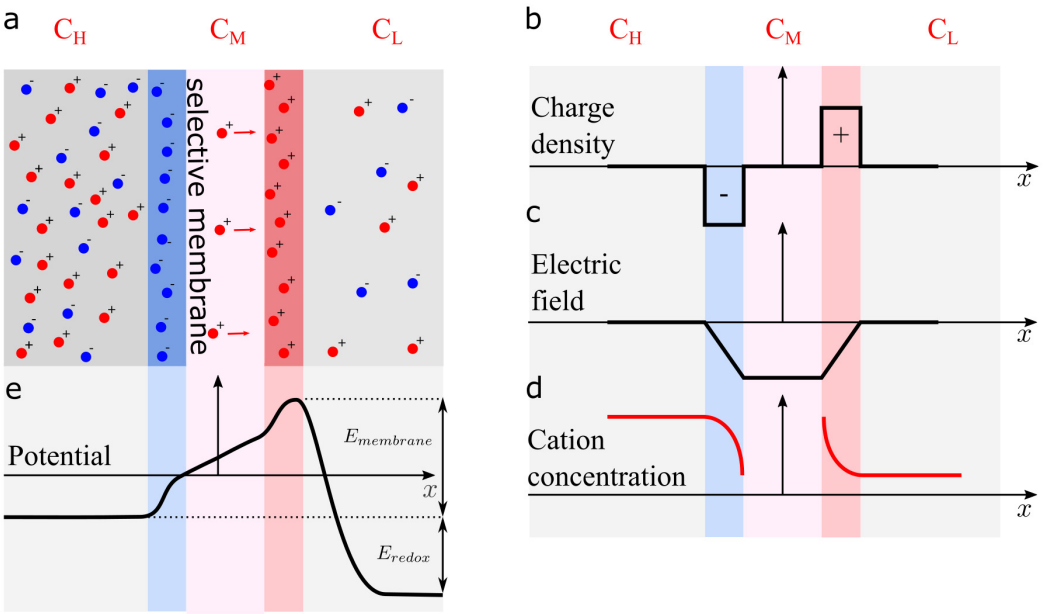

Figure 2.2: Ion transport at the selective membrane interface. (**a**) Illustration of ion transport at a cation selective membrane. Positive charge accumulates at the lower concentration reservoir, also depicted in (**b**) interfacing with the membrane, balancing charge transport. The electric field is illustrated in (**c**) and cation concentration is depicted in (**d**). The membrane and redox potential is shown in panel (**e**). The potential change in the red and blue shaded regions are from Donnan potentials.

ion transport of semi-permeable selective membranes? What follows is an introduction to a set of equations to describe such a case.

2.2.2 Ion Transport Through a Selective Membrane

Selective ion transport is the major topic of Chapter 6. Therefore, let us introduce this. Firstly, we should imagine two reservoirs of solution containing two different ion concentrations where the solution is comprised of both a monovalent cation and anion. The membrane separates a high and a low concentration reservoir denoted as C_H and C_L, respectively. The membrane allows ions to pass, but with differing mobility for each ion type i. The fraction of which being the apparent[3] ion transport number t_i

$$t_i = \frac{\mu_i C_i}{\sum_j C_j \mu_j} \tag{2.11}$$

where μ_i is the mobility of each cation. The transport number, as equation (2.11) describes, is directly proportional to fractional mobilities that contribute to total ionic mobility, and the sum of all transport numbers is unity. The advantage of using transport[4] numbers are that we can incorporate multiple mobilites together (see appendix B), where perhaps individual val-

[3]The word apparent being used to highlight the fact that the true transport number may be different, yet our measurements will reveal this value.

[4]Also known as transference numbers

ues are not known. Therefore, this approach is more generalised than considering mobilities alone. Further, selectivity may arise from complex local mobility variations at a membrane interface, thus we can account for this using transport numbers. Although ultimately, transport numbers can arise from differing mobilities of ions, across a selective system. Now, for a selective interface, the ion that diffuses through the membrane at the faster rate, will accumulate across into the C_L reservoir, resulting in an electrical potential being established as the imbalance of charge accumulates. However, such a separation of charge cannot continue indefinitely. Indeed, a membrane potential is established which then opposes and restricts the flow of ions to an equilibrium. Now, this potential across a selective membrane (also accounting for Ag/AgCl electrode effects used in Chapter 6 and derived in more detail in Appendix B), is given from the Nernst equation (B.4) as

$$E_{cell} = -2t_+ \frac{\mathrm{RT}}{\mathrm{F}} \ln \frac{a_H}{a_L} \tag{2.12}$$

where a_H and a_L are the activities of the high and low concentration side respectively. We can relate activities to concentrations via the relation $a_i = \gamma_i C_i$ where γ is the activity coefficient [10]. Equation 2.12 is significant to the work presented in Chapter 6 as we can use this expression to characterise transport numbers via measured cell voltages across a 2D material membrane.

The general integral equation to determine the potential for a given ionic activity, neglecting the unchanging standard potential, pressure, volume and convective term, is obtained by integrating the infinitesimal change in electrochemical potential

$$\frac{t_i}{z_i} d\mu_i = \frac{t_i}{z_i} \mathrm{RT} d\ln(a_i) + t_i \mathrm{F} d\psi. \tag{2.13}$$

Further, if we allow our hypothetical membrane system to equilibrate, the change in chemical potential across the membrane, from phase α to phase β, for all ions will be zero. This is a requirement for no net ion flux once equilibrium is established, as we have seen in equation 2.3. Therefore, if we integrate the chemical potential, for all ion species, from one phase α to another β, the net change after the membrane establishes a potential, due to selective transport shall be zero

$$\int_\alpha^\beta \sum_i \frac{t_i}{z_i} d\mu_i = 0 = \mathrm{RT} \int_\alpha^\beta \sum_i \frac{t_i}{z_i}, d\ln(a_i) + \sum_i t_i \mathrm{F} \int_\alpha^\beta d\phi \tag{2.14}$$

when the ion flux and therefore chemical potential gradient is zero across the membrane. Equation 2.14 applies to any potential where selectivity occurs. This could well be a liquid junction potential between two immiscible fluids as well as a physical barrier. It is necessary for there to be at least one cation and one anion, for charge neutrality, so we must sum the contributions from equation 2.14. It is possible to consider the general case where we have more than two ion species present. Indeed, two well-known solutions, using differing assumptions on concentration and potential profile to the integral equation 2.14, are the Henderson and Goldman (presented in section 2.3.4.3) equations respectively [14].

However, we should consider that an electric potential will also be established across a liquid junction, where two differing concentrations interface, even in the absence of a membrane, for the case of varying ion mobilities. The liquid junction potential (E_{lj}) at a liquid interface consisting of differing concentrations is also of the form

$$E_{lj} = (t_+ - t_-)\frac{\mathrm{RT}}{\mathrm{F}}\ln\left(\frac{a_H}{a_L}\right) \tag{2.15}$$

where we can rely upon known transference numbers for a given electrolyte and concentration [10]. Hence, when measurements are made across a concentration gradient, we must not conflate selective transport due to the liquid junction potential and that of a selective membrane. This potential can be an undesirable effect when measuring electrochemical systems. Let us now explore models for the underlying mechanisms of ion mobility and consider the electrolyte used in studies presented in Chapter 6, hydrochloric acid.

2.3 Ion Mobilities and Properties

Here in this subsection, we will consider some basic properties of ion mobility in relevant systems and present specific examples of how nanoscale systems can be ion selective, due to electrostatic and steric[5] effects which give rise to dehydration based and Donnan exclusion derived ion selectivity. This will assist us in discussing the experimental results presented in Chapters 6 and 7. Firstly, we will discuss interactions between ions and water, how and why ion mobilities may differ and why protons are a unique case.

2.3.1 Ion Hydration

We are now turning to dissolved ions in an aqueous electrolyte. First, one has to consider that the ways in which ions interact within aqueous solutions are highly complex [16]–[18]. This is at least in part due to the peculiar properties of water itself [19]. Unlike many liquids, the density of water decreases upon freezing, it melts when pressure is applied and can shrink upon heating [18]–[20]. Hydrogen bonds, discussed in more detail later, are a strong feature of water, playing a prominent role in many of the oddities of water-ion interactions. Each ion can interact in a unique way with one another and with the water molecules. Ion–ion interactions, ion–ion complex and chelate formations and the polarisation of ions are just a few processes. It would be incorrect, in general, to think of ions dissolved in an aqueous electrolyte as charged particles drifting in isolation through a dielectric medium, especially at high concentrations. With that preamble considered, we will keep our focus and consideration of ion-water and ion-surface interactions that are known to give rise to ion selectivity across nanoscale systems.

Let us introduce the concept of the hydration sphere. When immersed in aqueous solutions, ions will be surrounded by hydration 'atmospheres' known as solvation shells due to

[5]The spatial arrangement of atoms.

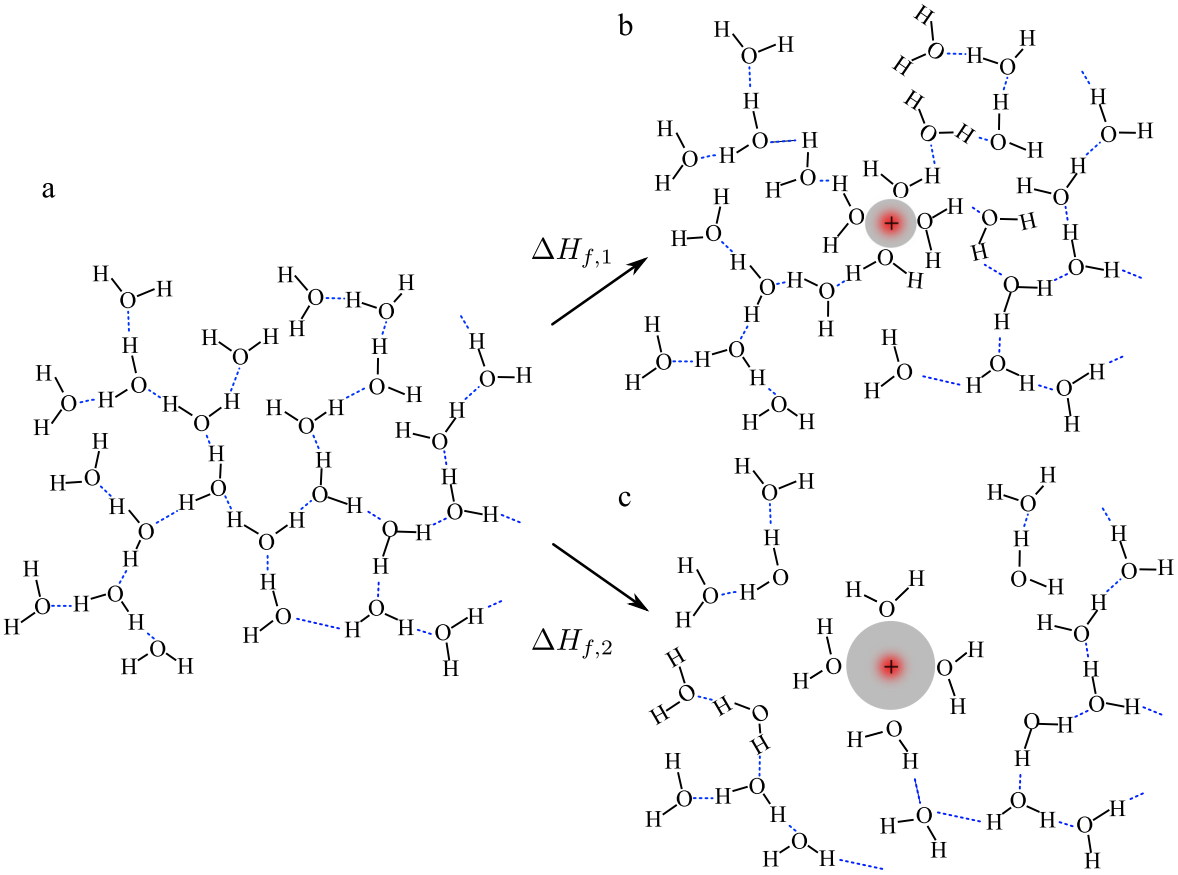

Figure 2.3: Ordering and disordering of bulk water matrix upon the incorporation of a small and large ion. (**a**) Illustration of bulk water ordering. The ice-like tetrahedral network remains, but the structure is now disordered and labile. (**b**) Increased structuring of the water network around the ion. This can occur when the charge density is sufficient to create this structure. (**c**) The larger (lower charge density) ion breaks the bulk water structure by breaking hydrogen bonds, yet lacks the charge density required to rebuild a water network surrounding the ion. Figure adapted from [15]

their interactions with dipolar water molecules. These interactions are stronger than thermal energies, often >5 k_BT [18], and, hence, result in stable chemical complexes [21]. The nature and differences in these complexes arise from the varying characteristics of each ion, such as physical size and charge valance. It would be useful to assign a 'hydration number' characterising how many water molecules interact with a given ion. However, different methods to obtain this property can give significantly, and occasionally dramatically different numbers [22], [23]. Thus, the question concerning the number of water molecules associated with an ion, cannot be answered unequivocally. Now, the size of the ion will significantly determine how it resides within the water network, as illustrated in Figure 2.3, whereas the ion charge valence will affect the degree and strength to which water molecules interact. Water molecules closest to the ion are strongly orientated toward the ion, whereas those beyond this first layer, may still have a disrupted matrix, but orientated in a less organised fashion than those residing closer to the ion. Beyond these water molecules, we then enter into the bulk water matrix [24].

Two values that indicate the strength of such ion-solvent interactions are the values of

Table 2.1: Data for monovalent ions taken from Tissandier et al [25] and represent absolute enthalpies of hydration. Higher valance ions are reported as conventional enthalpies, taken from Burgess et al [22]. Mobilities are taken from Haynes et al [26]. Ion values are presented from small mass (top) to larger mass (bottom) for each valance ion.

Ion	Bare Ion Radius (nm)	Enthalpy of Hydration (kJ/mol)	Hydration Radius (nm)	Mobility 298 K(10^{-8}m^2 s^{-}1 V^{-1})
H^+		-1150.1	-	-
Li^+	0.068	-578.9	0.38	4.01
H_3O^+	-	-503	0.28	36.23
Na^+	0.095	-405	0.36	5.19
K^+	0.133	-321	0.33	7.62
Cs^+	0.169	-263	0.33	7.90
Be^2+	0.031	-2387	0.46	4.67
Mg^2+	0.065	-1922	0.43	5.50
Ca^2+	0.099	-1592	0.41	6.17
Al^3+	0.050	-4660	0.48	6.32
Cl^-	0.181	-288.7	0.33	7.91
I^-	0.216	-246.8	0.33	7.96

ion hydration enthalpy and partial molar entropy of hydration [22]. The enthalpy change (amount of heat passing into or out of the system at constant pressure) signifies the degree of polarisation, bonding or other energetic interactions occurring between water molecules and the ions themselves. A table of absolute[6] and conventional hydration enthalpies for common cations and anions is provided in table 2.1. Let us evaluate these.

For a given ion valence, the values presented in Table 2.1, indicate a general trend of decreasing hydration enthalpy with increasing ion mass. This is primarily due to the charge density decrease as an ion mass increases. Consequently, a water molecule dipole will have a weaker interaction with the ion as its size increases (as stylised in Figure 2.3). As a result, the monovalent cation of lithium has the largest hydration atmosphere of all the alkali metal cations. It is worth noting that hydration radii measurements can vary with experimental technique, so they should be viewed with caution [18]. Another important factor affecting solvent-ion interactions is the entropy change before and after ion incorporation into the water matrix. This is depicted in Figure 2.3 for a high (a) and low (b) charge density cation. So-called 'structure breaking' ions increase the entropy of the water matrix, whereas 'structure making' ions will result in a decrease in entropy. Such an increase or decrease can alter the solubility of the electrolyte and its hydration shell properties. Having introduced basic hydration interactions, let us now look at the case of hydrochloric acid (HCl) as this electrolyte is utilised in later ion selectivity experiments within Chapter 6.

[6]Values are often presented as conventional enthalpies, which set the heat of formation of aqueous H^+ to be zero.

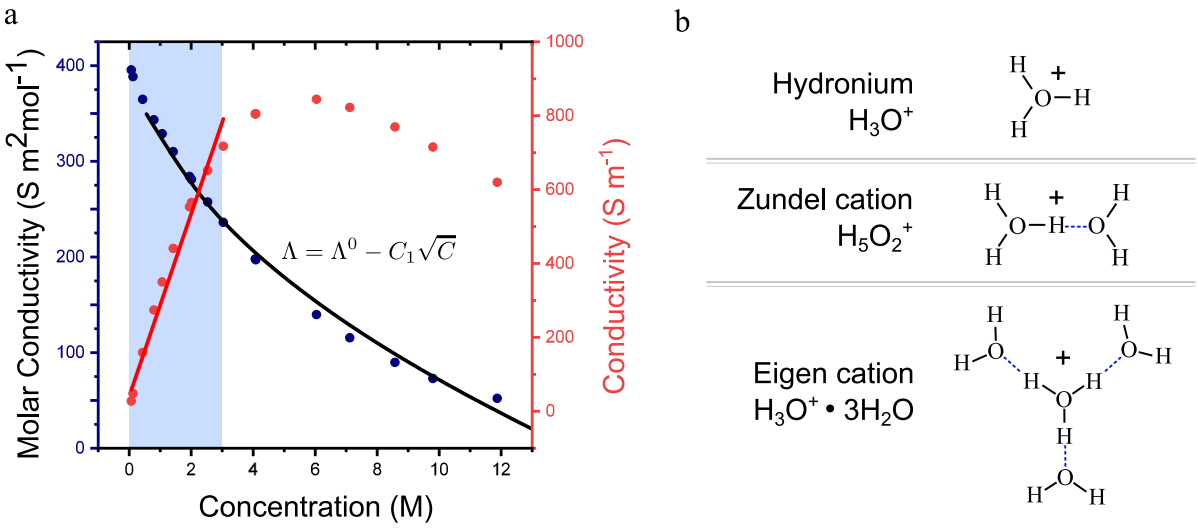

Figure 2.4: (**a**) conductivity (red) and molar conductivity (blue) measurements of an HCl solution at 25 °C at varying concentrations. Molar conductivity has been fitted (black line) using the Fuoss-Onsager limiting law. Data was taken from [27]. (**b**) Three different forms of the hydrogen ion.

2.3.1.1 Hydrochloric Acid

Hydrochloric acid is a solution of hydrogen chloride and water. It is the simplest chloride containing acid in water. The dissociation mechanism of HCl is

$$\mathrm{Cl{-}H{\cdots}OH_2} \overset{1}{\rightleftharpoons} \mathrm{Cl^-{\cdots}H_3O^+} \overset{2}{\rightleftharpoons} \mathrm{Cl^-} + \mathrm{H_3O^+} \qquad \{1\}$$

Where the dashed element is that of a hydrogen bond (H-bond). Reaction 1 shows how the polar nature of water 'captures' the hydrogen from the HCl molecule, forming hydronium which is H-bonded to the chloride anion. During step two, this then dissociates, to form the liberated chloride anion and hydronium cation. The conductivity of HCl increases linearly with concentration until around a concentration of 3 M. Beyond this, the ion conductivity of HCl solution plateaus, where it then begins to decline as concentration is increased further. These two properties of HCl can be seen in figure 2.4 a. The reasons for this phenomenon shall be discussed in the next subsection, but it is due to ion–ion interactions. The blue shaded region, between 0 and 3 M in figure 2.4 is brought to the reader's attention as this is where experiments in Chapter 6 are performed within. Next, let us discuss specific ion mobility phenomena. Before we do, the properties of the ions of HCl: H_3O^+ and Cl^- will be introduced.

2.3.1.2 Hydronium Cation

Until the early 21st century, the structure of the hydrated proton was poorly understood [28]. However, X-ray as well as neutron diffraction measurements and X-ray absorption fine structure measurements implicated that O-H bonding distances vary with HCl concentration [29]–[31]. From these studies, it was concluded that this shift in O-H distance is due to

the formation of the hydronium ion H_3O^+. This hydrated proton takes the form of a water molecule hydrogen-bonded to a proton. A 'free' proton would strongly interact with the dipole nature of water. Thus it is unlikely to exist for long in a hydrous environment [32]. Work by Headrick et al, investigating hydrated clusters of H_3O^+ ions, attribute vibrational spectra to that of two H_3O^+ hydration isomers, the eigen H_3O^+(aq) and zundel $H_5O_2{}^+$(aq) complexes [28]. The putative configurations of both isomers are illustrated in Figure 2.4 b. Studies suggest that both occur in HCl solutions, but the extent to which each occurs, is not clear [33], [34]. The mobility of H_3O^+ in aqueous solutions is significantly higher than that of other cations. Current understandings of this are introduced in section 2.3.2.2.

2.3.1.3 Chloride Anion

Chloride accepts an electron to become the negative Cl^- anion, resulting in an increased bare ion size compared to its atomic dimensions. Table 2.1 provides the bare ion size of Cl^- highlighting the relatively large radius of this anion. This translates to a lower charge density, which, as discussed previously, reduces the water-ion interaction. Neutron diffraction experiments indicate that the chloride ion has been associated with six water molecules with distances to the farthest hydrogen of the water molecule being 3.7 Å[35]. Although, previous studies using freezing point depression data, assign the hydration number as zero [23]. However, this publication makes it clear that there may well exist water interactions, consisting of a weaker nature. Due to its low charge density and specific size, the chloride ion resides within the water matrix without disturbing the structure to the degree of other ions [30], [36], requiring a small decrease in entropy upon hydration [16]. This is also reflected in the smaller change in enthalpy of hydration compared with other ions, shown in Table 2.1. Using isotopic difference methods of neutron diffraction, the hydration of the chloride ion has been reported to be relatively independent of the cation present in the solution [37]. With both the ions of HCl introduced, let us return to discuss ion mobility in the solid and liquid state.

2.3.2 Ionic Mobility

The aim of this subsection is to provide the reader with a higher resolution picture of the governing factors of ion mobility. This will help supplement the overarching theory provided in the earlier Section 2.2, so far as is necessary to understand systems of relevance to this thesis. Firstly, we shall consider ion mobility in aqueous solution and secondly, we shall examine ion mobility in the solid state as systems of study in this thesis involve both.

2.3.2.1 Ion Mobility in Aqueous Solutions

To begin with, let us define mobility. In the presence of an electric field, an ion will drift through a solution at constant velocity v_d balanced by viscous (and other) forces preventing any further acceleration

$$v_d^i = \mu_i E \tag{2.16}$$

where μ_i is the ion mobility which will be dictated by all underlying interactions. We shall next proceed to introduce some of these interactions. Now, in a uniform electric field E, a charged particle will experience an electrostatic force F_E with magnitude

$$F_E = z_i e E \tag{2.17}$$

where z_i is the ion valance, e is the elementary electron charge. Next, from Stokes' law, a solid sphere moving through a viscous solution will experience a frictional force F_{fric} given as

$$F_{fric} = 6\pi r_i \eta v_d^i \tag{2.18}$$

where r_i is the effective ion radius and η is the viscosity of the solution. Despite our prior discussion regarding the complexities of ions in solution, we can (with caution) treat ions as having an 'effective' radius, as presented in Equation 2.18. This encapsulates all the underlying complex interactions into a term in which we can apply Stokes' law. Next, when an ion, in the presence of an electric field, reaches a balance of forces, we can equate equations 2.18 and 2.17, combining with 2.16 to give

$$\mu_i = \frac{z_i e}{6\pi r_i \eta} \tag{2.19}$$

For completeness, we return to the forces that retard ion motion in a solution. To account for electrophoretic, relaxation and other effects, for an ion at a constant drift velocity, the electrostatic force will balance the friction and retarding forces, giving

$$z_i e E = F_{fric} + F_{ep} + F_{relax} + F_{\Delta E} \tag{2.20}$$

Where F_{ep} is the force due to electrophoresis, F_{relax} is the force due to ion atmosphere relaxation effects and $F_{\Delta E}$ is the force due to perturbations to the electric field, from local charge separation. These forces are now briefly discussed.

We have already seen, from Figure 2.4 a, that the value of conductivity decreases with concentration for HCl. This effect arises because, at elevated concentrations, increased electrostatic interactions between ions result in effects such as electrophoretic retardation and relaxation effects, which reduce the solution conductivity [16]. Electrophoretic interactions occur due to ionic atmospheres, rather than hydration spheres. These 'atmospheric' ions are bound to a central ion and are dragged through cross solution flow as opposite central charges move in opposing directions, resulting in enhanced viscous drag. Relaxation effects arise from the same ion cloud, taking a finite time (relaxation time) to respond to ion motion. Therefore, these atmospheric ions lag behind the central ion as it moves in an electric field. This results in an attractive force pulling the ion against its direction of travel. An empirically derived equation for these effects, which was also derived theoretically [16], is known as the Debye-Hucckel-Onsager equation.

$$\Lambda = \Lambda^0 - (a + b\Lambda_0)\sqrt{c_i} \tag{2.21}$$

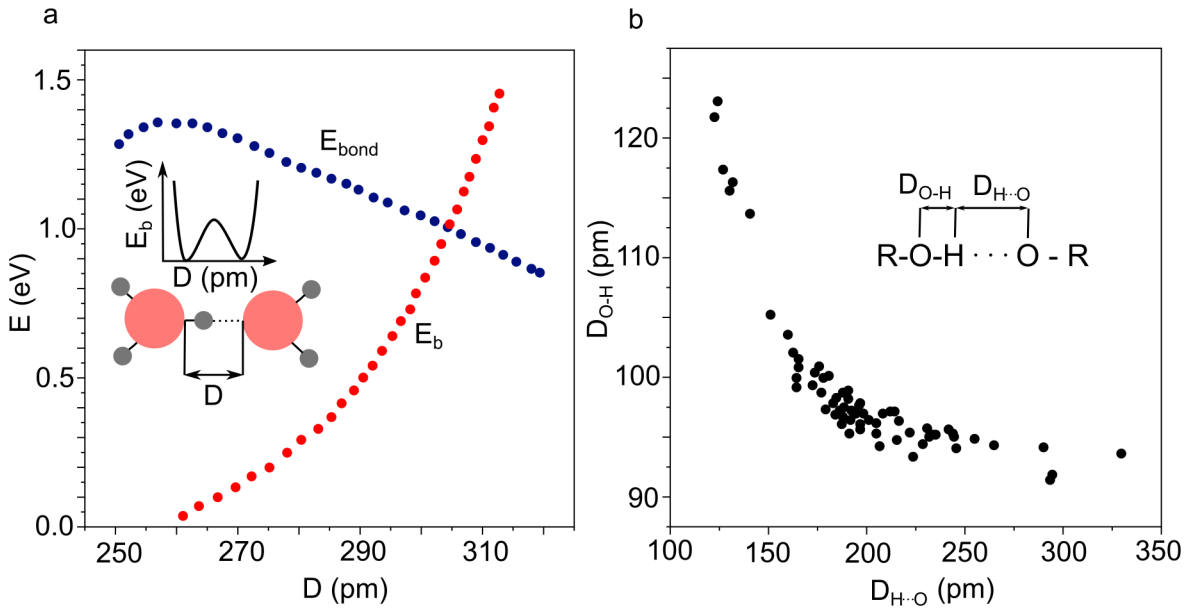

Figure 2.5: (**a**) Hydrogen bond energy (E_{bond}) and proton transfer barrier for the central hydrogen bond of an isolated $H_5O^+_2$ dimer as obtained from ab initio calculations. Adapted from [38]. (**b**) Bond distance relationship for hydrogen bonds of the type R-O-H· · ·O-R in a variety of compounds. Adapted from [39]

.

where Λ is the molar conductivity, Λ_0 is the molar conductivity at infinite dilution, c_i is the concentration of the solution and a and b are both constants that depend upon temperature, the charges of the ions, the dielectric constant and viscosity. The expression presented in Equation 2.21 has been fitted[7] to HCl concentration-dependent data in Figure 2.4 a. Later theories, which took some 30 years to develop, account for perturbations in the applied electric field, and model ion conduction, in aqueous solutions, to a higher degree of precision. These can be derived using Stokes' law (Equation 2.18), the Debeye–Huckel equation for non-ideal activity coefficients, Poisson's equation of electrostatics and Maxwell-Boltzmann distribution functions. The reader is directed to reference [16] for a detailed derivation.

Lastly, in this section, where deviations from high concentration effects are not significant, and there is more than one ion in an aqueous solution, we can introduce the overall solution conductivity (κ), given as

$$\kappa = F \sum_i |z_i| \mu_i C_i \tag{2.22}$$

where F is the Faraday constant, z_i is the ion valence, μ_i is the ion mobility (at infinite dilution) and C_i is the molar concentration of the solution.

Having introduced the key formulae and other interactions in the preceding sections, we can now start to build a picture of ions in solution. They alter the bulk water matrix where they can contain water and ionic atmospheres which affect ion mobility, especially at higher concentration due to ion–ion interactions. Let us now turn our attention to the case of protons, important for research in this thesis, where we highlight some of their unusual properties.

[7] Using Python module 'SciPy'.

2.3.2.2 Proton Mobility and The Hydrogen Bond

Since the early nineteenth century, it has been known that the conductive properties of protons in aqueous solutions differ from that of the other ions [40]. The hydronium cation has the highest mobility of all ions at 36.23×10^{-8}m^2 s^{-1} V^{-1} which is anomalously high for its size and hydration enthalpy. As the mobility of H_3O^+ is ~ 6.5 times higher than expected, if from diffusive transport [20], [41], another mechanism is expected to explain this high mobility. One model accounting for this is the 'Grötthuss mechanism', where protons 'jump' from one water molecule to the next along water chains [41], [42]. Such a transfer involves inter-conversion between the two defect complexes Eigen and Zundel type [17], [34], previously described and shown in Figure 2.3. The jump frequency can be measured from NMR relaxation times [43] and snapshots of the proton-transfer mechanism have also been reported in small water cluster experiments, measuring vibrational spectra [44]. The ability of protons to transfer from one water molecule to another is a direct consequence of the hydrogen bond, now discussed and as already briefly mentioned, responsible for many of the peculiarities of water.

A hydrogen bond (H-bond) is an attractive interaction, between two species, arising from a link of the form $\mathrm{A-H\cdots B}$, as presented in reaction 1, where A and B are electronegative elements and B possesses a lone pair of electrons. At bonding energies as high as $\sim$ 5-10 k_BT, the bond energy is stronger than typical van der Waals bonds which are $\sim 1\ k_BT$ but weaker than covalent bonds of $\sim 100\ k_BT$. The hydrogen bond is a Coulombic interaction but bears semblance to weak covalent bonds [18], which can be relatively directional, giving them the ability to form weak three-dimensional structures in solids. In liquids, the short-range order can be long range whenever hydrogen bonds are involved, giving rise to loose ordering. The binding and barrier energies of the Zundel cation are presented in Figure 2.5 (a), and hydrogen bond length scales (for an arbitrary species R) are given in Figure 2.5 (b).

Hydrogen bonds can be either symmetric or asymmetric. A symmetric hydrogen bond is one in which the hydrogen sits equidistant between (using our earlier example) A and B, such as is the case for $\mathrm{F-H\cdot\cdot F}$ (both 120 pm), but this is a relatively rare case. Asymmetrical bonds, whereby the bonding hydrogen sits at different distances from A and B are relatively more common, such as the hydrogen bond in typical compounds $\mathrm{O-H\cdots O}$ with an intra $\mathrm{O-H}$ distance of 100 pm and inter $\mathrm{O\cdots H}$ bond length of 176 pm [18]. This trend is highlighted in the bonding distances in Figure 2.5 (b). The strengths of hydrogen bonds typically follow a $\frac{1}{r^2}$ dependence, such as that of a charge-dipole interaction. Crucially, for biological systems, hydrogen bonds can occur inter-molecularly as well as intra-molecularly and form in non-polar environments. Thus, they are responsible for many macro-molecular and biological structures, including proteins. They link different segments inside the molecules and in nucleic acids, where they hold the double strands of DNA together. As H-bonds can be easily disrupted, they permit the DNA strands to separate for transcription. Such structures are referred to as hydrogen-bond-derived polymers. Now, the hydrogen bonds in solids also contribute to proton mobility in the solid state, which is the topic of the next subsection.

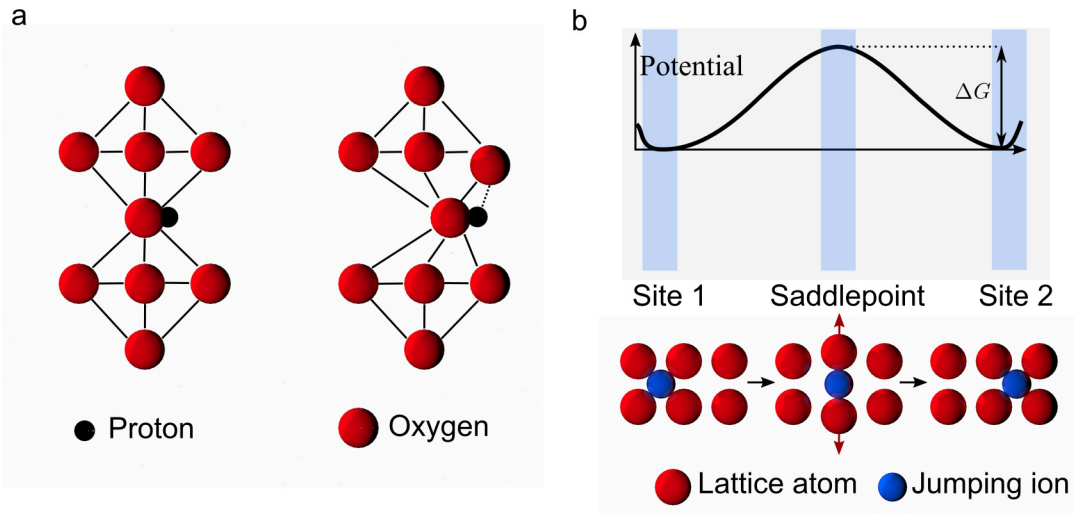

Figure 2.6: (**a**) Transient hydrogen bonding in perovskite-type oxides providing a proton transfer route. [38] (**b**) Ion jump process in a crystalline solid: the blue atom transits from an initial position (left) to a final position (right) pushing through a saddlepoint configuration (middle) [12]

.

2.3.3 Ion Mobility in the Solid State

Moving away from a (purely) aqueous electrolyte, let us turn our attention to how ions can be mobile within the solid state. There is an array of materials that are classed as solid-state ion conductors. Our focus is maintained on systems that are relevant for materials that are utilised in Chapter 7. These being crystalline and polymer ion conductors. First, ion transport in crystalline structures is introduced.

2.3.3.1 Crystalline Ion Transport

In crystalline structures, thermal agitation can create Frenkel disorder within the lattice resulting in thermally created interstitial sites and lattice vacancies. Such defects can act as vehicles for ion diffusion [12]. Fick's law of diffusion and the equations presented in Section 2.2 still apply to ion transport in the solid state, just as in the aqueous environment [12]. From a macroscopic standpoint, diffusion not arising from electro-diffusion is facilitated by Brownian motion, whereby ions make atomic 'jumps' within the lattice, often through Arhhenius activated diffusion. Activated transport has to overcome a potential barrier, as depicted in Figure 2.6 (b). Ion migration in a solid is often the result of such localised jumps, depicted in the same figure.

Ion transport through crystalline materials need not be defect mediated. Jumps across intrinsic interstitial sites offer ion transport pathways, especially for small ions such as H^+ which can often be transported via such interstitial and transient bond pathways. It is also worth noting that small foreign atoms, especially hydrogen, can diffuse via these interstitial sites [12]. The process of transport by interstitial and transient reorientation mechanisms

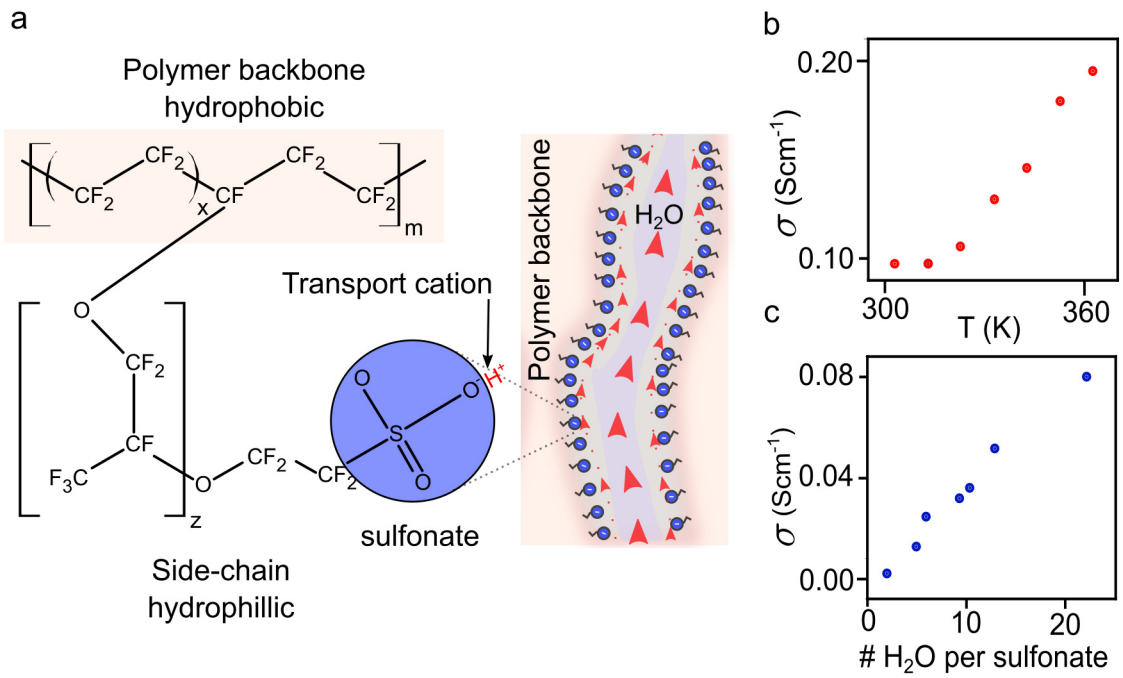

Figure 2.7: (**a**) molecular structure of Nafion showing the poly(tetrafluoroethylene) backbone and perfluoroether pendant side chains terminated by sulfonic acid groups. A depiction of the super–molecular structure, highlighting the proton-conducting channel is also shown. The larger red arrows within the blue hydrated channel, depict the bulk transport region, whereas the smaller red arrows denote the surface proton hopping sites. Nafion proton conductivity dependence on temperature, at constant humidity (**b**) and water content within the polymer (**c**). Data from [46].

are stylised in Figure 2.6 (a). Solid state perovskite ion conductors can transport protons via temporary hydroxide (OH) reorientation [45] and between oxygen atoms. Reorientation of hydroxide and transient bond formation is a two-step process, requiring a distortion of the lattice to accommodate the proton. This shift and a change in the bond environment manifest in OH-infra red absorption spectral changes. Further, oxygen bending modes of the form O – A – O are also thought to provide proton transition state facilitated transport, over oxygen separation distances as large as 312 pm. From Figure 2.5 (b), we can see that this is at the upper end of the H-bond length. Let us look now at a quasi-crystalline or amorphous ion transport through a sulphonated polymer because doing so is important for the work in Chapter 7.

2.3.3.2 Proton-Conducting-Ionomer (Nafion)

Nafion is a widely-used proton-conducting membrane in fuel cell technologies [45] and used as somewhat of a benchmark polymer electrolyte membrane [47]. It is an amphiphilic, sulfonated fluoropolymer-copolymer, comprised of three phases [48]. The first being of an ordered poly(tetrafluoroethylene) backbone, the second being the perfluoroether pendant side chains, terminated with sulfonic acid groups and the third is an amorphous fluorocarbon phase. This is stylised in Figure 2.7 a. Due to its Teflon-like backbone structure, it is chemi-

cally stable and mechanically strong. The cluster-network model of its properties, is a long-enduring one that was introduced in 1981 by Gierke et al [49]. This model is of ion-exchange sites (sulfonic acid groups) aggregating to form nanometre sized clusters [48], indicated by a variety of physical studies, such as small-angle X-ray scattering (SAXS), NMR, electron microscopy and others [49]. In a hydrated environment, the sulfonic acid groups become surrounded by water, and due to their electrostatic interactions, result in proton dissociation, allowing for their mobility via vehicular and molecular transport mechanisms. Vehicular transport, as the name suggests, is due to the proton being transported via a vehicle molecule, such as H_2O, where as molecular transport of ions is proton hopping between molecules, such as is the case of the aforementioned Grötthuss mechanism. The two pathways are shown in an illustration of Nafion proton transport nanochannel in Figure 2.7 a. The parallel nanochannel like features have been elucidated via small-angle X-ray and neutron scattering and matching this to a simulated model [50]. The nanochannel conductivity is highly linked to the hydration properties of the polymer and, hence, water content within the polymer matrix [51]. This is shown in a plot of the conductivity of Nafion 117 (a commercial extruded Nafion membrane of known thickness, fabricated in controlled conditions), in Figure 2.7 c. The temperature dependence of Nafion proton conductivity at a fixed hydration level is given in Figure 2.7 b. Practical upper limits of operating temperature arise from the difficulty in maintaining an adequately high hydration level of both membrane and membrane–electrode interfaces. Research also suggests that the swelling properties of Nafion, due to humidity/water conditions, impact its conductive properties [51]. This 'osmotic swelling' of Nafion can, in some circumstances, be a drawback [48].

Another important consideration of the proton conductivity of Nafion is its dependence on processing history [52]. This is because the proton-conducting properties are related to the complex morphology and the supermolecular organisation of crystalline and ionic domains [52] which form during fabrication. Conditions, such as humidity, temperature and solvent type, impact the structure of the polymer and channel network, especially in the case of re-cast films [52], [53]. Let us now discuss these re-cast films, as they are implemented to make electrolytic contacts in this work, as presented in Chapter 7. Cast polymer films may be semi-crystalline or amorphous, depending on their fabrication history. These Nafion films can be fabricated due to their solubility in ethanol-water mixtures, allowing for the solvent casting of thin films, which once made, are insoluble in water [54], a useful property for aqueous cell use [52]. In the solution phase, SAXS studies have shown Nafion dispersions are comprised of colloidal suspensions of anisotropic polymeric particles [55], although the exact nature of these suspensions is not agreed upon [52]. Room temperature casting, at low humidity, suffers from 'mud-cracking' and can be brittle [52]. This (common) way of making Nafion films can also produce membranes that are soluble in polar organic solvents, which is typically an undesirable feature. It has been reported that casting at high humidty with subsequent heat treatment can improve the longer-range ordering of cast films [52], [56] and their chemical stability. To make films of a consistent nature, we can utilise commercial dispersions of Nafion, such as a perfluorinated resin. These dispersions are typically a mixture of lower aliphatic alcohols and water solutions. Moreover, varying equivalent weight (EW) of

Nafion can be obtained, where the EW of the polymer being the weight of the polymer needed to yield 1 mole of exchangeable protons, the inverse of the ion-exchange capacity (IEC). The EW is dependent upon the ratio of tetrafluoroethylene and side-chain fictionalised tetrafluoroethylene of the Nafion polymer. Applications of Nafion and Nafion resin cast membranes are plentiful. Recently, it has found use as a dehumidifier membrane for the SpaceX Dragon capsule [57]. It can be used to form a proton exchange membrane fuel cell [48], as a molecular sensor [58] composite membranes, to extract solar energy to drive chemical reactions and used as a superacid catalyst [59].

2.3.4 Ion Selectivity

Having gained insight into ionic transport phenomena, in this penultimate section, we shall cover the topic of ion selectivity in more specific systems as this is a central topic in Chapter 6. In Section 2.2.2, a set of equations were presented describing charge selective transport for a given ion transference number. However, minor consideration has been paid to gain mechanistic insights into how the transference numbers arise. The goal of this section is to help address this point. We will cover selectivity via ion hydration, Donnan and nanopore mechanisms.

2.3.4.1 Selectivity Via Ion Hydration

As introduced in Section 2.3.1, each ion will undergo hydration when in an aqueous solvent, and as we have seen, the characteristics of hydration will be unique for each case. Therefore, the energy penalty incurred for dehydration of each ion is distinct. This uniqueness allows for selectivity in systems that, by one way or another, constrict ion transport down to length scales comparable to the hydration radius. Evidence that such dehydration derived selectivity exists in cellular ion-selective channels exists [3], where pores can be selective to potassium over sodium ions. These pores have strategically-situated helices where dipoles are orientated in such a way as to effectively replace the hydration sphere around a K^+ ion, more effectively than a Na^+ ion. This then lowers the energy barrier for potassium ion transport through a constriction. Replicating this feat synthetically, with reasonable fidelity, is a significant technical challenge [60].

2.3.4.2 Selectivity by Donnan Exclusion

Ion-exchange membranes rely upon fixed charge sites within the lattice or framework, where these are negative for cation-exchange membranes (including Nafion) and positive for anion-exchange membranes. The (often) relatively high concentration of these charges in a membrane phase compared to the electrolyte result in Donnan potentials at both interfaces between electrolyte and membrane phases. Fixed charge sites allow higher diffusivity for counter-ions (ions of the opposite sign to the fixed charge) to pass through the membrane,

and restrict the transport of co-ions (ions of the same charge). This electrostatic attraction/repulsion is behind much of the selective properties of systems. Donnan equilibrium theory is a model describing ionic flux through such ion-exchange membranes. This theory rests upon equating the electrochemical potential (see Equation 2.1), in membrane and electrolyte phases. Once we equate this potential for both phases, solution (x) and membrane ($\bar{x}$), we arrive at the expressions (derived in Appendix C) for membrane concentration of cations ($\overline{C}_+$) and anions ($\overline{C}_-$) as

$$\overline{C}_\pm = \frac{1}{2}\sqrt{\overline{C}_R^2 - 4C_-C_+} \pm \overline{C}_R \tag{2.23}$$

where $\overline{C_R}$ is the concentration of fixed charge sites in the membrane and C_- and C_+ are the bulk ion concentrations of anions and cations respectively. The total potential across an ion-exchange membrane can be expressed, from Teorell, Meyer and Sievers (TMS) theory. This is a theory based on Donnan equilibrium, and constrains ionic mobility and activity coefficient to be constant through each exchanger phase [61]. From this assumption, the potential can be given as

$$\Delta\psi = -\frac{RT}{F}\ln\left(\frac{C2}{C_1}\frac{\sqrt{\overline{C}_R^2 - 4C_1^2} + \overline{C}_R}{\sqrt{\overline{C}_R^2 - 4C_2^2} + \overline{C}_R}\right) - \frac{RT}{F}\bar{\mu}\ln\left(\frac{C2}{C_1}\frac{\sqrt{\overline{C}_R^2 - 4C_1^2} + \bar{\mu}\overline{C}_R}{\sqrt{\overline{C}_R^2 - 4C_2^2} + \bar{\mu}\overline{C}_R}\right) \tag{2.24}$$

where the membrane phase mobility is given as

$$\bar{\mu} = \frac{\bar{\mu}_+ - \bar{\mu}_-}{\bar{\mu}_+ + \bar{\mu}_-}$$

and the current flux through an ion-exchange membrane is

$$J_+ = \frac{\overline{D}_+\overline{D}_-(z_+^2\overline{C}_+ z_-^2\overline{C}_-)}{z_+^2\overline{D}_+\overline{C}_+ + z_-^2\overline{D}_-\overline{C}_-}\frac{d\overline{C}_+}{dx},\ J_- = \frac{\overline{D}_+\overline{D}_-(z_+^2\overline{C}_+ z_-^2\overline{C}_-)}{z_+^2\overline{D}_+\overline{C}_+ + z_-^2\overline{D}_-\overline{C}_-}\frac{d\overline{C}_-}{dx} \tag{2.25}$$

Taking the limiting cases for both J_+ and J_-

$$\lim_{\overline{C}_-\to 0} J_+ = -\overline{D}_-\frac{d\overline{C}_+}{dx}$$

$$\lim_{\overline{C}_-\to 0} J_- = 0$$

Donnan exclusion, typically within polymers, allows for a wide range of separation and transport technologies (or has the potential to). For example, Donnan dialysis has been applied in the recovery of free acids or bases from spent treatment bath solutions [62]. Nafion finds uses in fuel cell applications [62] and generally speaking, they hold promise for vanadium redox flow batteries [63] (a rechargeable flow battery that utilises vanadium ions in different oxidation states, storing chemical potential energy).

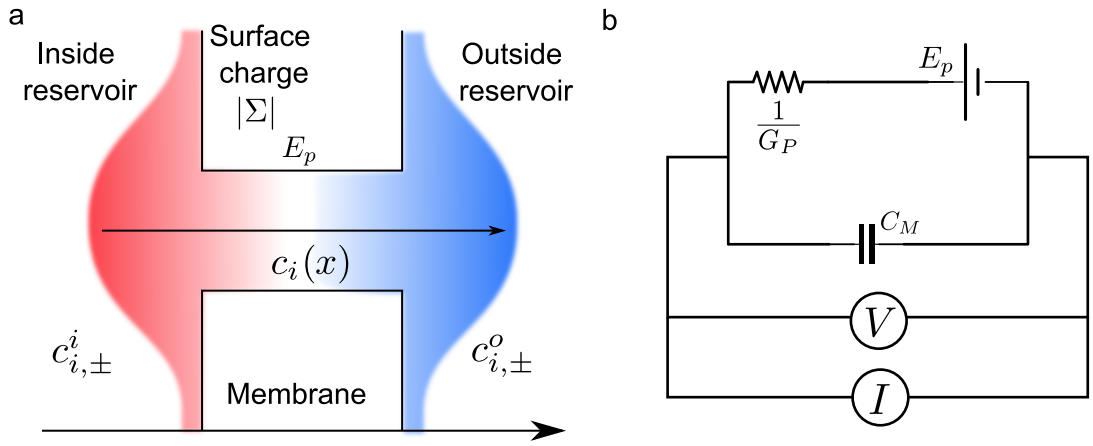

Figure 2.8: (**a**) Potential profile within the vicinity of the nanopore. The pore is shown within a membrane with surface charge $|\Sigma|$. Surface effects extend the effective potential range of the pore. (**b**) An equivalent electrical circuit of a nanopore, incorporating the capacitance from the membrane. The voltage across the pore E_P can be thought of as a 'Nernst Battery'. Measurement configuration of a nanopore is also shown. Adapted from [11]

2.3.4.3 Selectivity of Nanopores

Nanopores are physical constrictions separating electrolyte phases, typically having diameters of less than 100 nm, but can cover a broader definition of 1–1000 nm. Their ionic transport properties diverge from bulk behaviour due to their restrictive size. Entrance, passage and exit effects can produce ion selective phenomena [11], [64]–[66]. Effective selectivity is achieved when the characteristic length scale of the screened surface charge is comparable to the physical dimensions of the pore or if there is such a high level of confinement that the hydration radius is commensurate to pore size [66]. This results in the surface charge effects overlapping with the pore. To describe the ion transport properties of nanopores, we must turn to the equations presented in section 2.2. By solving either the PNP or PNP-NS set of equations, which are difficult, and often impossible, to solve analytically, it is possible to model their properties. Nevertheless, solutions can be found for some ideal cases, such as the constant electric field approximation, where the field is assumed constant inside the pore. This is known as the Goldman-Hodgkin-Katz (GHK) equation [11] for the pore potential E_p, is

$$E_p = \frac{RT}{F} \ln \left(\frac{\sum_{i,\ cations} P_{i,+} c^o_{i,+} + \sum_{i,\ anions} P_{i,-} c^i_{i,-}}{\sum_{i,\ cations} P_{i,+} c^i_{i,+} + \sum_{i,\ anions} P_{i,-} c^o_{i,-}} \right) \tag{2.26}$$

where $P_{i,\pm}$ are the permeability coefficients, c^o is the concentration of ion species outside and c^i is the concentration of ion species inside the nanopore. The GHK equations have a significant shortcoming, surface charge effects are neglected. The pore conductance (G_P) through a nanopore was also modelled by solving the PNP equations [67]:

$$G_P = k_b \left[\frac{4L}{\pi D^2} \frac{1}{1 + 4\frac{l_{Du}}{D}} + \frac{2}{\alpha D} \right]^{-1} \tag{2.27}$$

where k_b is the bulk conductivity, L and D is the pore length and diameter respectively, l_{Du} is the Dukhin length (defined as the surface to bulk conductivity ratio) and α is a geometrical prefactor. The Dukhin length characterises the channel scale below which surface conduction dominates over the bulk one [68], given as

$$l_{Du} = \frac{|\Sigma|}{c_i} \tag{2.28}$$

where Σ is the surface charge density, c_i is the solute concentration. Let a surface possess a charge of 0.3 e nm^{-2}. The Durkhin length will correspondingly be 0.5 nm and 5 μm for concentrations of 1M and 10^{-4} M respectively. This highlights the wide-ranging length scales of this value. The current-voltage (I-V) relationships of nanopores can be of various forms. For example, nonlinear currents through single-layer MoS_2 sub-nm nanopores have been observed at elevated voltages [65]. Intrinsic nanopores in chemical-vapour-deposited (CVD) graphene have been shown to possess different current-voltage behaviour and three orders of magnitude variance in ion conduction [69]. Graphene nanopores displaying linear, voltage-activated (nonlinear) and rectified ion transport were reported in the same work. This different behaviour is attributed to surface charge and dissociable group entry/exit effects on the pore.

The applications of nanopores merit attention. A significant application is the use of nanopores as DNA sequencers. Oxford Nanopore Technologies Ltd have commercialised sequencing utilising an engineered derivative of Escherichia coli Curlin sigma S-dependent growth (CsgG) pore protein [70], [71]. This company challenged the convention that one must remove the negative sites within nanopores to allow DNA translocation. The technology, in essence, works by measuring base pair specific ion current fluctuations during DNA translocation through the pore. For solid-state synthetic nanopores, there remain gaps in the knowledge of ion transport, especially for those with pore diameters smaller than 10 nm [60]. The effects of slip flow enhancement, where atomically-smooth walls of the pore invalidate no-slip conditions, [72] are typical of fluid mechanics. Other effects to study are those of phase changes and solvation behaviours within the confined pore space, to name a few [60].

2.3.5 Electrical Double Layer

Here, in the final section of this chapter, we shall look at how ions within water interact with a charged solid surface. A surface immersed in water often becomes charged with co-ions due to the high dielectric constant of water [73]. This can occur via three charge regulation mechanisms. First, via the ionisation or dissociation of surface groups, for example

$$-\mathrm{COOH} \rightarrow -\mathrm{COO}^- + \mathrm{H}^+ \qquad \{2\}$$

leaving behind a negatively charged surface and a dissociated proton. Which can, in turn, allow for positively charged co-ion formation

$$-\mathrm{COO}^- + \mathrm{Ca}^{2+} \rightarrow -\mathrm{COOCa}^+ \qquad \{3\}$$

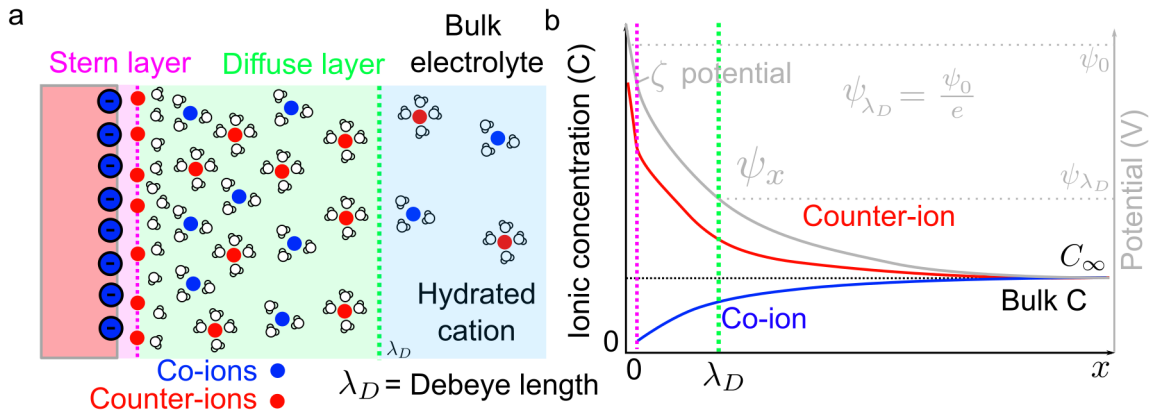

Figure 2.9: (**a**) Electrical double layer (EDL) concentration profile showing the Stern layer and effects within the EDL. (**b**) Ion concentration and potential profile through the double layer region. The Helmholtz plane is the interface between the diffuse and Stern layers. Figures adapted from [18].

in which the anionic sites are initially vacated by reactions, such as that in Reaction 2. Secondly, by the adsorption or binding of ions from solution to an uncharged surface, such as Ca^{2+} binding to zwitterionic groups[8] or OH^- adsorption. Sites that facilitate ion adsorption, as shown in Reaction 3, are known ion-exchangers (discussed at length in Chapter 4) consisting of ion-exchangeable groups/surfaces. A third mechanism is the charge exchange between two surfaces that are brought in close proximity to one another. The charge can transfer between them. Now, once a surface is charged with co-ions, an oppositely charged layer of counter-ions will form to (at least in part) neutralise this layer. These are typically transiently bound[9] via physisorption or chemically bound. Beyond this, ions are considered 'free' but still interact with the charge, as a diffuse atmosphere known as the diffuse double layer, where the concentration will be different to that of the bulk value, as shown in Figure 2.9. The electrostatic screening length λ_D, termed the Debye length, determines the effective range of electrostatic interactions in the solution [66]. By solving the Poisson-Boltzmann equations, presented in Appendix D, we can characterise this length, as well as the concentration profile, as a function of distance, from the charged surface [18], [73]. For low surface potentials (where $e|\psi| \ll k_B T$) which is typically the case when $\psi \leq 25$mV, we can express the Debye length, from the Grahame equation [18], [73] as

$$\lambda_D = \left(\frac{\epsilon_0 \epsilon_r k_B T}{\sum_i \rho_{\infty,i} e^2 z_i^2} \right)^{\frac{1}{2}} \text{m} \tag{2.29}$$

where $\rho_{\infty,i}$ is the bulk concentration value of ion species i. The physical significance of the Debye length is as follows. For the same low potential conditions, it is the characteristic length at which the potential, away from the surface, decays by a factor 1/e. This is a result of the potential, as a function of distance x, approximated as

$$\psi_x \approx \psi_0 \cdot \exp^{-\frac{x}{\lambda_D}} \tag{2.30}$$

[8] molecules containing an equal number of positively- and negatively-charged sites
[9] with lifetimes varying from nanoseconds to hours

as is shown in Figure 2.9. The ionic concentrations within the double layer region, can be high compared to the bulk. For a surface charge of 0.2 Cm^{-2}, using the Poisson-Boltzmann model, we can estimate that the density of counter-ions at the surface. This may well be as high as 12 M given a bulk concentration of 0.7 M. [18]. However, the model is a simplification and neglects important effects, such as ion hydration [74]. We can better model the double layer as two distinct layers. The first, being the Stern layer, consists of immobile ions adsorbed onto the surface, forming a sharp increase in concentration and potential at the boundary. The finite size of the counter-ions (and their associated hydration radii) result in a layer of definite width. The second layer is consisted of a diffuse (also known as Gouy–Chapman) layer consisting of hydrated mobile ions, which obey Poisson–Boltzmann statistics. Both of these layers are illustrated in figure 2.9. Further, the boundary interface between the diffuse and Stern layers is known as the Helmholtz plane, and at this interface, the potential is defined as the zeta potential [73]. Finally, the interface between an ion exchanging membrane exhibiting Donnan exclusion, will also have an electrical double layer at the interface, where the screening of fixed charges in the membrane, constitute the so called 'Nernst-layer', discussed in Chapter 4.

2.4 Summary

In this chapter, we introduced the reader to the fundamental concepts of ion transport within bulk electrolytes and ion-selective behaviour. It was shown that the underlying cause of transport is a gradient in the electrochemical potential, a simple example of which being Fick's first law of diffusion. This states that particles will tend to disperse along concentration gradients. Taking our discussion further, we have the PNP equations, which we can solve for more complex scenarios, such as nanopore ion transport. For dynamic transport, we can incorporate the Navier–Stokes equations, where the solutions to which allow for a rich and diverse array of phenomena. We have seen that ion transport within the solid state is often an Arhennius activated process, with diffusion described by Equation 2.9. In the liquid state, ionic mobility and diffusion are related via the Einstein-Smoluchowski relation. We have briefly explored Donnan selectivity theory as well as ion hydration effects. Hydrochloric acid and it's constituent ions of hydronium and chloride were presented. At elevated concentrations, the ion–ion interactions reduce bulk mobility, as given by the Debeye-Hucckel-Onsager Equation 2.21. Because HCl was used in the work presented in Chapter 6, it is an important consideration. The specific and unique case of proton mobility was introduced along with a basic description of ion transport within the crystalline and semi-crystalline (polymer) phases. We then explored the selectivity using three different, yet ultimately related, means, those of hydration, Donnan exclusion and nanopores. Lastly, the concept of the EDL was introduced to the reader. Ion transport is a rich and diverse area of research, especially for nanoscopic systems. This is, as we have seen, a result of confinement effects that can be steric, electrostatic or both, as well as concentration gradients within a membrane phase, resulting in ion-selective behaviour.

References

[1] E. Gouaux and R. MacKinnon, "Principles of selective ion transport in channels and pumps," *Science*, vol. 310, no. 5753, pp. 1461–1465, 2005, ISSN: 00368075. DOI: 10.1126/science.1113666.

[2] J. P. Abrahams, A. G. Leslie, R. Lutter, and J. E. Walker, "Structure at 2.8 Å resolution of F1-ATPase from bovine heart mitochondria," *Nature*, vol. 370, no. 6491, pp. 621–628, 1994.

[3] D. A. Doyle, J. M. Cabral, R. A. Pfuetzner, A. Kuo, J. M. Gulbis, S. L. Cohen, B. T. Chait, and R. MacKinnon, "The structure of the potassium channel: Molecular basis of K^+ conduction and selectivity," *Science*, vol. 280, no. 5360, pp. 69–77, 1998.

[4] M. Jain, S. Koren, K. H. Miga, J. Quick, A. C. Rand, T. A. Sasani, J. R. Tyson, A. D. Beggs, A. T. Dilthey, I. T. Fiddes, *et al.*, "Nanopore sequencing and assembly of a human genome with ultra-long reads," *Nature Biotechnology*, vol. 36, no. 4, pp. 338–345, 2018.

[5] J. Feng, M. Graf, K. Liu, D. Ovchinnikov, D. Dumcenco, M. Heiranian, V. Nandigana, N. R. Aluru, A. Kis, and A. Radenovic, "Single-layer MoS_2 nanopores as nanopower generators," *Nature*, vol. 536, no. 7615, pp. 197–200, 2016.

[6] P. Długołęcki, K. Nymeijer, S. Metz, and M. Wessling, "Current status of ion exchange membranes for power generation from salinity gradients," *Journal of Membrane Science*, vol. 319, no. 1-2, pp. 214–222, 2008.

[7] S. J. Peighambardoust, S. Rowshanzamir, and M. Amjadi, "Review of the proton exchange membranes for fuel cell applications," *International Journal of Hydrogen Energy*, vol. 35, no. 17, pp. 9349–9384, 2010.

[8] G. Merle, M. Wessling, and K. Nijmeijer, "Anion exchange membranes for alkaline fuel cells: A review," *Journal of Membrane Science*, vol. 377, no. 1-2, pp. 1–35, 2011.

[9] A. Parasuraman, T. M. Lim, C. Menictas, and M. Skyllas-Kazacos, "Review of material research and development for vanadium redox flow battery applications," *Electrochimica Acta*, vol. 101, pp. 27–40, 2013.

[10] A. J. Bard, L. R. Faulkner, *et al.*, "Fundamentals and applications," *Electrochemical Methods*, vol. 2, no. 482, pp. 580–632, 2001.

[11] M. Muthukumar, *Polymer Translocation*. CRC press, 2016, pp. 209–306.

[12] H. Mehrer, *Diffusion in solids: fundamentals, methods, materials, diffusion-controlled processes*. Springer Science & Business Media, 2007, vol. 155, pp. 100–200.

[13] M. Kunst and J. M. Warman, "Proton mobility in ice," *Nature*, vol. 288, no. 5790, pp. 465–467, 1980.

[14] J. W. Perram and P. J. Stiles, "On the nature of liquid junction and membrane potentials," *Physical Chemistry Chemical Physics*, vol. 8, no. 36, pp. 4200–4213, 2006.

[15] J. Mähler and I. Persson, "A study of the hydration of the alkali metal ions in aqueous solution," *Inorganic Chemistry*, vol. 51, no. 1, pp. 425–438, 2012.

[16] M. R. Wright, *An introduction to aqueous electrolyte solutions*. John Wiley & Sons, 2007, pp. 2–29.

[17] N. Agmon, H. J. Bakker, R. K. Campen, R. H. Henchman, P. Pohl, S. Roke, M. Thämer, and A. Hassanali, "Protons and hydroxide ions in aqueous systems," *Chemical Reviews*, vol. 116, no. 13, pp. 7642–7672, 2016.

[18] J. N. Israelachvili, *Intermolecular and surface forces*. Academic Press, 2011, pp. 50–600.

[19] E. Brini, C. J. Fennell, M. Fernandez-Serra, B. Hribar-Lee, M. Luksic, and K. A. Dill, "How water's properties are encoded in its molecular structure and energies," *Chemical Reviews*, vol. 117, no. 19, pp. 12 385–12 414, 2017.

[20] P. Atkins and J. De Paula, *Atkins' physical chemistry*, 11th ed. Oxford University press Oxford, 2017.

[21] D. Asthagiri, L. R. Pratt, and H. Ashbaugh, "Absolute hydration free energies of ions, ion–water clusters, and quasichemical theory," *The Journal of Chemical Physics*, vol. 119, no. 5, pp. 2702–2708, 2003.

[22] J. Burgess, *Ions in solution: basic principles of chemical interactions*. Elsevier, 1999, pp. 50–100.

[23] A. A. Zavitsas, "Properties of water solutions of electrolytes and non-electrolytes," *The Journal of Physical Chemistry B*, vol. 105, no. 32, pp. 7805–7817, 2001.

[24] R. Impey, P. Madden, and I. McDonald, "Hydration and mobility of ions in solution," *The Journal of Physical Chemistry*, vol. 87, no. 25, pp. 5071–5083, 1983.

[25] M. D. Tissandier, K. A. Cowen, W. Y. Feng, E. Gundlach, M. H. Cohen, A. D. Earhart, J. V. Coe, and T. R. Tuttle, "The proton's absolute aqueous enthalpy and Gibbs free energy of solvation from cluster-ion solvation data," *The Journal of Physical Chemistry A*, vol. 102, no. 40, pp. 7787–7794, 1998.

[26] W. M. Haynes, *CRC handbook of chemistry and physics*. CRC press, 2014, pp. 900–1000.

[27] B. B. Owen and F. H. Sweeton, "The conductance of hydrochloric acid in aqueous solutions," *Journal of the American Chemical Society*, vol. 63, no. 10, pp. 2811–2817, 1941.

[28] J. M. Headrick, E. G. Diken, R. S. Walters, N. I. Hammer, R. A. Christie, J. Cui, E. M. Myshakin, M. A. Duncan, M. A. Johnson, and K. D. Jordan, "Spectral signatures of hydrated proton vibrations in water clusters," *Science*, vol. 308, no. 5729, pp. 1765–1769, 2005.

[29] R. Triolo and A. Narten, "Diffraction pattern and structure of aqueous hydrochloric acid solutions at 20° C," *The Journal of Chemical Physics*, vol. 63, no. 8, pp. 3624–3631, 1975.

[30] A. Botti, F. Bruni, S. Imberti, M. Ricci, and A. Soper, "Ions in water: The microscopic structure of a concentrated HCl solution," *The Journal of Chemical Physics*, vol. 121, no. 16, pp. 7840–7848, 2004.

[31] J. L. Fulton and M. Balasubramanian, "Structure of hydronium (H_3O^+)/chloride (Cl^-) contact ion pairs in aqueous hydrochloric acid solution: A Zundel-like local configuration," *Journal of the American Chemical Society*, vol. 132, no. 36, pp. 12 597–12 604, 2010.

[32] G. Tawa, I. Topol, S. Burt, R. Caldwell, and A. Rashin, "Calculation of the aqueous solvation free energy of the proton," *The Journal of Chemical Physics*, vol. 109, no. 12, pp. 4852–4863, 1998.

[33] A. Botti, F. Bruni, M. Ricci, and A. Soper, "Eigen versus Zundel complexes in HCl-water mixtures," *The Journal of Chemical Physics*, vol. 125, no. 1, p. 014 508, 2006.

[34] M. Chen, L. Zheng, B. Santra, H.-Y. Ko, R. A. DiStasio Jr, M. L. Klein, R. Car, and X. Wu, "Hydroxide diffuses slower than hydronium in water because its solvated structure inhibits correlated proton transfer," *Nature Chemistry*, vol. 10, no. 4, pp. 413–419, 2018.

[35] D. Powell, G. Neilson, and J. Enderby, "The structure of Cl^- in aqueous solution: An experimental determination of gClH(r) and gClO(r)," *Journal of Physics: Condensed Matter*, vol. 5, no. 32, p. 5723, 1993.

[36] R. Mancinelli, A. Botti, F. Bruni, M. Ricci, and A. Soper, "Hydration of sodium, potassium, and chloride ions in solution and the concept of structure maker/breaker," *The Journal of Physical Chemistry B*, vol. 111, no. 48, pp. 13 570–13 577, 2007.

[37] S. Cummings, J. Enderby, G. W. Neilson, J. Newsome, R. Howe, W. Howells, and A. Soper, "Chloride ions in aqueous solutions," *Nature*, vol. 287, no. 5784, pp. 714–716, 1980.

[38] K. Kreuer, "On the complexity of proton conduction phenomena," *Solid State Ionics*, vol. 136, pp. 149–160, 2000.

[39] K.-D. Kreuer, "Proton conductivity: Materials and applications," *Chemistry of Materials*, vol. 8, no. 3, pp. 610–641, 1996.

[40] D. Marx, "Proton transfer 200 years after von Grotthuss: Insights from ab initio simulations," *ChemPhysChem*, vol. 7, no. 9, pp. 1848–1870, 2006.

[41] S. Cukierman, "Et tu, Grotthuss! and other unfinished stories," *Biochimica et Biophysica Acta (BBA)-Bioenergetics*, vol. 1757, no. 8, pp. 876–885, 2006.

[42] D. P. Wilkinson, J. Zhang, R. Hui, J. Fergus, and X. Li, *Proton exchange membrane fuel cells: materials properties and performance*. CRC press, 2009.

[43] B. Halle and G. Karlström, "Prototropic charge migration in water. part 2.—interpretation of nuclear magnetic resonance and conductivity data in terms of model mechanisms," *Journal of the Chemical Society, Faraday Transactions 2: Molecular and Chemical Physics*, vol. 79, no. 7, pp. 1047–1073, 1983.

[44] C. T. Wolke, J. A. Fournier, L. C. Dzugan, M. R. Fagiani, T. T. Odbadrakh, H. Knorke, K. D. Jordan, A. B. McCoy, K. R. Asmis, and M. A. Johnson, "Spectroscopic snapshots of the proton-transfer mechanism in water," *Science*, vol. 354, no. 6316, pp. 1131–1135, 2016.

[45] K. Kreuer, "On the development of proton conducting materials for technological applications," *The Journal of Chemical Physics*, vol. 97, no. 1-4, pp. 1–15, 1997.

[46] T. A. Zawodzinski Jr, T. E. Springer, J. Davey, R. Jestel, C. Lopez, J. Valerio, and S. Gottesfeld, "A comparative study of water uptake by and transport through ionomeric fuel cell membranes," *Journal of the Electrochemical Society*, vol. 140, no. 7, p. 1981, 1993.

[47] M. B. Karimi, F. Mohammadi, and K. Hooshyari, "Recent approaches to improve Nafion performance for fuel cell applications: A review," *International Journal of Hydrogen Energy*, vol. 44, no. 54, pp. 28 919–28 938, 2019.

[48] M. Mishra, *Encyclopedia of Polymer Applications, 3 Volume Set*. CRC press, 2018.

[49] T. D. Gierke, G. Munn, and F. Wilson, "The morphology in Nafion perfluorinated membrane products, as determined by wide-and small-angle X-ray studies," *Journal of Polymer Science: Polymer Physics Edition*, vol. 19, no. 11, pp. 1687–1704, 1981.

[50] K. Schmidt-Rohr and Q. Chen, "Parallel cylindrical water nanochannels in Nafion fuel-cell membranes," *Nature Materials*, vol. 7, no. 1, pp. 75–83, 2008.

[51] M. Casciola, G. Alberti, M. Sganappa, and R. Narducci, "On the decay of Nafion proton conductivity at high temperature and relative humidity," *Journal of Power Sources*, vol. 162, no. 1, pp. 141–145, 2006.

[52] K. A. Mauritz and R. B. Moore, "State of understanding of Nafion," *Chemical Reviews*, vol. 104, no. 10, pp. 4535–4586, 2004.

[53] R. Silva, M. De Francesco, and A. Pozio, "Solution-cast Nafion® ionomer membranes: Preparation and characterization," *Electrochimica Acta*, vol. 49, no. 19, pp. 3211–3219, 2004.

[54] C. R. Martin, T. A. Rhoades, and J. A. Ferguson, "Dissolution of perfluorinated ion-containing polymers," *Analytical Chemistry*, vol. 54, no. 9, pp. 1639–1641, 1982.

[55] A. Rebrov, A. Ozerin, D. Svergun, L. Bobrova, and N. Bakeyev, "Small angle x-ray scatter study of the aggregation of macromolecules of the perfluorosulphonated ionomer in solution," *Polymer Science USSR*, vol. 32, no. 8, pp. 1515–1521, 1990.

[56] J. Halim, G. G. Scherer, and M. Stamm, "Characterization of recast Nafion films by small-and wide-angle X-ray scattering," *Macromolecular Chemistry and Physics*, vol. 195, no. 12, pp. 3783–3788, 1994.

[57] J. Silverman, A. Irby, and T. Agerton, "Development of the crew dragon ECLSS," presented at the International Conference on Environmental Systems ICES-2020-333, 2020.

[58] D. Baba, A. S. Nugraha, M. Iqbal, J. Bo, C. Li, A. A. Alshehri, J. You, V. Malgras, Y. Yamachi, and T. Asahi, "Nafion®-coated mesoporous Pd film toward remarkably enhanced detection of lactic acid," *RSC Advances*, vol. 8, no. 19, pp. 10 446–10 449, 2018.

[59] G. A. Olah, P. S. Iyer, and G. S. Prakash, "Perfluorinated resin sulfonic acid (Nafion-H®) catalysis in synthesis," *Synthesis*, vol. 1986, no. 07, pp. 513–531, 1986.

[60] S. Faucher, N. Aluru, M. Z. Bazant, D. Blankschtein, A. H. Brozena, J. Cumings, J. Pedro de Souza, M. Elimelech, R. Epsztein, J. T. Fourkas, *et al.*, "Critical knowledge gaps in mass transport through single-digit nanopores: A review and perspective," *The Journal of Physical Chemistry C*, vol. 123, no. 35, pp. 21 309–21 326, 2019.

[61] Y. Tanaka, *Ion Exchange Membranes: Fundamentals and Applications*, 2nd ed. Elsevier, 2015, pp. 29–100.

[62] J. Ran, L. Wu, Y. He, Z. Yang, Y. Wang, C. Jiang, L. Ge, E. Bakangura, and T. Xu, "Ion exchange membranes: New developments and applications," *Journal of Membrane Science*, vol. 522, pp. 267–291, 2017.

[63] Y. Shi, C. Eze, B. Xiong, W. He, H. Zhang, T. Lim, A. Ukil, and J. Zhao, "Recent development of membrane for vanadium redox flow battery applications: A review," *Applied Energy*, vol. 238, pp. 202–224, 2019.

[64] M. Tagliazucchi and I. Szleifer, *Chemically Modified Nanopores and Nanochannels*. William Andrew, 2016, pp. 40–50.

[65] J. Feng, K. Liu, M. Graf, D. Dumcenco, A. Kis, M. Di Ventra, and A. Radenovic, "Observation of ionic coulomb blockade in nanopores," *Nature Materials*, vol. 15, no. 8, pp. 850–855, 2016.

[66] M. Macha, S. Marion, V. V. Nandigana, and A. Radenovic, "2D materials as an emerging platform for nanopore-based power generation," *Nature Reviews Materials*, vol. 4, no. 9, pp. 588–605, 2019.

[67] C. Lee, L. Joly, A. Siria, A.-L. Biance, R. Fulcrand, and L. Bocquet, "Large apparent electric size of solid-state nanopores due to spatially extended surface conduction," *Nano Letters*, vol. 12, no. 8, pp. 4037–4044, 2012.

[68] L. Bocquet and E. Charlaix, "Nanofluidics, from bulk to interfaces," *Chemical Society Reviews*, vol. 39, no. 3, pp. 1073–1095, 2010.

[69] T. Jain, B. C. Rasera, R. J. S. Guerrero, M. S. Boutilier, S. C. O'hern, J.-C. Idrobo, and R. Karnik, "Heterogeneous sub-continuum ionic transport in statistically isolated graphene nanopores," *Nature Nanotechnology*, vol. 10, no. 12, pp. 1053–1057, 2015.

[70] C. G. Brown and J. Clarke, "Nanopore development at Oxford nanopore," *Nature Biotechnology*, vol. 34, no. 8, pp. 810–811, 2016.

[71] F. J. Rang, W. P. Kloosterman, and J. de Ridder, "From squiggle to basepair: Computational approaches for improving nanopore sequencing read accuracy," *Genome Biology*, vol. 19, no. 1, p. 90, 2018.

[72] K. Falk, F. Sedlmeier, L. Joly, R. R. Netz, and L. Bocquet, "Molecular origin of fast water transport in carbon nanotube membranes: Superlubricity versus curvature dependent friction," *Nano Letters*, vol. 10, no. 10, pp. 4067–4073, 2010.

[73] H.-J. Butt, K. Graf, and M. Kappl, *Physics and chemistry of interfaces*, 1st ed. John Wiley & Sons, 2003, pp. 42–116.

[74] S. S. Lee, P. Fenter, C. Park, N. C. Sturchio, and K. L. Nagy, "Hydrated cation speciation at the muscovite (001)- water interface," *Langmuir*, vol. 26, no. 22, pp. 16 647–16 651, 2010.

Chapter 3

Proton Transport Through 2D Materials

Having considered ion transport in a general sense, let us look at a relatively new class of membranes, that has attracted considerable attention as proton-conductors - 2D materials. In this chapter, we shall first define a 2D material and then present three examples of such, namely graphene, hexagonal boron nitride (hBN) and the mica family of crystals. Their basic crystallographic and electronic properties are presented. After which, we shall consider existing experimental and theoretical work related to 2D materials as proton-conducting membranes.

3.1 2D Materials

With restricted precision, we can describe 2D materials as those that possess one spatial dimension confined to the few nanometre length scale. Graphene can unequivocally be described as 2D [1], because it is comprised of a single plane of carbon atoms. However, bi- and tri-atomic-layer materials, in some sense, can also be regarded as 2D materials by a more precise definition. This being: if a material's properties (such as electronic) diverge from that of the bulk, due to nanometre-scale restrictions of one dimension, it can be regarded as a 2D material [1]. Now, bulk graphite is made of atomic stacks comprised of innumerable sheets of graphene (see figure 3.1 b), and since the pioneering work of Novoselov et al [2], we are now able to extract these layers utilising relatively simple techniques. Graphene and other atomically-thin crystals were believed to be purely 'academic' materials and not stable enough to exist in isolation [1], [3]. However, reports of few-layer graphite did emerge during the twentieth century [4], [5], but did not receive substantial attention until graphene was first mechanically exfoliated [2] and it's rich electronic properties revealed [6], [7]. In crystallographic terms, if a material exhibits basal cleavage, then it splits along definite crystallographic structural planes. This is a characteristic of many materials, synthetic as well as naturally occurring. These can, very often, be mechanically peeled to create 2D materials. We should at this stage distinguish between mechanically exfoliated (isolated from bulk crystals) to deposited (i.e., from CVD) 2D materials. Said materials can be stacked and interfaced in van der Waals heterostructure assemblies [8], allowing for a vast array of material functionality. This process is somewhat akin to building with Lego, with blocks defined with single atomic-plane precision [9]. Let us now introduce the first, and most studied of the 2D materials, graphene.

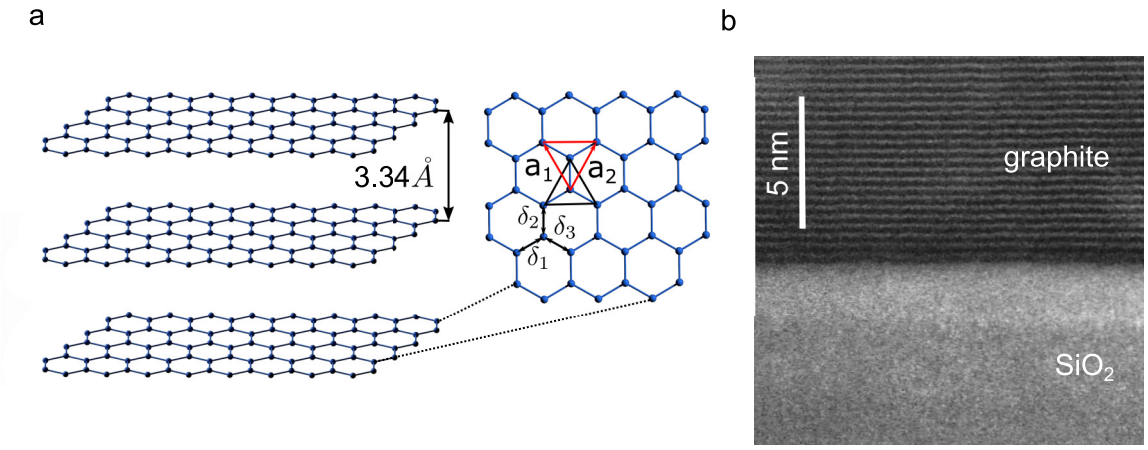

Figure 3.1: (**a**) The crystal structure of few layer graphene showing the lattice vectors a_1 and a_2. Carbon-carbon distances (δ_1, δ_2 and δ_3) are 1.42 Å. (**b**) S/TEM image of graphite on SiO_2 showing the constituent layers of graphene Credit: Dr Yichao Zho. By measuring the distance of multiple sheets and dividing by the number of layers, we crudely arrive at an estimate of the interlayer spacing (neglecting the graphene thickness itself) as 3.35 Å.

3.1.1 Graphene

Graphene is by far the more well-known 2D material. It is an allotrope[1] of carbon. Bulk graphite, the common form of carbon, is made of stacks of graphene separated by an interlayer distance of 3.33 Å to 3.35 Å [10]. This interlayer distance can be measured to a high degree of precision using X-ray diffraction [11] and be measured directly from scanning transmission electron microscopy (S/TEM) cross-section imaging, an example (produced during this work) is presented in Figure 3.1 b. The inter-atomic distance between carbon atoms, within the plane, is 1.42 Å [12], [13] also shown in the same figure. The trigonal structure of graphene is a result of the sp^2 hybridisation between one s orbital and two p orbitals. This results in a σ bond between carbon atoms and is responsible for its mechanical strength. The remaining p orbital forms π electron bands, responsible for the conduction properties of graphene, discussed shortly. The pristine sheets of graphene have some remarkable mechanical strength properties. It has an ultimate tensile strength[2] of 130 GPa when measured via a diamond atomic force microscopy (AFM) tip [14]. For context, the ultimate tensile strength of high-strength low-alloy sheet steel is 549 MPa [15]. However, (direct) comparisons between pristine monolayer graphene and steel are arguably not fair. This is because the mechanical strengths of materials typically depend upon their average crystalline defects, or dislocations, rather than their intrinsic properties [16]. Indeed, theoretical perfect crystals have been modelled to have strengths many times greater than those actually measured [16].

We are now returning to the electronic properties of graphene because they also warrant further attention. Graphene is classed as a semi-metal where valence and conduction bands cross at six vertices of the Brillouin zone, forming linearly dispersing Dirac cones. In each unit cell of graphene, there are 12 electrons, two of which are in the 1 s band, 6 of which are

[1] A different physical form of which an element can exist.
[2] The maximum stress that a material can withstand while being stretched or pulled before breaking.

in the sp^2 σ bands. The bonding π band is doubly occupied with the remaining two electrons per cell. These π band electrons, according to the single-particle tight-binding model [17], have the energy band-structure

$$E_{\pi}^{\pm}(k) = \pm\gamma \left[1 + 4\, cos\left(k_x \frac{a}{2}\right) cos\left(\sqrt{3}k_y \frac{a}{2}\right) + 4cos^2\left(k_x \frac{a}{2}\right)\right]^{1/2} \tag{3.1}$$

where k is the in-plane momentum, a is the lattice constant and γ is the near-neighbour hopping energy. This dispersion relation has since been confirmed using angle-resolved photoemission spectroscopy (ARPES) [18] and has some interesting properties. A notable one being its linear dispersion relation at low energies. This is to be expected if we expand Equation 3.1 and use the relation for the effective speed (c^*) of the electron in solid-state physics

$$c^* = \hbar^{-1} \frac{dE(k)}{dk} \tag{3.2}$$

where $\hbar$ is the reduced Planck's constant. This results in graphene's charge carriers being described as massless relativistic Dirac fermions [7], obeying the Dirac equation, with $c^* \approx \frac{c}{300}$ where c is the speed of light. The mobilities of graphene at room temperature are also remarkable. Values as high as 140,000 $cm^2\ V^{-1}s^{-1}$ and ballistic transport (without scattering) lengths of over 15 μm have been reported [19]. These values are well above those seen in typical semiconductors, such as Si and GaAs, both below 10,000 $cm^2\ V^{-1}s^{-1}$ [20]. Because graphene is a semi-metal with quasiparticles obeying the linear dispersion of Equation 3.1, this results in a low density of states at the Fermi level (for typical doping levels). Hence, pristine graphene is inert in catalysis [21]. This is an important point to consider concerning the activity of the graphene surface membrane. In graphene, the π electron system of sp^2 carbons is characterised by strong polarisability, so dispersion and induction interactions dominate [22], [23]. Electron transport research in graphene has proved to be a cornucopia of rich phenomena over the years [12]. Recently, twisted bilayer-graphene was reported to be superconductive at so-called magic angles [24] and exotic hydrodynamic 'viscous' electron fluids have been revealed [25], [26] along with above–room temperature quantum 'Brown Zak' oscillations [27]. Exploring graphene provides researchers 'bench top' systems enabling a seemingly limitless set of experiments to be performed upon. Even this many years on from its first isolation [2], it is still producing exciting scientific surprises. Let us now look at another 2D material, which has in many ways allowed researchers to isolate graphene from substrate interference. Such interference can alter the lattice constant and the electronic structure [28]. Now, let us introduce this 2D material, that of so-called 'white graphene'.

3.1.2 Hexagonal Boron Nitride

Hexagonal boron nitride (hBN) is an allotrope of boron nitride. Similar to graphene, hBN is comprised of stacks of B-N atomic-plane layers. These are separated by an interlayer distance of 3.33 Å [29] with a B-N inter-atomic distance (slightly larger than graphene) of 1.45 Å [29] and, thus, have a lattice mismatch of around 1.7 % [30]. Boron nitride also occurs in

other crystalline forms, including zincblende, and wurtzite. This is due to various hybridisation modes of the constituent boron and nitrogen atoms. However, hexagonal boron nitride is the most stable form at room temperature and is isostructural to graphite. The key difference between graphene and hBN is that the unit cell of the hBN lattice is comprised of two different atoms. This results in the hybridisation of atomic orbitals in a differing fashion than that of graphene, resulting in hBN being a wide band gap (5.96 eV) material [31], [32]. This has been evaluated theoretically using density functional theory (DFT) and projector augmented wave (PAW) potentials [33]. Fabrication of high-quality hBN [34] facilitates it's use to encapsulate and elucidate the properties of graphene [34], as well as other 2D materials [8], a particularly useful feature for their research. This is because previous studies of graphene, which had graphene supported atop of silicon or silicon oxide, suffered from substrate interactions, masking the intrinsic properties.

The mechanical strength of monolayer hBN has been measured, byway of AFM, and an ultimate tensile strength of 70.5$\pm$5.5 GPa has been reported [35]. In contrast to graphene, whose strength decreases significantly with increased thickness, few-layer BN nanosheets (up to 9 L) have a strength similar to that of 1 L BN. Now, as mentioned for graphene, a monolayer of hBN is polarisable, also consisting of slightly polar B-N bonds [22], [23]. Let us now consider the final 2D material of those important to our results, mica.

3.1.3 Mica

The mica group is a large collection of sheet silicate minerals that share a common crystal unit but have significant diversity in chemical composition. They can also contain rare and trace element[3] chemistry within the lattice. This diversity reflects the stability and accommodating nature of its structure [36]. Let us now describe this lattice, where the reader is referred to Figure 3.2 to help clarify the proceeding description.

The atomic framework of mica diverges from the single-layer 'honeycomb' of graphene and hBN, and in its simplest terms, can be described in the following 'sandwich-like' stack structure. It is made from a repeating tetrahedra-octahedra-tetrahedra 'TOT' unit that is electrostatically bound to it's neighbour with interlayer cations, where the crystal can be made 2D by cleaving along this ion plane, thus exfoliating the crystal down to few or single layers. This TOT-c structure is comprised of silica (Si^{4+} or Al^{3+} centred) tetrahedra (T) and an octahedral sheet (O) which can encompass different central cations, such as Al^{3+} or Mg^{2+}. Depending on the cation valence of the octahedral layer, the mica is said to be dioctahedral or trioctahedral, resulting in 1 in 3 vacant and filled octahedra, respectively. An important characteristic of micas is their excess negative charge of the TOT unit, which is -1 e per formula unit (pfu) for the ideal crystal, but can be as high as -3 e and below -0.65 e pfu [36]. This can arise from, or due in combination from, four distinct ways. (1) Substitution of the Si^{4+} tetrahedral cation with a T^{3+} ion. (2) Substitution of a lower valence cation in the octahedra. (3) Vacancies forming in cation sites of the octahedra and finally (4) where the dehydroxylation of OH^- to

[3]For example, roscoelite is a vanadium-containing mica and there also exists a barium rich muscovite.

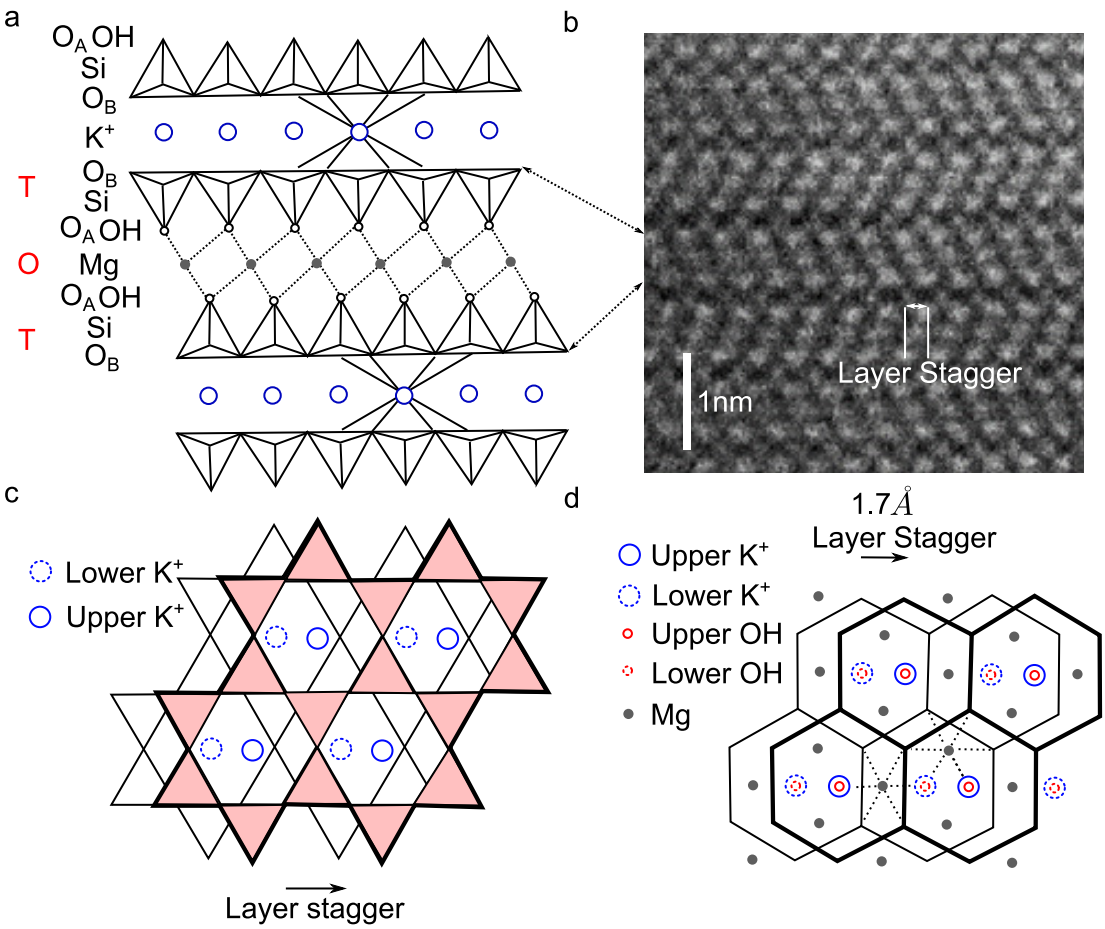

Figure 3.2: (**a**) (010) projection representing one mica layer with adjacent parts of the next layers. The O_A oxygens overlap and obscure the OH ions, which sit directly underneath the potassium K^+ ions. The Si,K,Mg and OH ions may be substituted in other micas. Figure adapted from [36]. **b**) S/TEM image of muscovite (010) projection. Observable is the monoclinic $2M_1$ structure. Credit: Dr Yichao Zho. **c**) and **d**) Plan view showing a TOT-c layer. Adapted from [36]

O^{2-} can occur [36]. This fixed negative charge in the lattice must be compensated to satisfy electroneutrality. This is achieved by way of the interlayer binding cations. Now, crucially for the results of Chapter 7 and 8, these compensating ions on the surface and, to some extent, within the lattice, can be exchanged stoichiometrically with other ions. The proceeding chapter shall explore this concept further, so we shall intentionally limit the description here. Further, along with cations, neutral atoms such as H_2O and Ar are permissible within the interlayer gallery.

There are many polytypes of mica [36]. This topic is covered in additional detail in the proceeding chapter. These polytypes are variations in the stacking of neighbouring TOT units. An example of such being the $2M_1$ muscovite polytype presented in figure 3.2 b which is comprised of an alternating 120° rotation of the lattice, normal to the TOT layer. Along with differing polytypes, there are two sub-groups of mica: the 2:1 group (which we have already introduced) and 1:1 type mica that have a TO-TO structure, such as kaolinte. However, we will keep our consideration to the former, as this is the group related to later results in Chapter 7 and 8. Finally, the electronic properties of mica are now briefly discussed. We

have already seen that micas are a broad class of crystals with varying compositions. The electrical properties of mica therefore naturally vary from one type to another, associated with transition metal atoms in the lattice. Naturally occurring micas such as muscovite and biotite, give measurable pre-breakdown currents and have a temperature-dependent breakdown strength. Synthetic micas, on the contrary, have negligible pre-breakdown currents and have a breakdown strength that is independent of temperature [37]. The fundamental band gap of muscovite mica is thought to be around 7.85 eV [38], [39]. One study reports a decreasing band gap as the layer thickness is reduced [40]. Using conducting-AFM-based characterisation, this work provides experimental evidence for a band gap decrease to 2.5 eV for bilayer muscovite. Biotite mica often has a significant Fe content within the octahedral layer and an experimental study reported that its conductivity exponentially depends upon such impurity content [41].

3.1.4 Isolating 2D Materials

Having introduced three different 2D materials, we will now consider how we can isolate them. This topic will also be expanded upon in the experimental techniques chapter (Chapter 5). Firstly, a common laboratory method to isolate 2D materials, from bulk crystals, is the use of micro-mechanical cleavage, typically via the 'scotch tape' method [7], [42]. This deceptively simple-sounding technique involves peeling the crystals down to 2D thicknesses using adhesive tape and then transferring the materials to a selected substrate, often silicon oxide or polymer-coated silicon wafer. Remarkably, we can observe such atomically-thin crystals using optical microscopy if we optimise the substrate optical interference effects [43]. Next, they can be micro-manipulated and manoeuvred into the desired position using techniques such as 'dry peeling' [44] or 'wet transferring' [45]. Lastly, to measure and characterise the thickness of the 2D material, we can perform AFM microscopy or exploit folded edges of the material, which we can observe via TEM to see individual atomic layers (see Figure 3.1 b). For the case of graphene, we can infer whether it is monolayer using Raman spectroscopy via measurement of the 2D and G peak [46] and we can use Raman to characterise defect properties, by measurement of the D and D' peaks [47]. Raman spectroscopy is discussed in more detail in Chapter 5, Section 5.1.5. Having introduced 2D materials and how we can isolate them, let us now introduce the background to proton transport through these materials.

3.2 Proton-Conducting Properties

Excluding hydrogen, pristine 2D materials have experimentally shown to be impermeable to all gases [48], [49] with accuracy down to permeation rates of 10^5–10^6 atoms s^{-1}. A study, with improved accuracy [50], also demonstrated such impermeability. Both results have been supported by density function theory calculations [51], [52], where prohibitively-high barriers, in the absence of defects, restrict atomic transport through the lattice. Further, pristine graphene and 2D-hBN are chemically inert [23], [53], [54] and believed to be hydrophobic

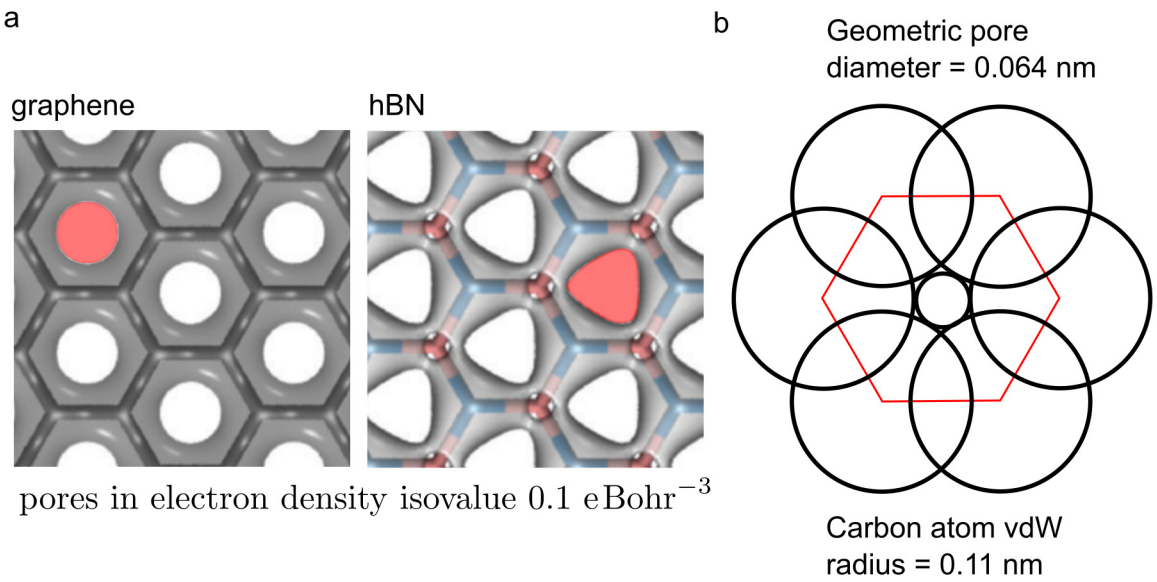

Figure 3.3: (**a**) Pores in the charge density isovalue of 0.1 e Bohr^{-3} for graphene (left) and hBN (right). The ratio of pore areas $\frac{A_{hBN}}{A_{graphene}}$ is approximately 1.3. Adapted from [23]. (**b**) The geometric pore of graphene using the van der Waals radius of carbon of 0.11 nm. Adapted from [48].

materials, when in ambient conditions [55]. Therefore, it has generally been expected that no ions should penetrate their dense electron clouds, unless they possess kinetic energies significantly higher than ambient thermal values [56], [57]. Let us examine the intrinsic lattice pores of monolayer graphene and hBN, stylised in figures 3.3 a and b.

In the centre of the hexagonal structure of graphene and hBN, there are regions of reduced electron density (see Figure 3.3 a). The approximate ratio of hBN and graphene pore area (in the 0.1 e Bohr^{-3} isovalue) is 1.3. This region could, in principle, provide a permeation route for ions, as we have seen from nanopore transport in Chapter 2. Figure 3.3 b also depicts the geometric pore, estimated from the van der Waals (vdW) radius of carbon value at 0.11 nm. Although we must treat (often empirically derived) effective vdW radii and kinetic diameters with caution, such values have proven useful in characterising gas transport through pores in previous studies [58], [59]. With this caveat in mind, the effective geometrical pore of graphene is presented in Figure 3.3, with a diameter of 0.064 nm. This value is smaller than most typical bare ionic radii and significantly smaller than estimated hydration radii (see Table 2.1). An exception would be the unique case of the proton having a bare ion size far smaller than other ions [60]. However, although a proton is unlikely to exist in a free state for long, especially in a hydrous environment [61]. Therefore, this would likely correspond to ion transport, through such a restriction, being an energetically unfavourable process. DFT modelling supports this restrictive barrier view, as we shall discuss in the proceeding subsection 3.2.2. Surprisingly and unpredictably however, experimentally-observed proton transport through graphene and hBN was reported by Hu et al [62]. We shall now discuss this publication in some detail, as this work is foundational to this subject matter. Other related experimental work is also provided in the proceeding subsection along with

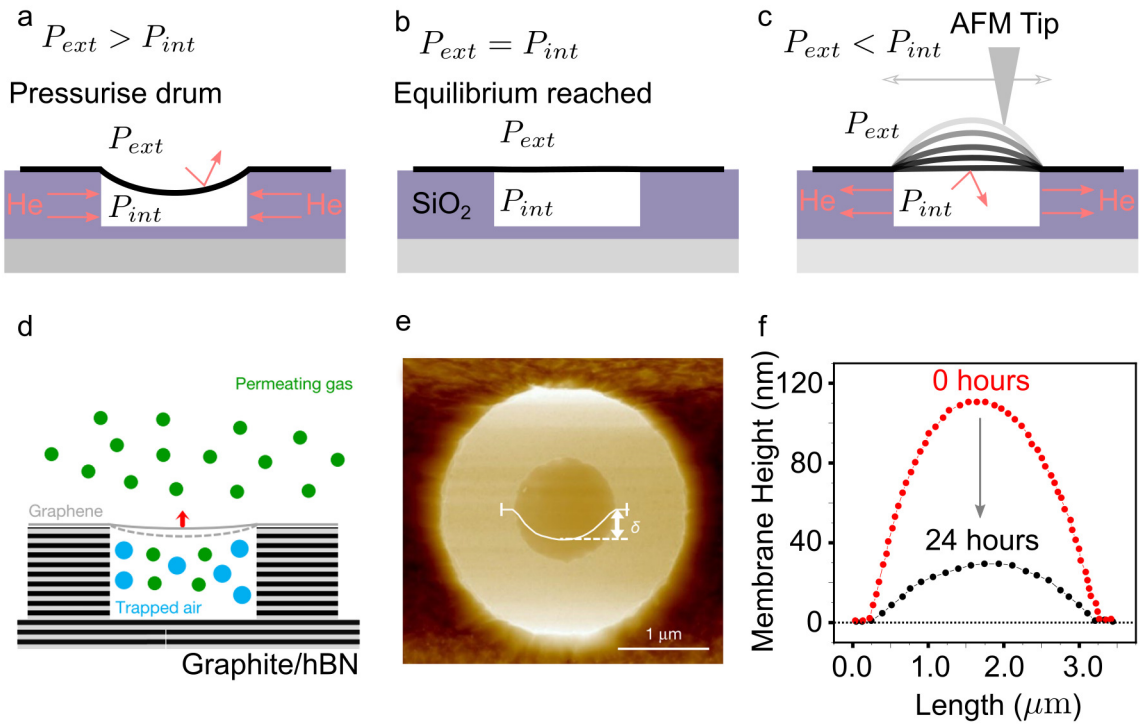

Figure 3.4: (**a**) 2D material suspended over a cavity in SiO_2 creating a micro balloon. (**b**) After some time (typically, a few days) the pressure equilibrates across the membrane. (**c**) The device is removed from higher pressure to ambient conditions, where the rate of balloon deflation is monitored over time. (**d**) A microchamber using a graphite/hBN drum rather than SiO_2. Adapted from [50] (**e**) AFM image of such a graphite well micro chamber before gas filling of the microcavity. The AFM deflection profile is superimposed in the centre of the image. Adapted from [50]. (**f**) deflection change of a graphene micro balloon over 24 hours. Adapted from [62].

complimentary theoretical modelling of proton transport through 2D materials.

3.2.1 Previous Experimental Work

Before we review the unexpected experimental results of Hu et al and other related proton transport studies, let us briefly return to reviewing publications on the impermeability of 2D crystal membranes in additional detail.

3.2.1.1 Impermeability of Bulk Crystal Exfoliated Graphene

Measurements of the gas impermeability of 2D materials have involved inflation and/or deflation of mechanically-exfoliated 2D material capped micro-chamber cavities, etched in SiO_2 [49], graphite or hBN [50]. The reported advantage of using monocrystalline graphite or hBN micro-chambers is the reduced substrate diffusion compared to SiO_2. 2D materials, suspended over such cavities, create a 'drumhead' with the 'skin' being a 2D material membrane. If a pressure gradient exists, then the drum will bulge or depress to a certain degree.

The pressure difference is established by slowly filling, or attempting to fill, the drum volume through the substrate or 2D material itself. The former case exploits the slow diffusion constant of gases such as He through the substrate (or interface), for example, SiO_2 [63]. This is illustrated in Figure 3.4 a-c. Thereafter, the membrane bulges when returned to ambient pressures and can readily be measured using time-dependent AFM microscopy. In work by Sun et al., a partial pressure differential outside versus inside the microchamber is established and if the membrane is permeable to this gas, the partial pressures inside and outside should equalise so that the total pressure inside the containers would increase with time (concerning ambient air), resulting in a measurable gradual bulging of membranes. The diffusion of gases through the membrane (or chamber walls/interface) is characterised by monitoring the deflation or inflation of the nano-balloon with time, depicted in Figure 3.4 f. In the context of the results presented in this thesis, the conclusions of these studies based on measurements of the membrane deflection show that mechanically-exfoliated graphene is often impermeable and defect-free and are significant. As we shall see, the significance lies in its contribution to the debate as to the defective nature of these membranes, with such defects potentially providing an ion transport pathway. We shall return to the impermeability of graphene publication by Sun et al. [50] at the end of the next subsection, as the measurement of significant diffusion of molecular hydrogen is notable. Let us now review the experimental reports of thermal proton transport through atomically-thin crystals.

3.2.1.2 Proton Transport

Hu et al. demonstrated experimental evidence for proton transport through pristine 2D materials [62]. Let us describe this seminal work in more detail. Devices were fabricated by suspending mechanically exfoliated (via the 'scotch tape' method) 2D materials hBN, graphene and MoS_2 membranes across few micron SiN perforations. Exfoliated membranes were tested for measurable defects using the same procedure used to measure micro-chamber cavities described in section 3.2.1.1. Proton-conducting contacts were then made to the 2D material byway of Nafion, Pt, Pd or HCl electrolyte. Shown in Figure 3.5 b and Figure 3.6 c is such a setup for Nafion and HCl contacted membranes, respectively. Electrical measurements were performed using PdHx contacts or Pt decorated carbon cloth contacts in a hydrated, hydrogen-rich atmosphere, which, as we saw in Chapter 2, Section 2.3.3.2, is required for the proton conductivity of the polymer. Along with direct (DC) proton current measurements, devices were configured to capture and measure the evolved hydrogen at the cathode. This demonstrated that the electrical current applied through these devices translated to (close to Faradaic[4]) hydrogen flux, measured using mass flow spectrometry. Next, the proton conductivity of the suspended 2D materials was enhanced by decorating the graphene and hBN membranes with catalytic metal nanoparticles (Pt or Pd). This enhances the conductivity of monolayer hBN devices to such an extent that the current is limited by Nafion's series resistance rather than transport through the Pt-activated monolayer hBN. Lastly, proton conductivity measurements were shown to be the same for HCl liquid cell measurements as that

[4]Where we can correlate electrical measurements to electrochemical reactions.

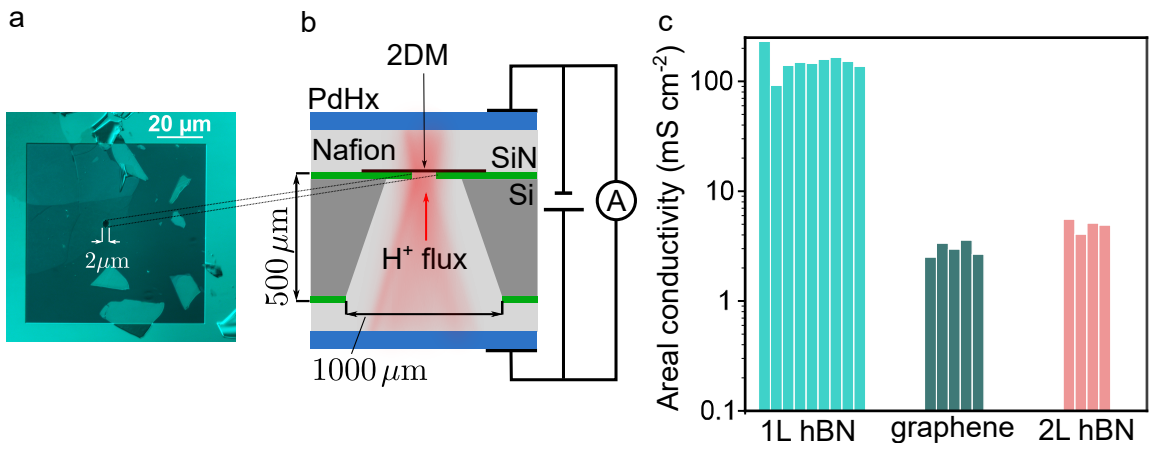

Figure 3.5: (**a**) Optical image of a suspended 2D material over an aperture in SiN projected onto a device schematic (**a**). (**c**) Measurements of areal proton conductivity of multiple devices of the design shown in b. Adapted from [62].

of using the solid polymer electrolyte, Nafion. This was stated to demonstrate the generality of proton transport measurements. HCl was used as the electrolyte and Ag/AgCl working electrodes rather than Nafion solid-state electrolyte and PdHx electrodes, respectively. Now, we shall discuss the findings of this study.

The significant results of this work are the following. Firstly, proton conductance measurements are presented, revealing experimental evidence for proton conduction through defect-free[5] 2D materials. Secondly, temperature dependence measurements reveal Arhhenius activated transport (discussed in Chapter 2), with energy barriers lower than anticipated from previous modelling [52], [64], [65]. These barriers were reported to be 0.3 ± 0.02 eV and 0.78 ± 0.03 eV for monolayer hBN and graphene, respectively. Thirdly, the below background proton transport measurements of MoS_2 are attributed to the higher density of electron clouds of monolayer MoS_2, implying that the higher proton permeation through graphene and hBN is due to their lower electron cloud density. This is, therefore, assumed by the authors to be an intrinsic property of the materials, rather than a defect mediated effect. Lastly, proton transport was reported to be enhanced by decorating the 2D materials with catalytically active nanoparticles, to such an extent that they were 'invisible' in Nafion devices. Having considered this pioneering study on 2D material proton transport, let us now discuss subsequent related work.

Using similar device designs as those of Hu et al., Lozada et al. report isotopic selectivity between protons and deuterons, with a separation factor (α) of ~ 10 [66]. This is significantly higher than state of the art commercially relevant separation factors, typically being below 2.5 [67]. Isotopic selectivity is something not hitherto discussed. Therefore, let us briefly consider this. Isotope separation mechanisms often depend upon the isotopic differences in mass, which for the mass ratio of protons (M_P) and deuterons (M_D) is significant at $\frac{M_D}{M_P} = 2$ but relatively less pronounced for higher atomic number elements. The kinetic isotope effect [68] is a phenomenon whereby the extra mass of heavier isotopes, can alter equilibrium constants

[5] In so much as what we have discussed in the 'Impermeability of graphene' section.

between isotopes. For example, the Girdler sulphide process, important for separating heavy water (D_2O), relies upon the isotopic difference in equilibrium constant dependence on temperature [69]. Fundamentally, this effect arises from differences in vibrational ground states due to isotopic perturbation along energy pathway minima [70]. Consequently, the isotope selectivity of pristine graphene is attributed to a difference of ~ 60 meV between zero-point energies of incident protons and deuterons bound to water molecules within Nafion. If the concentration of one of the isotopes is low, then the separation factor (α) is

$$\alpha = \frac{[H][D^+]}{[D][H^+]} \approx exp\left(\frac{\Delta E}{k_B T}\right) \tag{3.3}$$

where ΔE is the difference in zero-point vibrational energy. This separation factor neglects differences in attempt frequency between deuterons and hydrons. The concept of attempt frequency is linked back to that of the Arrhenius equation given in chapter 2, equation 2.9. It is also worth considering that kinetic isotope effects have also been reported in Nafion-only fuel cells [71], where (deuterium concentration-dependent) separation factors as high as $\alpha = 4$ have been reported. Further, the difference in diffusion constants between hydrogen isotopes in Nafion was reported using NMR diffusometry [72]. No such Nafion only selectivity was observed by Lozada et al, [66] from their Nafion control experiments. Let us now turn to CVD graphene proton transport studies.

Experimental reports of isotope separation through a few centimetre-sized membranes, based on large-scale CVD graphene, have been reported in the related literature with separation factors of 8 [73] and 14 [74]. This is, perhaps, surprising when selective isotope transport is predicated upon transport through the intrinsic lattice of graphene. The typically defective nature of CVD graphene [75]–[78], would allow Nafion to circumvent the graphene membrane, and likely deteriorate membrane selectivity. Banhart et al. wrote a comprehensive review of structural defects in graphene [57]. Suffice to say, there a multitude of sp^2 preserving defects possible in the graphene lattice. To (experimentally) highlight this nature of CVD graphene, Walker et al. report minimally proton selective[6] transport through CVD graphene in a liquid HCl cell configuration, as shown in figure 3.6 b. However, when CVD defects were blocked via atomic layer deposition (ALD) of Al_2O_3 [78], [79], membranes subsequently display partial proton selectivity, alluding to the steric nature of proton selectivity in this experimental system. The ALD sealing of membranes is made possible by exploiting the increased surface energy at graphene defect sites. This results in preferentially adsorbed gas precursor molecules at such lattice defects [78]. The authors of this publication challenge the suggestion that proton transport occurs through the lattice, as proposed by Hu et al. [62], because if it were so, then proton conductivity should not decrease significantly before and after defect blocking of CVD graphene when the lattice is significantly permeable, contrary to their findings.

Further work yielding experimental evidence for proton transport through CVD graphene, lacking macroscopic defects, have been reported. Achytyl et al. present proton transport via

[6]Which, as we have discussed, may indicate a lack of physical ionic constriction through the membrane.

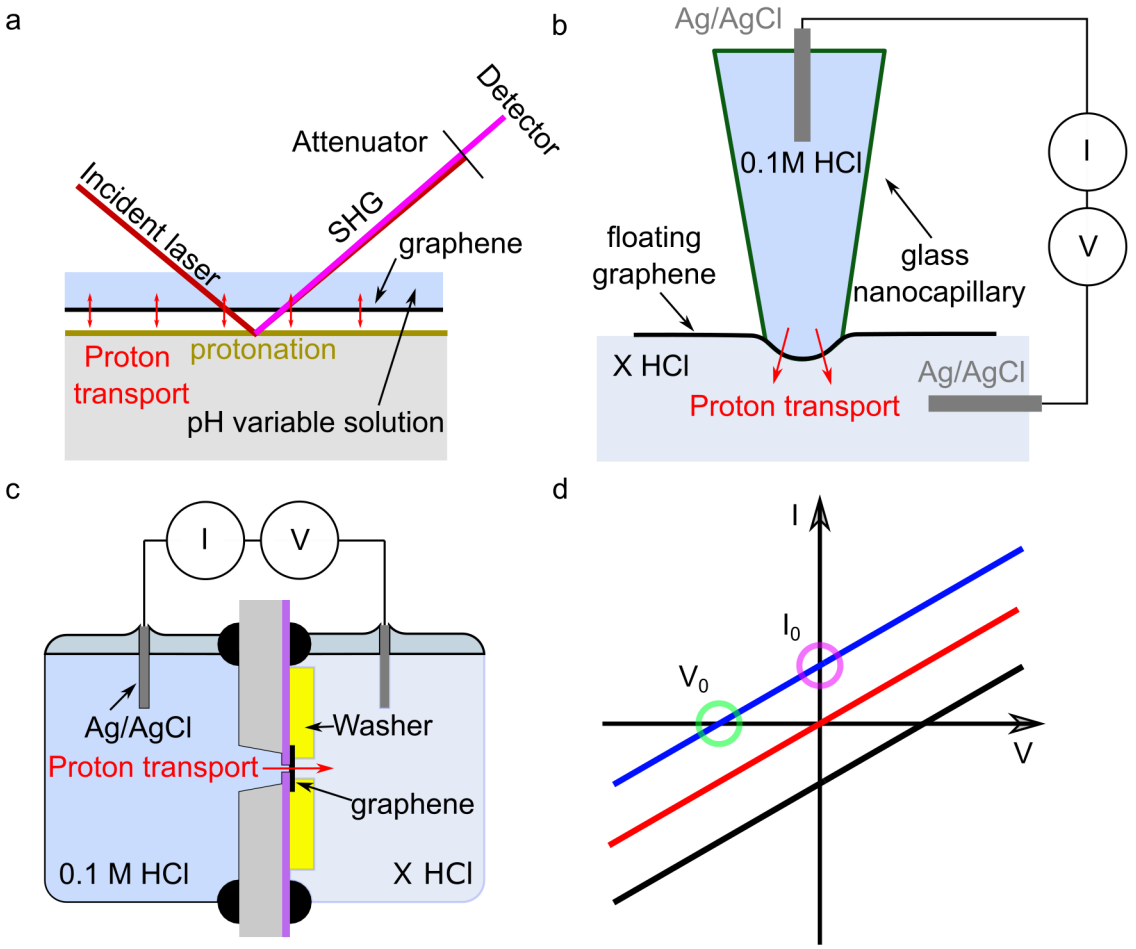

Figure 3.6: (**a**) Experimental setup for measurement of underlying substrate protonation through graphene using SHG detection. Adapted from Achtyl et al. [80]. (**b**) Glass nanocapillary measurement of graphene, similar to the 'patch clamp' technique used to measure cell ion transport. This technique is implemented by Walker et al. [79]. (**c**) Liquid cell setup with the 2D material suspended over an aperture in a SiN substrate. One reservoir typically has a fixed concentration, with the other variable, denoted as X HCl. This method was employed by Hu et al. and Qi et al. (**d**) Illustration of expected alterations in I-V characteristics when a concentration gradient across a selective membrane drives a diffusion current at zero potential I_0 and the zero current potential required to stop the current V_0.

measurements of an (optical) inter-facial potential-dependent version of second harmonic generation (SHG) [80]. In essence, CVD graphene membranes are transferred onto a silica window, as reported in previous work [81], [82], where protonation and deprotonation of the underlying silanol groups can be detected by measuring the optical SHG signal from applied pH jumps (using a pH switchable flow cell) see figure 3.6 a to clarify the experimental setup. The key findings of this study are that protonation of the underlying silanol groups is indeed observed, and attributed to proton transport via rare OH terminated defects.

Qi et al. [83] studied ion transport through sub-nanometre pores in mechanically-exfoliated graphene by exposing a suspended graphene membrane (of 2 μm diameter) to argon or oxygen plasma, and then subsequently measuring HCl and NaCl transport of said pores using

Table 3.1: Data from publications reporting measurements of proton transport through unmodified graphene. All studies utilise Ag/AgCl electrodes and HCl as the electrolyte.

Ref	Substrate/ Method	Membrane Area (um^2)	Conductance (nS)	Areal Conductivity ($mScm^{-2}$)
Hu et al [62]	SiN suspended (mechanically exfoliated)	3.14	0.061	2.15 +- 0.6
Walker et al [79]	Free-standing (CVD graphene)	2.54×10^{-2}	0.170	669.29
Qi et al [83]	SiN suspended (mechanically exfoliated)	3.14	0.367	11.69

a liquid cell configuration. The power and pressures of plasma were kept the same for both plasma types and the liquid cell setup implemented is illustrated in Figure 3.6 c. Findings from this study are as follows. Control (unexposed to plasma) membranes show conductance values, at 0.1 M HCl electrolyte, of 0.37 nS and when exposed to argon plasma for 30 s and oxygen plasma for 10 s, this subsequently increased conductance values to 0.61 nS and 110 nS respectively. Oxygen plasma was shown to increase defect density more significantly than argon plasma and within shorter periods, as reflected by measurements of the defect (D) Raman peak at $\sim$ 1350 cm^{-1} [84]. The increased defective nature of the suspended graphene was attributed to higher conductance values. Further, the authors report NaCl measurements of conductance values, for unexposed membranes, of 0.34 nS and attribute this to leakage current. Measurements of NaCl conductance, after exposure to argon plasma for 30 s and oxygen plasma for 10 s, were 0.44 nS and 3.37 nS respectively. Finally, proton permselectivity over sodium ions was observed in oxygen plasma exposed samples, with a ratio of HCl conductance (G_{HCl}) and NaCl conductance (G_{NaCl}) of $\frac{G_{HCl}}{G_{NaCl}} \approx 33$. This is above an expected bulk electrolyte ratio, which we can readily obtain as ≈ 3.37, using Equation 2.22 in conjunction with mobilities given in Table 2.1 from Chapter 2. This permselectivity is attributed to oxygen atom terminated nanopores.

A related (intrinsic CVD) defect dependent conductance of 1M KCl electrolyte, has been reported by Jain et al. [85]. This study, experimentally reports 10 separate 30–40 nm diameter suspended membranes with statistically isolated nanopores of various diameters (6 Å-2.5 nm). Conductance values varied over two orders of magnitude from 0.068 nS to 16 nS for these 10 devices and these were matched to a DFT model for ion conduction through these various sized nanopores. Let us now draw comparisons between three studies with HCl conductivity measurements of graphene membranes. These three publications are those of Hu et al [62], Walker et al [79] and Qi et al [83].

In table 3.1, liquid cell measurements by these authors have been compared. We can readily observe that areal conductivities across the three studies, possess disagreement. This is most starkly demonstrated between measurements by Walker et al. and Hu et al. with the former having a conductance value 311 times higher than the latter. The measurements of

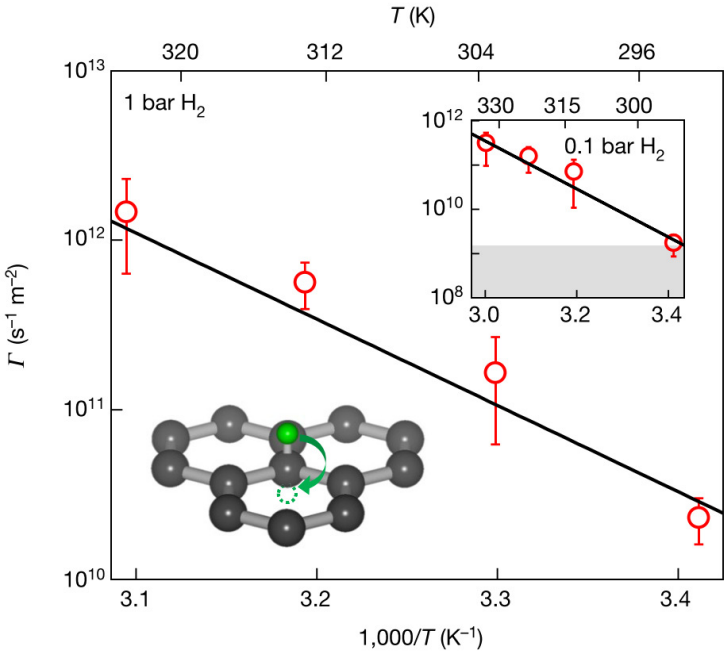

Figure 3.7: Hydrogen permeation rates at different temperatures. Red circles are experimental data with the solid curve being the best fit to activation behaviour with E_a = 1.0 $\pm$ 0.1 eV. Top inset: same as the main panel, but for P = 0.1 bar where the grey area indicates our detection limit. Error bars show the standard deviations of at least six devices for each temperature. Bottom inset: depiction of the flipping process in the suggested mechanism of hydrogen permeation. Adapted from [50].

Qi et al. and Hu et al. vary to a lesser extent. The measured proton-conductance values are 5.4 times higher for Qi et al. than those measured by Hu et al. Now, If the mechanism of proton transport is through the intrinsic lattice, as Hu et al and Lozada et al reported, one would hope for areal conductivity agreement across studies, as long as parallel leakage proton transport is insignificant, or the graphene membrane itself is of a consistent (defect containing) nature. However, if the dominant conductance pathway is through defects, then a statistical spread of conductivity values would be expected, especially for large[7] membranes. However, the consistency of conductance values across devices by Hu et al. as well as Lozada et al., alongside the impermeability tests performed during these studies and Bunch et al [49], suggests transport independent of statistically formed defects. Further experimental work would be of benefit to advance the fundamental understanding of proton permeation through 2D materials. Our final experimental study which we will consider in this section is that of measurements of significant hydrogen permeation through graphene by Sun et al.

As alluded to in the preceding subsection, Sun et al. [50] reported measurable molecular hydrogen permeation through graphene membrane capped monocrystalline containers. See Figure 3.4 d and e for an illustration of the experimental setup. Let us discuss the hydrogen permeation findings. Graphene capped micro-cavities were exposed to molecular hydrogen gas at 1 bar for up to 27 days. In accordance with Dalton's Law, if the membrane is permeable to hydrogen, yet not permeable to the (initially sealed) air, then the partial pressure equalisa-

[7] relative to average defect spacing distance.

tion will result in a total pressure increase, within the microchamber. This would manifest as a gradual bulging of the membrane when the device is measured in ambient conditions. This bulging is quantified as small changes in membrane position ($\Delta\delta$) and related to the change in the number of molecules (ΔN) as [86], [87]

$$\Delta N = c\frac{P_a}{k_B T} S\Delta\delta \tag{3.4}$$

where c is a coefficient accounting for the curvature of membrane, P_a is the external pressure and S is the membrane area. Such a deflection $\Delta\delta$ was indeed reported for molecular hydrogen but not for argon, helium, neon, nitrogen, oxygen, krypton and xenon, up to exposures at 1 bar for 30 days. First, let us discuss the gas permeation rates of hydrogen (Γ_{H_2}). The rate for hydrogen at 295 $\pm$2 K is reported to be $\Gamma_{H_2} \approx 2 \times 10^{10}$ s^{-1}m^{-2} whereas the upper bound for helium permeation through these membranes is reported to be $\Gamma_{He} \approx 10^{9}$ s^{-1}m^{-2}. It should be noted that prior to this study, this small permeation value was not attainable using studies such as those by Bunch et al [49]. Next, the significant permeation of hydrogen was investigated at elevated temperatures from 20 °C to 50 °C. A temperature-dependent activated behaviour (Arrhenius) was reported, with an activation energy of 1.0 $\pm$ 0.1 eV extracted (see Figure 3.7). The same activated transport of helium atoms was not observed (within measurement limits). This is quite remarkable for the following reasons. Firstly, theoretical expectations for hydrogen permeation are expected to be between 2.6-4.6 eV [52], [65], [88]. Secondly, the lack of observed increase in helium permeance with temperature is striking, as helium is typically regarded to have a smaller kinetic diameter of 260 pm [59], [89] vs hydrogen 289 pm [59], [90], but, as we previously discussed, we must treat these kinetic diameters with some degree of caution.

Typically, the permeation of gases is a two-step process. The initial step is adsorption on the surface. Next, the second stage is the diffusion of the gas through the solid where the rate of permeance through the solid depends upon the un-idealness of the solid, for the case of graphene, defect density and the chemical affinity of the gas for the solid [91]. Sun et al. suggested this latter point to explain the enhanced permeability of hydrogen gas through the lattice. The proposed mechanism for hydrogen permeation is as follows. Firstly, molecular hydrogen is chemisorbed where the molecule is adsorbed and subsequently dissociates at local catalytically active curved and strained graphene surfaces. Graphene is otherwise rather catalytically inert, as discussed in section 3.1.1. Next, these chemisorbed adatoms proceed to flip (depicted in figure 3.7 inset) to the other side of the lattice, where they recombine and desorb, completing the passage through the lattice. The measured activation energy, extracted from Figure 3.7, is 1.0 $\pm$ 0.1 eV, being comparable to that of proton energy barriers through graphene, measured by Hu et al. (0.78 $\pm$ 0.03 eV) [62] is noted by the authors. Chemisorbed hydrogen is regarded as indistinguishable from a proton [50]. Therefore, its passage is seen as a phenomenon related to that of proton transport reported by Hu et al. [62]. This close match is suggested by the authors to be evidence that flipping through the lattice being the limiting factor of transport. Indeed, chemisorbed foreign atoms are thought to reside at high symmetry points of the lattice [57], such as directly above carbon atoms, or in the centre of the carbon

rings. Also, there is a low energy barrier for the chemisorption C-H bond formation of 0.18 eV [52]. Further, such protonated graphene is a proposed theoretical explanation supported by DFT calculations. Indeed, such a DFT study by Bartolomei et al report proton permeation barriers of 1.0 eV, and this result is in agreement with the findings of Sun et al [92].

Now, we have extensively reviewed some of the pre-eminent experimental work of proton transport through graphene, let us review some theoretical models of proton transport through graphene.

3.2.2 Modelling

The underlying mechanisms of proton and deuteron transport through graphene membranes have been controversially discussed during the last few years [93], with considerable effort being devoted to understanding how both of these isotopes penetrate 2D materials. Several different scenarios of proton permeation have been explored theoretically: permeation through defect-free graphene, chemisorption/hydrogenation of the lattice (something also reported experimentally [94], [95]) and transport via atomic vacancy or topological defects. Models typically report transfer energy barriers through a pristine sheet of 1.4-1.6 eV, which are beyond thermal proton energy access [23], [52], [88], [96] and in disagreement with experiment [62], [66]. Hence, other more elaborate modelling has been undertaken to lower prohibitively-high barrier energies with a realistic transport mechanism. However, some scholars have concluded that the problem may be beyond the scope of computational theory if the lattice is assumed to be defect free [23]. A complication that is often neglected in modelling is the high polarisability of graphene and hBN, as discussed in section 3.1. Such polarisability is thought to result in the donation of electrons to the proton, creating a neutral hydrogen in its ground state and a charged membrane [23], which is a different scenario to that being modelled. Moreover, given the peculiar nature of hydrogen bonding and transport, the use of ab initio DFT calculations for hydrogen/proton energy barriers is challenging [97], and a separate topic of discussion. Despite the successes of DFT and post-Hartree-Fock methods [96], [98] in calculations, dispersion forces can limit the accuracy of such modelling [97], [98]. With these caveats discussed, let us now proceed to consider models and their findings in more detail.

The main method to date for modelling energy barriers to proton transport through 2D materials, is that of DFT. Within this approach, there are multiple routes to model. DFT is a computational quantum mechanical modelling method, which is used to model many-body systems, to evaluate their ground states for electronic (or nuclear) configuration. It is based upon two theorems by Hohenberg and Kohn [99]. The first being: the ground-state energy from Schrodinger's equation is a unique functional[8] of the electron density [99]. The second theorem is that the electron density that minimises the energy of the overall functional is the true electron density corresponding to the full solution of the Schrodinger equation [99]. By applying a suitable functional and minimising the energy, we can arrive at the electron density

[8] A function of a function.

of a system. A detailed description of DFT is beyond the scope of this section. Suffice to say is that we can model many–body systems by implementing various functionals to arrive at ground–state energies and probability densities. A popular choice of model for recent DFT calculations is that of circumcoronene, which is a polyaromatic hydrocarbon composed of 19 benzene rings, representing a finite graphene sheet. The advantages of using such molecular prototypes is that an arbitrary number of protons can be included [92]. Further, using this approach can have the advantage that the large toolkit of modern quantum chemistry and comparisons to experimental measurements are available to provide estimates about the quality of results [88].

The first and simplest model for modelling proton penetration barriers, is the static lattice configuration, where the impinging proton is modelled to pass through pores in the 2D material lattice [52], [96]. A further proposed mechanism is the chemisorption of hydrogen and bond rotation, resulting in hydrogen flipping across the membrane. The last model presented here is that of permeation through (the simplest) defects in graphene, Stone-Wales defects. Let us now cover these in turn.

3.2.2.1 Static Pores

In the simplest case, static energy barriers can be calculated when the proton is modelled to pass through the centre of graphene's hexagonal pore (see Figure 3.3), with the lattice staying fixed. The energy barrier height for such a model typically falls within the range of 1.4-1.6 eV for graphene [52], [62], [64], [65]. Let us take a closer look at a couple of examples of such studies. Proton permeation through the lattice pores of graphene was modelled by Miao et al. [52] using the programme 'Quantum-Espresso'. A Perdew-Wang 91 (PW91) gradient-corrected functional was used. Proton diffusion was calculated using the climbing-image nudged elastic band method, whereby kinetics were evaluated using a combined DFT and harmonic transition state theory model. The key findings of the work are as follows. Physisorbed hydrogen showed an energy barrier to permeation of 2.64 eV. Physisorbed protons were modelled to have a lower barrier of 1.41 eV and it was shown to be more difficult for a hydrogen atom to tunnel through the graphene sheet after a C–H bond is made. Further, defects were modelled to greatly reduce the penetration energy barrier and the actual region of influence of the defect extended beyond the defect location [52]. Seel et al. calculated barrier heights for proton and hydrogen permeation using a B3LYP cluster model. Off-centre (of the lattice pore) barrier heights for proton permeation through graphene and hBN are given as 1.38 eV and 0.11 eV respectively [88]. The latter energy barrier being even lower than that observed by Hu et al. ($\sim$ 0.3 eV). Further, this work provides theoretical reasoning for which monolayer MoS_2 is an efficient proton barrier. It is suggested that protons and H atoms can become trapped between the outer S layers in the Mo plane, possibly explaining why no measurable proton transport for monolayer MoS_2 was observed in work by Hu et al. In summary, this method of modelling typically yields energy barriers significantly higher than that of experimental measurement.

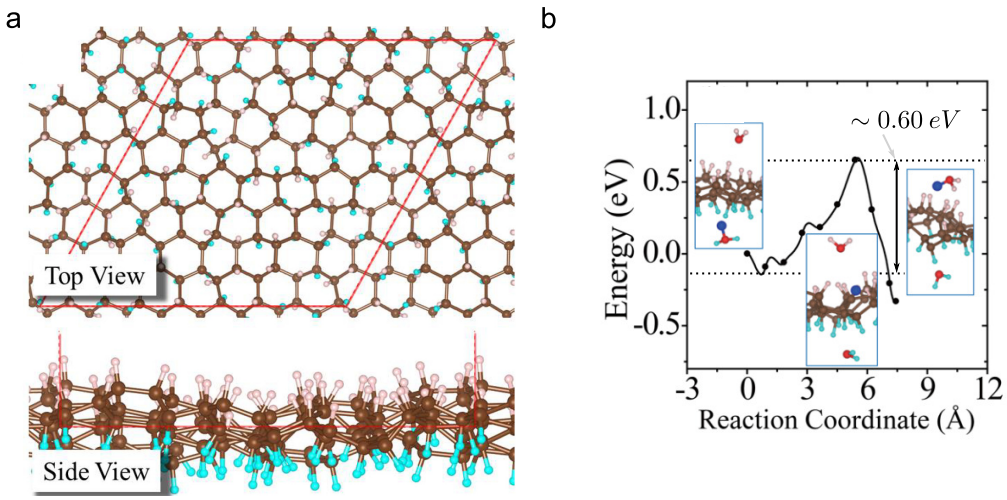

Figure 3.8: (**a**) Atomic structure of hydrogenated (disordered) graphene, a promising candidate model to match experimental results to theory. For clarity, the H adatoms below the sheets are coloured in cyan whereas those on top are white. Carbon atoms are brown. (**b**) Proton penetration barrier height for such disordered hydrogenated graphene. Adapted from [100].

3.2.2.2 Chemisorption and Flipping

For hydrogen, chemisorption is believed to be a more stable state than that of physisorption [101]. This is due to the latter having a shallow energy minimum (47 meV) versus the more stable chemisorption well (800 meV). The two states being separated by approximately 200 meV [101]. Now, the proposed proton permeation via chemisorption and flipping through the lattice have been modelled in work by Miao et al. [52], Feng et al. [100] and Bartolomei et al. [92] among others. We shall now consider these three studies.

Miao et al [52] modelled chemisorbed H atoms on the graphene sheet and were shown to require more energy to overcome the chemical bond breaking to tunnel compared to the physisorbed case. This barrier was modelled to be 3.44 eV where the migration process is also accompanied by the expansion of the hexagonal ring and a rotation of the C–H bond from one side to the other, not directly through the centre of the hexagonal ring [52].

Feng et al. further modelled chemisorption and the passage of protons through the graphene lattice [100]. The novelty of this publication is the inclusion of hydrogenation effects and a simple water model to better mimic the hydrated conditions of Nafion or HCl. Yet, the author makes no claim regarding the aim of modelling such an electrolyte surround. Using ab initio path-integral molecular dynamics (PIMD), nuclear quantum effects are included within the modelling. These effects include quantum tunnelling and zero–point motion. The model also incorporated hydrogen bonding and dispersion forces using the optB88-vdW functional. The key findings of the work are that the hydrogenation of the lattice results in a substantial decrease in the theoretical proton permeation barrier. At the penetration site, the barrier energy is modelled to be 0.61 eV and 0.51 eV for graphene and monolayer hBN respectively. See Figure 3.8 b for the modelled barrier height. This is for the case of the ‘disordered hy-

drogenated' graphene model. In the disordered arrangement, each side of the graphene is hydrogenated to different extents, where asymmetric decoration creates structures yet more permeable for proton penetration. This reduction occurs because the hydrogenation induces sp^2 to sp^3 transformation and destabilises the chemisorption state in which the proton can get trapped on the pristine membranes. The honeycomb lattice is subsequently expanded providing a permeation route. See figure 3.8 for an illustration of the disordered lattice. It should also be noted that Feng et al. report a difference of 50 meV in barrier height for protons and deuterons, in close agreement with Lozada et al. [66].

Another publication exploring proton penetration barriers by way of a chemisorption process, using DFT, is that of work by Bartolomei et al. [92]. The key differences between the two studies are that for Bartolomei et al., strictly protons are used in the simulation and these are modelled as chemisorbed from initialisation, whereas in the Feng et al. modelled chemisorbed hydrogen and protons impinging on the lattice. Moreover, Bartolomei et al. proposed the use of a transport mechanism facilitated by the transitory state of a proton transiting through a C-C bond. If two protons respectively attach to two neighbouring carbon atoms, then the permeation mechanism is different to that of an isolated chemisorbed proton. In the study by Bartolomei et al., proton barrier heights of 1.0 eV are also modelled. The process presented by Bartolomei et al. bears semblance to that of hydrogen insertion within a single walled carbon nanotube stretched C-C bond, modelled to have an energy barrier of 1.51 eV [102].

To summarise, hydrogenated graphene offers a promising theoretical model with which to explain <1 eV proton permeation barrier heights and predicts a high barrier for deuterons versus protons. The models of Feng et al and Bartolomei et al are in close agreement with the experimental results of Hu et al [62] and Lozada et al [66].

3.2.2.3 Stone-Wales Defects

Stone-Wales defects are the simplest defects in graphene. They arise from 90° rotations of C-C bonds in graphene, resulting in four hexagons of the lattice being transformed into two pentagons and two heptagons, known as a 55-77 defect [103]. See Figure 3.9 h for an illustration. Because these defects keep an average of six carbon atoms (per polygon) in the graphene lattice, they can be removed by annealing at sufficiently high temperatures [104]. High temperatures are required because there is large formation (and removal) energy for the defect of $\sim$ 5 eV [105]. This is due to the significant atomic rearrangements needed, including the breaking of two C-C bonds at the transition state [106]. Through such Stone-Wales defects, permeation barrier heights, along with separation factors for deuterons versus protons were studied using DFT (PBE0 functional) by An et al. [93]. In the same study, the expanded (7) carbon membered rings (MR) show a decreased proton permeation barrier to that of 0.99 eV resulting in proton flow through the 7MR ring being 10^6 times larger than that through the 6MR ring. This would result in a significant transport pathway, for a defect density as low as 1 ppm [93]. Further, modelling of proton over deuteron selectivity is reported as

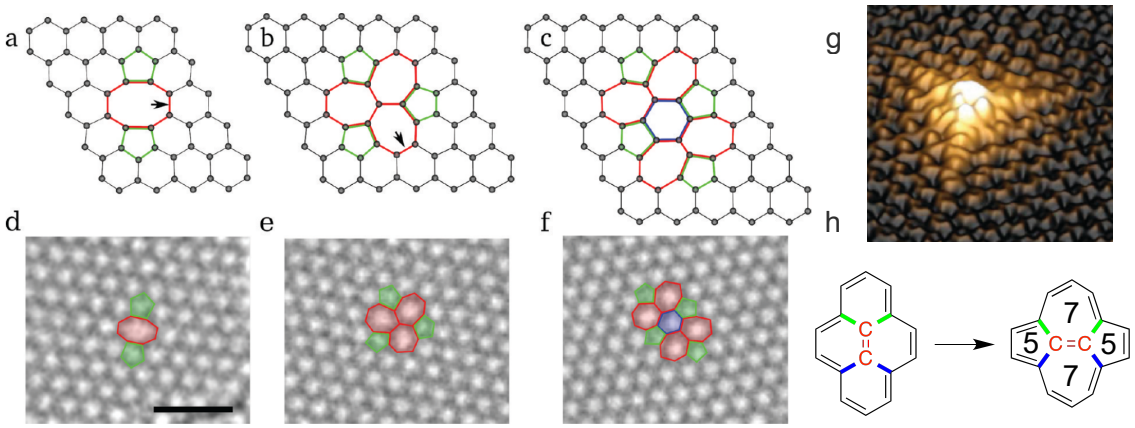

Figure 3.9: (**a**-**c**) Atomic structures of modelled double vacancy defects in graphene as obtained from DFT calculations and matched with experimental TEM images (**d**-**f**) of the same structures. Adapted from [57]. (**d**) Experimental STM image of a single vacancy defect. The defect site appears as a protrusion in STM due to an increase in the local density of states at the dangling bond. Adapted from [107]. (**h**) The formation of a Stone-Wales defect by rotation of the C-C bond. Labelled are the 5- and 7-membered rings of the 55-77 defect.

$\alpha_{H^+/D^+} = 6.9$ for the 7MR, whereas for the 6MR case, the same selectivity is modelled to be 66.5, significantly higher than the experimentally-observed value. Both the barrier height and selectivity ratio for the 7MR are in close agreement with those of Hu et al. [62] and Lozada et al. [66]. Thus, we arrive at two separate routes to model the same experimental results.

3.3 Summary

The landmark experimental reportings of thermal proton transport and proton versus deuteron selectivity through the lattice of (what appear to be pristine) 2D materials triggered a flurry of subsequent studies. Firstly, there is an incentive to use these membranes in scaled-up devices as they offer potential benefits [73], [74], [108], secondly to explore novel transport phenomena and thirdly to understand the origins of this transport, as it was so unexpected. There have been extensive efforts to resolve the discrepancy between experimental results and theoretical modelling. However, the debate regarding how proton transport occurs through graphene and other 2D materials remains an active one, despite some authors suggestions of unanimity on the issue [109]. This is, in part, the motivation for the work undertaken during this study. Further experimental studies relating to proton selective transport through 2D Materials would be a welcome addition to the literature. Indeed, this is one motivation for the work presented in Chapter 6. Identifying the reasons for such a large spread in modelled barrier energy is a significant investigation and large topic of discussion in itself.

References

[1] A. K. Geim and K. S. Novoselov, "The rise of graphene," in *Nanoscience and technology: a collection of reviews from Nature journals*, World Scientific, 2010, pp. 11–19.

[2] K. S. Novoselov, A. K. Geim, S. V. Morozov, D. Jiang, Y. Zhang, S. V. Dubonos, I. V. Grigorieva, and A. A. Firsov, "Electric field effect in atomically thin carbon films," *Science*, vol. 306, no. 5696, pp. 666–669, 2004.

[3] N. D. Mermin, "Crystalline order in two dimensions," *Physical Review*, vol. 176, no. 1, p. 250, 1968.

[4] G. Ruess and F. Vogt, "Carbon from graphite oxyhydroxide," *Monthly books for chemistry and related parts of other sciences*, vol. 78, no. 3-4, pp. 222–242, 1948.

[5] H.-P. Boehm, A. Clauss, G. Fischer, and U. Hofmann, "The adsorption behavior of very thin carbon foils," *Magazine for inorganic and general chemistry*, vol. 316, no. 3-4, pp. 119–127, 1962.

[6] Y. Zhang, Y.-W. Tan, H. L. Stormer, and P. Kim, "Experimental observation of the quantum hall effect and Berry's phase in graphene," *Nature*, vol. 438, no. 7065, pp. 201–204, 2005.

[7] K. S. Novoselov, A. K. Geim, S. V. Morozov, D. Jiang, M. I. Katsnelson, I. Grigorieva, S. Dubonos, Firsov, and AA, "Two-dimensional gas of massless dirac fermions in graphene," *Nature*, vol. 438, no. 7065, pp. 197–200, 2005.

[8] K. Novoselov, o. A. Mishchenko, o. A. Carvalho, and A. C. Neto, "2D materials and van der Waals heterostructures," *Science*, vol. 353, no. 6298, 2016.

[9] A. K. Geim and I. V. Grigorieva, "Van der Waals heterostructures," *Nature*, vol. 499, no. 7459, pp. 419–425, 2013.

[10] O. Hod, "Graphite and hexagonal boron-nitride have the same interlayer distance. why?" *Journal of Chemical Theory and Computation*, vol. 8, no. 4, pp. 1360–1369, 2012.

[11] H.-K. Jeong, Y. P. Lee, R. J. Lahaye, M.-H. Park, K. H. An, I. J. Kim, C.-W. Yang, C. Y. Park, R. S. Ruoff, and Y. H. Lee, "Evidence of graphitic ab stacking order of graphite oxides," *Journal of the American Chemical Society*, vol. 130, no. 4, pp. 1362–1366, 2008.

[12] A. C. Neto, F. Guinea, N. M. Peres, K. S. Novoselov, and A. K. Geim, "The electronic properties of graphene," *Reviews of modern physics*, vol. 81, no. 1, p. 109, 2009.

[13] J. Wang, F. Ma, and M. Sun, "Graphene, hexagonal boron nitride, and their heterostructures: Properties and applications," *RSC Advances*, vol. 7, no. 27, pp. 16 801–16 822, 2017.

[14] C. Lee, X. Wei, J. W. Kysar, and J. Hone, "Measurement of the elastic properties and intrinsic strength of monolayer graphene," *Science*, vol. 321, no. 5887, pp. 385–388, 2008.

[15] H. E. Boyer, "Atlas of stress–strain curves," *ASM International, Metals Park, Ohio 44073, USA, 1987. 630*, pp. 130–140, 1987.

[16] W. D. Callister Jr and D. G. Rethwisch, *Fundamentals of materials science and engineering: an integrated approach*, 5th ed. John Wiley & Sons, 2015, pp. 200–300.

[17] P. R. Wallace, "The band theory of graphite," *Physical Review*, vol. 71, no. 9, p. 622, 1947.

[18] A. Bostwick, T. Ohta, T. Seyller, K. Horn, and E. Rotenberg, "Quasiparticle dynamics in graphene," *Nature Physics*, vol. 3, no. 1, pp. 36–40, 2007.

[19] L. Wang, I. Meric, P. Huang, Q. Gao, Y. Gao, H. Tran, T. Taniguchi, K. Watanabe, L. Campos, D. Muller, *et al.*, "One-dimensional electrical contact to a two-dimensional material," *Science*, vol. 342, no. 6158, pp. 614–617, 2013.

[20] C. Kittel, P. McEuen, and P. McEuen, *Introduction to solid state physics*. Wiley New York, 1996, vol. 8.

[21] D. Deng, K. Novoselov, Q. Fu, N. Zheng, Z. Tian, and X. Bao, "Catalysis with two-dimensional materials and their heterostructures," *Nature Nanotechnology*, vol. 11, no. 3, pp. 218–230, 2016.

[22] É. Bordes, J. Szala-Bilnik, and A. A. Pádua, "Exfoliation of graphene and fluorographene in molecular and ionic liquids," *Faraday discussions*, vol. 206, pp. 61–75, 2017.

[23] J. Kroes, A. Fasolino, and M. Katsnelson, "Density functional based simulations of proton permeation of graphene and hexagonal boron nitride," *Physical Chemistry Chemical Physics*, vol. 19, no. 8, pp. 5813–5817, 2017.

[24] Y. Cao, V. Fatemi, S. Fang, K. Watanabe, T. Taniguchi, E. Kaxiras, and P. Jarillo-Herrero, "Unconventional superconductivity in magic-angle graphene superlattices," *Nature*, vol. 556, no. 7699, pp. 43–50, 2018.

[25] R. K. Kumar, D. Bandurin, F. Pellegrino, Y. Cao, A. Principi, H. Guo, G. Auton, M. B. Shalom, L. A. Ponomarenko, G. Falkovich, *et al.*, "Superballistic flow of viscous electron fluid through graphene constrictions," *Nature Physics*, vol. 13, no. 12, pp. 1182–1185, 2017.

[26] D. Bandurin, I. Torre, R. K. Kumar, M. B. Shalom, A. Tomadin, A. Principi, G. Auton, E. Khestanova, K. Novoselov, I. Grigorieva, *et al.*, "Negative local resistance caused by viscous electron backflow in graphene," *Science*, vol. 351, no. 6277, pp. 1055–1058, 2016.

[27] R. K. Kumar, X. Chen, G. Auton, A. Mishchenko, D. A. Bandurin, S. V. Morozov, Y. Cao, E. Khestanova, M. B. Shalom, A. Kretinin, *et al.*, "High-temperature quantum oscillations caused by recurring bloch states in graphene superlattices," *Science*, vol. 357, no. 6347, pp. 181–184, 2017.

[28] Y. Y. Wang, Z. H. Ni, T. Yu, Z. X. Shen, H. M. Wang, Y. H. Wu, W. Chen, and A. T. Shen Wee, "Raman studies of monolayer graphene: The substrate effect," *The Journal of Physical Chemistry C*, vol. 112, no. 29, pp. 10 637–10 640, 2008.

[29] R. S. Pease, "An X-ray study of boron nitride," *Acta Crystallographica*, vol. 5, no. 3, pp. 356–361, 1952.

[30] G. Giovannetti, P. A. Khomyakov, G. Brocks, P. J. Kelly, and J. Van Den Brink, "Substrate-induced band gap in graphene on hexagonal boron nitride: Ab initio density functional calculations," *Physical Review B*, vol. 76, no. 7, p. 073 103, 2007.

[31] K. Watanabe, T. Taniguchi, and H. Kanda, "Direct-bandgap properties and evidence for ultraviolet lasing of hexagonal boron nitride single crystal," *Nature Materials*, vol. 3, no. 6, pp. 404–409, 2004.

[32] G. Cassabois, P. Valvin, and B. Gil, "Hexagonal boron nitride is an indirect bandgap semiconductor," *Nature Photonics*, vol. 10, no. 4, pp. 262–266, 2016.

[33] M. Topsakal, E. Aktürk, and S. Ciraci, "First-principles study of two-and one-dimensional honeycomb structures of boron nitride," *Physical Review B*, vol. 79, no. 11, p. 115 442, 2009.

[34] C. R. Dean, A. F. Young, I. Meric, C. Lee, L. Wang, S. Sorgenfrei, K. Watanabe, T. Taniguchi, P. Kim, K. L. Shepard, *et al.*, "Boron nitride substrates for high-quality graphene electronics," *Nature nanotechnology*, vol. 5, no. 10, pp. 722–726, 2010.

[35] A. Falin, Q. Cai, E. J. Santos, D. Scullion, D. Qian, R. Zhang, Z. Yang, S. Huang, K. Watanabe, T. Taniguchi, *et al.*, "Mechanical properties of atomically thin boron nitride and the role of interlayer interactions," *Nature Communications*, vol. 8, no. 1, pp. 1–9, 2017.

[36] M. E. Fleet, W. A. Deer, R. A. Howie, and J. Zussman, *Rock-forming minerals: micas*. 2003.

[37] A. Davidson and A. Yoffe, "Hopping electrical conduction and thermal breakdown in natural and synthetic mica," *Physica Status Solidi (b)*, vol. 30, no. 2, pp. 741–754, 1968.

[38] J. Weeks Jr, "The dielectric constant of mica," *Physical Review*, vol. 19, no. 4, p. 319, 1922.

[39] A. Davidson and A. Vickers, "The optical properties of mica in the vacuum ultraviolet," *Journal of Physics C: Solid State Physics*, vol. 5, no. 8, p. 879, 1972.

[40] S. S. Kim, T. V. Khai, V. Kulish, Y.-H. Kim, H. G. Na, A. Katoch, M. Osada, P. Wu, and H. W. Kim, "Tunable bandgap narrowing induced by controlled molecular thickness in 2D mica nanosheets," *Chemistry of Materials*, vol. 27, no. 12, pp. 4222–4228, 2015.

[41] M. Meunier, J. Currie, M. Wertheimer, and A. Yelon, "Electrical conduction in biotite micas," *Journal of Applied Physics*, vol. 54, no. 2, pp. 898–905, 1983.

[42] K. Novoselov, "Nobel lecture: Graphene: Materials in the flatland," *Reviews of Modern Physics*, vol. 83, no. 3, p. 837, 2011.

[43] P. Blake, E. Hill, A. Castro Neto, K. Novoselov, D. Jiang, R. Yang, T. Booth, and A. Geim, "Making graphene visible," *Applied Physics Letters*, vol. 91, no. 6, p. 063 124, 2007.

[44] T. Uwanno, Y. Hattori, T. Taniguchi, K. Watanabe, and K. Nagashio, "Fully dry pmma transfer of graphene on hBN using a heating/cooling system," *2D Materials*, vol. 2, no. 4, p. 041 002, 2015.

[45] J. W. Suk, A. Kitt, C. W. Magnuson, Y. Hao, S. Ahmed, J. An, A. K. Swan, B. B. Goldberg, and R. S. Ruoff, "Transfer of CVD-grown monolayer graphene onto arbitrary substrates," *ACS Nano*, vol. 5, no. 9, pp. 6916–6924, 2011.

[46] A. C. Ferrari, J. Meyer, V. Scardaci, C. Casiraghi, M. Lazzeri, F. Mauri, S. Piscanec, D. Jiang, K. Novoselov, S. Roth, *et al.*, "Raman spectrum of graphene and graphene layers," *Physical Review Letters*, vol. 97, no. 18, p. 187 401, 2006.

[47] A. Eckmann, A. Felten, A. Mishchenko, L. Britnell, R. Krupke, K. S. Novoselov, and C. Casiraghi, "Probing the nature of defects in graphene by Raman spectroscopy," *Nano Letters*, vol. 12, no. 8, pp. 3925–3930, 2012.

[48] V. Berry, "Impermeability of graphene and its applications," *Carbon*, vol. 62, pp. 1–10, 2013.

[49] J. S. Bunch, S. S. Verbridge, J. S. Alden, A. M. Van Der Zande, J. M. Parpia, H. G. Craighead, and P. L. McEuen, "Impermeable atomic membranes from graphene sheets," *Nano Letters*, vol. 8, no. 8, pp. 2458–2462, 2008.

[50] P. Sun, Q. Yang, W. Kuang, Y. Stebunov, W. Xiong, J. Yu, R. Nair, M. Katsnelson, S. Yuan, I. Grigorieva, *et al.*, "Limits on gas impermeability of graphene," *Nature*, vol. 579, no. 7798, pp. 229–232, 2020.

[51] O. Leenaerts, B. Partoens, and F. Peeters, "Graphene: A perfect nanoballoon," *Applied Physics Letters*, vol. 93, no. 19, p. 193 107, 2008.

[52] M. Miao, M. B. Nardelli, Q. Wang, and Y. Liu, "First principles study of the permeability of graphene to hydrogen atoms," *Physical Chemistry Chemical Physics*, vol. 15, no. 38, pp. 16 132–16 137, 2013.

[53] K. Zhang, Y. Feng, F. Wang, Z. Yang, and J. Wang, "Two dimensional hexagonal boron nitride (2D-hBN): Synthesis, properties and applications," *Journal of Materials Chemistry C*, vol. 5, no. 46, pp. 11 992–12 022, 2017.

[54] L. Liao, H. Peng, and Z. Liu, "Chemistry makes graphene beyond graphene," *Journal of the American chemical society*, vol. 136, no. 35, pp. 12 194–12 200, 2014.

[55] Z. Li, Y. Wang, A. Kozbial, G. Shenoy, F. Zhou, R. McGinley, P. Ireland, B. Morganstein, A. Kunkel, S. P. Surwade, *et al.*, "Effect of airborne contaminants on the wettability of supported graphene and graphite," *Nature Materials*, vol. 12, no. 10, pp. 925–931, 2013.

[56] E. Stolyarova, D. Stolyarov, K. Bolotin, S. Ryu, L. Liu, K. Rim, M. Klima, M. Hybertsen, I. Pogorelsky, I. Pavlishin, *et al.*, "Observation of graphene bubbles and effective mass transport under graphene films," *Nano Letters*, vol. 9, no. 1, pp. 332–337, 2009.

[57] F. Banhart, J. Kotakoski, and A. V. Krasheninnikov, "Structural defects in graphene," *ACS Nano*, vol. 5, no. 1, pp. 26–41, 2011.

[58] N. Mehio, S. Dai, and D.-e. Jiang, "Quantum mechanical basis for kinetic diameters of small gaseous molecules," *The Journal of Physical Chemistry A*, vol. 118, no. 6, pp. 1150–1154, 2014.

[59] D. W. Breck, *Zeolite molecular sieves: structure, chemistry and use*. Krieger, 1984.

[60] A. Beyer, L. Maisenbacher, A. Matveev, R. Pohl, K. Khabarova, A. Grinin, T. Lamour, D. C. Yost, T. W. Hänsch, N. Kolachevsky, *et al.*, "The Rydberg constant and proton size from atomic hydrogen," *Science*, vol. 358, no. 6359, pp. 79–85, 2017.

[61] G. Tawa, I. Topol, S. Burt, R. Caldwell, and A. Rashin, "Calculation of the aqueous solvation free energy of the proton," *The Journal of Chemical Physics*, vol. 109, no. 12, pp. 4852–4863, 1998.

[62] S. Hu, M. Lozada-Hidalgo, F. Wang, A. Mishchenko, F. Schedin, R. Nair, E. Hill, D. Boukhvalov, M. Katsnelson, R. Dryfe, *et al.*, "Proton transport through one-atom-thick crystals," *Nature*, vol. 516, no. 7530, pp. 227–230, 2014.

[63] W. Perkins and D. Begeal, "Diffusion and permeation of He, Ne, Ar, Kr, and deuterium through silicon oxide thin-films," *The Journal of Chemical Physics*, vol. 54, no. 4, pp. 1683–1694, 1971.

[64] W. L. Wang and E. Kaxiras, "Graphene hydrate: Theoretical prediction of a new insulating form of graphene," *New Journal of Physics*, vol. 12, no. 12, p. 125 012, 2010.

[65] L. Tsetseris and S. Pantelides, "Graphene: An impermeable or selectively permeable membrane for atomic species?" *Carbon*, vol. 67, pp. 58–63, 2014.

[66] M. Lozada-Hidalgo, S. Hu, O. Marshall, A. Mishchenko, A. Grigorenko, R. Dryfe, B. Radha, I. Grigorieva, and A. Geim, "Sieving hydrogen isotopes through two-dimensional crystals," *Science*, vol. 351, no. 6268, pp. 68–70, 2016.

[67] A. I. Miller, "Heavy water: A manufacturers' guide for the hydrogen century," *Canadian Nuclear Society Bulletin*, vol. 22, no. 1, pp. 1–14, 2001.

[68] F. Westheimer, "The magnitude of the primary kinetic isotope effect for compounds of hydrogen and deuterium.," *Chemical Reviews*, vol. 61, no. 3, pp. 265–273, 1961.

[69] H. Rae, "Selecting heavy water processes," in, ACS Publications, 1978.

[70] J. Bigeleisen and M. Wolfsberg, "Theoretical and experimental aspects of isotope effects in chemical kinetics," *Advances in Chemical Physics*, pp. 15–76, 1957.

[71] H. Matsushima, R. Ogawa, S. Shibuya, and M. Ueda, "Novel PEFC application for deuterium isotope separation," *Materials*, vol. 10, no. 3, p. 303, 2017.

[72] A. F. Privalov, E. Galitskaya, V. Sinitsyn, and M. Vogel, "Isotope effect on diffusion in Nafion studied by NMR diffusometry," *Applied Magnetic Resonance*, vol. 51, no. 2, pp. 145–153, 2020.

[73] M. Lozada-Hidalgo, S. Zhang, S. Hu, A. Esfandiar, I. Grigorieva, and A. Geim, "Scalable and efficient separation of hydrogen isotopes using graphene-based electrochemical pumping," *Nature Communications*, vol. 8, no. 1, pp. 1–5, 2017.

[74] S. Bukola, Y. Liang, C. Korzeniewski, J. Harris, and S. Creager, "Selective proton/deuteron transport through Nafion graphene Nafion sandwich structures at high current density," *Journal of the American Chemical Society*, vol. 140, no. 5, pp. 1743–1752, 2018.

[75] S. C. O'Hern, C. A. Stewart, M. S. Boutilier, J.-C. Idrobo, S. Bhaviripudi, S. K. Das, J. Kong, T. Laoui, M. Atieh, and R. Karnik, "Selective molecular transport through intrinsic defects in a single layer of CVD graphene," *ACS nano*, vol. 6, no. 11, pp. 10 130–10 138, 2012.

[76] X. Li, C. W. Magnuson, A. Venugopal, J. An, J. W. Suk, B. Han, M. Borysiak, W. Cai, A. Velamakanni, Y. Zhu, *et al.*, "Graphene films with large domain size by a two-step chemical vapor deposition process," *Nano Letters*, vol. 10, no. 11, pp. 4328–4334, 2010.

[77] B.-J. Park, J.-S. Choi, J.-H. Eom, H. Ha, H. Y. Kim, S. Lee, H. Shin, and S.-G. Yoon, "Defect-free graphene synthesized directly at 150 C via chemical vapor deposition with no transfer," *ACS Nano*, vol. 12, no. 2, pp. 2008–2016, 2018.

[78] S. C. O'Hern, D. Jang, S. Bose, J.-C. Idrobo, Y. Song, T. Laoui, J. Kong, and R. Karnik, "Nanofiltration across defect-sealed nanoporous monolayer graphene," *Nano Letters*, vol. 15, no. 5, pp. 3254–3260, 2015.

[79] M. I. Walker, P. Braeuninger-Weimer, R. S. Weatherup, S. Hofmann, and U. F. Keyser, "Measuring the proton selectivity of graphene membranes," *Applied Physics Letters*, vol. 107, no. 21, p. 213 104, 2015.

[80] J. L. Achtyl, R. R. Unocic, L. Xu, Y. Cai, M. Raju, W. Zhang, R. L. Sacci, I. V. Vlassiouk, P. F. Fulvio, P. Ganesh, *et al.*, "Aqueous proton transfer across single-layer graphene," *Nature Communications*, vol. 6, no. 1, pp. 1–7, 2015.

[81] J. L. Achtyl, I. V. Vlassiouk, P. F. Fulvio, S. M. Mahurin, S. Dai, and F. M. Geiger, "Free energy relationships in the electrical double layer over single-layer graphene," *Journal of the American Chemical Society*, vol. 135, no. 3, pp. 979–981, 2013.

[82] J. L. Achtyl, I. V. Vlassiouk, S. P. Surwade, P. F. Fulvio, S. Dai, and F. M. Geiger, "Interaction of magnesium ions with pristine single-layer and defected graphene/water interfaces studied by second harmonic generation," *The Journal of Physical Chemistry B*, vol. 118, no. 28, pp. 7739–7749, 2014.

[83] H. Qi, Z. Li, Y. Tao, W. Zhao, K. Lin, Z. Ni, C. Jin, Y. Zhang, K. Bi, and Y. Chen, "Fabrication of sub-nanometer pores on graphene membrane for ion selective transport," *Nanoscale*, vol. 10, no. 11, pp. 5350–5357, 2018.

[84] L. G. Cançado, A. Jorio, E. M. Ferreira, F. Stavale, C. A. Achete, R. B. Capaz, M. V. d. O. Moutinho, A. Lombardo, T. Kulmala, and A. C. Ferrari, "Quantifying defects in graphene via Raman spectroscopy at different excitation energies," *Nano Letters*, vol. 11, no. 8, pp. 3190–3196, 2011.

[85] T. Jain, B. C. Rasera, R. J. S. Guerrero, M. S. Boutilier, S. C. O'hern, J.-C. Idrobo, and R. Karnik, "Heterogeneous sub-continuum ionic transport in statistically isolated graphene nanopores," *Nature Nanotechnology*, vol. 10, no. 12, pp. 1053–1057, 2015.

[86] S. P. Koenig, L. Wang, J. Pellegrino, and J. S. Bunch, "Selective molecular sieving through porous graphene," *Nature Nanotechnology*, vol. 7, no. 11, pp. 728–732, 2012.

[87] S. P. Koenig, N. G. Boddeti, M. L. Dunn, and J. S. Bunch, "Ultrastrong adhesion of graphene membranes," *Nature Nanotechnology*, vol. 6, no. 9, p. 543, 2011.

[88] M. Seel and R. Pandey, "Proton and hydrogen transport through two-dimensional monolayers," *2D Materials*, vol. 3, no. 2, p. 025 004, 2016.

[89] S. Matteucci, Y. Yampolskii, B. D. Freeman, and I. Pinnau, "Transport of gases and vapors in glassy and rubbery polymers," *Materials science of membranes for gas and vapor separation*, vol. 1, pp. 1–2, 2006.

[90] A. Chambers, C. Park, R. T. K. Baker, and N. M. Rodriguez, "Hydrogen storage in graphite nanofibers," *The journal of physical chemistry B*, vol. 102, no. 22, pp. 4253–4256, 1998.

[91] H. Greenhouse, *Hermeticity of electronic packages*. Elsevier, 2000.

[92] M. Bartolomei, M. I. Hernández, J. Campos-Martínez, and R. Hernández-Lamoneda, "Graphene multi-protonation: A cooperative mechanism for proton permeation," *Carbon*, vol. 144, pp. 724–730, 2019.

[93] Y. An, A. F. Oliveira, T. Brumme, A. Kuc, and T. Heine, "Stone-Wales defects cause high proton permeability and isotope selectivity of single-layer graphene," *Advanced Materials*, vol. 32, no. 37, p. 2 002 442, 2020.

[94] D. C. Elias, R. R. Nair, T. Mohiuddin, S. Morozov, P. Blake, M. Halsall, A. C. Ferrari, D. Boukhvalov, M. Katsnelson, A. Geim, *et al.*, "Control of graphene's properties by reversible hydrogenation: Evidence for graphane," *Science*, vol. 323, no. 5914, pp. 610–613, 2009.

[95] Z. Ni, L. Ponomarenko, R. Nair, R. Yang, S. Anissimova, I. Grigorieva, F. Schedin, P. Blake, Z. Shen, E. Hill, *et al.*, "On resonant scatterers as a factor limiting carrier mobility in graphene," *Nano Letters*, vol. 10, no. 10, pp. 3868–3872, 2010.

[96] Q. Zhang, M. Ju, L. Chen, and X. C. Zeng, "Differential permeability of proton isotopes through graphene and graphene analogue monolayer," *The journal of physical chemistry letters*, vol. 7, no. 17, pp. 3395–3400, 2016.

[97] W. Koch and M. C. Holthausen, *A chemist's guide to density functional theory*. John Wiley & Sons, 2015, pp. 217–236.

[98] A. D. Boese, "Assessment of coupled cluster theory and more approximate methods for hydrogen bonded systems," *Journal of chemical theory and computation*, vol. 9, no. 10, pp. 4403–4413, 2013.

[99] D. Sholl and J. A. Steckel, *Density functional theory: a practical introduction*. John Wiley & Sons, 2011.

[100] Y. Feng, J. Chen, W. Fang, E.-G. Wang, A. Michaelides, and X.-Z. Li, "Hydrogenation facilitates proton transfer through two-dimensional honeycomb crystals," *The journal of physical chemistry letters*, vol. 8, no. 24, pp. 6009–6014, 2017.

[101] E. R. Davidson, J. Klimes, D. Alfe, and A. Michaelides, "Cooperative interplay of Van der Waals forces and quantum nuclear effects on adsorption: H at graphene and at coronene," *ACS nano*, vol. 8, no. 10, pp. 9905–9913, 2014.

[102] S. M. Lee, K. H. An, Y. H. Lee, G. Seifert, and T. Frauenheim, "A hydrogen storage mechanism in single-walled carbon nanotubes," *Journal of the American Chemical Society*, vol. 123, no. 21, pp. 5059–5063, 2001.

[103] A. Podlivaev and L. Openov, "Dynamics of the Stone-Wales defect in graphene," *Physics of the Solid State*, vol. 57, no. 4, pp. 820–824, 2015.

[104] P. T. Araujo, M. Terrones, and M. S. Dresselhaus, "Defects and impurities in graphene-like materials," *Materials Today*, vol. 15, no. 3, pp. 98–109, 2012.

[105] M. T. Lusk and L. D. Carr, "Nanoengineering defect structures on graphene," *Physical Review Letters*, vol. 100, no. 17, p. 175 503, 2008.

[106] L. Li, S. Reich, and J. Robertson, "Defect energies of graphite: Density-functional calculations," *Physical Review B*, vol. 72, no. 18, p. 184 109, 2005.

[107] M. M. Ugeda, I. Brihuega, F. Guinea, and J. M. Gómez-Rodríguez, "Missing atom as a source of carbon magnetism," *Physical Review Letters*, vol. 104, no. 9, p. 096 804, 2010.

[108] G. Liu, W. Jin, and N. Xu, "Two-dimensional-material membranes: A new family of high-performance separation membranes," *Angewandte Chemie International Edition*, vol. 55, no. 43, pp. 13 384–13 397, 2016.

[109] M. Caglar, I. Silkina, B. T. Brown, A. L. Thorneywork, O. J. Burton, V. Babenko, S. M. Gilbert, A. Zettl, S. Hofmann, and U. F. Keyser, “Tunable anion-selective transport through monolayer graphene and hexagonal boron nitride,” *ACS nano*, vol. 14, no. 3, pp. 2729–2738, 2019.

Chapter 4

Mica and Clay: Ion-Exchange Properties

Upon treating a column of soil with a solution of ammonium sulphate it was found that most of the ammonia was absorbed while the calcium contained originally in the soil was released and passed out of the column [1]. Exchange involves equivalent quantities of ions and certain ions can often exchange easier than others. This process of the cation exchange of ammonia and calcium occurs naturally in soils, specifically for clay and humus particles. Related to this, soil clay exchange of radionuclides such as radiocaesium (^{134}Cs and ^{137}Cs) from nuclear disaster sites, such as Fukushima Daiichi or Chernobyl, can be long term problems [2] where costly soil remediation is required due to uptake of these nuclides [3]–[5]. The cation exchange capacity (CEC) of soils is an important general property that is significant for plant nutrient bio-availability. Root exudates help plants access these nutrients by acidifying or altering the redox conditions within the root surround (rhizosphere), liberating ions/nutrients via exchange from clay minerals and dissolution of pH-sensitive mineral phases. Thus, ion-exchange plays a role that is of the utmost importance in agriculture and the natural world as a means to transport, store and release ions. In this chapter, we shall introduce the topic of ion-exchange in a general sense. Further, we shall distinguish between mica and clay minerals and then finally explore some of their specific ion-exchange properties. An understanding of this process is important for both chapters 7 and 8. These exploit ion-exchange properties of atomically thin micas, to make proton-conducting membranes and explore novel imaging and phenomena of few-layer clays, respectively. In this chapter, we shall only consider ion-exchange for aqueous ionic solutions.

4.0.1 Ion-Exchange

Ion exchange can be defined as the interchanging of ions of the same charge sign between an interfaced insoluble solid and solution phase. Applications of this process are many-fold. These include, but are not limited to, water purification [6], [7], the storage of nuclear waste [8], [9], use of artificial soils [10]–[12] and isotope separation [13]–[15]. It is not typically thought of strictly as a chemical interaction, rather it is a physicochemical distribution and redistribution of ions transferred to and from the interphase boundary [11]. Although, strong chemical interactions between binding sites and specific exchangeable ions can occur, resulting in an affinity toward that ion. The exchange process is generally a reversible one, but if the specific affinity of exchangeable sites is strong enough or structural reconfigurations entrap

ions, this can reduce the exchange rate considerably [16]. This distribution of ions within an exchanger typically occurs at specific sites which bind them, to varying degrees, and these bound ions are exchangeable. Describing ion-exchange theoretically in a broad sense is a challenge, because the phenomenon is so diverse that no single approach can be used to fit most experimental dependencies, and comparisons of numeric coefficients for different functions are not always insightful [11], yet some models have proven useful. Ion exchanging materials typically contain fixed charges and counter-ions at much higher concentrations than the surrounding solution, resulting in a Donnan potential between phases (see Chapter 2 Section 2.3.4.2). This potential results in a 'Nernst layer' at the interface, which ions must diffuse across. Further, because of the high relative concentration, the exchanger phase tends to swell, as osmotic pressure forces water within to balance solution concentrations. The large CEC exchangers typically undergo such swelling as they imbibe solvent in an ion solution, allowing for greater participation in ion-exchange processes. The solvent within the exchanger phase allows for more freely-diffusable ions. Early models of ion-exchange are of swelling as the main driving force for ion-exchange. Now, almost all ion-exchange reactions involve the internal solution of the exchanger, but surface site exchange can also be significant. Let us proceed to look at the equilibria, selectivity and kinetics of ion-exchange.

4.0.1.1 Thermodynamics, Equilibria and Selectivity

If we place an exchanger of type ($\underset{\text{clay}}{\mathrm{M^-\,A^+}}$), denoted here as clay for relevance, where $\mathrm{A^+}$ is initially bound to a fixed anionic group $\mathrm{M^-}$, into the solution phase containing a different cation $\mathrm{B^+}$ (and the solution can be in contact with or be assimilated into the exchanger), we can describe an exchange reaction as the physico-chemical reaction [1]

$$\underset{\text{clay}}{\mathrm{M^-\,A^+}} + \underset{\text{solution}}{\mathrm{B^+}} \rightleftharpoons \underset{\text{clay}}{\mathrm{M^-\,B^+}} + \underset{\text{solution}}{\mathrm{A^+}}\,. \tag{4.1}$$

Figure 4.1 illustrates a (highly stylised) ion-exchange process between a monovalent and a divalent ion. Figure 4.1 a shows that initially, the ion binding sites are occupied by two monovalent ions and are subsequently exchanged with a divalent ion as shown in Figure 4.1 b. We can describe this and the general case of variable valance ion-exchange as

$$Z_B\overline{A^{Z_A}} + Z_A B^{Z_B} = Z_A\overline{B^{Z_B}} + Z_B A^{Z_A} \tag{4.2}$$

where the 'overline' or 'bar' notation denotes that the ion is within the exchanger phase. Now, ions of the same charge in the solution as those of the fixed group, are termed 'co-ions' (blue in Figure 4.1) whereas ions that undergo exchange or enter the exchanger phase and opposite in charge sign to the co-ions are known as 'counter-ions' (red in Figure 4.1). For the case of the ion-exchanger presented in Equation 4.1, this corresponds to co-ions $\mathrm{M^-}$ and counter-ions $\mathrm{A^+}$ and $\mathrm{B^+}$. From the law of mass action [17] and Equation 4.2, we obtain the equilibrium

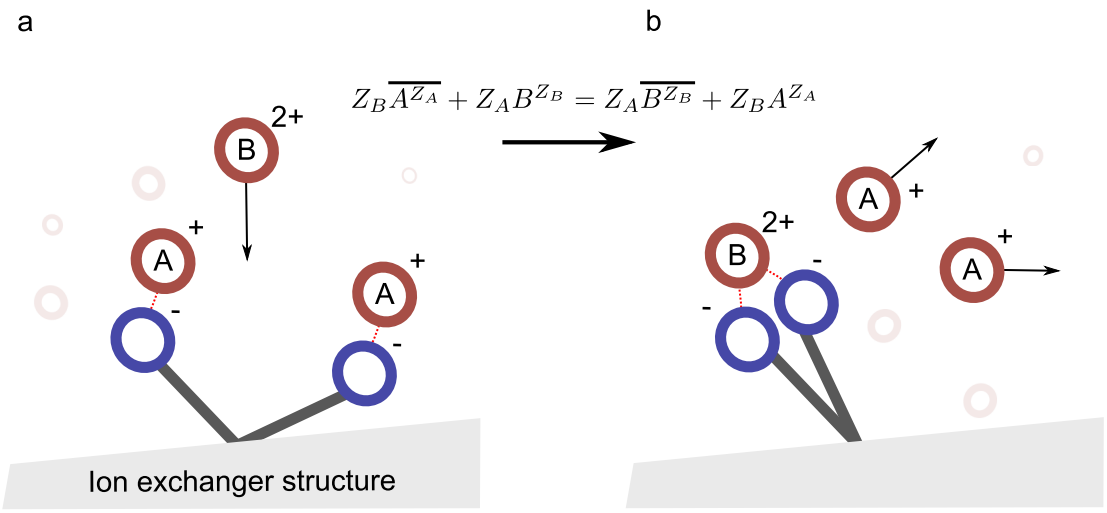

Figure 4.1: Illustration of the ion-exchange process between a monovalent (A) and divalent cation (B). (**a**) Initially two binding sites (blue) are fully occupied by two monovalent ions A (red) and subsequently exchanged for a single divalent cation B (red). (**b**) Red dashed lines represent bonding, which can be: ionic, covalent, dative or dispersion forces.

constant of ion-exchange B $\rightarrow$ A ($\bar{K}_{B\rightarrow A}$) as

$$\bar{K}_{B\rightarrow A} = \frac{(\overline{C_B})^{Z_A}\bar{\gamma}_B(C_A)^{Z_B}\gamma_A}{(\overline{C_A})^{Z_B}\bar{\gamma}_A(C_B)^{Z_A}\gamma_A} \tag{4.3}$$

where γ_i is the activity coefficient in the solution phase and $\bar{\gamma}_i$ is the activity coefficient in the exchange material phase, where the experimentally-determined selectivity coefficient is

$$\alpha_B^A = \frac{\overline{C_B}C_A}{\overline{C_A}C_B}. \tag{4.4}$$

We can externally control the solution phase concentrations C_A and C_B and measure $\overline{C_A}$ as well as $\overline{C_B}$ via various analytical techniques such as flame photometry, atomic emission and absorption [18], inductively coupled plasma and X-ray fluorescence spectroscopy [19]. For the case where the ratio of activities in the solution phase is unity ($\gamma_B/\gamma_A = 1$) and assuming monovalent ion-exchange, the thermodynamic equilibrium constant and experimentally determined selectivity coefficient are related by

$$\bar{K}_{B\rightarrow A} = (\alpha_B^A)\frac{\bar{\gamma}_B}{\bar{\gamma}_A} \tag{4.5}$$

where $\bar{\gamma}_B$, $\bar{\gamma}_A$ and $\bar{K}_{B\rightarrow A}$ can be determined from the measurable α_B^A, using the integral over exchange isotherm [17], [20], which we shall discuss shortly. Before we consider exchange isotherms, it is worth noting that thermodynamic parameters such as the Gibbs free energy of exchange (ΔG_{ex}^0) can be extracted from the equilibrium exchange constant (Equation 4.3) using

$$\Delta G_{ex}^0 = -\mathrm{RTln}(\bar{K}_{B\rightarrow A}). \tag{4.6}$$

and by means of the van 't Hoff equation (see Appendix E) [21], we can use the relation for exchange equilibria evaluated for differing temperatures (T_1 and T_2) to obtain the standard enthalpy of exchange (ΔH^0_{ex}), as [22]

$$\ln\left(\frac{\bar{K}^{\mathrm{T_2}}_{B\to A}}{\bar{K}^{\mathrm{T_1}}_{B\to A}}\right) = -\left(\frac{\Delta H^0_{ex}}{\mathrm{R}}\right)\left(\frac{1}{\mathrm{T_2}} - \frac{1}{\mathrm{T_1}}\right) \tag{4.7}$$

which we can then link to the standard change in entropy of exchange as

$$\Delta S^0_{ex} = \frac{\Delta H^0_{ex} - \Delta G^0_{ex}}{\mathrm{T}}. \tag{4.8}$$

We, therefore, have a route to obtain typical thermodynamic values from the experimentally observable quantities. We shall now discuss the isotherm, from which we can extract the discussed parameters.

Isotherms (and their integration of) can be used to extract thermodynamic equilibrium constants, thus characterise the equilibrium of ion-exchange. If we immerse an exchanger within a known fraction of ions within a solution until equilibrium is reached, then we can measure the concentration of all ionic species in the solution and exchanger phase. It is then possible to build an isotherm, describing the equilibrium fraction of ion-exchange occurring at varying solution fractional concentrations. To illustrate this, two examples of such isotherms are presented in Figure 4.2. One being a fictitious case (a) and the other experimental data of Cs ion-exchange of phlogopite mica (b). The separation factor (α^B_A) of an ion-exchanger is given as

$$\alpha^B_A = \frac{\overline{X}_B \cdot (1 - X_B)}{(1 - \overline{X}_B) \cdot X_B} = \frac{\overline{X}_B X_A}{\overline{X_A} X_B} = \frac{\overline{C_B} C_A}{\overline{C_A} C_B}. \tag{4.9}$$

where $\overline{X}_B$ is the fraction of ion B in the membrane phase, X_B is the fraction of ion B in the solution phase. Which we can relate to the measurable α^A_B from equations 4.4 and 4.5. There are several factors that can affect selectivity: physical sieving and steric hindrance, protonation (selective to H^+) and the distance to the closest approach of the fixed charge by the counter-ion. Isotherms describe the equivalent fraction of an occurred ion (say of ion i) exchange in the exchanger versus the equivalent fraction of ion i in the solution phase. Two examples are given in Figure 4.2, representing a fictitious ion-exchange isotherm, and the parameters we can readily extract to quantify the separation factor α^B_A given in Equation 4.9. Moreover, an equilibrium isotherm is a graphical representation of the relationship between the equilibrium and all possible experimental conditions at a constant temperature [11]. In summary, we now have a method to characterise ion-exchange equilibria and separation factors by measuring the exchange isotherm and extracting the discussed parameters, via the relations presented within this section.

Lastly in this section, we shall briefly discuss two other models which have been used to describe ion-exchange, although limiting our discussion for brevity. Firstly, Soldatov devised a model with the intention to explain the phenomenon of enhanced selectivity toward ions of small concentrations. This assumes different exchange sites can exist within the ion-

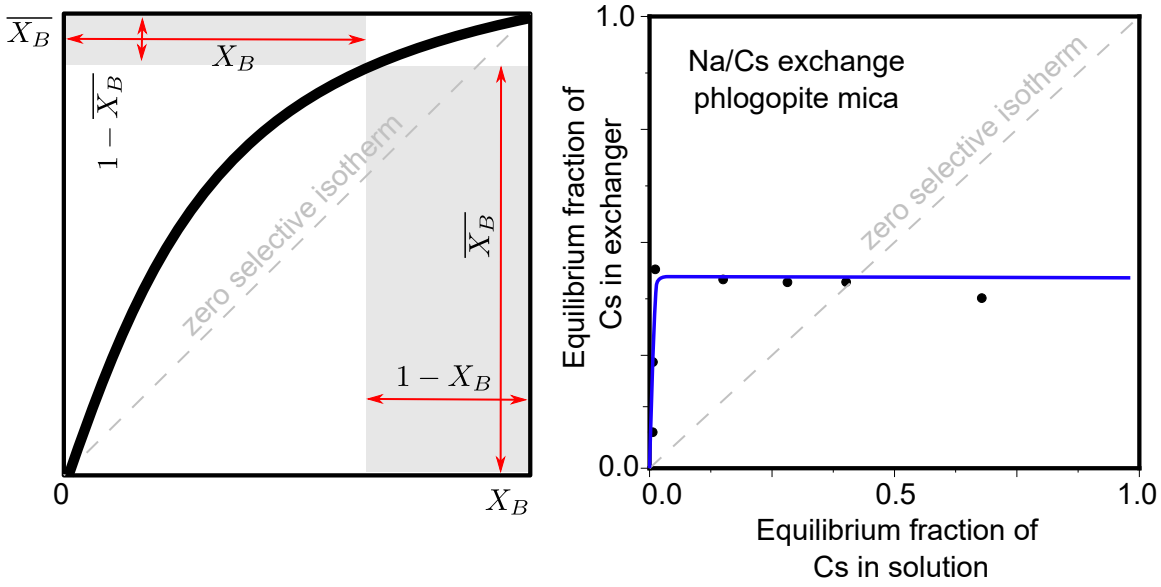

Figure 4.2: (**a**) Relation between ion-exchange isotherm and separation factor. The heavy line represents the isotherm. The separation factor can be visualised as the ratio between two rectangular areas in contact with one another at the corresponding point on the isotherm. Adapted from [11]. (**b**) Na/Cs exchange isotherm of K-depleted phlogopite mica, where the diagonal line represents an equal preference for both the cations. A Horizontal isotherm represents an absolute preference of phlogopite to Cs ion-exchange. Adapted from [18], [23]

exchanger, depending on the physical structure or nearest neighbour occupancies [24]. Consequently, Gibbs energies for different exchange sites are not the same, and this is not considered in most models of ion-exchange. Another approach is the so-called surface complexation model, which treats the ion-exchanger as a plane of uniformly distributed ion-exchange sites, modelled as a charged plane [25]. Protons are considered differently in the model and can reside within the plane, whereas other ions form Stern and diffuse layers. Ion selectivity is accounted for by the formation of surface complexes, where different ions form different surface structures. This model uses concepts borrowed from the EDL formation, presented in Chapter 2, Section 2.3.5. Next, let us consider how ion-exchange varies as a function of time.

4.0.1.2 Kinetics of Ion-Exchange

During exchange reactions, electroneutrality is preserved and the kinetics of exchange are very often diffusion-rate-limited, although reactions between counter-ions and fixed groups, can in some instances be significant and limit the exchange rate [11]. Kinetic modelling is undertaken using differing approaches [11], commonly being derived from the electrochemical potential. One such approach is a physicochemical model, evaluating rate constants. Many exchange processes are time-dependent, and the fate of ions that undergo exchange can only be predicted with knowledge of the kinetics. In this section, we introduce an overview of the kinetics of ion-exchange. To begin with, let us return to the previously presented reaction,

this time including the forward and reverse reaction rates $k_{\rightarrow}$ and $k_{\leftarrow}$, respectively,

$$\underset{\text{clay}}{\mathrm{M}^{-}\mathrm{A}^{+}} + \underset{\text{solution}}{\mathrm{B}^{+}} \underset{k_{\leftarrow}}{\overset{k_{\rightarrow}}{\rightleftharpoons}} \underset{\text{clay}}{\mathrm{M}^{-}\mathrm{B}^{+}} + \underset{\text{solution}}{\mathrm{A}^{+}} . \tag{4.10}$$

from which we can obtain the forward and reverse rate laws as [22]

$$\frac{\mathrm{d}C_B}{\mathrm{dt}} = -k_{\rightarrow}C_{MA}^{\alpha}C_B^{\beta} + k_{\leftarrow}C_{MB}^{\gamma}C_A^{\delta} \tag{4.11}$$

where C_X are concentrations of component X of the ion-exchange process and α, β, γ and δ are the partial orders whereas the overall order is $n = \alpha + \beta + \gamma + \delta$. If we neglect the reverse reaction rate, which can be justifiable by measurement of the initial reaction rate, or by having a large initial excess of ion A^{+} [22], then Equation 4.11 becomes

$$\frac{\mathrm{d}\overline{C_A}}{\mathrm{dt}} = -k_{\rightarrow}(C_A) \tag{4.12}$$

where C_A^0 is the initial concentration of ion A which we can readily integrate (assuming first-order reaction), using the initial conditions at t=0, C=C_0 to give

$$\log\left(C_B(\mathrm{t})\right) = \log\left(C_0\right) - \left(\frac{k_{\rightarrow}}{2.303}\mathrm{t}\right). \tag{4.13}$$

If the measured plot of $\log C_B(\mathrm{t})$ against time results in a linear slope with an intercept at $\log\left(C_0\right)$, then we can extract the forward rate coefficients. It is worth noting that the observed rate coefficients are often a combination of

$$k_{\rightarrow} = k_R + k_P + k_F \tag{4.14}$$

Where the rate coefficients k_R, k_P and k_F are the reaction, particle and Nernst film rate coefficients respectively. These characterise the rate-limiting process (discussed shortly). These three separate rate coefficients can be identified by running exchange experiments in various modes such as static, stirred and vortex batch [26]. Now, there are cases where the exchange reaction is not first-order. Thus, Equation 4.13 is invalid. We can therefore test other integral solutions to equations 4.11 and 4.13, including zero-order, second-order, Elovich, parabolic diffusion and power functions [22]. These models do not always match experimental observations and can be empirically based.

We can also approach the kinetic modelling of ion-exchange using mass and charge transfer equations. Let us now briefly introduce this approach. Firstly, it was observed (during work undertaken in conjunction with the Manhattan Project) that the rate of ion-exchange increases as the average exchange particle size decreases [27]. From this observation, it was assumed that the kinetics of ion-exchange are typically mass-transfer (diffusion) rate-controlled rather than chemical reaction rate-controlled. The diffusive properties can, in turn, be at least partly defined by the material structure and macro/micro structure. This diffusion limit can arise from two separate mechanisms. The first being 'particle diffusion' (PD) limited and the second being 'film diffusion' (FD) limited. The former case is where the speed of diffusion

through the exchanger phase is itself the rate-limiting factor, whereas the latter is for the case for diffusion across the Nernst layer being rate-limiting. The FD rate has been observed to be inversely proportional to particle size, whereas the PD rate is proportional to the inverse square of particle size [27]. Hence, if we can perform measurements of the exchange rate as a function of particle size, then we could readily distinguish between the two cases. We can model diffusion using a Markov chain process [28], which we shall describe in more detail in the experimental techniques chapter (Chapter 5). Now, let us recall Fick's laws of diffusion, which we have already seen in the background chapter of ion transport (chapter 2). Mass transport diffusion processes can be described by these laws of diffusion (Equations 2.5 and 2.6), the first law being

$$\bar{J}_{ex} = -D_i \nabla C_i. \tag{4.15}$$

where $\bar{J}_{ex}$ is the ion-exchange flux. Fick's second law, also termed the condition of continuity, is

$$\frac{dC_i}{dt} = D_i \nabla^2 C_i = -\nabla \overline{J}_{ex}. \tag{4.16}$$

Other models of ion-exchange kinetics take into consideration the charge interactions of ions through the inclusion of the Nernst–Planck equation (from Chapter 2, Equation 2.3)

$$\boldsymbol{J_i} = -D_i \nabla C_i - \frac{z_i F}{RT} D_i C_i \nabla \psi + C_i \boldsymbol{v_i} \tag{4.17}$$

Solving this set of equations (equations 4.15-4.17) for a given set of initial and boundary conditions is the basis for conventional modelling of (diffusion-limited) ion-exchange kinetics, allowing for a broad set of solutions. Returning, once again, to the ion-exchange process in Equation 4.10, for the conditions

$$|z_A| \overline{C}_A + |z_B| \overline{C}_B = \overline{C} \tag{4.18}$$

where $\overline{C}$ is the total ion concentration in the exchanger phase, and

$$z_A \overline{J}_A + z_B \overline{J}_B = 0. \tag{4.19}$$

When combined with the Nernst–Planck equations (Equation 4.17), for zero convective transport, we can arrive at the interdiffusion constant within the exchanger phase ($\overline{D}$), known as the Helfferich-Plesset Equation

$$\overline{D} = \overline{D}_A \overline{D}_B (z_A^2 \overline{C}_A + z_B^2 \overline{C}_B) / (z_A^2 \overline{C}_A \overline{D}_A + z_B^2 \overline{C}_B \overline{D}_B) \tag{4.20}$$

yielding a total diffusion coefficient that depends on each of the counter-ion concentrations ($\overline{C}_A$ and $\overline{C}_B$). For the case where $\overline{C}_A \ll \overline{C}_B$ (trace content of ion A), the interdiffusion constant approaches $\overline{D}_A$ inferring that the rate of diffusion for a trace element remains constant and equal to the individual diffusion coefficient irrespective of the mobility of the macrocomponent ion. However, this trace cation effect has not been observed in some studies of ion-exchange resins [29]. The divergence is thought in part to arrive from non-constant diffusion

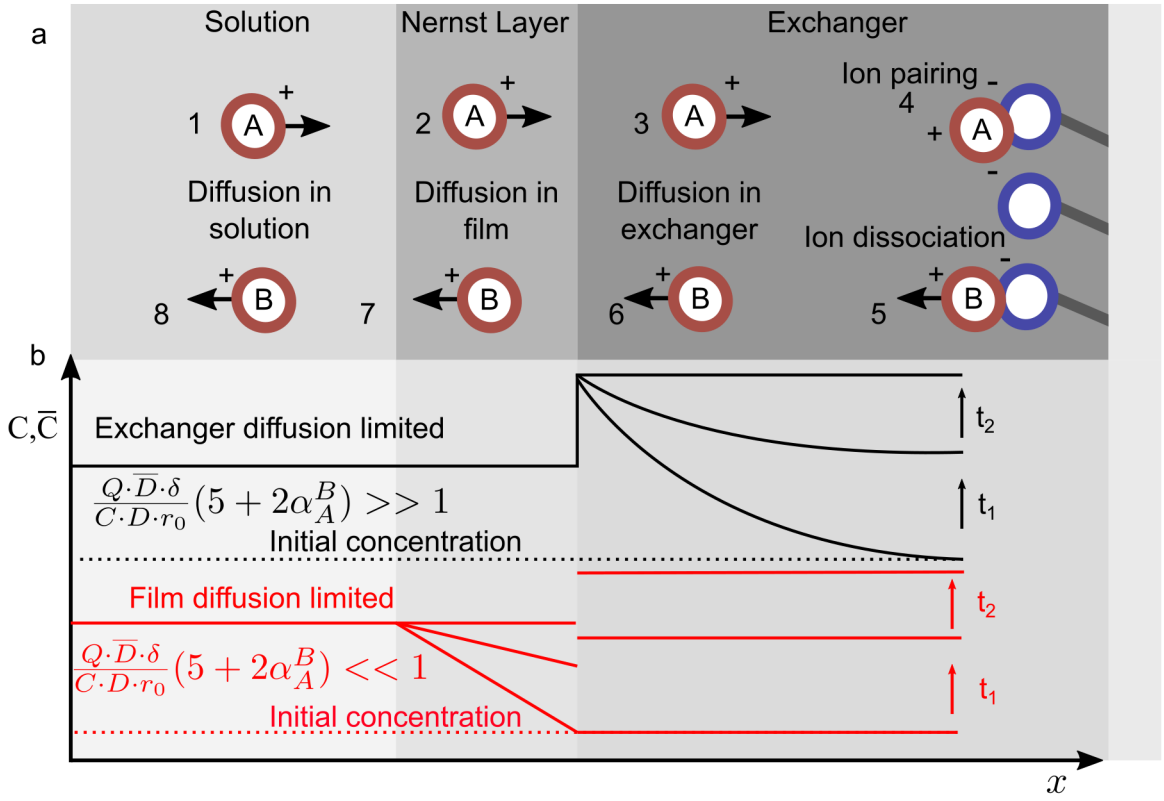

Figure 4.3: Illustration of the various ion diffusion processes and concentrations at the solution-exchanger interface. The exchange rate can be limited by either the diffusion rate across the interfacial film or within the exchanger itself. (**a**) Description of ion-exchange kinetics. Diffusion through the Nernst Layer or exchanger phase (any of steps 2-7) may be the rate limiting step. (**b**) concentration profiles (shown for two incrementing time intervals) for the FD and exchanger diffusion rate-limiting cases when a bulk solution concentration is instantaneously changed to the arbitrary concentration portrayed in the figure. Q is the concentration of fixed groups, C is the solution concentration, δ is the Nernst Layer thickness, r_0 is the characteristic length of exchanger and $\overline{D}$ and D are the diffusion constants in exchanger and Nernst Layer phases, respectively. Adapted from [11].

coefficients and solvent activity changes. Yet, the selectivity of trace cations is a widely–encountered effect in exchangers [11]. Upon the substitution of Equation 4.20 into the condition of continuity (Equation 4.16), it is possible to arrive at time-dependent relations for a wide variety of initial and boundary conditions representing ion-exchange processes. Models that incorporate accompanied reactions in the exchanger phase have also been developed [30]. The above approach falls short to describe processes besides mass transfer, such as that of diffusion through the Nernst layer [26] or where ionic mobilities are not constant. Let us now discuss this Donnan potential derived layer.

The Nernst layer is established across the exchanger-solution phase boundary (due to the differing concentrations of the solution and exchanger phases), as presented in Figure 4.3 a. Any of the steps in Figure 4.3 a can be bottlenecks for limiting the rate of ion-exchange. Although, diffusion in the solution is very rarely the limiting case (it can easily be assisted by stirring). There can also be complex formation in the solution phases, not shown in Figure 4.3

a, which can limit the rate. Figure 4.3 b also presents stylised concentration profiles for either the Nernst film layer (red) or bulk exchanger diffusion rate-limited (black) case. For the film layer rate-limiting case, as one would expect, after a change in bulk ion concentration, the gradient occurs within the Nernst layer. However, for the exchanger phase rate limiting case, an alteration to the bulk concentration manifests as a gradient across the exchanger phase. Now, increasing the external solution concentration can result in a switch from Nernst layer diffusion-limited to exchanger rate-limited exchange. This is because the Nernst layer itself can be altered by changing the solution concentration. Let us briefly summarise the key differences between the two limiting cases. For the PD limited case, it generally proceeds at a high rate of exchange, where this rate is approximately proportional to the concentration of fixed charges as well as diffusion constant. The exchange flux is independent of solution concentration, Nernst layer thickness and diffusion constants. For the Nernst layer limited case, the exchange flux is independent of ion-exchange fixed-site concentration and diffusivity of the exchanger phase, whereas it is dependent on solution concentration and inversely proportional to Nernst layer thicknesses. A dilute solution can result in a Nernst layer transport limited process. Now, a simple experimental technique to differentiate between the two cases is the so-called 'interruption test' where the exchange process is temporarily interrupted and then restarted. The two cases will then proceed at different rates for either rate-limited case [31]. Finally, the Nernst layer and bulk exchanger can comparably limit the diffusion rate. A study showed such as case to be that of vermiculite [26], but we model the exchange process using an effective diffusion rate in Chapter 8. Exchanger (PD) limited exchange proceeds at a significantly higher rate and importantly, the ion-exchange flux $\overline{J_{ex}}$ is also often proportional to the concentration of fixed charges. Donnan exclusion (see chapter 2 section 2.3.4.2) results in restriction of co-ion transport across the interphase boundary. Therefore, co-ions do not participate in the overall exchange process thus do not affect the rate. Let us now consider the properties of Muscovite and Vermiculite, the two materials used for ion-exchange processes in chapters 7 and 8.

4.0.2 Muscovite and Vermiculite Clay Properties

We have introduced the mica family of crystals, within the context of 2D materials in Chapter 3. Here, we shall consider them in further detail as Chapter 8 will present S/TEM observations of clay and mica ion-exchange phenomena and in Chapter 7, we shall explore work exploiting ion-exchange to fabricate a proton-conducting membrane. Both vermiculite and muscovite are 2:1 (TOT-c) silicate structures (see Chapter 3 Section 3.1.3). These both contain internal and external exchange sites, arising from charge imbalances within the lattice. A key difference between these minerals is that micas have a more restricted interlayer space compared to vermiculite, with the latter also being hydrated within the interlayer gallery. Let us now consider the various properties of these minerals.

4.0.2.1 Surface

The highly hydrophilic surface of mica is often used as an atomically smooth substrate for a multitude of surface force and imaging studies [32]–[34], or more recently for elaborate water confinement effects [35]. However, when cleaved in an ambient atmosphere or immersed in aqueous solutions, is likely far from an inert and atomically smooth substrate that many assume [36]. Among other important properties, the high surface energy and water wettability are desirable for use in studies that involve adsorbing molecules or nanoscale objects to immobilise them for measurements in either air, vapour or liquid phases. Interestingly, these mineral surfaces have been suggested to have been involved in mineral-assisted biogenesis of life [37]–[39]. Where they may have played a role in protecting, selecting, concentrating, templating, and catalysing reactions of prebiotic organic molecules. Now, the surface of mica and vermiculite both consist of SiO_4 tetrahedral hexagonal rings with hydroxyl groups underlying the centre, as illustrated in figure 4.4. It is worth noting that divergence from the ideal structure occurs due to strain induced by the size misfit between the octahedra and tetrahedra [36]. This creates a ditrigonal symmetry rather than the ideal hexagonal symmetry. Now, interlayer and surface cations reside close to the cavity containing the hydroxyl, where some cations such as K^+ can reside deeper within the lattice. Importantly, for the work presented in Chapter 7, the surface native ion can be readily and exchanged for protons, shown via X-ray photoelectron spectroscopy (XPS) studies [40], [41]. Detailed atomic resolution of the mica surface lattice is possible using force modulated AFM in liquid [42] where features such as subnanometre-scale structural defects are resolvable. The imaging of mica-bound nanoscale materials enables high levels of conformational characterisation. Ion distribution on the mica surface has remained quite elusive in literature, although has been reported in AFM studies as protrusions from the surface above the Al^{3+} substituted tetrahedra [43]. It was also found, via friction force microscopy, that different surface exchanged ions significantly modify the tribological properties of mica [44] and that these ions are often mobile in a hydrated environment, yet the proton (or hydronium) was shown to be less mobile across a range of humidity levels, suggesting it may bind in a different fashion to that of the other ions. This has also been suggested by other studies on hydronium ion interactions with mica. where protons assimilating within the lattice may explain findings [45], [46]. Lastly, an extensive review by Christenson et al. presented a compelling argument for the surface reactivity of freshly cleaved mica, whereby ions on the surface undergo chemical reactions with CO_2 and water to form carbonates such as K_2CO_3 [36]. In summary, the surface of mica is likely an active and dynamic charged surface that can be readily modified via ion-exchange.

4.0.2.2 Exposed Hydroxyls

A notable feature of the mica and clay lattice are the hydroxyls residing approximately 2 Å beneath the hexagonal ring of silicate tetrahedra, as shown in Figure 4.5. A further contribution to the exchange capacity of clay minerals is made by the hydrogens of exposed hydroxyl groups which may be replaced by exchangeable cations. Exposed groups may also

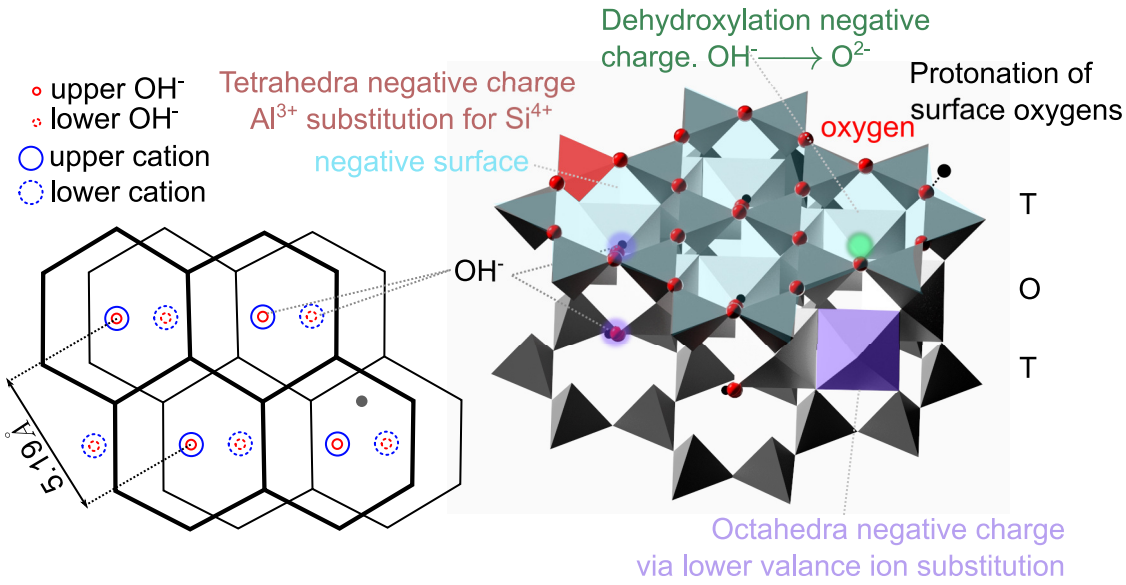

Figure 4.4: An illustration of the properties of negatively charged mica surface showing the locations of exposed hydroxyl groups and regions where layer negative charge can originate.

exhibit a slight but reversible affinity for exchangeable anions [1], at least in part explaining their anion exchange capacity. The orientation of these OH groups has been probed using pleochroism[1] where the dipole moment of the subsurface OH groups is thought to be tilted out of the cleavage plan by approximately 15-16° for muscovite [47], [48], but can vary across the mineral family. These hydroxyls are highlighted in figures 4.4 and 4.5. The significance of these OH groups is brought to the reader's attention because it is important for the proposed mechanism to explain experimental findings in Chapter 7. Vibrational spectroscopy can readily characterise the OH stretching mode. The complementary techniques of Raman, Fourier-transform infrared spectroscopy (FTIR) and sum-frequency generation spectroscopy can probe the 3500-3750 cm^{-1} broad OH stretching modes [48]–[50]. This broad band of stretching modes reflects the wide range of possible OH bond configurations, as discussed in Chapter 2, Section 2.3.2.2.

4.0.2.3 Muscovite Mica

Having already introduced mica as a 2D material in Section 3.1.3 and preceding sections in this chapter, we shall expand upon our description of muscovite here due to its importance in Chapter 7 and 8. Muscovite is named after the Russian province of Muscovy, the name being derived from Muscovy glass, comprised of large sheets of the material. Now, the general formula for mica minerals, including muscovite is: $I_2M_{4\text{-}6}X_{2\text{-}0}T_8O_{20}A_4$, where I is the interlayer exchangeable cation, M is the octahedral cation, X is a vacant site, T is the tetrahedral cation, often Si^{4+} and Al^{3+}, O is oxygen and A is an anion underlying the tetrahedral rings, often OH. The full possible composition of each component is provided in Appendix G. This formula provides some indication as to how compositionally diverse this group of minerals can be. The SiO_4 tetrahedra of muscovite are rotated by 11-13° in alternating sequence, creat-

[1] Analysing the absorption spectrum at varying angles.

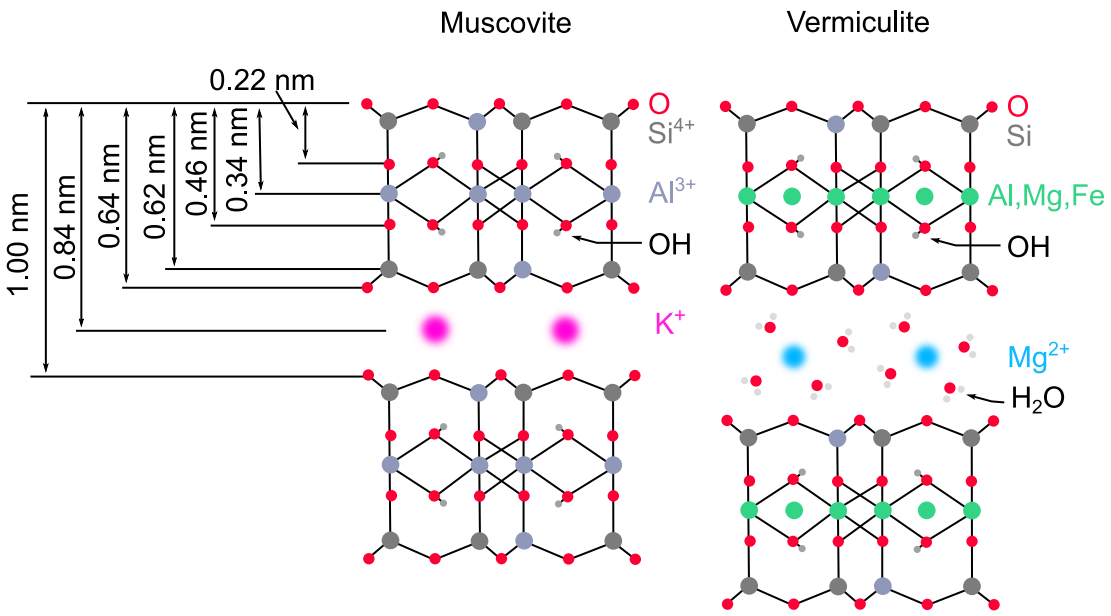

Figure 4.5: Cross-section of muscovite and vermiculite. Muscovite is most often a dioctahedral mica (2/3 of octahedral ion sites are occupied) whereas vermiculite is a trioctahedral clay (most octahedral ion sites are occupied). This is shown in the green atomic sites, filling all octahedra. Vermiculite has a larger interlayer space by about 4Å due to the interlayer water. Figure adapted from [60] and [53].

ing ditrigonal symmetry [51]. A common space group of the crystal is $2M_1$, being a staggered stacking sequence with a unit cell crossing two structural units. The chemical composition of muscovite varies as outlined in the general formula above. It is distinguished between other micas as having a low iron content, substitution ratio in the tetrahedra of Al:Si = 1:3 [52], high potassium interlayer fraction and having an optical axial plane perpendicular to the [010] direction [53]. The Al:Si substitution, often then origin for micas negative TOT charge, is thought to obey Lowenstein's rule (avoiding Al-O-Al linkages) [54] possibly displaying short-range ordering [52], [55] but does not typically display longer-range order [51]. The TOT layer charge is typically close to -1 e per formula unit [51]. Powdered muscovite has been shown to be rather chemically inert, with only a small fraction (approximately 6%) of the available aluminium and potassium leaching out into a 1 M HCl solution over the course of 2 hours [56]. Dissolution rates at pH 1.4 have been estimated to be 6.35 $\times 10^{-16}$ mol s^{-1} [57]. Now, muscovite has been used as a thin dielectric layer in electronics components due to its large band gap of 7.85 eV [58]. Due to this, it was labelled as one of the most important materials during the second world war [59]. Its atomically flat surface is desirable for many nanoscale imaging applications. In the natural environment, muscovite can weather to illite and montmorillonite clays and eventually into the 1:1 clay kaolinite as potassium and interlayer charges are lost. These weathered products are abundant in soils.

4.0.2.4 Vermiculite Clay

Vermiculite is a weathered mica [54], particularly derived from biotite or phlogopite, and while it is similar to micas, it contains interlayer water and a lower negative layer charge of 0.6-

0.9 e due to trivalent substitution in the octahedra or protonation of the lattice, reducing the net negative charge of the TOT structure [54]. The residual charge is balanced by hydrated cations within the interlayer and surface. Vermiculite does not typically swell to the extent of other clays, such as montmorillonite. This is because its high relative lattice charge increases the binding strength between layers. The interlayer separation depends on ion type and hydration spheres and is often between 12 Å and 14 Å and measurable by X-ray diffraction. The lattice cross-section is given in Figure 4.5. Vermiculite is from the Latin word for worm, *vermis* because the crystal expands in a worm-like manner upon heating at around 800 °C. This expanded vermiculite finds uses in agriculture to improve soil properties, such as its IEC, aeration and water retention. It is also useful as a thermal insulator due to its thermal stability and low thermal conductivity.

4.0.2.5 S/TEM Imaging of Clay

TEM is a useful tool for investigating ion-exchange processes, in particular, elucidation of ion-exchange kinetic effects in clays such as the links between selectivity and rate [26]. Conventional TEM images pass a parallel beam of electrons through a thin specimen, whereas scanning TEM (S/TEM) scans a focused electron beam over the sample. Both modes are capable of imaging ions within clays directly, yet imaging on the surface has proven challenging, due to difficulty in isolation [61] and beam sensitivity [62]. High-angle annular dark-field imaging (HAADF) is a S/TEM technique that operates by detecting Rutherford scattered electrons at high angles and creating a dark-field image from them. The scattering intensity is proportional to the charge of the nuclei. Hence, the measured signal is highly related to the atomic number of atoms that the electron beam interacts with. Now, pioneering work by Buseck et al. presented high-quality lattice images of thin silicate minerals using TEM [63]. In this study, structural images of many silicate framework minerals were presented but did not conclusively image thin muscovite sections. Later work by Kogure et al were able to distinguish cross-sections of biotite and vermiculite layer spacings using high-resolution TEM (HRTEM). This measurement was complimented by selected area electron diffraction (SAED) patterns to further characterise basal spacing [64]. The technique of SAED exploits the wave-like properties of electrons. A broad parallel electron beam impinges on the sample, and the lattice then acts as a diffraction grating, producing a pattern characteristic of the sample. Further work using HRTEM, from the same author, imaged higher resolution images of Pyrophyllite[2] revealing a varying stacking sequence arrangement [65]. The development of the spherical aberration corrector at the end of the twentieth century [66], [67], helped dramatically improve the resolution of electron microscopy. This aberration corrected technique was employed by Kogure et al to resolve high-quality images of silicate structures [66]. Another approach to imaging near-atomic resolution images of clay minerals is that of cryogenic TEM [68], where this technique has measured calcium and sodium montmorillonite swelling properties [69] in situ. This technique likely offers the advantage of decreased dehydration during imaging, compared to non-vitrified samples. The imaging of ions within silicate structures

[2] A talc like neutral layer charge 2:1 silicate mineral containing a vacant interlayer region.

has been accomplished using the aforementioned HAADF S/TEM approach [67] an example of which (from work conducted in chapter 8) is also presented in figure 3.2 in chapter 3. More related to the study presented in chapter 8, caesium ion-exchange for existing Ca^{2+} ions in illite have been observed using HAADF S/TEM [5]. In that work, in combination with extended X-ray absorption fine structure spectroscopy (EXAFS), caesium was shown to bind to frayed clay edges and then collapse the layers, preventing further rapid exchange, yet over longer time-scales, the caesium migrated into the interlayer region. Recently, suspended monolayer montmorillonite clay has been observed at atomic resolution using annular dark-field (ADF) S/TEM [62], [70]. Electron acceleration voltages of 300 kV and 3 s dwell time were employed for this investigation. Mica and clay minerals are known to be quite beam-sensitive, with mechanisms for this damage arising from effects such as radiolysis from the electrons and sample heating (heat cannot easily dissipate due to the low thermal conductivity of these minerals). In summary, electron microscopy is a useful tool to probe clay/mica lattices directly, with high levels of detail. Insights into exchange mechanisms and ion distribution can be gained from such measurements.

4.0.3 Mica and Vermiculite Clay Ion-Exchange

To recall, mica TOT layers are bound together by cation interlayers, such as those of K^+, shown in Figure 3.2. This TOT-c-TOT interaction is electrostatic in nature and stronger than those of van der Waals bonds between adjacent graphene and hBN layers, making isolation of very thin layers arguably more challenging [61]. Micas can exchange most cations that are electrostatically bound to the lattice. This can be the exchange of ions of the surface [46], [71] or, to a lesser extent, the interlayer cations [17]. This is not the case for smaller TOT layer charge clays, which can readily exchange ions within the interlayer gallery. The cation-exchange capacities of clays typically increase with pH [22], due to the deprotonation of functional groups as the pH of the solution increases. For a given group of elements, sharing the same valance, ions with the smallest hydration radius will typically be preferentially exchanged. Such ordering of preferred ion-exchange for monovalent group one elements is Cs^+>Rb^+>K^+>Na^+>Li^+>H^+ [22]. Furthermore, higher valance ions are generally preferred where Al^{3+}>Ca^{2+}>K^+=NH_4^+>Na^+. Ca-vermiculite exchange of caesium ions displays two distinct reaction rates. The first being rapid exchange at planar surfaces and interlattice edge sites. The second being attributed to the slower process of caesium diffusion into the interlayer of vermiculite. For K^+ adsorption under static conditions, the rate coefficients for film and PD, at 283 K were 0.037 and 0.055 min^{-1}, respectively [72]. Because the rates are comparable, both Nernst-Layer and PD are rate-limiting for this case of transport for vermiculite and this may also be the case for caesium exchange processes, important for Chapter 8.

4.1 Summary

The ion-exchange of mica and clays is a process so fundamental to ion uptake and transport in soils as well as for plant nutrient absorption. Generally, it is also a process vital for water treatment and other industries. The removal of heavy metal cations and other pollutants via ion-exchangers assists us with purifying drinking water. With clays and micas being so commonplace in the environment, a rigorous understanding of their ion-exchange properties is paramount, especially in the context of managing soils, which are now significantly under the stewardship of mankind [73], [74]. Lastly, these minerals can be made nanometre-thin through controlled exfoliation[3], and if the research on graphene has taught researchers anything, it is that the properties of low dimensional systems can diverge from their bulk counterparts. Therefore, new properties of these minerals in the atomically-thin limit may arise. Indeed, this is a significant aspect of the topics in chapters 7 and 8.

References

[1] C. Harland, *Ion Exchange: Theory and Practice*. Royal Society of Chemistry, 2007, pp. 10–300.

[2] Y. Takahashi, Q. Fan, H. Suga, K. Tanaka, A. Sakaguchi, Y. Takeichi, K. Ono, K. Mase, K. Kato, and V. V. Kanivets, "Comparison of solid-water partitions of radiocesium in river waters in Fukushima and Chernobyl areas," *Scientific Reports*, vol. 7, no. 1, pp. 1–11, 2017.

[3] M. Okumura, S. Kerisit, I. C. Bourg, L. N. Lammers, T. Ikeda, M. Sassi, K. M. Rosso, and M. Machida, "Radiocesium interaction with clay minerals: Theory and simulation advances Post–Fukushima," *Journal of Environmental Radioactivity*, vol. 189, pp. 135–145, 2018.

[4] B. J. Howard, S. Fesenko, M. Balonov, G. Pröhl, and S. Nakayama, "A comparison of remediation after the Chernobyl and Fukushima Daiichi accidents," *Radiation Protection Dosimetry*, vol. 173, no. 1-3, pp. 170–176, 2017.

[5] A. J. Fuller, S. Shaw, M. B. Ward, S. J. Haigh, J. F. W. Mosselmans, C. L. Peacock, S. Stackhouse, A. J. Dent, D. Trivedi, and I. T. Burke, "Caesium incorporation and retention in illite interlayers," *Applied Clay Science*, vol. 108, pp. 128–134, 2015.

[6] W. Agui, M. Takeuchi, M. Abe, and K. Ogino, "Fundamental study on the production of ultrapure water. removal of leachables from mixed-bed ion exchange resins," *Bulletin of the Chemical Society of Japan*, vol. 63, no. 10, pp. 2872–2876, 1990.

[3] Of course, with the possibility to be embedded in composites.

[7] Y. Tanaka, *Ion Exchange Membranes: Fundamentals and Applications*, 2nd ed. Elsevier, 2015, pp. 29–100.

[8] R. Harjula, J. Lehto, A. Paajanen, L. Brodkin, and E. Tusa, "Removal of radioactive cesium from nuclear waste solutions with the transition metal hexacyanoferrate ion exchanger CsTreat," *Nuclear Science and Engineering*, vol. 137, no. 2, pp. 206–214, 2001.

[9] R. Harjula, J. Lehto, A. Paajanen, E. Tusa, and P. Yarnell, "Use inorganic ion exchange materials as precoat filters for nuclear waste effluent treatment," *Reactive and Functional Polymers*, vol. 60, pp. 85–95, 2004.

[10] V. Soldatov, S. Kasandrovich, and O. Ionova, "Preparation of ion exchange substrates for plants," *Proceedings of the National Academy of Sciences of Belarus, Chemical Series*, no. 1, pp. 7–13, 2017.

[11] A. A. Zagorodni, *Ion exchange materials: properties and applications*. Elsevier, 2006, pp. 221–243.

[12] Y. A. Berkovich, N. Krivobok, S. Krivobok, V. Matusevich, and V. Soldatov, "Development of a root feeding system based on a fiber ion-exchange substrate for space plant growth chamber "vitacycle"," *Habitation*, vol. 9, no. 1, pp. 59–65, 2003.

[13] H. Araki, M. Umeda, Y. Enokida, and I. Yamamoto, "Effect of development speed on separative performance of displacement chromatography using porous ion exchange resin for Li isotope separation," *Fusion Engineering and Design*, vol. 39, pp. 1009–1013, 1998.

[14] T. Tsukamoto, T. Oi, M. Hosoe, and H. Kakihana, "Boron isotope separation by ion-exchange chromatography using an anion exchange resin in halide forms. temperature dependence of separation factor," 1991.

[15] A. V. Kruglov, B. M. Andreev, and Y. E. Pojidaev, "Continuous isotope separation in systems with solid phase. Separation of nitrogen isotopes with use of ion-exchange resin," *Separation Science and Technology*, vol. 31, no. 4, pp. 471–490, 1996.

[16] N. Li, L. Zhang, Y. Chen, M. Fang, J. Zhang, and H. Wang, "Highly efficient, irreversible and selective ion exchange property of layered titanate nanostructures," *Advanced Functional Materials*, vol. 22, no. 4, pp. 835–841, 2012.

[17] G. L. Gaines Jr and H. C. Thomas, "Adsorption studies on clay minerals. ii. a formulation of the thermodynamics of exchange adsorption," *The Journal of Chemical Physics*, vol. 21, no. 4, pp. 714–718, 1953.

[18] S. Komarneni and R. Roy, "A cesium-selective ion sieve made by topotactic leaching of phlogopite mica," *Science*, vol. 239, no. 4845, pp. 1286–1288, 1988.

[19] M. Wilson, "Clay mineralogy: Spectroscopic and chemical determinative methods," pp. 300–327, 1994.

[20] R. Gast and W. Klobe, "Sodium-lithium exchange equilibria on vermiculite at 25 C and 50 C," *Clays and Clay minerals*, vol. 19, no. 5, pp. 311–319, 1971.

[21] P. Atkins and J. De Paula, *Atkins' physical chemistry*, 11th ed. Oxford University press Oxford, 2017.

[22] D. L. Sparks, *Environmental soil chemistry*. Elsevier, 2003, pp. 150–190.

[23] T. Nakato, J. Kawamata, and S. Takagi, *Materials Chemistry of Inorganic Nanosheets Overview and History*. Springer, 2017, pp. 263–365.

[24] V. Soldatov, "Mathematical modelling of ion exchange equilibria on resinous ion exchangers," *Reactive Polymers*, vol. 19, no. 1-2, pp. 105–121, 1993.

[25] J. Horst, W. H. Höll, and S. H. Eberle, "Application of the surface complex formation model to exchange equilibria on ion exchange resins. part i. weak-acid resins," *Reactive Polymers*, vol. 13, no. 3, pp. 209–231, 1990.

[26] D. L. Sparks, *Kinetics of soil chemical processes*. Academic Press, 1989, pp. 99–127.

[27] G. Boyd, A. Adamson, and L. Myers Jr, "The exchange adsorption of ions from aqueous solutions by organic zeolites.," *Journal of the American Chemical Society*, vol. 69, no. 11, pp. 2836–2848, 1947.

[28] O. C. Ibe, *Elements of random walk and diffusion processes*. John Wiley & Sons, 2013, pp. 1–113.

[29] H. Sharma, R. Jervis, and L. McMillen, "Kinetics of ion exchange. diffusion of trace component," *The Journal of Physical Chemistry*, vol. 74, no. 5, pp. 969–978, 1970.

[30] F. Helfferich, "Ion-exchange kinetics. ion exchange accompanied by reactions," *The Journal of Physical Chemistry*, vol. 69, no. 4, pp. 1178–1187, 1965.

[31] F. Helfferich and J. Dranoff, *Ion exchange, mcgraw-hill, new york (1962), 624*, 1963.

[32] B. Drake, C. Prater, A. Weisenhorn, S. Gould, T. Albrecht, C. Quate, D. Cannell, H. Hansma, and P. Hansma, "Imaging crystals, polymers, and processes in water with the atomic force microscope," *Science*, vol. 243, no. 4898, pp. 1586–1589, 1989.

[33] J. Israelachvili, "Thin film studies using multiple-beam interferometry," *Journal of Colloid and Interface Science*, vol. 44, no. 2, pp. 259–272, 1973.

[34] M. A. Gebbie, A. M. Smith, H. A. Dobbs, G. G. Warr, X. Banquy, M. Valtiner, M. W. Rutland, J. N. Israelachvili, S. Perkin, R. Atkin, *et al.*, "Long range electrostatic forces in ionic liquids," *Chemical communications*, vol. 53, no. 7, pp. 1214–1224, 2017.

[35] Q. Yang, P. Sun, L. Fumagalli, Y. Stebunov, S. Haigh, Z. Zhou, I. Grigorieva, F. Wang, and A. Geim, "Capillary condensation under atomic-scale confinement," *Nature*, vol. 588, no. 7837, pp. 250–253, 2020.

[36] H. K. Christenson and N. H. Thomson, "The nature of the air-cleaved mica surface," *Surface Science Reports*, vol. 71, no. 2, pp. 367–390, 2016.

[37] H. J. Cleaves II, A. M. Scott, F. C. Hill, J. Leszczynski, N. Sahai, and R. Hazen, "Mineral–organic interfacial processes: Potential roles in the origins of life," *Chemical Society Reviews*, vol. 41, no. 16, pp. 5502–5525, 2012.

[38] G. Ertem and J. P. Ferris, "Synthesis of RNA oligomers on heterogeneous templates," *Nature*, vol. 379, no. 6562, pp. 238–240, 1996.

[39] J. P. Ferris and G. Ertem, "Oligomerization of ribonucleotides on montmorillonite: Reaction of the 5-phosphorimidazolide of adenosine," *Science*, vol. 257, no. 5075, pp. 1387–1389, 1992.

[40] P. J. Sides, D. Faruqui, and A. J. Gellman, "Dynamics of charging of muscovite mica: Measurement and modeling," *Langmuir*, vol. 25, no. 3, pp. 1475–1481, 2009.

[41] L. Xu and M. Salmeron, "An XPS and scanning polarization force microscopy study of the exchange and mobility of surface ions on mica," *Langmuir*, vol. 14, no. 20, pp. 5841–5844, 1998.

[42] T. Fukuma, K. Kobayashi, K. Matsushige, and H. Yamada, "True atomic resolution in liquid by frequency-modulation atomic force microscopy," *Applied Physics Letters*, vol. 87, no. 3, p. 034 101, 2005.

[43] S.-H. Loh and S. P. Jarvis, "Visualization of ion distribution at the mica- electrolyte interface," *Langmuir*, vol. 26, no. 12, pp. 9176–9178, 2010.

[44] L. Xu and M. Salmeron, "Effects of surface ions on the friction and adhesion properties of mica," *Langmuir*, vol. 14, no. 8, pp. 2187–2190, 1998.

[45] R. S. Bradley, "The surface reaction between oxonium ions and mica," *Transactions of the Faraday Society*, vol. 35, pp. 1361–1366, 1939.

[46] P. Claesson, P. Herder, P. Stenius, J. Eriksson, and R. Pashley, "An esca and aes study of ion-exchange on the basal plane of mica," *Journal of colloid and interface science*, vol. 109, no. 1, pp. 31–39, 1986.

[47] W. Vedder and R. McDonald, "Vibrations of the OH ions in muscovite," *The Journal of Chemical Physics*, vol. 38, no. 7, pp. 1583–1590, 1963.

[48] A. Tuladhar, Z. A. Chase, M. D. Baer, B. A. Legg, J. Tao, S. Zhang, A. D. Winkelman, Z. Wang, C. J. Mundy, J. J. De Yoreo, *et al.*, "Direct observation of the orientational anisotropy of buried hydroxyl groups inside muscovite mica," *Journal of the American Chemical Society*, vol. 141, no. 5, pp. 2135–2142, 2019.

[49] A. Tlili, D. Smith, J.-M. Beny, and H. Boyer, "A Raman microprobe study of natural micas," *Mineralogical Magazine*, vol. 53, no. 370, pp. 165–179, 1989.

[50] P. S. Nayak and B. Singh, "Instrumental characterization of clay by XRF, XRD and FTIR," *Bulletin of Materials Science*, vol. 30, no. 3, pp. 235–238, 2007.

[51] M. E. Fleet, W. A. Deer, R. A. Howie, and J. Zussman, *Rock-forming minerals: micas*. 2003.

[52] E. J. Palin and M. T. Dove, "Investigation of Al/Si ordering in tetrahedral phyllosilicate sheets by monte carlo simulation," *American Mineralogist*, vol. 89, no. 1, pp. 176–184, 2004.

[53] W. Deer, R. Howie, and J. Zussman, *An Introduction to the Rock-Forming Minerals*, 3rd. The Mineralogical Society, 2014.

[54] M. Wilson, W. Deer, R. Howie, and J. Zussman, *Rock-forming minerals, volume 3C, sheet silicates: Clay minerals*. 2013.

[55] H. Haselton Jr, G. Cygan, and D. Jenkins, "Experimental study of muscovite stability in pure H_2O and 1 molal KCl-HCl solutions," *Geochimica et Cosmochimica Acta*, vol. 59, no. 3, pp. 429–442, 1995.

[56] S. Snäll and T. Liljefors, "Leachability of major elements from minerals in strong acids," *Journal of Geochemical Exploration*, vol. 71, no. 1, pp. 1–12, 2000.

[57] K. G. Knauss *et al.*, "Muscovite dissolution kinetics as a function of pH and time at 70 C," *Geochimica et Cosmochimica Acta*, vol. 53, no. 7, pp. 1493–1501, 1989.

[58] A. Davidson and A. Vickers, "The optical properties of mica in the vacuum ultraviolet," *Journal of Physics C: Solid State Physics*, vol. 5, no. 8, p. 879, 1972.

[59] L. McNeil and M. Grimsditch, "Elastic moduli of muscovite mica," *Journal of Physics: Condensed Matter*, vol. 5, no. 11, p. 1681, 1993.

[60] S. Miyake, "Atomic-scale wear properties of muscovite mica evaluated by scanning probe microscopy," *Applied Physics Letters*, vol. 65, no. 8, pp. 980–982, 1994.

[61] F. Jia and S. Song, "Preparation of monolayer muscovite through exfoliation of natural muscovite," *RSC Advances*, vol. 5, no. 65, pp. 52 882–52 887, 2015.

[62] I. Akita, Y. Ishida, and T. Yonezawa, "Distinctive stability of a free-standing monolayer clay mineral nanosheet via transmission electron microscopy," *Physical Chemistry Chemical Physics*, vol. 22, no. 43, pp. 25 095–25 102, 2020.

[63] P. R. Buseck and I. Sumio, "High resolution electron microscopy of silicates," *American Mineralogist: Journal of Earth and Planetary Materials*, vol. 59, no. 1-2, pp. 1–21, 1974.

[64] T. Kogure and T. Murakami, "Direct identification of biotite/vermiculite layers in hydrobiotite using high-resolution tem," *Mineralogical Journal*, vol. 18, no. 4, pp. 131–137, 1996.

[65] T. Kogure, M. Jige, J. Kameda, A. Yamagishi, R. Miyawaki, and R. Kitagawa, "Stacking structures in pyrophyllite revealed by high-resolution transmission electron microscopy (HRTEM)," *American Mineralogist*, vol. 91, no. 8-9, pp. 1293–1299, 2006.

[66] C. Hetherington, "Aberration correction for TEM," *Materials Today*, vol. 7, no. 12, pp. 50–55, 2004.

[67] T. Kogure and E. Okunishi, "Cs-corrected HAADF–STEM imaging of silicate minerals," *Journal of electron microscopy*, vol. 59, no. 4, pp. 263–271, 2010.

[68] M. L. Whittaker, L. N. Lammers, S. Carrero, B. Gilbert, and J. F. Banfield, "Ion exchange selectivity in clay is controlled by nanoscale chemical–mechanical coupling," *Proceedings of the National Academy of Sciences*, vol. 116, no. 44, pp. 22 052–22 057, 2019.

[69] M. Segad, S. Hanski, U. Olsson, J. Ruokolainen, T. Åkesson, and B. Jönsson, "Microstructural and swelling properties of Ca and Na montmorillonite:(in situ) observations with cryo-TEM and SAXS," *The Journal of Physical Chemistry C*, vol. 116, no. 13, pp. 7596–7601, 2012.

[70] I. Akita, Y. Ishida, and T. Yonezawa, "Atomic-scale imaging of a free-standing monolayer clay mineral nanosheet using scanning transmission electron microscopy," *The Journal of Physical Chemistry Letters*, vol. 11, no. 9, pp. 3357–3361, 2020.

[71] S. S. Lee, P. Fenter, K. L. Nagy, and N. C. Sturchio, "Real-time observation of cation exchange kinetics and dynamics at the muscovite-water interface," *Nature Communications*, vol. 8, no. 1, pp. 1–9, 2017.

[72] R. Ogwada and D. Sparks, "Kinetics of ion exchange on clay minerals and soil: Elucidation of rate-limiting steps," *Soil Science Society of America Journal*, vol. 50, no. 5, pp. 1162–1166, 1986.

[73] R. Lal and B. Stewart, "Soil degradation: A global threat," *Advances in Soil*, 1990.

[74] W. Amelung, D. Bossio, W. de Vries, I. Kögel-Knabner, J. Lehmann, R. Amundson, R. Bol, C. Collins, R. Lal, J. Leifeld, *et al.*, "Towards a global-scale soil climate mitigation strategy," *Nature Communications*, vol. 11, no. 1, pp. 1–10, 2020.

Chapter 5

Experimental Techniques

In this chapter, we will introduce the device fabrication and characterisation techniques used for work presented in the proceeding chapters. In the subsequent discussed work, the general device architectures are as follows. A 2D material is suspended across SiN_x aperture(s) or exfoliated onto an SiO_x substrate. Suspended samples are then either S/TEM imaged or are contacted on both sides with electrolyte, either solid or liquid as well as proton-conducting electrodes deposited directly. As the 2D materials are suspended over a restricted area (fixed by SiN_x aperture), we can readily extract areal conductivity measurements via current-voltage (I-V) measurements. Atomically-thin clays are exfoliated directly onto SiO_x substrates for cross-sectional S/TEM imaging. Let us now discuss the specific techniques to these ends.

5.1 General Techniques

We start by describing the sample preparation steps for our studies, as they share many in common. Firstly, we obtain well-characterised minerals, either by means of a supplier that has previously characterised or characterise-as-received samples. The latter case was required for sourced vermiculite, as these were sent directly from the crystal mine source (despite also receiving a chemical analysis certificate, see Appendix M). Our initial characterisation of vermiculite was performed via XRD and Raman spectroscopy, provided in appendices H and I, respectively. Now, all fabrication steps, apart from final electrical contacting, were performed within a class-100 clean room environment at the National Graphene Institute, UK. The first step for ion transport and plan-view S/TEM imaging sample preparation involves the fabrication of the SiN_x supporting structures for various studies. We shall now discuss the fabrication steps for this supporting structure.

5.1.1 SiN_x Supporting Substrate

An illustration of the process for fabricating SiN_x apertures and TEM grids are provided in Figure 5.1. This is achieved by photolithography, specifically using a mask aligner (SUSS Microtec MJB4) and laser writer (Microtech LW405B standard+) using S1813 resist. The steps are as follows. (1) Lithography of 800 x 800 μm squares on side 1 of a double-sided

SiN_x(500 nm) 525 μm thick wafer are first performed[1]. The area excluding the squares are then used as etch masks for reactive ion etching (Oxford Instruments RIE System). Our recipe uses sulphur hexafluoride (SF_6) to etch through the SiN layer. (2) Next, these exposed SiN_x squares are then anisotropically etched using 80 °C KOH solution[2]. (3) The KOH etches SiN significantly slower than Si. Therefore the V etch forms a window on side 2 of the double-sided SiN_x wafer. These (already patterned) windows can be seen in microscope images in figures 5.1 e and f. (4) Lithography on side 2 of the wafer is performed, making either a single or few perforations using S1813 photoresist as a reactive ion etch mask. Resolutions close to 1 μm diameter holes can be achieved in this way. (5) Thorough solvent cleaning to remove residual S1813 from the substrate. This is typically undertaken using Microposit Remover MR1165 and then a subsequent semiconductor-grade acetone and isopropyl alcohol rinse. These are the standard steps of fabrication for the 2D material SiN_x support structure. Now, let us discuss the 2D material exfoliation in more detail and how we micro-manipulate 2D materials, placing them over the apertures in SiN_x.

5.1.2 Exfoliation of 2D Materials

All of the 2D materials used in this thesis were mechanically exfoliated from larger bulk starting crystals. To fabricate thin 2D materials, we should endeavour to begin with a high-quality bulk crystal, characterised by methods such as XRD, Raman and EDX. Our starting muscovite mica crystals were obtained from Agar Scientific (Grade V1, highest purity natural crystal). Graphite and hBN crystals were obtained from NGS Naturgraphit and HQ Graphene respectively. The latter being characterised fully by XRD, Raman and EDX. Vermiculite was sourced direct from the mine (São Luís De Montes Belos near Goiania in the State of Goias, Brazil). This was delivered along with an analysis certificate of the crystal, performed using ICP mass spectrometry by the company SGS GEOSOL, provided in Appendix M.

These crystals were then brought into a class-100 clean room environment to be mechanically cleaved using the scotch tape method (see section 3.1.4). Thinned crystal preparation was undertaken as follows. Firstly, fresh graphite, mica and clay surfaces are exposed from bulk crystals via cleavage using clean scalpel blades. This minimises accumulated contaminants on the topmost surfaces. This step is omitted for hBN due to the small starting crystal. Next, this freshly exposed surface is further cleaved by utilising adhesive backgrinding tapes (Nitto BT-50E-FR and Nitto Denko tape, both selected for high adhesive retention and cleanliness), isolating the top few layers of the desired material. The crystals were peeled several times onto the tape until good coverage can be observed. The tape containing the flakes is then swiftly pressed against either an O_2/Ar plasma-cleaned SiO_x substrate (for S/TEM cross-sectional sample), or silicon- polyvinyl alcohol (PVA)- polypropylene carbonate (PPC) transfer stack (for plan view sample), where some of the few-layer flakes remain on either type of substrate after peeling off the tape gently. Next, candidate flakes of the desired thicknesses

[1]The mask aligner is the preferred route to pattern multiple SiN_x substrates with one exposure, thus saving considerable time of fabrication.

[2]KOH is an etchant that attacks silicon preferentially in the <100> plane, producing an anisotropic V-etch with sidewalls that form a 54.7 ° angle.

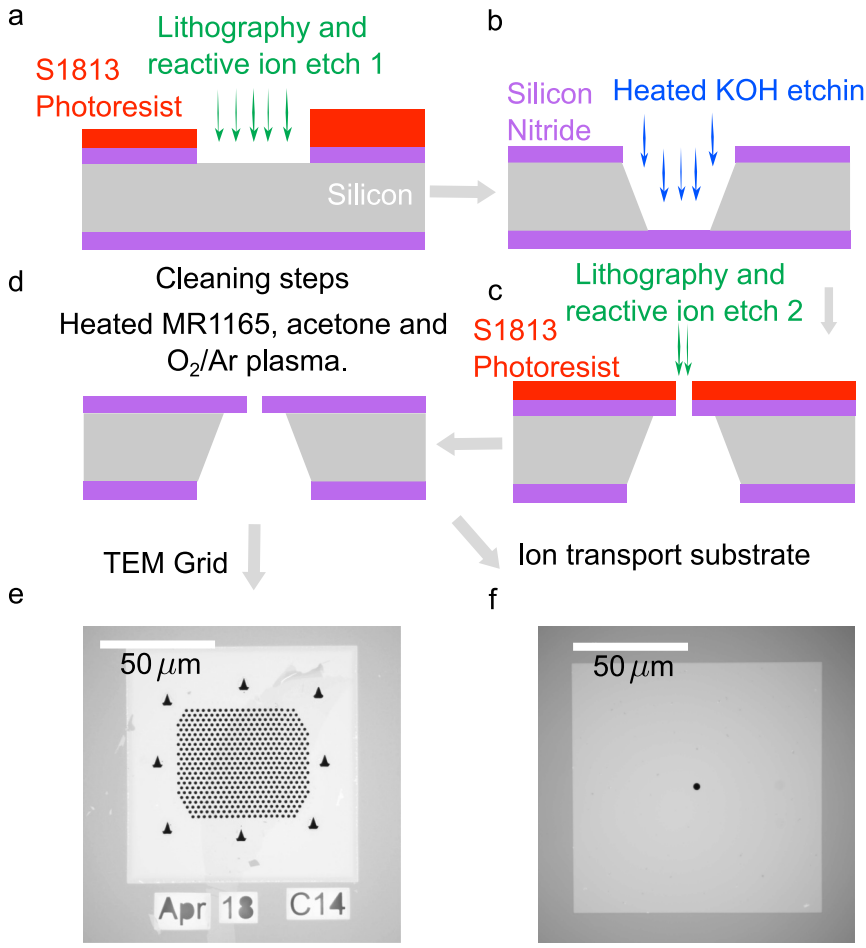

Figure 5.1: Schematics and pictures of SiN_x device support fabrication. (**a**) Reactive ion etch away a square of SiN_x to allow a KOH etch through (**b**) to create a SiN_x window on the underside. (**c**) SiN_x face reversed to perform lithography and subsequent plasma etch either a single aperture for ion transport measurements or an array for TEM microscopy. (**d**) Cleaning steps. The array of holes increase the chances of suspending a suitable sample for imaging. (**e**) Finished TEM SiN_x grid with 2D mica transferred where the outline is visible. (**f**) Completed ion transport SiN_x support structure without 2D material transferred.

were optically identified and confirmed using differential interference contrast microscopy (DIC). The technique of DIC, also known as Nomarski microscopy, exploits optical path length interference effects to enhance the contrast for transparent samples [1]. Images, such as those shown in figure 5.3 are typical of what thinned down crystals appear like under the microscope, with appropriate colour filtering, to enhance contrast[3]. The exfoliation technique is general to all the starting crystals, although, other polymers besides PPC can be used to optimise adhesion. Finally, the thickness and cleanliness of the target flakes are confirmed via AFM and Raman, where both techniques are discussed in sections 5.1.4 and 5.1.5 respectively. The key steps involved in exfoliating the 2D materials are depicted in figure 5.2. Let us now consider how we move these materials from one substrate to another.

[3]This is dependent on silicon oxide thickness.

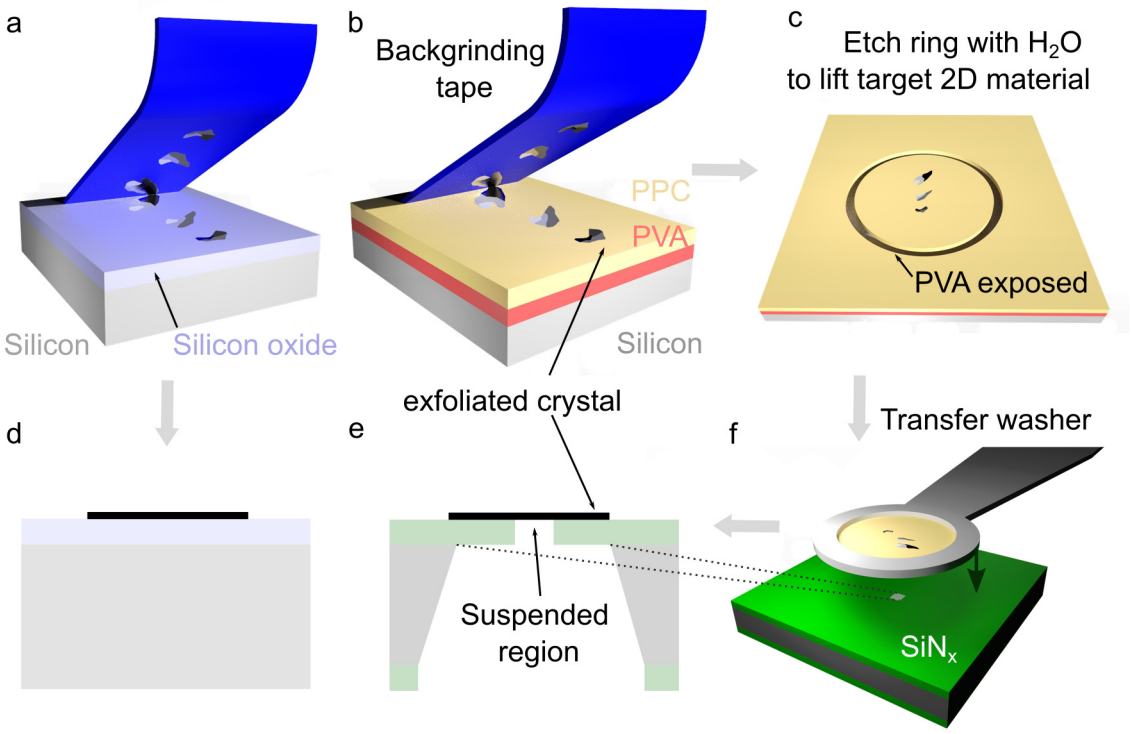

Figure 5.2: Devices are fabricated via exfoliation on either an SiO_x substrate (**a** and **d**) or are exfoliated onto a transfer polymer and suspended atop of a SiN_x substrate (**b**,**c**,**e** and **f**).

5.1.3 Micro-Manipulation of 2D Materials

After suitable 2D materials are identified on the transfer polymer layer (see Figure 5.3 c, we can manually scratch a small ring around the target flake, as shown in Figure 5.2 c. Next, it is possible to under etch the soluble PVA layer using water. Once this releases the PPC disc (which has the 2D material affixed on top), this frees the 2D material from the underlying silicon, which can be transferred to a larger volume of clean DI water, and the disc will float on the surface. After leaving this for >10 minutes to remove as much PVA residue as possible, we can 'fish' the material out of the DI water using a small metal washer to capture the 2D material on the disc of PPC. We then can transfer the disc to a targeted area, in our case, the SiN aperture(s), by use of a micro-manipulator stage (such as the Newport M-562-XYZ ULTRAlign), an image of the setup is provided in Appendix J and the transfer process is depicted in Figure 5.2 f. Once the 2D material is transferred, we then heat the stage to around 60 °C to improve the bonding between 2D material and substrate and then cut the disc to free it from the rig. Finally, we can remove the transfer PPC polymer via a thorough solvent cycling process. This is achieved by immersing the sample in (semiconductor grade) (1) acetone (120 s) → (2) isopropyl alcohol (120 s) → (3) DI water (120 s) → (4) N_2 dry (60 s) repeatedly, until optically free from contamination, using DIC microscopy.

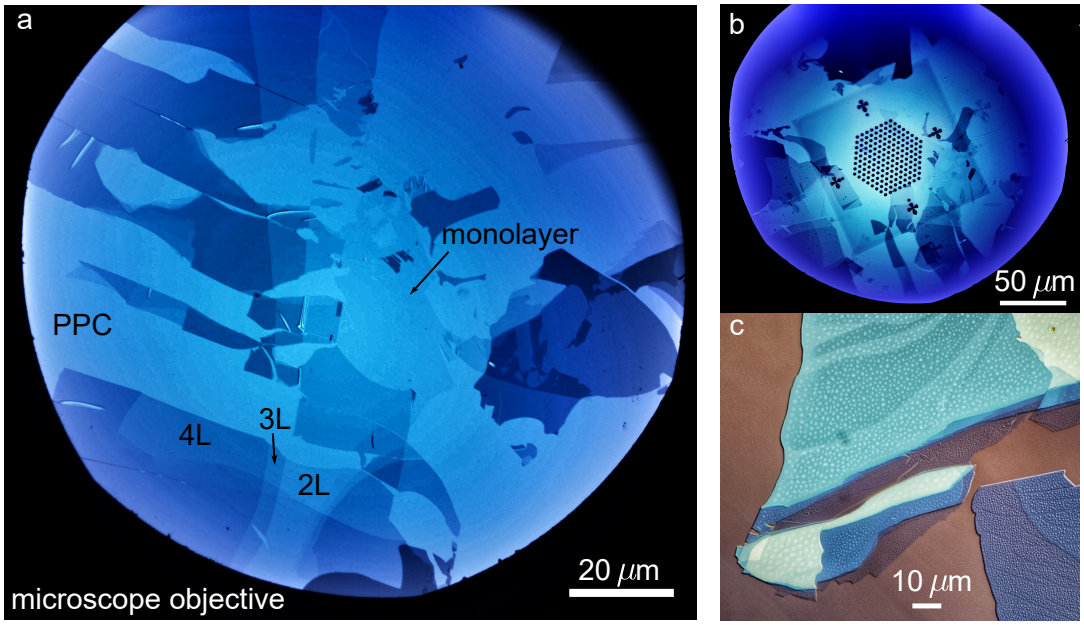

Figure 5.3: (**a**) few-layer muscovite mica minerals exfoliated onto PPC. The contrast is enhanced using a blue filter. (**b**) The same membrane shown in **a** now transferred onto a SiN_x grid, solvent cleaned and ready for S/TEM imaging. (**c**) DIC optical image of few-layer mica without colour filtering. Substrate-mica interaction cause trapped adsorbed bubbles to form at the interface, where the size of bubble is smaller for thinner crystals.

5.1.4 AFM

Let us now briefly introduce AFM, an important characterisation tool used in this thesis. This is a method to probe the shape, height and various other properties of a surface in 3D detail at the nanometre scale, thereby gaining insight into surface topography along with many other properties. A comprehensive review of AFM modes is beyond the scope of this section. Here, we focus on surface height profile mapping and 2D membrane deflections. This technique can be used either in air, liquid or vacuum. In 'contact mode' the tip comes into contact with the sample and reaches a maximum approach point with indentation into the sample and repulsive forces balance. For a suspended membrane over a μm diameter aperture, this deformation can be >10 nm, as shown in Figure 5.4 d. We exploit this height profile mapping for two main purposes. (1) The step height measured can give an accurate indication of the atomic thickness of our sample. See figure 5.4 b for an example of such a characterisation of 2D hBN. (2) We can measure suspended membranes to test their integrity, ensuring they are free of significant fractures, tears, dislocations and larger pin holes. An example of such a measurement is given in Figure 5.4 d.

The basic operating principle of AFM is provided in figure 5.4 a and c. Here, the concept of laser deflection from a cantilever is shown as well as the tip-sample force curve. As the tip is scanned across the surface, its deflection (either from contact, electrostatic or other forces) causes the tip to reflect the laser at varying positions on a quad photodiode. The forces of pico-Newtons to micro-Newtons can be applied between tip and sample [2]. Measurements made during work presented in chapters 3-8 were typically below 5 nN. This force can be

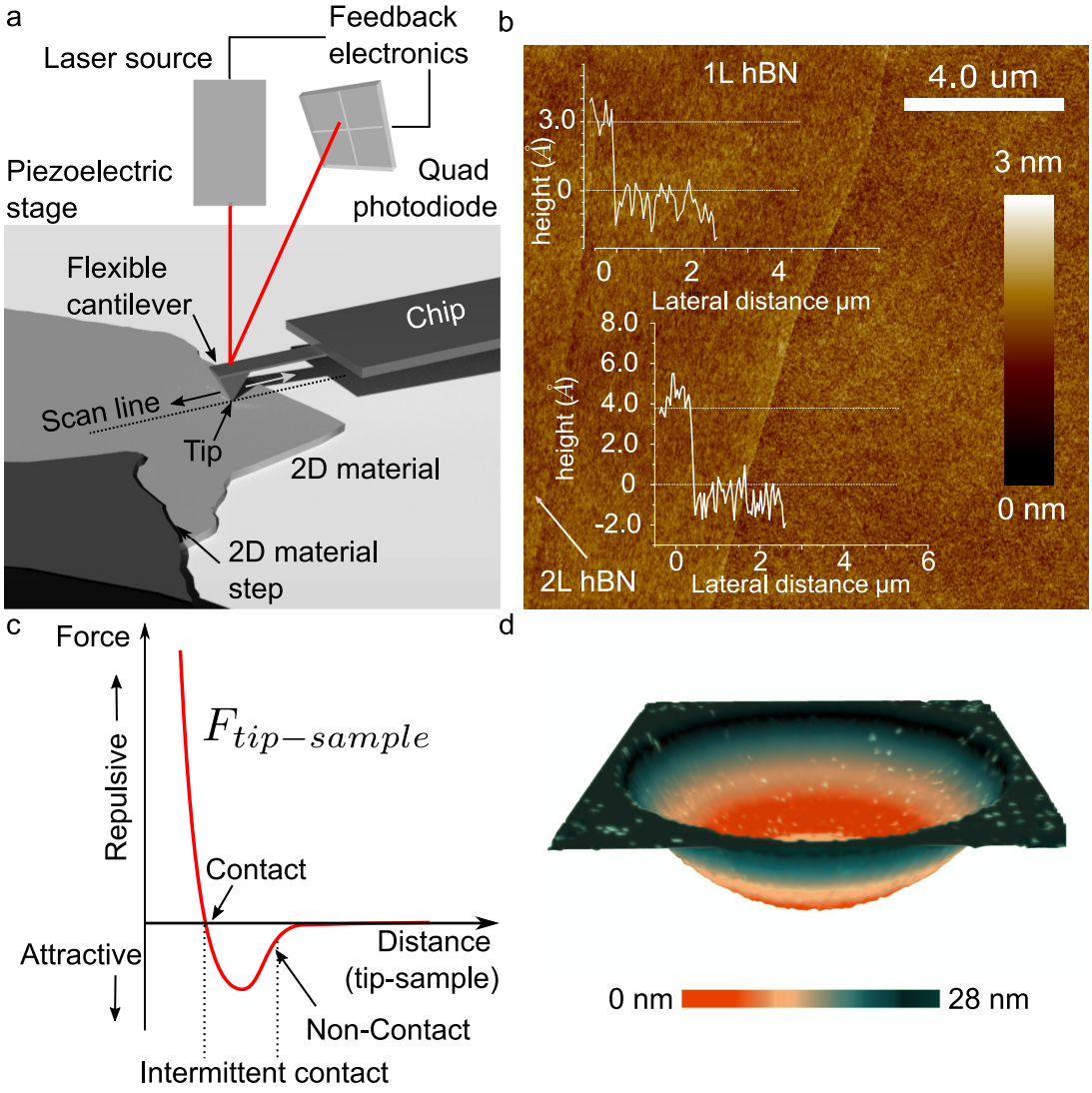

Figure 5.4: (**a**) Illustration presenting an overview of AFM-sample operating principle. (**b**) An AFM height map of monolayer and bilayer hexagonal boron nitride and overlaid height profiles showing the step heights, adapted from [3]. (**c**) Tip-sample force-distance curve highlighting the attractive and repulsive regions. Adapted from [4] d) AFM height profile of a suspended 2D material membrane. Adapted from [5]

translated as a tip-surface interaction and mapped as the scan lines build an image, as shown in figure 5.4 b. Also shown in the same figure are two examples of height profiles from such scans. The systems used during studies here are Bruker Dimension Icon and Dimension FastScan, utilising the 'ScanAsyst in Air' mode.

5.1.5 Raman of 2D Materials

Raman is a useful tool for characterising 2D materials, especially graphene, insitu. Let us briefly introduce the phenomenon of Raman scattering. If we illuminate a molecule with UV-visible light of frequency ν_0, then two types of scattering occur. The first is Rayleigh scattering, which maintains the incident frequency ν_0, and the second is Raman scattering, which alters the incident light frequency by $\nu_0 \pm \nu_m$, where ν_m is the vibrational frequency of the molecule. The decreased frequency scattering is Stokes and the increased frequency

component are known as the anti-Stokes lines. Thus, we measure the vibrational frequency as a shift in incident illumination light (typically a UV-visible laser source) [6]. Only molecular vibrations that alter the polarisability of the molecule are 'Raman active'. Now, Raman scattering is very weak. Approximately only 10^{-5} of the incident beam is scattered this way. Thus we require sensitive instrumentation to detect the signal. It is quite remarkable that Chandrasekhara Venkata Raman observed this effect using sunlight as the illumination source and only his eyes to detect the effect, for which he was awarded the Nobel Prize in Physics. Let us now consider the importance of Raman spectroscopy for 2D material characterisation.

We can both differentiate between single-layer (graphene) and multilayer graphite [7] and probe its defective nature by use of Raman spectroscopy [8]. The spectral changes reflect alterations in the electronic structure and electron-phonon interactions [7]. The former can be achieved by measuring the ratio between the 2D and G Raman peaks whereas the latter is characterised by measuring the intensity ratio of D/D' peaks. This is a very convenient method with which to characterise suspended graphene samples. The Raman spectra of monolayer hBN is less distinguishable from its multilayer counterpart than graphene is [9]. However, a slight shift of $\sim$3 cm^{-1} in E_{2g} peak has been reported in the literature [10]. Although, this was not observed for suspended monolayer hBN during this study, therefore, AFM was used as the main method to distinguish between monolayer and multilayer hBN. The signal for Raman of clays and micas appeared too weak for use of this method. However, the spectra for bulk minerals can be used to characterise OH stretching modes and unambiguously detect interlayer water (as well as local OH ordering) within clays. See Appendix H for the Raman spectra of three bulk mica/clay samples. All spectra were aquired using a Renishaw inVia Confocal Raman Microscope. Let us now discuss the experimental techniques which are specific to each results chapter.

5.2 Proton Selectivity of 2D Materials Techniques

5.2.1 Device Fabrication

The objective of device assembly was to assemble 2D materials to be measured in a liquid electrolyte setup in which we could vary HCl concentration across the membrane. To achieve this, we first suspend 2D materials across a 2 μm aperture in SiN_x, as was the case for device assembly presented in section 5.3.1. We next seal the outer edge of the 2D membrane using an SU8 washer, hard-baked to minimise the path for parallel leakage current. This is illustrated in Figure 5.5 b,c and d. SiN_x substrates are cut to a larger size than for mica devices, to seal the substrate with O-rings. Reservoirs are made from polyether ether ketone (PEEK) cavities, the schematic of which is shown in figure 5.5 c. Each reservoir is filled with an HCl electrolyte containing Ag/AgCl electrodes.

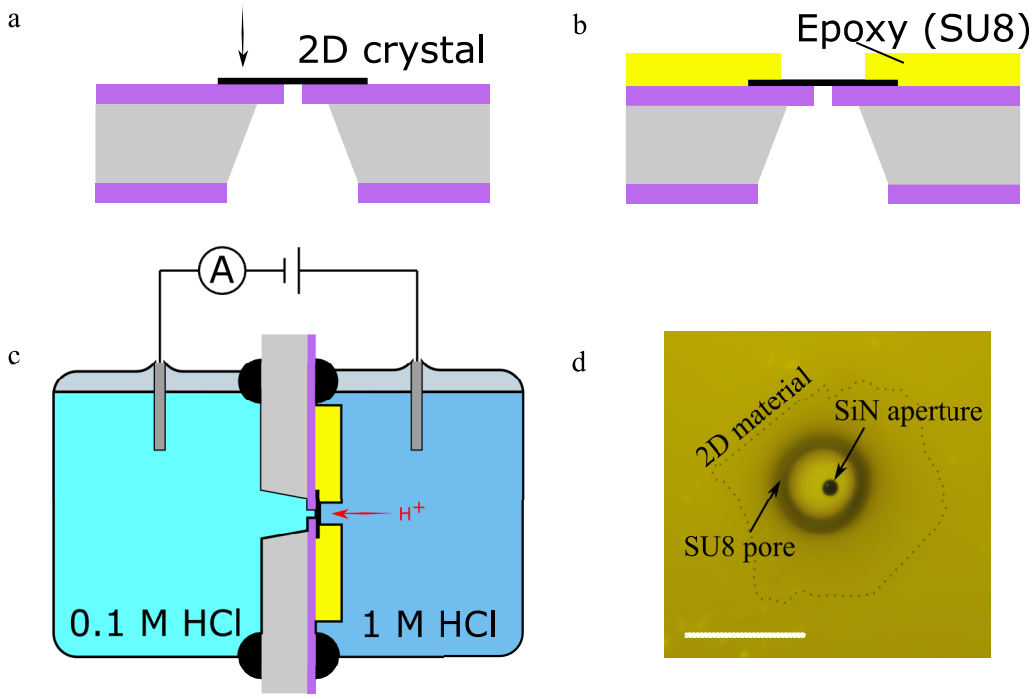

Figure 5.5: a) Devices are fabricated by first suspending the 2D crystal and then b) securing with a polymer washer. c) Measurement setup. Two reservoirs are filled with differing HCl electrolyte where the membrane potential can be measured using two Ag/AgCl electrodes. d) Microscope image of a suspended and SU8 secured 2D material membrane.

5.2.2 Characterisation

Direct current-voltage measurements were performed while the Ag/AgCl electrodes were connected to a Keithley SourceMeter 2636A. Membranes were wetted using isopropanol and then background checked with DI water in each reservoir. For intact devices, we observe I-V curves as shown in Appendix L, where typical examples of DI background and 0.1 M HCl measurements for monolayer graphene are presented. By varying the concentration gradient across the membrane, we can extract the membrane potential and, hence, the proton selectivity of the suspended membrane, in accordance with Section 2.2.2 in Chapter 2.

5.3 Proton Conduction Through Mica Techniques

5.3.1 Device Fabrication

Single 2 μm aperture SiN_x substrates are used to suspend few-layer mica crystals, in the manner described in Section 5.1. The thicknesses of the mica and vermiculite were determined by AFM microscopy. Membranes are then proton exchanged by (1) immersing devices in an 80 °C 10 mM acetic acid solution for one hour and subsequently thoroughly rinsed with deionised water, (2) left to dry in air and then (3) heated at 150 °C to remove remnant moisture. Non-exchanged devices skipped this exchange process. Next, we contacted the proton-conducting electrolyte or electrodes directly to the suspended membrane. To that

end, we solvent cast a (5%, 1,100 equiv. wt) Nafion perfluorinated resin (discussed in Section 2.3.3.2 of Chapter 2) proton-conducting electrolyte or deposit a porous, yet conductive, platinum contact to the membrane for the electrolyte and electrodes respectively. Platinum deposition was achieved through the use of an AJA sputter deposition system with parameters optimised to achieve desirable film qualities. Electrodes that contact Nafion are made using Pt decorated carbon cloth. Lastly, to access temperature regimes beyond the working range of Nafion, we contact both sides of the 2D membrane with platinum.

5.3.2 Measurements

For this study, we aim to measure proton flux through few layer mica and clay layers. To this end, we contact our proton injecting/evolving electrodes using silver paste and gold wire. This enables DC current-voltage (I-V) measurements, using a Keithley SourceMeter 2636A and a custom-made LabVIEW programme. Conductance can be calculated by performing linear fittings of the I-V data, typically measured between $\pm$ 100 mV to minimise side electrochemical electrode effects. Hydrogen evolution at the Pt contacted cathode was measured using a mass spectrometer (Inficon UL200), and the setup for this experiment is shown in Appendix K. This measurement illustrates that the electric current through 2D membranes is carried by hydrogen ions that evolve at the electrodes. The temperature-dependent measurements were performed by heating the device assembly on a hotplate with a thermocouple fastened to the device holder heating incrementally while recording conductance measurements.

5.4 Ion-Exchange in Atomically-Thin Clays Techniques

5.4.1 Sample Fabrication

The major objective of this study was to investigate the ion distribution and exchange rate of few-atomic-layer-thick crystal clay/mica. To that end, we fabricate both suspended and non-suspended device types (figures 5.2 d and e). Suspended atomically thin-clay is suitable for plan-view surface ion distribution S/TEM imaging, whereas interlayer imaging demands cross-sectional samples. In both cases, ion-exchange was undertaken for a desired time (from 1 s to 9 months) using an aqueous 0.1 M $CsNO_3$ solution. Caesium ions are readily distinguishable using the HAADF-S/TEM imaging mode, due to its high atomic number, resulting in a large scattering cross-section. We shall now discuss both sample preparation processes in turn.

Cross-sectional clay interlayer ion imaging was undertaken through the use of a fast ion beam (FIB) miller to reveal a cross-sectional slice through an encapsulating graphite layer, clay sample and underlying SiO_x. The purpose of encapsulation by graphite, is to help avoid surface damage during FIB sample preparation, where the graphite flake was between 5 and 200 layers thick. The sample is further protected from beam damage by depositing platinum

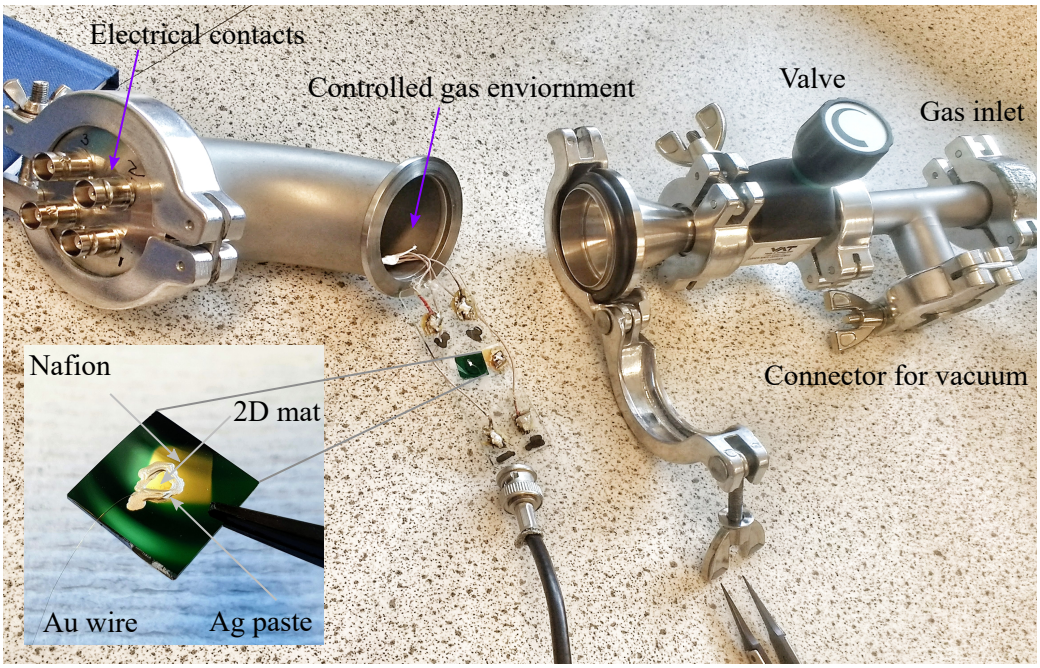

Figure 5.6: Experimental setup for Nafion measurements. The chamber is first evacuated down to few mbars of pressure. Then a 10 % hydrogen/argon mix is introduced to the chamber. The humidity of the chamber is increased by placing a DI water-laden cotton wool pad within the chamber. Inset: Close up view of a SiN_x device.

onto the graphite. Next, standard milling protocols are used to cut the lamella free from the substrate and transfer it to a pillar of a specialist OmniProbe Cu TEM support grid, followed by 30 kV, 16 kV, 5 kV and 2 kV ion beam milling and polishing to electron transparency. See reference [11] for a comprehensive description of these processes.

Plan-view sample preparation follows the steps as outlined in the general sample preparation section, for suspended 2D materials. We suspend thin clay layers atop of SiN_x grids (shown in Figure 5.1 e). Multiple solvent cycling steps are used to clean residue transfer polymer from the sample. Further, samples are dried using nitrogen and stored and transported in a desiccator before S/TEM imaging.

5.4.2 S/TEM Characterisation

We can perform ion distribution on both the clay surface and interlayer space using S/TEM. We also aimed to measure 'snapshots' of the exchange process for a given exchange time, and as a function of clay thickness. To this end, a probe-side aberration-corrected FEI Titan G2 80-200 S/TEM 'ChemiSTEM' microscope was used for ADF imaging. This microscope was operated at 200 kV with a probe current of 8-15 pA, a convergence angle of 21 mrad and a high-angle ADF (HAADF) detector with an inner (outer) collection angle of 48(196) mrad. SAED patterns were obtained using the same microscope operated in TEM mode. High-resolution images were obtained using A JEOL ARM300CF double aberration-corrected microscope, to simultaneously acquire HAADF- and annular bright field (ABF)-STEM images.

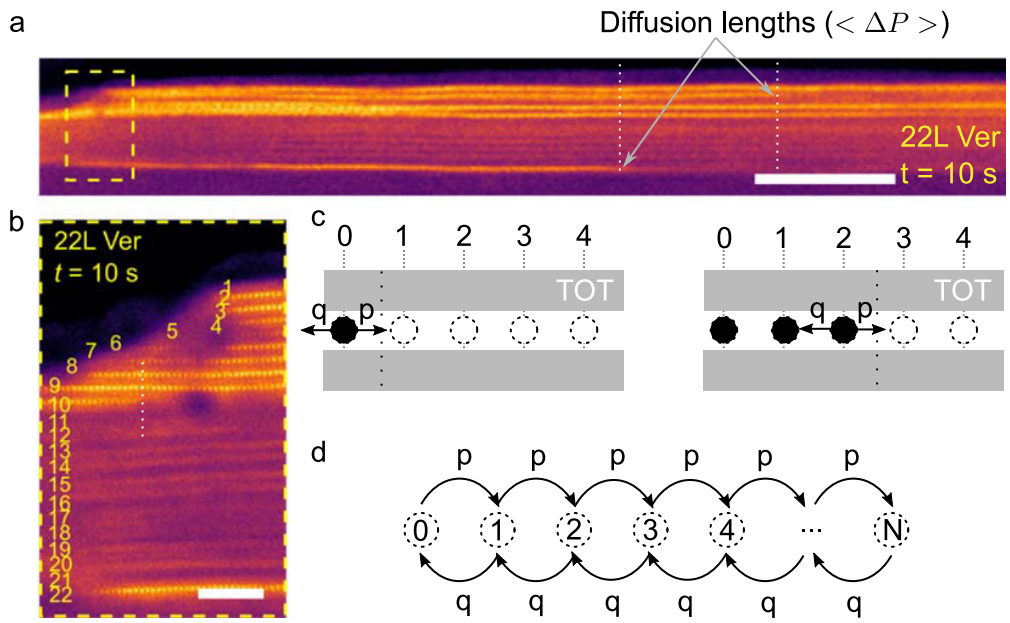

Figure 5.7: (**a**) Low-magnification cross-sectional HAADF-STEM images taken from a 22-layer vermiculite crystal exposed to electrolytes for 10 s. Scale bar, 50 nm. (**b**) Magnified region with the total number of layers labelled. Scale bar, 5 nm. (**c**) Stylised Markov chain process showing how we can model the diffusion process as steps with the probability of diffusing from left to right as q and p, respectively. (**d**) The same Markov chain process for an arbitrary number N of exchange sites.

This instrument has a cold FEG electron source and operated at 80kV with a probe current of 6 pA and a convergence angle of 24.8 mrad. Images were acquired with a HAADF detector with a collection angle of 50-150 mrad and an ABF detector having a 12-24 mrad collection angle. Multi-slice image simulation for high-resolution STEM images was conducted using atomic models created under the Atomic Simulation Environment5, and the QSTEM software6 with the above experimental parameters, and a source size of 0.8-1 Å.

5.4.3 Diffusion Coefficient Estimates

Let us define an effective diffusion rate through vermiculite clay (D). As discussed in Chapter 4, previous ion-exchange studies of vermiculite have shown that FD may well be significant. With our S/TEM snapshot technique, we are unable to distinguish between the two rate limiting steps of Nernst FD and clay bulk diffusion. Nonetheless, we aimed to arrive at an effective diffusion rate for which we assumed a 1D diffusion Markov chain process [12] was responsible for ion-exchange, and at the initial time (t_0), the caesium content within the lattice is zero (justified from the chemical analysis in Appendix M), we can arrive at an expression for D.

$$D = \frac{< \Delta P^2 >}{2t} \tag{5.1}$$

where $< \Delta P >$ is the caesium ion penetration distance and t is the time of ion-exchange. We can measure ΔP by taking S/TEM snapshots after a fixed time t within the ion-exchange 0.1

M caesium nitrate solution.

References

[1] W. Lang, *Nomarski differential interference-contrast microscopy*. Carl Zeiss, 1982, pp. 11–17.

[2] G. Haugstad, *Atomic force microscopy: understanding basic modes and advanced applications*. John Wiley & Sons, 2012, pp. 1–130.

[3] L. Mogg, S. Zhang, G.-P. Hao, K. Gopinadhan, D. Barry, B. Liu, H. Cheng, A. Geim, and M. Lozada-Hidalgo, "Perfect proton selectivity in ion transport through two-dimensional crystals," *Nature Communications*, vol. 10, no. 1, pp. 1–5, 2019.

[4] S. Maghsoudy-Louyeh, M. Kropf, and B. Tittmann, "Review of progress in atomic force microscopy," *The Open Neuroimaging Journal*, vol. 12, no. 1, 2018.

[5] L. Mogg, G.-P. Hao, S. Zhang, C. Bacaksiz, Y.-C. Zou, S. Haigh, F. Peeters, A. Geim, and M. Lozada-Hidalgo, "Atomically thin micas as proton-conducting membranes," *Nature Nanotechnology*, vol. 14, no. 10, pp. 962–966, 2019.

[6] J. R. Ferraro, *Introductory Raman spectroscopy*. Elsevier, 2003, pp. 1–30.

[7] A. C. Ferrari, J. Meyer, V. Scardaci, C. Casiraghi, M. Lazzeri, F. Mauri, S. Piscanec, D. Jiang, K. Novoselov, S. Roth, *et al.*, "Raman spectrum of graphene and graphene layers," *Physical Review Letters*, vol. 97, no. 18, p. 187 401, 2006.

[8] A. Eckmann, A. Felten, A. Mishchenko, L. Britnell, R. Krupke, K. S. Novoselov, and C. Casiraghi, "Probing the nature of defects in graphene by Raman spectroscopy," *Nano Letters*, vol. 12, no. 8, pp. 3925–3930, 2012.

[9] K. Zhang, Y. Feng, F. Wang, Z. Yang, and J. Wang, "Two dimensional hexagonal boron nitride (2D-hBN): Synthesis, properties and applications," *Journal of Materials Chemistry C*, vol. 5, no. 46, pp. 11 992–12 022, 2017.

[10] R. V. Gorbachev, I. Riaz, R. R. Nair, R. Jalil, L. Britnell, B. D. Belle, E. W. Hill, K. S. Novoselov, K. Watanabe, T. Taniguchi, *et al.*, "Hunting for monolayer boron nitride: Optical and Raman signatures," *Small*, vol. 7, no. 4, pp. 465–468, 2011.

[11] J. Mayer, L. A. Giannuzzi, T. Kamino, and J. Michael, "TEM sample preparation and FIB-induced damage," *MRS Bulletin*, vol. 32, no. 5, pp. 400–407, 2007.

[12] O. C. Ibe, *Elements of random walk and diffusion processes*. John Wiley & Sons, 2013, pp. 1–113.

Chapter 6

Perfect Proton Selectivity Through 2D Crystals

The discovery that the 2D materials graphene and hBN were both permeable to thermal protons was a surprise, given previously predicted energy barriers. However, whether other small ions could pierce the crystal lattice in these materials remains unknown. This work presents experimental measurements showing total proton selectivity over chloride ions through such 2D material membranes. In this work, we utilised HCl as the electrolyte on either side of the membrane and kept concentrations within the linearly-increasing conductivity regime (as shown in Chapter 2, figure 2.4 a). The results have implications for membrane technologies that use graphene as a material. The proton permeation through the pristine 2D crystal bulk is typically not considered. However, it could be important for membrane design and optimisation, especially when operating in acidic conditions. The results also provide support for the view that the activation barriers found for proton transport through mechanically-exfoliated graphene and hBN do not involve vacancies and other atomic-scale defects. This is an important conclusion for further theory developments.

The results presented in Chapter 6 are reported in the Nature Communications publication entitled "Perfect proton selectivity in ion transport through two-dimensional crystals" M.L.-H. and A.K.G. designed and directed the project. L.M. fabricated devices, performed measurements, and carried out data analysis with help from S.Z., K.G., G.-P. H., and D.B. B.L.L. H.M.C. helped with interpretation. L.M., A.K.G., and M.L.-H. wrote the manuscript. All authors contributed to discussions.

Perfect proton selectivity in ion transport through two-dimensional crystals

L. Mogg[1,2], S. Zhang[2,3], G.-P. Hao[2,4], K. Gopinadhan[2,5], D. Barry[2], B. L. Liu[6], H. M. Cheng[6], A. K. Geim[1,2], M. Lozada-Hidalgo[1,2]

[1]National Graphene Institute, The University of Manchester, Manchester M13 9PL, UK

[2]Department of Physics and Astronomy, The University of Manchester, Manchester M13 9PL, UK

[3]Key Laboratory for Green Chemical Technology of Ministry of Education, Collaborative Innovation Center of Chemical Science and Engineering, School of Chemical Engineering and Technology, Tianjin University, Tianjin 300072, China.

[4]State Key Laboratory of Fine Chemicals, School of Chemical Engineering, Dalian University of Technology, Dalian 116024, China

[5]Department of Physics, Indian Institute of Technology Gandhinagar, Gujarat 382355, India

[6]Shenzhen Graphene Center Tsinghua-Berkeley Shenzhen Institute, Tsinghua University 1001 Xueyuan Road, Shenzhen 518055, China

Abstract

Defect-free monolayers of graphene and hexagonal boron nitride were previously shown to be surprisingly permeable to thermal protons, despite being completely impenetrable to all gases. It remains untested whether small ions can permeate through the two-dimensional crystals. Here we show that mechanically exfoliated graphene and hexagonal boron nitride exhibit perfect Nernst selectivity such that only protons can permeate through, with no detectable flow of counterions. In the experiments, we used suspended monolayers that had few if any atomic-scale defects, as shown by gas permeation tests, and placed them to separate reservoirs filled with hydrochloric acid solutions. Protons accounted for all the electrical current and chloride ions were blocked. This result corroborates the previous conclusion that thermal protons can pierce defect-free two-dimensional crystals. Besides importance for theoretical developments, our results are also of interest for research on various separation technologies based on two-dimensional materials.

Two sentence summary

Defect-free monolayers of graphene and hexagonal boron nitride were previously shown to be highly permeable to protons. Here the authors demonstrate that these crystals exhibit perfect proton selectivity, corroborating that proton transport through the two-dimensional crystals occurs through their bulk and does not require atomic-scale defects.

Introduction

Proton transport through two-dimensional (2D) crystals has recently been studied both experimentally and theoretically[1-9]. As for experiment, it was found that proton permeation through

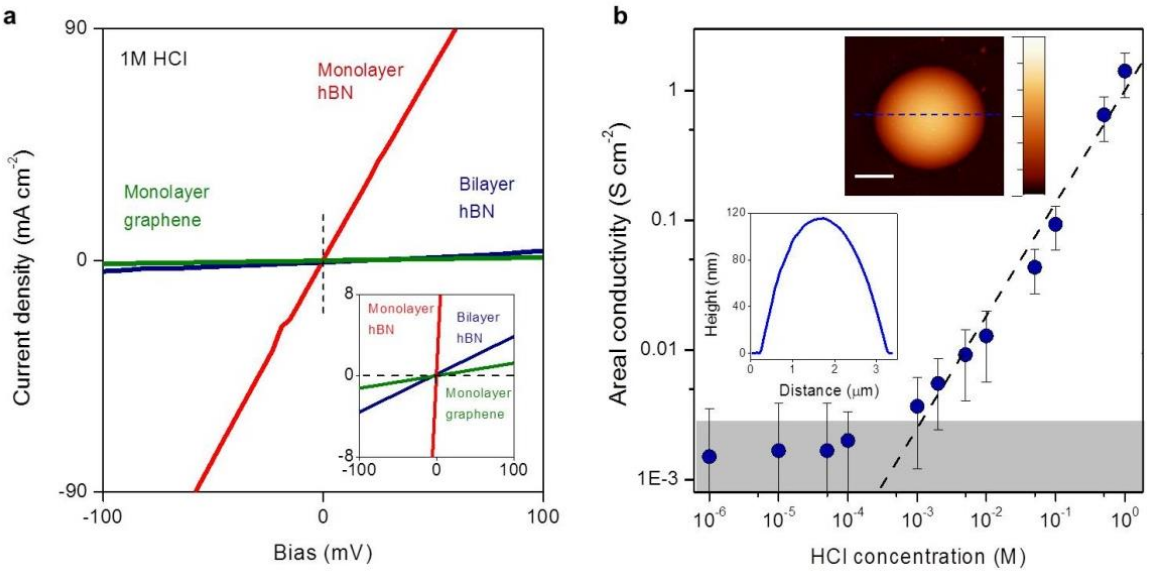

Figure 1| Proton transport through 2D crystals studied using aqueous solutions. (**a**) Examples of *I-V* characteristics for 1 M HCl. Bottom inset: Zoom-in. (**b**) Concentration dependence of the areal conductivity σ for monolayer hBN. Grey area indicates our detection limit given by parasitic leakage currents. Error bars: s.d. from different measurements. Dashed line: Best linear fit to the data. Top inset: atomic force microscopy (AFM) height profile of an 'inflated nanoballoon'. Here, graphene monolayer seals a micron-sized cavity containing pressurized Ar. The pressure difference across the membrane makes it to bulge up. Lateral scale bar, 1 μm; color scale, 130 nm. Bottom inset: AFM line trace taken along the blue dotted line in the top inset.

mechanically-exfoliated crystals was thermally activated with energy barriers of ≈0.8 eV for graphene and ≈0.3 eV for monolayer hexagonal boron nitride (hBN)[1]. Further measurements using deuterons, nuclei of hydrogen isotope deuterium, showed that quantum oscillations raised the energy of incoming protons by 0.2 eV[2]. This correction yielded the total barriers of ≈0.5 eV for monolayer hBN and ≈1 eV for graphene. From a theory perspective, the latter value is notably lower (by at least 30% but typically a factor of 2) than that found in density-functional calculations for graphene[3-7]. To account for the difference, a recent theory suggested that graphene can be partially hydrogenated during the measurements, which makes its lattice slightly sparser, thus more permeable to protons[8,9]. An alternative explanation put forward was to attribute the observed proton currents to atomic-scale lattice defects including vacancies[10,11]. This was argued on the basis of ion-selectivity measurements using chemical-vapor-deposited (CVD) graphene[11]. Indeed, CVD graphene is known to possess a large density of atomic-scale defects that appear during growth[12-14]. Such defects are generally absent

in mechanically exfoliated 2D crystals, which was proven conclusively in gas leak experiments using so-called nanoballoons[15-17]. Even a single angstrom-sized vacancy per micrometer-size area could be detected in those experiments[16,17]. Whereas it is plausible that vacancies and similar defects played a dominant role in experiments using CVD graphene[10,11], extrapolation of those results to mechanically exfoliated 2D crystals is unjustifiable. To resolve the controversy, it is crucial to carry out similar ion-selectivity studies using mechanically exfoliated crystals with little or no defects[1,2,15].

In this communication, we report ion-selectivity measurements using mechanically exfoliated graphene and hBN monolayers. The crystals are found to be perfectly selective with respect to protons. The latter can permeate through the 2D membranes whereas even such small ions as chlorine are blocked. The results support the previous conclusion[1] that transport of thermal protons through high-quality graphene and hBN occurs through their bulk and does not involve vacancies and other atomic-scale defects.

Results

Device fabrication and characterization. The investigated devices were fabricated using monolayer graphene and mono- and bi- layer hBN crystals that were isolated by micromechanical cleavage[18] (see Methods and Supplementary Figure 1). The crystals were suspended over microfabricated apertures (2 μm in diameter) etched in free-standing silicon-nitride (SiN) membranes[1] (Supplementary Figure 2). A prefabricated polymer washer with a 10 μm diameter hole was then transferred on top of the crystal so that the hole was aligned with the aperture in the SiN membrane (Supplementary Figure 2). The assembly was baked at ~150 °C to ensure that the washer firmly clamped the 2D crystal to SiN and sealed the crystal edges in order to prevent any possible leak along the substrate. In a series of control experiments, we checked that there were no microscopic defects in our exfoliated 2D crystals by employing the approach described in Refs. [15,16] and previously also used in our experiments[1]. To this end, we made hBN and graphene membranes to cover micron-sized cavities etched in an oxidized Si wafer and tested the enclosures for possible gas leaks (see inset Fig. 1b and Supplementary section 'Leak tests using nanoballoons'). Even a single vacancy would be detectable in these measurements[16,17], but neither of the dozens of tested 2D crystals showed such leakage (Supplementary Figure 3). In contrast, similar devices made from CVD graphene normally exhibited notable gas permeation.

Ion conductivity measurements. The chips containing the individual 2D membranes (Supplementary Figure 2) were then used to separate two compartments filled with hydrochloric acid (HCl) at chosen concentrations[19]. Electrical conductance through the membranes was probed using Ag/AgCl electrodes placed inside the compartments. Fig. 1a shows the current density I as a function of applied voltage V for representative devices made from graphene and hBN. The I-V response was linear, which allowed us to determine the areal conductivity $\sigma = I/V$. We found monolayer hBN to be most conductive of the studied crystals, followed by bilayer hBN and monolayer graphene. For example, using 1 M HCl we found $\sigma \approx 1{,}000$ mS cm^{-2} for monolayer hBN, ≈40 mS cm^{-2} for bilayer hBN and ≈12 mS cm^{-2} for monolayer graphene. The relative conductivities agree well with those found in the previous studies using Nafion (rather than HCl) as the proton-conducting medium[1].

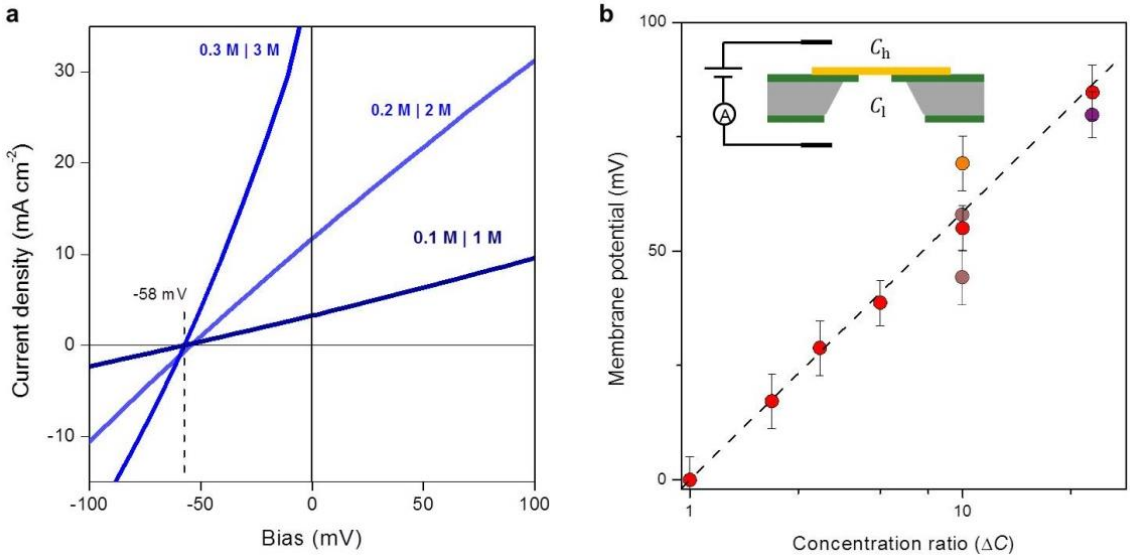

Figure 2| Proton selectivity. (**a**) Examples of *I-V* characteristics for various HCl concentrations across a monolayer hBN membrane at a fixed $\Delta C = 10$. The current at zero voltage (intersection with the y-axis) was always positive. The reversal potential V_0 is given by the intersection of the *I-V* curves with the x-axis and was $V_0 \approx$ -58 mV as marked by the dotted line. (**b**) V_0 for different ΔC and 4 different hBN devices (symbols of different color). Error bars, s.d. from different measurements. The black line is given by Eq. (1) for $t_H = 1$ and $t_{Cl} = 0$. Inset: Schematic of the experimental setup.

Thicker crystals (e.g., bilayer graphene) exhibited no discernable conductance, again in agreement with the previous report[1].

Because monolayer hBN exhibited the highest conductivity, we focus our discussion below on this particular 2D material, as it allowed the most accurate ion-selectivity measurements (results for graphene are presented in Supplementary Information). Fig. 1b shows σ found for hBN at various HCl concentrations (the same concentration was used in both compartments). For concentrations above 1 mM, σ increased linearly with HCl concentration. At lower concentrations, the measured current was below our detection limit. The latter was determined by electrical leakage along surfaces of the liquid cell and was of the order of 1 pA as found using control devices with no holes in SiN membranes[19]. In another control experiment, we used devices with the same SiN aperture but without a 2D crystal. They exhibited conductance at least ~1000 times larger than that for the devices with graphene or hBN crystals covering the aperture (Supplementary Figure 4). This demonstrates that the reported values of σ were limited by the relatively low ion permeation through 2D crystals, and the series resistance due to the electrolyte itself could be neglected.

Proton selectivity. The measured conductivity could be due to either H^+ or Cl^- or both ions permeating through 2D crystals. For the purpose described in the introduction, it is necessary to determine the fraction of *I* carried by each of these species. Such fractions are usually referred to as transport numbers[20] (t_H and t_{Cl} for protons and chloride, respectively) and, by definition, they satisfy $t_H + t_{Cl} \equiv 1$ and the inequality: $0 \leq$ both t_H and $t_{Cl} \leq 1$. To find their values for our 2D membranes, we

used the same setup as in the measurements discussed in Fig. 1 but with different HCl concentrations in the two compartments (inset of Fig. 2b). The concentration gradient drives both H^+ and Cl^- ions towards equilibrium, from the high concentration (C_h) compartment to the low concentration (C_l) one. Therefore, the sign of the total ionic current at zero V indicates whether the majority carriers are protons (positive I) or chloride ions (negative). Fig. 2a shows typical I-V characteristics for monolayer hBN devices and concentration ratio $\Delta C \equiv C_h/C_l = 10$. Independently of the absolute values of HCl concentrations, the zero-V current was always positive proving that protons dominate ion transport through our membranes. The same behavior was found for graphene devices (Supplementary Figure 5).

The force pushing ions across the membrane, due to the concentration gradient, can be counteracted by applying voltage V. The value V_0 at which the current becomes zero is known as the membrane or reversal potential and is given by the Nernst equation[21]

$$V_0 = (t_{Cl} - t_H)\,(k_B T/e)\,\ln(\Delta C) = -\,(2t_H - 1)\,(k_B T/e)\,\ln(\Delta C) \qquad (1)$$

where k_B is the Boltzmann constant, T is the temperature and e is the elementary charge. If one of the transport numbers is unity, the other must be zero and, then, it is said that a membrane displays perfect Nernst selectivity. Fig. 2a shows that for $\Delta C = 10$, the I-V curves intersected the x-axis at the same V, which means that our membranes exhibited $V_0 \approx -58$ mV, regardless of the absolute values of the HCl concentrations. This value is equal to $-(k_B T/e)\ln(\Delta C=10) \approx -58$ meV at our measurement temperature of ~20 °C and, therefore, the observation implies $t_H \approx 1$ or, equivalently, that all the ionic current through the membrane is due to proton transport. Within our experimental accuracy, the same perfect selectivity was also found for graphene (Supplementary Figure 5).

To corroborate the above result and obtain better statistics for the ion selectivity, we carried out similar measurements using different devices and several concentration ratios ranging from $\Delta C = 1$ to 30 (Fig. 2b). For all of them, we found membrane potentials consistent with the perfect proton selectivity in Eq. (1). The best fit to the data in Fig. 2b yields $t_H = 0.99 \pm 0.02$, or $t_H \approx 1$. In control experiments, we verified our experimental approach using porous glass membranes. They allow large concentrations gradients but provide no ion selectivity because of large pore sizes. The latter experiments yielded $t_H = 0.81 \pm 0.04$ (Supplementary Figure 6), in agreement with the transport numbers known for bulk hydrochloric acid ($t_H \approx 0.83$, $t_{Cl} \approx 0.17$)[20].

Discussion

Finally, it is instructive to compare our results with those obtained previously in conceptually similar experiments but using CVD graphene[11]. The latter was reported to have $\sigma \approx 4$ S cm^{-2} at 1 M HCl, in clear disagreement with our experiments for mechanically exfoliated graphene where σ was nearly three orders of magnitude smaller. Furthermore, no current could be detected for 1 mM HCl concentration in our experiments; but large current densities of ~10 mA cm^{-2} were reported in ref. [11] for CVD graphene membranes of the same area. The membrane potential reported for CVD

graphene was also different, reaching only ~8 mV for ΔC =10, or ~7 times smaller than what we found for our devices. All this shows that the ion transport properties of exfoliated 2D crystals are radically different from those of CVD films where atomic-scale defects and, possibly, even macroscopic ones[11] dominate ion transport. This conclusion is consistent with all the other evidence for intrinsic proton transport through 2D crystals, which was reported previously[1,2].

In conclusion, our experiments clearly demonstrate that mechanically exfoliated, defect-free 2D crystals allow only proton transport and block even small ions such as chlorine that has one of the smallest hydrated diameters[19]. This provides further support to the view that the activation barriers found for proton transport through high-quality graphene and hBN do not involve vacancies and other atomic-scale defects[1] a conclusion important for further theory developments (e.g., for the hydrogenation model proposed in refs. [8,9]). Our results also have implications for the widely-discussed use of atomically-thin crystals as a novel platform for various separation technologies. In such technologies, selectivity is typically achieved by either perforating nanopores[22-25] or exploiting those naturally occurring in CVD films[26,27]. The fast permeation of H^+ through the 2D bulk is usually ignored but can be important for designing and optimizing the membranes' properties.

Methods

Fabrication of 2D membranes. Device fabrication started by isolating atomically-thin layers of graphene and hBN from bulk crystals. The flake was first identified optically and then characterized using atomic force microscopy and Raman spectroscopy. Supplementary Figure 1 shows typical characterization data for one of the used hBN crystals. Similar characterization procedures were performed for graphene.

Supplementary Figure 2 illustrates the device fabrication process. Several lithography, reactive ion etching and wet etching steps were performed to obtain a fully suspended SiN membrane with a 2-μm-diameter aperture in the center. The exfoliated 2D crystals were then suspended over the apertures. The crystals were also clamped down to the SiN substrate with a polymer washer. To this end, an SU-8 photo-curable epoxy washer was prefabricated with a 10-μm-diameter hole in the middle and transferred over the devices with the hole and aperture aligned (Supplementary Figure 2). After the transfer, the seal was hard baked at 150 ˚C to ensure good adhesion to the SiN substrate.

Electrical measurements. Devices were clamped with O-rings to separate two reservoirs filled with HCl solutions, and Ag/AgCl electrodes were placed inside each reservoir. The *I-V* characteristics were measured applying voltages between typically ±200 mV at sweep rates <0.1 V min^{-1}.

References

1. Hu, S. *et al.* Proton transport through one-atom-thick crystals. *Nature* **516,** 227–230 (2014).

2. Lozada-Hidalgo, M. *et al.* Sieving hydrogen isotopes through two-dimensional crystals. *Science* **351,** 68–70 (2016).
3. Miao, M., Nardelli, M. B., Wang, Q. & Liu, Y. First principles study of the permeability of graphene to hydrogen atoms. *Phys. Chem. Chem. Phys.* **15,** 16132–7 (2013).
4. Wang, W. L. & Kaxiras, E. Graphene hydrate: theoretical prediction of a new insulating form of graphene. *New J. Phys.* **12,** 125012 (2010).
5. Poltavsky, I., Zheng, L., Mortazavi, M. & Tkatchenko, A. Quantum tunneling of thermal protons through pristine graphene. *J. Chem. Phys.* **148**, 204707 (2018).
6. Zhang, Q., Ju, M., Chen, L. & Zeng, X. C. Differential Permeability of Proton Isotopes through Graphene and Graphene Analogue Monolayer. *J. Phys. Chem. Lett.* **7,** 3395–3400 (2016).
7. Kroes, J., Fasolino, a & Katsnelson, M. Density Functional Based Simulations of Proton Permeation of Graphene and Hexagonal Boron Nitride. *Phys. Chem. Chem. Phys.* **19,** 5813–5817 (2017).
8. Feng, Y. *et al*. Hydrogenation Facilitates Proton Transfer through Two-Dimensional Honeycomb Crystals. *J. Phys. Chem. Lett.* **8,** 6009–6014 (2017).
9. Bartolomei, M., Hernández, M. I., Campos-Martínez, J. & Hernández-Lamoneda, R. Graphene multi-protonation: A cooperative mechanism for proton permeation. *Carbon* **144**, 724-730 (2019).
10. Achtyl, J. L. *et al.* Aqueous proton transfer across single-layer graphene. *Nat. Commun.* **6,** 6539 (2015).
11. Walker, M. I., Braeuninger-Weimer, P., Weatherup, R. S., Hofmann, S. & Keyser, U. F. Measuring the proton selectivity of graphene membranes. *Appl. Phys. Lett.* **107**, 213104 (2015).
12. Gao, L. *et al*. Repeated growth and bubbling transfer of graphene with millimetre-size single-crystal grains using platinum. *Nat. Commun.* **3**, 699(2012).
13. Huang, P. Y. *et al*. Grains and grain boundaries in single-layer graphene atomic patchwork quilts. *Nature* **469**, 389-392 (2011).
14. Lee, G. H. *et al*. High-strength chemical-vapor-deposited graphene and grain boundaries. *Science* **31**, 1073-1076 (2013).
15. Bunch, J. S. *et al*. Impermeable atomic membranes from graphene sheets. *Nano Lett.* **8,** 2458–62 (2008).
16. Koenig, S. P., Wang, L., Pellegrino, J. & Bunch, J. S. Selective molecular sieving through porous graphene. *Nat. Nanotechnol.* **7,** 728–732 (2012).
17. Wang, L. *et al*. Molecular valves for controlling gas phase transport made from discrete ångström-sized pores in graphene. *Nat. Nanotechnol.* **10,** 785–790 (2015).
18. Kretinin, A. V. *et al*. Electronic properties of graphene encapsulated with different two-dimensional atomic crystals. *Nano Lett.* **14,** 3270–3276 (2014).
19. Gopinadhan, K. *et al.* Complete steric exclusion of ions and proton transport through confined monolayer water. *Science* **11**, 145-148 (2019).

20. Bard, A. J. & Faulkner, L. R. *Electrochemical Methods*. (Wiley, 2001).
21. Helfferich, F. *Ion Exchange*. (McGraw Hill, 1962).
22. Wang, L. *et al.* Fundamental transport mechanisms, fabrication and potential applications of nanoporous atomically thin membranes. *Nature Nanotechnology* **12**, 509-522 (2017).
23. Surwade, S. P. *et al.* Water desalination using nanoporous single-layer graphene. *Nat. Nanotechnol.* **10**, 459-464 (2015).
24. Garaj, S. *et al.* Graphene as a subnanometre trans-electrode membrane. *Nature* **467,** 190–193 (2010).
25. Feng, J. *et al.* Single-layer MoS2 nanopores as nanopower generators. *Nature* **536,** 197–200 (2016).
26. O'Hern, S. C. *et al.* Selective molecular transport through intrinsic defects in a single layer of CVD graphene. *ACS Nano* **6,** 10130–10138 (2012).
27. Prozorovska, L. & Kidambi, P. R. State-of-the-Art and Future Prospects for Atomically Thin Membranes from 2D Materials. *Advanced Materials* **30**, 1801179 (2018).

Acknowledgments

The authors acknowledge support from EPSRC - EP/N010345/1, the Lloyd's Register Foundation, the European Research Council and from Graphene Flagship. M.L.-H. acknowledges a Leverhulme Early Career Fellowship. G-P.H. acknowledges a Marie Curie International Incoming Fellowship. L.M. acknowledges the EPSRC NowNANO programme.

Author contribution statement

M.L.-H. and A.K.G. designed and directed the project. L.M. fabricated devices, performed measurements and carried out data analysis with help from S.Z., K.G., G.-P. H. and D.B. B.L.L. and H.M.C. helped with interpretation. L.M., A.K.G. and M.L-H. wrote the manuscript. All authors contributed to discussions.

Competing financial interests

The authors declare no competing financial and/or non-financial interests.

Data availability

The data that support the findings of this study are available from the corresponding author upon request.

Data availability

The data that support the plots within this paper and other findings of this study are available from the corresponding authors upon reasonable request.

Additional Information

Supplementary information is available in the online version of the paper. Reprints and permission information is available online at www.nature.com/reprints. Correspondence and requests for materials should be addressed to S. Zhang, A. K. Geim or M. Lozada-Hidalgo.

* sheng.zhang@tju.edu.cn, geim@manchester.ac.uk, marcelo.lozadahidalgo@manchester.ac.uk

Perfect proton selectivity in ion transport through two-dimensional crystals

Supplementary Information

L. Mogg, S. Zhang, G.-P. Hao, K. Gopinadhan, D. Barry, B. L. Liu, H. M. Cheng, A. K. Geim, M. Lozada-Hidalgo

Fabrication procedures

Supplementary Figure 1 shows typical optical, atomic force microscopy and Raman spectroscopy[1] characterization data for one of the used hBN crystals. Similar characterization procedures were performed for graphene. Supplementary Figure 2 illustrates the fabrication flow process.

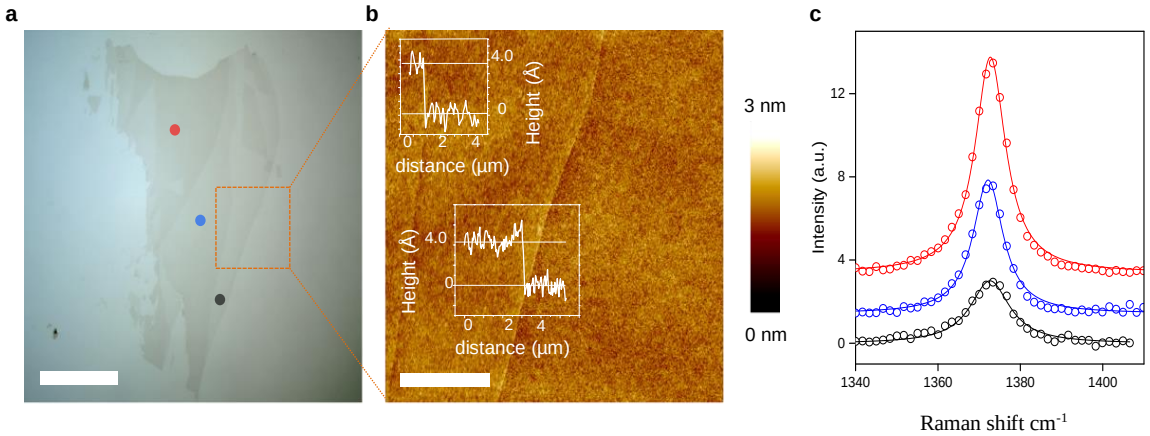

Supplementary Figure 1| Characterization of mono- and few- layer hBN. a, Optical image of a typical hBN flake. Mono-, bi- and tri- layer regions are marked by black, blue and red dots, respectively. Scale bar, 15 μm. **b**, AFM image of the area marked in panel **a** by the red square. The insets show the step heights corresponding to the mono- and bi- layer regions. Scale bar, 4 μm. **c**, Raman spectra from the three areas marked by the dots in panel **a** (color coded). The solid lines are Lorentzian fits.

Leak tests using nanoballoons

The most sensitive technique to detect microscopic defects in 2D crystals is gas-leak measurements using 'nanoballoons'[2,3]. In such experiments, a small (~1 μm^3) microcavity in an oxidized Si wafer is sealed with a 2D crystal membrane and then filled with a chosen gas (typically, Ar) pressurized above 1 bar[2,3]. The pressure difference between the gas inside and outside the microcavity causes the 2D membrane to bulge upwards (top inset Supplementary Figure 3). It is possible to monitor changes in the gas pressure inside the microcavity by measuring the membrane deflection using AFM. In the absence of atomic-scale defects, the gas slowly leaks along the silicon oxide layer until the pressure inside and outside the chamber is equalized, a process that typically takes many hours. However, in the presence of even a single angstrom-sized defect (such as a vacancy), the pressure inside the microcavity equalizes typically in seconds[3,4].

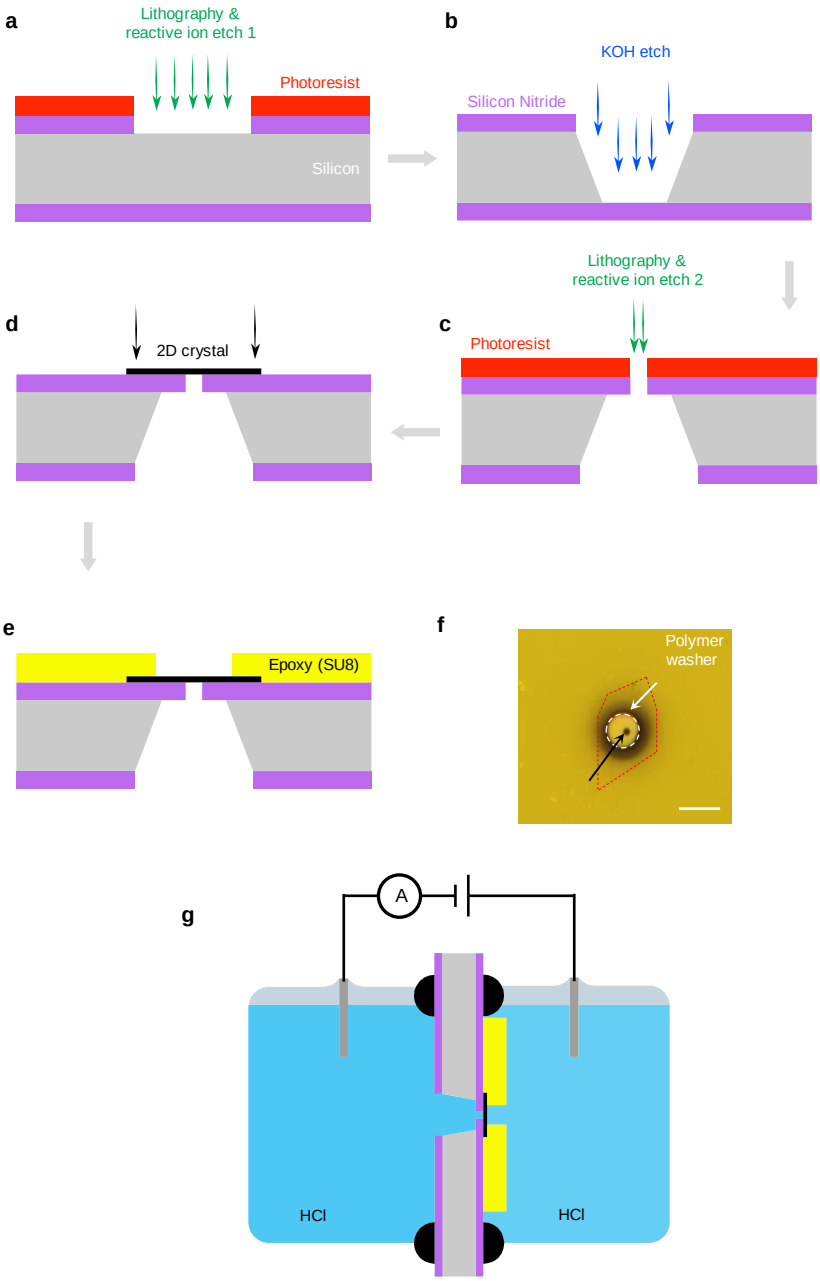

Supplementary Figure 2| Experimental details. **a-e**, Device fabrication flow. Arrows between panels indicate the order in which the different fabrication steps were performed. **f**, Optical micrograph of a final device (top view). The position of the 2D crystal is outlined by the red dotted curve; the circular aperture in SiN is marked with the black arrow; the hole in the polymer washer, with the white dotted circle. Scale bar, 10 μm. **g**, Schematic of our liquid cell. The O-rings used to seal devices are represented with black circles.

To check that our membranes are defect-free, we carried out the above gas-leak experiments following the approach of refs. [2,3]. To this end, we etched microcavities in a Si/SiO_2 wafer and sealed them with monolayer graphene. The microcavities were pressurized by placing the devices inside a 'charging' chamber filled with Ar at 2 bar. After several days, the devices were then taken out of the charging chamber and their height profile was measured with AFM. Supplementary Figure 3 shows typical results found for dozens of the membrane devices that were studied. The membranes

were found to bulge upwards and the Ar leak rate was found to be ~10^3 atoms per second, in agreement with permeability of the Si oxide layer[2]. Next, in control experiments, we intentionally introduced atomic scale vacancies by mild ultra-violet etch[3]. This procedure yields a defect density so low that it cannot be detected using Raman spectroscopy. Nevertheless, we found that the resulting nanoballoons did not inflate at all, even after leaving them in the charging chamber for over a month. This is consistent with rapid gas effusion through the 2D membranes such that angstrom-sized defects lead to their deflation within seconds, beyond time resolution of our approach[3,4]. The described experiments show that our mechanically-exfoliated crystals were defect-free, in agreement with the conclusions reached in refs. [3,4] for similar graphene devices.

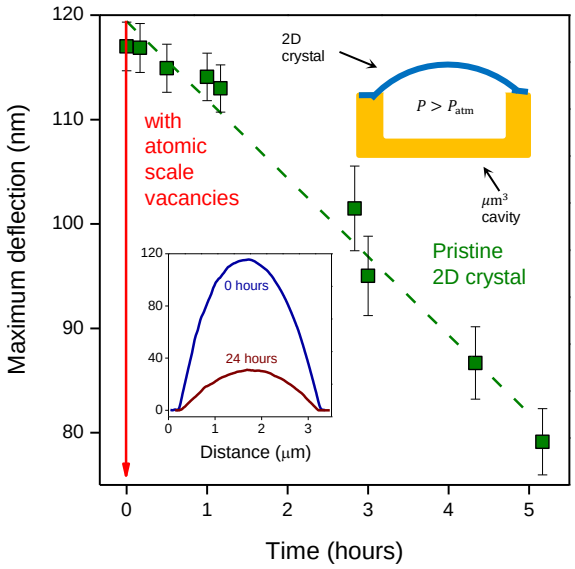

Supplementary Figure 3I Leak tests using nanoballoons. Maximum membrane deflection as a function of time. The data point at time zero hours corresponds to the first measurement after the device was taken out of the charging chamber. It normally took us only several minutes before the first data point was recorded. The red arrow indicates that in the presence of a few atomic-scale defects, we did not observe any bulging at all. Top inset: Schematic of our nanoballoons. Bottom inset: AFM traces taken through the center of an inflated nanoballoon at different times after taking it out of the charging chamber.

Characterization of electrical measurements setup

To characterize our setup, we first determined typical leakage currents, in the absence of any proton conductive path. This was done in two different ways. First, a SiN substrate without an aperture was used to separate two HCl solution reservoirs. Second, a suspended 2D membrane device was used to separate two reservoirs filled with deionized water. In both cases only minute currents of the order of 1 pA were detected. This shows that electrical leakage provided little contribution to the obtained *I-V* characteristics of our 2D-membrane devices. Next, we characterized the maximum possible conductance through our apertures at a given HCl concentration. To this end, we measured devices in which the apertures in SiN were not covered with a 2D crystal (referred to as 'bare aperture devices'). Supplementary Figure 4 shows that σ of such devices scaled linearly with electrolyte

concentration. Importantly, we found that for all concentrations, σ of bare-aperture devices was ≳1000 times larger than for those with a 2D-crystal membrane.

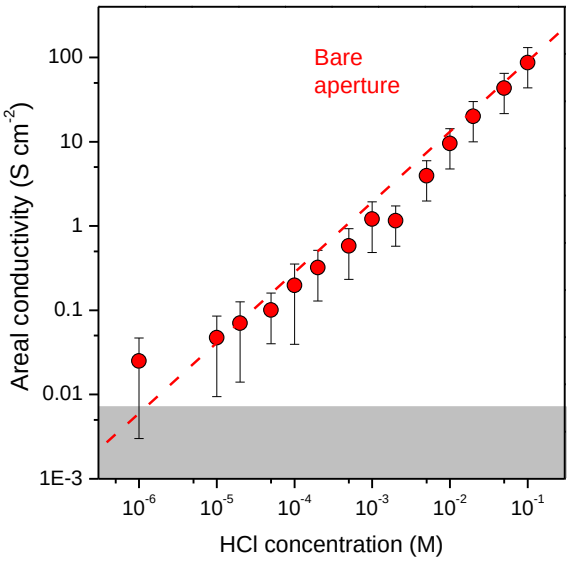

Supplementary Figure 4| Conductance of bare-aperture devices. Their σ as a function of HCl concentration. Dotted line: Best linear fit to the data. The grey area indicates our detection limit determined by pA-range leakage currents.

Membrane potential measurements

To measure the membrane potential for our membrane devices, they were placed to separate two reservoirs filled with HCl solutions at different concentrations. The membrane potential was measured by recording *I-V* characteristics and finding their intersection with the x-axis. Such intersection is known as the zero current or cell potential (V_{cell}) and has two components: the redox potential (V_{redox}) and the membrane potential (V_o):

$$V_{cell} = V_{redox} + V_o \qquad (1)$$

The redox potential appears due the electrodes' material and is independent of the studied membrane. Its value is well known for Ag/AgCl electrodes. For this reason, it is customary to remove this fixed contribution and report only V_0. We followed this convention. Nevertheless, to double-check this contribution, we also measured our devices using reference electrodes, instead of Ag/AgCl ones[5]. If using the reference electrodes, we indeed found $V_{cell} = V_0$, as expected.

Selectivity of graphene devices

The proton conductance through graphene membranes is at least ~50 times lower than that for monolayer hBN. For this reason, parasitic capacitive contributions from the setup become significant and induce notable errors in the membrane potential measurements. To minimize this problem, we fabricated a device with many (nine) apertures (each of 2 μm in diameter) and then covered all nine with one large mechanically-exfoliated graphene monolayer. This was possible with graphene because, unlike hBN, it can be mechanically exfoliated into crystals of up to hundreds of microns

across. Supplementary Figure 5 shows *I-V* characteristics for this device when it was used to separate two HCl solutions at the concentration ratio $\Delta C = 10$. Hysteresis in the *I-V* curve was much smaller than for individual 2 μm apertures but still contributed towards the uncertainty in determining V_0, which was somewhat larger than that for our typical hBN devices (Supplementary Figure 5). We obtained V_o = - 55±9 mV, which within the uncertainty corresponds to the perfect selectivity for protons.

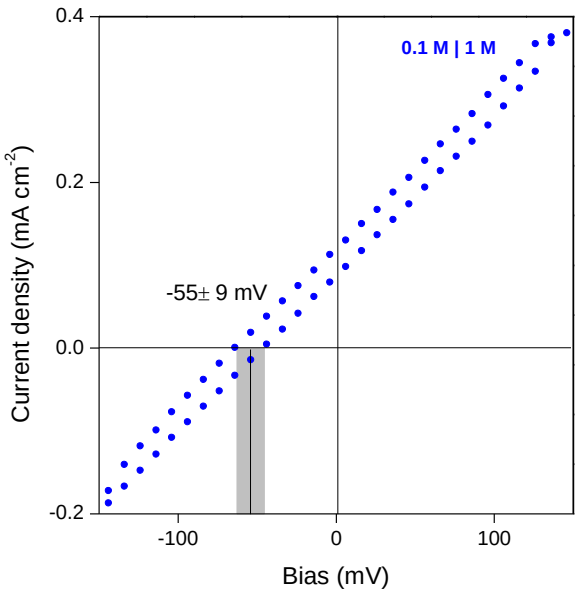

Supplementary Figure 5| Proton selectivity for graphene. *I-V* characteristics of a graphene-membrane device that separated two reservoirs with a concentration gradient of 10. The uncertainty in determining V_0 is marked by the grey rectangle.

Bulk transport numbers for HCl

As a reference, we carried out similar measurements of the membrane potential using a porous glass membrane. Supplementary Figure 6 shows the values of V_0 extracted from these experiments.

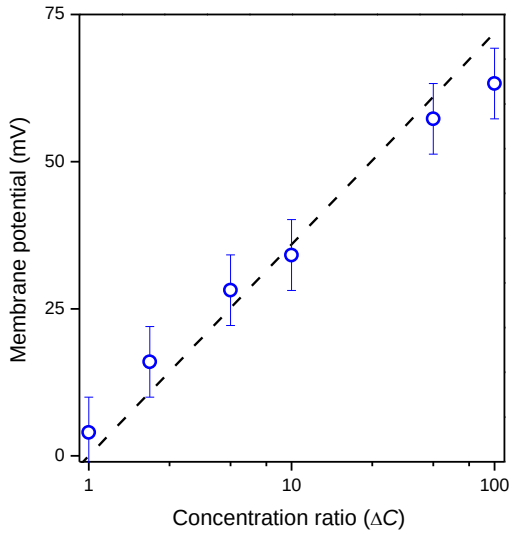

Supplementary Figure 6| Reference measurements of the membrane potential for porous glass. Symbols: Our experimental data. The black line is given by Eq. (1) and the literature values $t_H = 0.83$ and $t_{Cl} = 0.17$ for bulk hydrochloric acid[6].

Supplementary references

1. Gorbachev, R. V. *et al.* Hunting for monolayer boron nitride: Optical and raman signatures. *Small* **7**, 465–468 (2011).
2. Bunch, J. S. *et al.* Impermeable atomic membranes from graphene sheets. *Nano Lett.* **8**, 2458–62 (2008).
3. Koenig, S. P., Wang, L., Pellegrino, J. & Bunch, J. S. Selective molecular sieving through porous graphene. *Nat. Nanotechnol.* **7**, 728–732 (2012).
4. Wang, L. *et al.* Molecular valves for controlling gas phase transport made from discrete ångström-sized pores in graphene. *Nat. Nanotechnol.* **10**, 785–790 (2015).
5. Gopinadhan, K. *et al.* Complete steric exclusion of ions and proton transport through confined monolayer water. *Science* (2019). doi:10.1126/science.aau6771
6. Bard, A. J. & Faulkner, L. R. *Electrochemical Methods*. (Wiley, 2001).

Chapter 7

Proton Transport Through Atomically-Thin Micas

Given that MoS_2 was experimentally shown to be a poor proton-conductor, the ability for other few atomically-thin lattices, not isostructural to graphene, to conduct protons, was unknown. As discussed in Chapter 2, protons can transport through the solid state via neighbouring oxygen/hydroxide sites. We show in this publication that complex 2D materials that possess such oxygen/OH groups within the lattice, upon proton exchange, allow for high areal proton conductivity, indeed, exceeding that reported for graphene and hBN. We modelled the proton permeation route through mica to be that of proton wires through the lattice, where the proton exchange of the mica lattice unblocks the pathway. Same-thickness non-exchanged mica membranes display proton conductivity nearly three orders of magnitude smaller under ambient conditions. Crucially, the proton-conducting properties persist at elevated temperatures, beyond the reach of polymer membranes such as Nafion. Evidence for ion migration within the mica lattice isn't a new concept in itself. Lithium migration into vacant octahedral sites is thought to explain the decrease in montmorillonite swelling with temperature. This migration neutralises charge within the TOT layer, in a process known as the Hofmann-Klemen effect. We are proposing in this work, that similarly migrating protons transport through channels which have been 'activated' by proton-exchange. This is exciting, as it opens up the possibility for a wide range of 2D oxides to become proton-conductors via a similar activation or unblocking process. That ion-exchanged micas are highly efficient proton-conductors even when they are 10 atoms thick is a significant discovery. Compared to graphene and monolayer hBN, 10 layers of mica are relatively robust and even in the presence of atomic defects, this is unlikely to have such a deleterious effect on performance. This surprising new result could prove to be important for applications such as fuel cells and other hydrogen-related technologies.

The results presented in Chapter 7 are reported in the publication: "Atomically thin micas as proton-conducting membranes" published in Nature Nanotechnology. The researchers' contributions to the work are as follows. M.L.-H. and A.K.G. designed and directed the project. L.M. and G.-P.H. fabricated devices, performed measurements and carried out data analysis with help from S.Z. C.B. and F.M.P. provided theoretical support. Y.Z. and S.J.H. performed electron microscopy imaging and analysis. L.M., A.K.G. and M.L.-H. wrote the manuscript. All authors contributed to discussions.

Atomically-thin micas as proton conducting membranes

L. Mogg[1,2+], G.-P. Hao[1,3+]*, S. Zhang[1,4+], C. Bacaksiz[5], Y. Zou[6], S. J. Haigh[6], F. M. Peeters[5], A. K. Geim[1,2]*, M. Lozada-Hidalgo[1,2]*

[1]National Graphene Institute, The University of Manchester, Manchester M13 9PL, UK

[2]School of Physics and Astronomy, The University of Manchester, Manchester M13 9PL, UK

[3]State Key Laboratory of Fine Chemicals, School of Chemical Engineering, Dalian University of Technology, Dalian 116024, China

[4]Key Laboratory for Green Chemical Technology of Ministry of Education, School of Chemical Engineering and Technology, Tianjin University, Tianjin 300072, China

[5]Departement Fysica, Universiteit Antwerpen, Groenenborgerlaan 171, B-2020 Antwerp, Belgium

[6]School of Materials, The University of Manchester, Manchester M13 9PL, UK

Monolayers of graphene and hexagonal boron nitride (hBN) are highly permeable to thermal protons[1,2]. For thicker two-dimensional (2D) materials, proton conductivity diminishes exponentially so that, for example, monolayer MoS_2 that is just three atoms thick is completely impermeable to protons[1]. This seemed to suggest that only one-atom-thick crystals could be used as proton conducting membranes. Here we show that few-layer micas that are rather thick on the atomic scale become excellent proton conductors if native cations are ion-exchanged for protons. Their areal conductivity exceeds that of graphene and hBN by one-two orders of magnitude. Importantly, ion-exchanged 2D micas exhibit this high conductivity inside the infamous gap for proton-conducting materials[3], which extends from ~100 ˚C to 500 ˚C. Areal conductivity of proton-exchanged monolayer micas can reach above 100 S cm^{-2} at 500 ˚C, well above the current requirements for the industry roadmap[4]. We attribute the fast proton permeation to ~5 Å-wide tubular channels that perforate micas' crystal structure which, after ion exchange, contain only hydroxyl groups inside. Our work indicates that there could be other 2D crystals[5] with similar nm-scale channels, which could help close the materials gap in proton-conducting applications.

Ion exchangers are non-soluble materials that contain ions within their crystal structure. These ions are easily substituted with other ions of the same polarity, if the material is immersed in suitable electrolytes[6]. In essence, ion exchangers act as sponges that can absorb and release ions. Micas are well-known ion exchangers[7-10]. They consist of aluminosilicate layers that are normally covered with cations such as K^+. These native species can be exchanged for other ions, e.g. H^+, Li^+ or Cs^+, which adsorb both on the surface of aluminosilicate layers and in between them (see Fig. 1). Ion exchange at micas' surfaces proceeds much faster than that within the interlayer space, taking seconds rather than hours[8,9]. It is particularly easy to substitute native ions with protons (H^+) as shown by surface force[11,12], XPS[13], X-ray reflectivity[14,15], AFM[16,17], NMR[18] and zeta-potential[19] experiments. Besides being proton exchangers, micas have a relatively sparse crystal structure. Their basal planes contain

hexagonal rings of ~5.2 Å in size (Fig. 1b), which are considerably larger than the rings making up graphene and MoS_2 (~2.5 and 3.2 Å, respectively). From this perspective, micas can be considered as aluminosilicate slabs pierced by tubular channels (Fig. 1a). The channels are however not empty but filled with hydroxyl (OH^-) groups; which resembles proton-conducting 1D chains in water[20] (Fig. 1a). In this report, we investigate whether these atomic-scale channels in micas allow for proton permeation so that few-layer micas could be used as proton-conducting membranes, despite their relatively large thickness (~10 Å for monolayer micas as compared to 6.5 Å for impermeable MoS_2).

Two types of micas (muscovite and vermiculite) were used in our studies. Atomically-thin crystals of these micas were prepared by mechanical exfoliation (Fig. S1)[21] and first investigated using scanning transmission electron microscopy (STEM). To this end, a crystal was immersed in a 0.1 M $CsNO_3$ solution at 80 ˚C for typically a week so that there was sufficient time for Cs-ion exchange through their entire volume. Cs was chosen for this study as a heavy ion that provides bright contrast in STEM. Using the standard mechanical-polishing approach we then prepared thin slices of our micas for cross-sectional imaging[8]. Figs. 1c and d show examples of such atomic-resolution images for natural and Cs-exchanged vermiculite, respectively. Cs atoms in the ion-exchanged samples are easily distinguished from Mg ions (native for vermiculite) because the former give rise to notably brighter spots. For plan-view imaging, we used our thinnest mica crystals (mono- and bi- layers) which after exfoliation were suspended over microfabricated holes in a silicon nitride membrane[1] (Fig. 1e, Fig. S2). The structures were then immersed in heated $CsNO_3$ for about an hour, which was sufficient for the Cs exchange. Figs. 1f and g show images for one of our bilayer devices. Cs ions form a triangular lattice, in agreement with our density functional theory (DFT) simulations (Fig. S3). Such clear images of micas' basal plane were conspicuously absent in the literature and were possible in our experiments only if we used Cs-exchanged few-layer crystals. Because the plan-view samples were only exposed to the electrolyte for a short time, we believe that the observed Cs ions were adsorbed on the cleaved surface and not necessarily intercalated the interlayer space. Furthermore, imaging of the suspended mica structures allowed us to confirm that ion exchange (using either Cs^+ or H^+) did not introduce defects into the crystal lattice (Fig. S4), in agreement with previous studies on proton-exchanged[13-17] and ion-exchanged[9,13,17] micas.

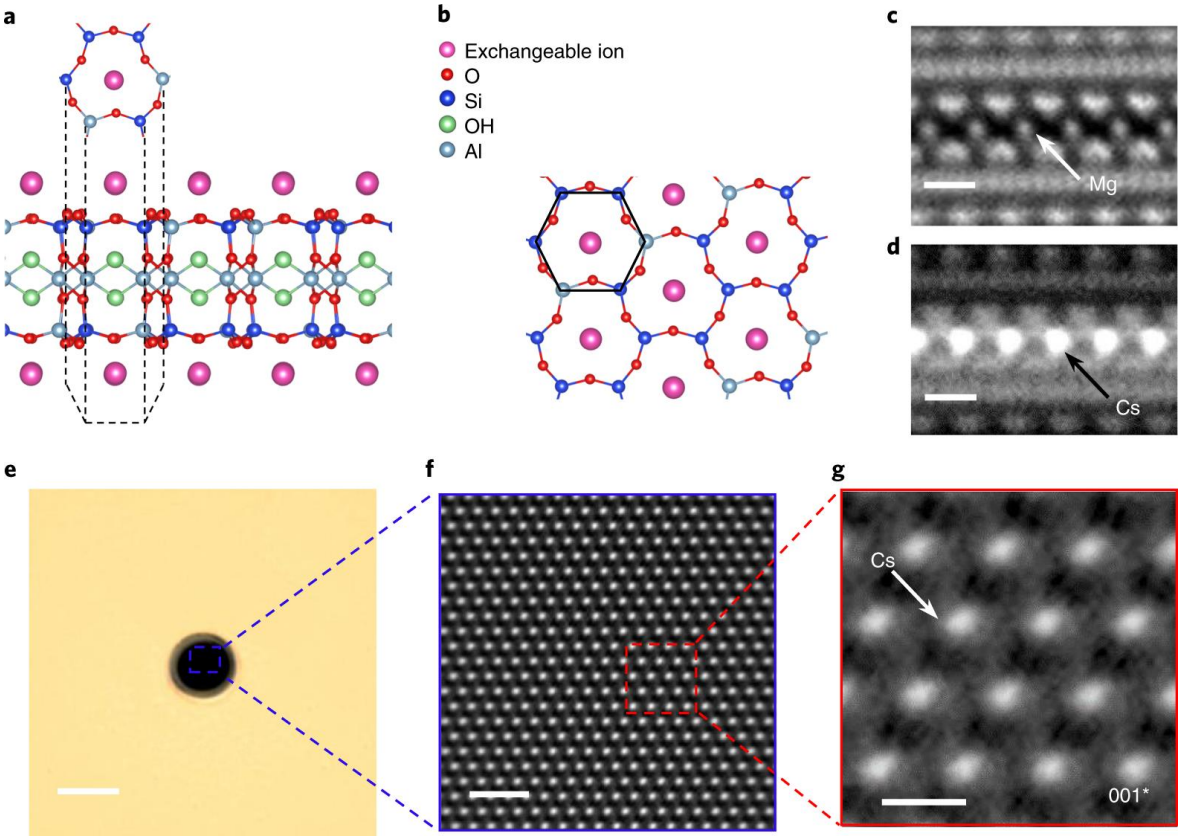

Figure 1|STEM characterization of ion-exchanged micas. a, Cross-sectional schematics of a monolayer mica. The crystal consists of Si-O tetrahedra and Al-O octahedra that form a 2D sheet which we refer to as the aluminosilicate layer. Exchangeable ions (magenta balls) are adsorbed onto these layers. **b**, Corresponding plan-view schematic. Si (dark blue), Al (light blue) and O (red) atoms form ~5 Å hexagonal rings (black lines) so that micas can be viewed as stacked aluminosilicate slabs pierced by tubular channels (see the 3D projection indicated by the dashed lines in panel a). The hexagonal channels contain OH groups (green) and exchangeable ions in the center. **c**, Cross-sectional STEM image of a non-exchanged vermiculite using the high-angle annular dark-field (HAADF) mode. The arrow indicates native Mg ions. Other ions comprising the aluminosilicate layers are also visible in the micrograph. Scale bar, 0.5 nm. **d**, Similar HAADF-STEM image but for Cs-exchanged vermiculite. Large bright spots are Cs atoms. Scale bar, 0.5 nm. **e**, Optical micrograph of a bilayer vermiculite device for plan-view STEM imaging. The silicon nitride membrane is seen in yellow and has a hole in the middle over which the bilayer mica is suspended. Scale bar, 2 μm. **f**, HAABF-STEM image of the bilayer device after Cs-ion exchange. Scale bar, 5 nm. **g**, Zoom-in from panel f. Scale bar, 0.5 nm.

Proton transport across the basal plane of atomically-thin micas was studied using electrical measurements[1,2]. In these experiments, monocrystals of muscovite and vermiculite were again suspended over micrometer holes similar to Fig. 1e. Then the structure was coated from both sides with a proton-conducting, electron-insulating polymer (Nafion[22]) and proton-injecting electrodes were attached as described previously[1,2] (inset of Fig. 2a and Fig. S2). It is important to note that Nafion is a proton electrolyte and, hence, micas in these devices inevitably become proton-exchanged, regardless of whether or not ion exchange procedures were implemented prior to the

Nafion deposition. Nonetheless, we normally performed such initial proton exchange, which involved immersing the suspended devices in a 10 mM acetic acid solution at 80 ˚C for 1 hour and then thoroughly rinsing them with deionized water. For electrical measurements, the devices were placed in a humid H_2 atmosphere to ensure high proton conductivity of Nafion[1]. The measured current density I varied linearly with applied voltage V for all the studied devices (Fig. 2a), which allowed us to define their areal resistivity, $R=V/I$. For both micas, R increased exponentially with their thickness (Fig. 2b) so that $R = R_0 \exp(\alpha N)$, where N is the number of layers, α is a material-specific coefficient and $R_0 \approx 1\ \Omega\ cm^2$ is the areal resistivity in the monolayer limit. Note that R_0 is much smaller than the corresponding values of ~100 and 10 $\Omega\ cm^2$ for monolayers of graphene and boron nitride, respectively[1].

To corroborate the results of our electrical measurements, the proton flux was also measured directly, using mass spectrometry[1,2]. In this case, one of the Nafion layers was effectively removed and, instead, a porous Pt electrode (~50 nm thick) was sputtered directly onto mica (inset of Fig. 2c, and Fig. S2). The device was then used to separate two chambers: one containing H_2 at 100% humidity and the other evacuated and connected to a mass spectrometer. If a positive or zero voltage was applied to the Pt electrode, no gas permeation could be discerned. This provides clear proof (in addition to the control experiments[1,2]) that the studied mica membranes were impermeable to gases, ruling out structural defects, in agreement with our STEM analysis. On the other hand, if a negative bias was applied, we readily detected H_2 flow (Fig. 2c). Crucially, for every two electrons in the electrical circuit (inset of Fig. 2c), one hydrogen molecule was detected in the vacuum chamber. This corresponds to 100% efficiency for charge-to-mass conservation as described by Faraday's law of electrolysis: $\Phi = I/2F$, where Φ is the hydrogen flux, F is Faraday's constant and the factor of 2 accounts for the two protons required to form a hydrogen molecule[1,2].

The mica membranes described above were proton-exchanged. To find out if the exchange increased or decreased their proton transparency, we compared proton-exchanged and natural (non-exchanged) mica devices. They were fabricated in a similar manner but, instead of using Nafion, porous Pt films were sputtered directly onto both sides of mica (inset of Fig. 3a and Fig. S2). If placed in a humid H_2 atmosphere, such Pt films are known to serve as source and sink reservoirs for protons[23]. Fig. 3a shows that proton exchange had a strong effect on proton permeation. The areal conductivity, $G=1/R$, of H-exchanged devices (G_x) was $\gtrsim$100 times larger than G of non-exchanged ones (G_n): $G_x \gtrsim 100\ G_n$. Furthermore, the strong dependence of G_x and G_n on both H_2 pressure and humidity proved that the observed conductance in both exchanged and non-exchanged micas was provided

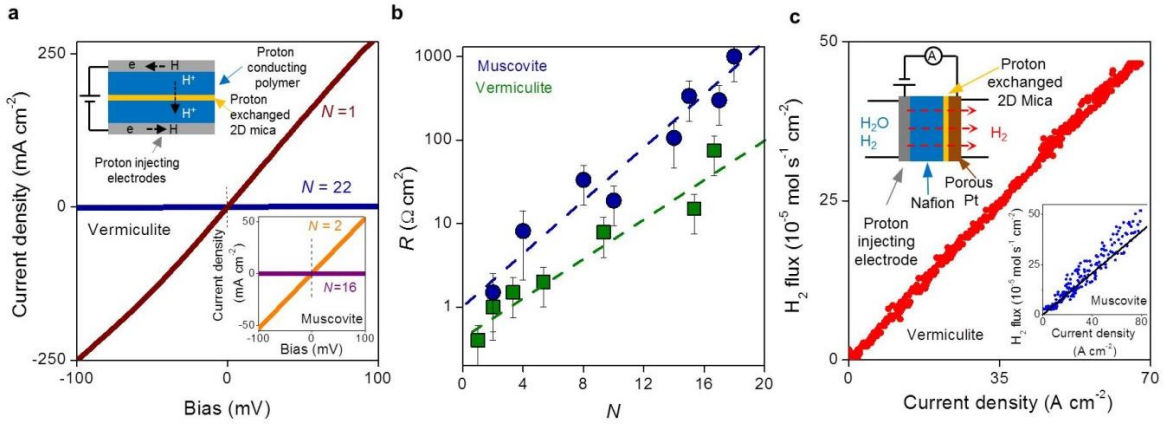

Figure 2|Proton transport through 2D micas studied using Nafion-coated devices. **a**, Examples of *I-V* characteristics for atomically-thin vermiculite (main panel) and muscovite (bottom inset). Top inset, devices' schematic. **b**, Areal resistivity *R* as a function of *N* for both micas. Dotted lines, best exponential fits to the data. Error bars: standard deviation from several devices. **c**, Mass spectrometry of the hydrogen flow through monolayer vermiculite (main panel) and bilayer muscovite (bottom inset). The measured current was induced by negative *V* (typically, < 3 V) applied as shown schematically in the top inset. The electrically driven protons pass through the micas and form hydrogen molecules in the porous Pt electrode: $2H^+ + 2e^- \rightarrow H_2$. The black line in the bottom inset denotes the 100% Faraday efficiency for charge-to-mass conversion.

by protons rather than electrons (Fig. S5). This also agrees with the fact that, for a given type of mica and its thickness, G_x closely matched the values of *G* found for Nafion-coated devices (Fig. 2b). These experiments show that protons can transport through both exchanged and non-exchanged micas but proton exchange increases *G* strongly, by over two orders of magnitude.

Unlike Nafion, the Pt-coated devices could sustain high temperatures (*T*), which allowed us to study *T* dependence of proton transport (Fig. 3a). To ensure that changes in devices' hydration at elevated temperatures did not introduce artefacts, our devices were normally placed in dry hydrogen. Nonetheless, we also checked in several cases that a humid hydrogen atmosphere gave rise to similar $G_x(T)$. We found that G_x strongly increased with *T*, by a factor of ~600 between 30 ˚C and 350 ˚C (Fig. 3b, red curve). The Arrhenius plot reveals two distinct *T* regions separated by the transition temperature T_p of ~200 ˚C. In both regions, G_x displayed activated behavior $G_x \propto \exp(-E/kT)$; but with different energy barriers *E* that we refer to as E_p and E_e below and above T_p, respectively (*k* is the Boltzmann constant). E_p was found to be ~0.2 eV for both muscovite and vermiculite and, within our experimental accuracy of 50 meV, the micas' thickness had little effect on it (Fig. 3b, bottom inset). On the other hand, the activation curves were notably steeper above T_p, indicating higher activation energies, $E_e \approx 0.8$ and ≈ 0.5 eV for muscovite and vermiculite, respectively

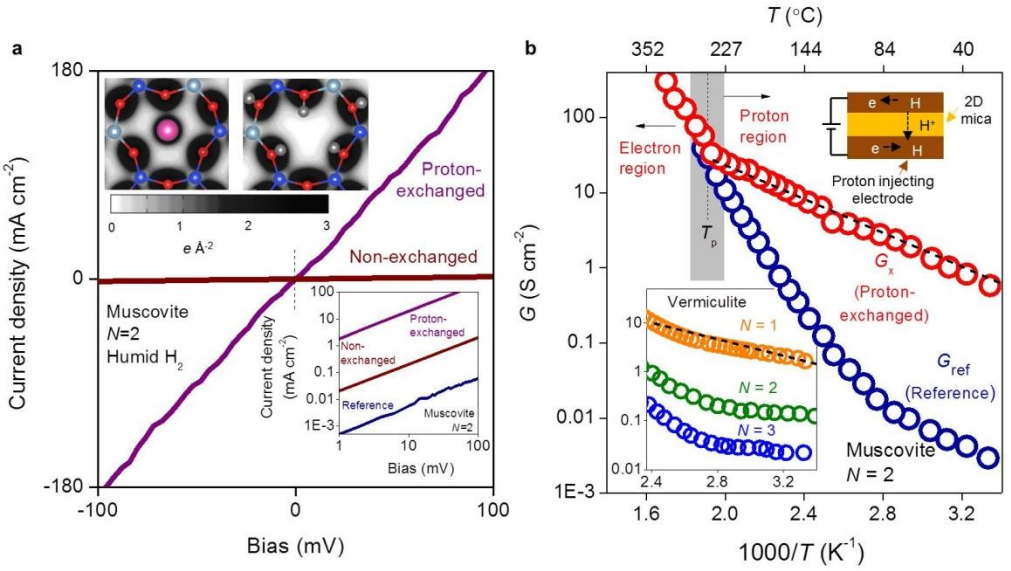

Figure 3 |Proton transport through micas measured using Pt-coated devices. a, *I-V* characteristics of proton-exchanged and non-exchanged bilayer mica in humid H_2. Top inset, plan view of electron charge density for non-exchanged (left) and proton-exchanged (right) monolayers of muscovite. For clarity, the crystal structure is overlaid as red balls indicating oxygen atoms; dark blue, silicon; light blue, aluminum; grey, hydrogen from proton exchange; magenta, exchangeable ion (potassium in this case). Grey scale, areal density in units of *e* per Å^2. Bottom inset: *I-V* characteristics from the main panel (purple and brown) are replotted on the log-log scale to compare them with the *I-V* response of reference devices (blue). **b**, G_x (red) and G_{ref} (blue) measured for bilayer muscovite using porous-Pt contacts as shown schematically in the top inset. The grey rectangle indicates $T_p \approx 250$°C separating regimes with different activation behavior. Below T_p, proton transport dominates G_x whereas electrons become responsible for conductivity at higher *T*. Bottom inset: Similar Arrhenius plots for proton-exchanged vermiculite of different thickness in the *T* range where proton transport is dominant. They show little dependence of $G_x(T)$ on *N*. The black dotted lines indicate $E_p = 0.2$ eV.

(Fig. 3b and Fig. S6). The Arrhenius plots were reproducible between different devices and displayed no hysteresis during heating and cooling cycles (Fig. S6).

The above measurements suggest that two transport mechanisms with different activation energies contribute to $G_x(T)$. To gain further information about them, we studied Pt-coated but non-exchanged devices that were placed in vacuum (referred to as reference devices). In the absence of a source of protons, electrons are the only possible charge carriers, leading to finite leakage currents. The bottom inset of Fig. 3a shows that at room *T* the conductivity G_{ref} of our reference devices was ~1,000 times lower than that for similar but proton-exchanged mica. On the other hand, G_{ref} increased with *T* more rapidly than G_x, exhibiting activation energy E_{ref} close to E_e. Above T_p, both reference and proton-exchanged devices displayed essentially the same conductivity, that is, $G_{ref} \approx G_x$ (Fig. 3b). These observations show that the dominant contribution to the micas' conductance above T_p is electron transport. This is not surprising as micas are known to allow activated hopping of electrons between

impurities, usually Fe atoms[24]. At lower T, proton transport clearly dominates, in agreement with our results using Nafion-coated devices, which did not allow for electron conductance[1,2]. Combining the observed T and N dependences (including those in the bottom inset of Fig. 3b), we obtain the following empirical formula for proton transport through micas' basal planes

$$R_p = 1/G_p \approx R_0 \cdot \exp(\alpha N) \cdot \exp(E_p/kT) \quad (1)$$

where $E_p \approx 0.2$ eV and $\alpha \approx 0.3$–0.35 for both studied micas.

The reason for easy proton transport through micas can be understood by considering their crystal structure. As shown in Fig. 1a, micas are essentially aluminosilicate slabs perforated by ~5 Å-wide tubular channels. The presence of such channels is substantiated by the DFT calculations in Fig. 3a, which shows the areal electronic density seen by protons as they try to pierce monolayer mica. If micas are non-exchanged, native ions block the channels' entrances, as evidenced by the dense electron cloud in the center of the hexagonal ring in the inset of Fig. 3a (left panel). After the ions are removed by proton exchange (right panel), clear voids emerge with a size notably larger than that found in similar analyses for graphene and boron nitride monolayers[1] (see also Fig. S7). As protons translocate through the tubules, they encounter two OH^- groups (see Fig. 1a), which act as traps between which protons jump. The exponential dependence of R on N (Fig. 2b) can then be attributed to hopping between such traps stationed in consecutive layers. Note that it is protons (H^+) rather than hydronium ions (H_3O^+) that hop across the lattice, since water molecules are sterically excluded[11,12,16,17]. Our DFT calculations support this interpretation. The minimum energy path for protons involves the two OH^- groups. These create local energy minima (Fig. S8), thus providing the traps for protons. The calculations also yield a maximum energy barrier for proton transport of ~0.35 eV. This agrees well with the experimentally measured $E_p \approx 0.2$ eV, especially if the role of surface-adsorbed water is taken into account. Indeed, protons in surface-adsorbed water are strongly attracted to OH^- groups inside the mica tubules[17]. Hence the first link in the transport chain can therefore be expected to be a proton (H^+) jump from surface adsorbed H_3O^+ towards OH^- groups. Quantum effects were shown to reduce proton transport barriers in graphene and hBN[2] and a similar reduction could be expected in micas.

To conclude, we have shown that proton-exchanged few-layer micas are good proton conductors. Comparison with much thinner monolayers of graphene, hBN and especially MoS_2, shows that tubular channels in micas enable this high conductivity. From this perspective, other 2D materials that may be relatively thick but possess similar tubular structures (for example, complex cuprates or 2D metal-organic frameworks) could be good proton conductors or turned into such via proton exchange. In terms of applications, the present work also merits attention. There is a lack of proton conducting materials that can operate between 100 ˚C and 500 ˚C, which is referred to as the materials gap[3]. Bridging this gap would enable higher efficiency and lower cost in a large number of energy conversion technologies[25,26]. Atomically-thin micas are good candidates to help fill this gap. Even at moderate temperatures of ~150 ˚C and in dry hydrogen, their G_p exceeds ~10 S cm^{-2} (Fig. 3b), twice higher than the industry benchmark placed by Nafion 117[27]. Furthermore, micas are highly stable in

both oxidizing and reducing atmospheres up to very high T (above 800 ˚C)[28]. Extrapolating our data to the other side of the materials gap yields extremely high conductance > 100 S cm^{-2} at 500 ˚C, which may be achievable by growing micas without impurities (such as Fe) to prevent the high-T electron leakage characteristic to natural micas. We envision that the reported membranes can be scaled up using vapor deposition of atomically-thin micas[29] and their subsequent transfer onto suitable porous substrates, as successfully demonstrated for graphene[30]. Ultrathin mica laminates similar to those reported in ref.[31] can be another viable option for scaling up.

1. Hu, S. *et al.* Proton transport through one-atom-thick crystals. *Nature* **516**, 227–230 (2014).
2. Lozada-Hidalgo, M. *et al.* Sieving hydrogen isotopes through two-dimensional crystals. *Science* **351**, 68–70 (2016).
3. Norby, T. Solid-state protonic conductors: principles, properties, progress and prospects. *Solid State Ionics* **125**, 1–11 (1999).
4. US Dept. Energy. Multi-year Research, Development and Demonstration Plan. (2012). Available at: http://energy.gov/sites/prod/files/2014/03/f12/fuel_cells.pdf. (Accessed: 1st June 2018)
5. Geim, A. K. & Grigorieva, I. V. Van der Waals heterostructures. *Nature* **499**, 419–425 (2013).
6. Helfferich, F. *Ion Exchange*. (McGraw Hill, 1962).
7. Christenson, H. K. & Thomson, N. H. The nature of the air-cleaved mica surface. *Surf. Sci. Rep.* **71**, 367–390 (2016).
8. Kogure, T., Morimoto, K., Tamura, K., Sato, H. & Yamagishi, A. XRD and HRTEM Evidence for Fixation of Cesium Ions in Vermiculite Clay. *Chem. Lett.* **41**, 380–382 (2012).
9. Lee, S. S., Fenter, P., Nagy, K. L. & Sturchio, N. C. Real-time observation of cation exchange kinetics and dynamics at the muscovite-water interface. *Nat. Commun.* **8**, 15826 (2017).
10. Shao, J.-J., Raidongia, K., Koltonow, A. R. & Huang, J. Self-assembled two-dimensional nanofluidic proton channels with high thermal stability. *Nat. Commun.* **6**, 7602 (2015).
11. Claesson, P. M., Herder, P., Stenius, P., Eriksson, J. C. & Pashley, R. M. An ESCA and AES study of ion-exchange on the basal plane of mica. *J. Colloid Interface Sci.* **109**, 31–39 (1986).
12. Alcantar, N., Israelachvili, J. & Boles, J. Forces and ionic transport between mica surfaces: Implications for pressure solution. *Geochim. Cosmochim. Acta* **67**, 1289–1304 (2003).
13. Xu, L. & Salmeron, M. An XPS and Scanning Polarization Force Microscopy Study of the Exchange and Mobility of Surface Ions on Mica. *Langmuir* **14**, 5841–5844 (1998).
14. Cheng, L., Fenter, P., Nagy, K. L., Schlegel, M. L. & Sturchio, N. C. Molecular-scale density oscillations in water adjacent to a mica surface. *Phys. Rev. Lett.* **87**, 156103-156103–4 (2001).
15. Lee, S. S., Fenter, P., Nagy, K. L. & Sturchio, N. C. Monovalent ion adsorption at the

muscovite (001)-solution interface: Relationships among ion coverage and speciation, interfacial water structure, and substrate relaxation. *Langmuir* **28**, 8637–8650 (2012).

16. Fukuma, T., Ueda, Y., Yoshioka, S. & Asakawa, H. Atomic-Scale distribution of water molecules at the mica-Water interface visualized by three-Dimensional scanning force microscopy. *Phys. Rev. Lett.* **104**, 016101 (2010).
17. Ricci, M., Trewby, W., Cafolla, C. & Voïtchovsky, K. Direct observation of the dynamics of single metal ions at the interface with solids in aqueous solutions. *Sci. Rep.* **7**, 43234 (2017).
18. Bowers, G. M., Bish, D. L. & Kirkpatrick, R. J. Cation exchange at the mineral-water interface: H3O +/K+ competition at the surface of nano-muscovite. *Langmuir* **24**, 10240–10244 (2008).
19. Sides, P. J., Faruqui, D. & Gellman, A. J. Dynamics of charging of muscovite mica: measurement and modeling. *Langmuir* **25**, 1475–1481 (2009).
20. Marx, D. Proton transfer 200 years after Von Grotthuss: Insights from ab initio simulations. *ChemPhysChem* **7**, 1849–1870 (2006).
21. Kretinin, A. V. *et al.* Electronic properties of graphene encapsulated with different two-dimensional atomic crystals. *Nano Lett.* **14**, 3270–3276 (2014).
22. Mauritz, K. & Moore, R. State of understanding of nafion. *Chem. Rev.* **104**, 4535–85 (2004).
23. Candy, J. P., Fouilloux, P. & Renouprez, A. J. Hydrogen adsorption on platinum catalysts: Quantitative determination of the various species population. *J. Chem. Soc. Faraday Trans. 1* **76**, 616–629 (1980).
24. Meunier, M., Currie, J. F., Wertheimer, M. R. & Yelon, A. Electrical conduction in biotite micas. *J. Appl. Phys.* **54**, 898–905 (1983).
25. Li, Q., Aili, D., Aage, H., Jens, H. & Jensen, O. *High Temperature Polymer Electrolyte Membrane Fuel Cells*. (Springer, 2016). doi:10.1007/978-3-319-17082-4
26. Zhang, Y. *et al.* Recent Progress on Advanced Materials for Solid-Oxide Fuel Cells Operating Below 500 °C. *Adv. Mater.* **29**, 1700132 (2017).
27. Casciola, M., Alberti, G., Sganappa, M. & Narducci, R. On the decay of Nafion proton conductivity at high temperature and relative humidity. *J. Power Sources* **162**, 141–145 (2006).
28. Simner, S. P. & Stevenson, J. W. Compressive mica seals for SOFC applications. *J. Power Sources* **102**, 310–316 (2001).
29. Boscoboinik, J. A., Yu, X., Shaikhutdinov, S. & Freund, H. J. Preparation of an ordered ultra-thin aluminosilicate framework composed of hexagonal prisms forming a percolated network. *Microporous Mesoporous Mater.* **189**, 91–96 (2014).
30. Bae, S. *et al.* 30 inch Roll-Based Production of High-Quality Graphene Films for Flexible Transparent Electrodes. *Nat. Nanotechnol.* **5**, 574–578 (2010).
31. Yang, Q. *et al.* Ultrathin graphene-based membrane with precise molecular sieving and ultrafast solvent permeation. *Nat. Mater.* **16**, 1198–1202 (2017).

Acknowledgments

The work was supported by the Lloyd's Register Foundation, EPSRC - EP/N010345/1, the European Research Council, the Graphene Flagship and the Royal Society. M.L.H. acknowledges Leverhulme Early Career Fellowship, G.P.H. acknowledges Marie Curie International Incoming Fellowship, and M.L.H. and L.M. acknowledge the EPSRC NowNANO programme for funding.

Author contribution statement

M.L.H. and A.K.G. designed and directed the project. L.M. and G.P.H. fabricated devices, performed measurements and carried out data analysis with help from S.Z. C.B. and F.M.P. provided theoretical support. Y.Z. and S.J.H. performed electron microscopy imaging and analysis. L.M., A.K.G. and M.L.H. wrote the manuscript. All authors contributed to discussions.

Competing financial interests

The authors declare no competing financial interests.

Methods

Device fabrication. Devices were fabricated by suspending mechanically exfoliated mica crystals over apertures (≈2 μm in diameter) etched into silicon-nitride membranes. The devices were then proton-exchanged. To that end, they were immersed for ~1 hour in a heated (~80 ˚C) 10 mM acetic acid solution, thoroughly rinsed with deionized water, left to dry in air and then heated at ~150 ˚C to remove remnant moisture. If working with non-exchanged devices, we skipped this step. For Nafion-coated devices, a Nafion solution (5% Nafion; 1100 EW) was drop cast on both sides of the suspended mica membrane and the device was electrically contacted with proton-injecting electrodes (PdH_x foil). The whole assembly was then annealed in a humid atmosphere at 130 °C to crosslink the polymer. For Pt-coated devices, instead of coating them with Nafion, thin porous Pt films (~50 nm) were sputtered directly on both sides of the suspended mica membrane. See Supplementary Information for further details.

Electrical measurements. For electrical measurements, the assembled devices were placed in a chamber with a controlled atmosphere of either H_2 at 100% H_2O relative humidity or, alternatively, ~10% humidity (see below). The *I-V* characteristics were measured with a *Keithley* SourceMeter 2636A at voltages typically varying between ±200 mV and using sweep rates <0.1 V min^{-1}.

Mass spectrometry. For mass spectrometry measurements, devices were used to separate two chambers: one filled with a gas mixture (10% H_2 in Ar, 100% humidity) and the other evacuated and

connected to a mass spectrometer. The porous Pt layer faced the vacuum chamber whereas the Nafion layer faced the gas chamber. A dc voltage was applied across the mass-spectrometry devices, and both electrical current and hydrogen flow were measured simultaneously. The mass spectrometer used was an Inficon UL200**.**

Data availability

The data that support the plots within this paper and other findings of this study are available from the corresponding authors upon reasonable request.

Additional Information

Supplementary information is available in the online version of the paper. Reprints and permission information is available online at www.nature.com/reprints. Correspondence and requests for materials should be addressed to G-P. Hao, A. K. Geim or M. Lozada-Hidalgo.

* guangpinghao@dlut.edu.cn, geim@manchester.ac.uk, marcelo.lozadahidalgo@manchester.ac.uk

+ These authors contributed equally

Atomically-thin micas as proton conducting membranes

Supplementary Material

Crystal characterization

Micas consist of two sheets of Si-O tetrahedral groups that sandwich an Al-O octahedral group sheet to form a 2D aluminosilicate layer. Micas are classified as trioctahedral and dioctahedral. In the former, all octahedral groups have a positive ion inside (e.g. Fe^{2+}); in the latter, two out of three octahedral groups in the 2D aluminosilicate layer contain a positive ion (e.g. Al^{3+}), with the remaining octahedral group lacking a central ion. These 2:1 layers stack on top of each other, separated by interlayer cations[1,2] (e.g. K^{+}) which can be exchanged, to form the crystal. These cations neutralize the excess negative charge in the 2:1 layers (see ref. [1,2] for details of the mica structure).

The micas studied in this work were natural vermiculite, sourced from Lanark, Ontario (Canada) and ruby muscovite, purchased from Agar Scientific. The chemical composition of laboratory grade ruby muscovite is readily found from the suppliers, water (2.99%), K_2O (9.87%), MgO (0.38%), Fe_2O_3 (2.48%), Si-O + Al-O (78.67%), Na_2O (0.62%), C (0.44%) and traces. Natural vermiculite was characterized in our experiments to establish its elemental composition. To that end we performed two sets of measurements. First, thermo-gravimetry was used to measure the amount of adsorbed water. Second**,** inductively coupled plasma atomic emission spectroscopy (ICP-AES) and X-ray spectroscopy were used to determine the elemental composition**.** To prepare samples for both experiments, bulk vermiculite crystals were first thermally expanded and then ground into powders with grain-size of 61-74 μm (200-250 mesh).

The weight fraction of adsorbed water was determined by thermo-gravimetry. The vermiculite powders (200 mg) were first dried at 80 ^{o}C for 24 h and then weighed. This yielded a 4.9% (9.8 mg) weight loss. Then the sample was further dried at 250 ^{o}C for another 24 h. This resulted in a 14.3% (28.6 mg) weight loss. Following the literature, the first weight loss at 80 ^{o}C is attributed to the surface adsorbed water whereas the 14.3% loss at 250 ^{o}C to the interlayer water[3,4]. This yields a total water mass fraction of 19.2%. The thermo-gravimetry behavior of our samples was consistent with that of typical vermiculites[3,4].

We then determined the elemental composition of our vermiculite via ICP-AES and X-ray spectroscopy. The interlayer cation composition was determined via ICP-AES. To that end, we extracted the cations via ion exchange. Vermiculite powders (400 mg) were dispersed in 1.0 M LiCl (100 mL) and the dispersion was stirred at 80 ^{o}C for 24 h. This served to exchange native cations for Li. The suspension was then centrifuged to yield precipitated vermiculite particles and the supernatant (i.e. the dissolved species). This procedure was repeated three times on the precipitate to ensure all interlayer cations were exchanged. The collected supernatants were combined, diluted with 2% HNO_3, filtered through a nylon membrane (0.20 μm pores) and analyzed by ICP-AES. The detected interlayer metal cation mass fractions were calculated to be 2.7% K^{+} (K_2O: 3.26%), 6.45% Mg^{2+} (MgO: 10.75%), 3.01% Al^{3+} (Al_2O_3: 5.68%), 1.97% Fe^{3+} (Fe_2O_3: 2.81%). This is consistent

with the composition of typical vermiculites[5]. After this, we turned our attention to determining the composition of the aluminosilicate slabs. To that end, the precipitate from the previous measurement was washed three times by re-dispersing it in DI water and then dried at 80 ^{o}C for 24 h. The collected undissolved powders were weighed and analyzed via energy dispersive X-ray spectroscopy. This revealed that the powders were composed of Si, Al and O, indicating that they are the Si-O/Al-O layers. They were then weighed and found to represent 54.9% mass fraction – again consistent with that of the typical vermiculite[6]. Combined, the thermo-gravimetry and ICP-AES analysis account for 96.6 wt% of the vermiculite. The additional, 3.4% is attributed to ignition and other type of losses during processing as well as possible traces of other elements.

Device fabrication

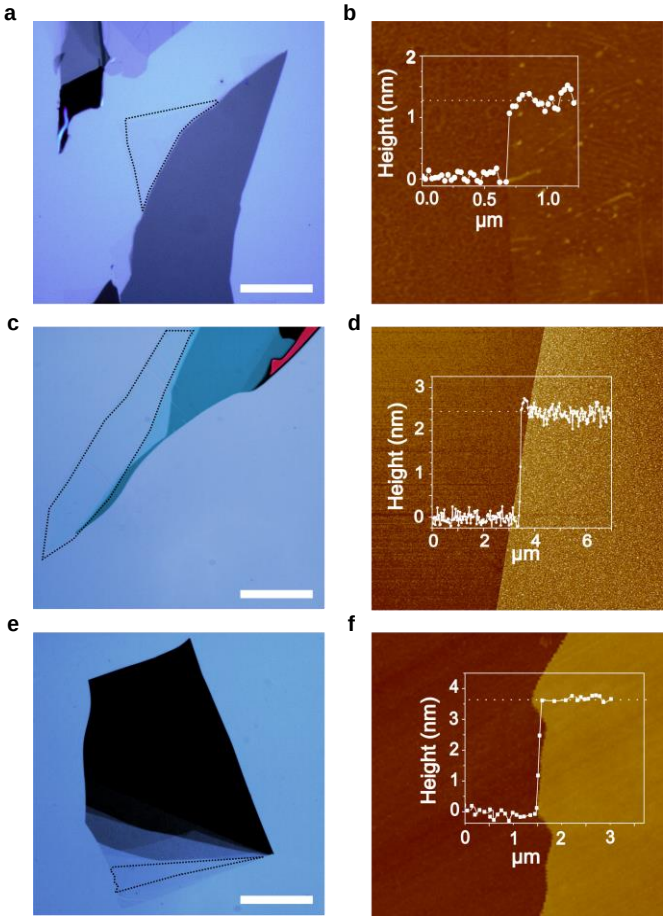

Supplementary Figure 1 | Flake preparation. Left panels show optical images of mica flakes. The areas marked with dark lines are mono- (a), bi- (c) and tri-(e) layers. Scale bars, 25 μm. Right panels show AFM images of the crystal edge for the images to the left. Insets in each panel show the height profile of the crystal edge, demonstrating that the crystal are 1-, 2- and 3-unit-cell thick.

The device fabrication process starts with micromechanical exfoliation of the crystals using the dry-transfer technique[7]. Micas can be exfoliated into flakes with precisely controlled thickness**.** Supplementary Fig. 1 shows optical and AFM images of three mica crystals that are 1, 2 and 3 unit-cell thick. The number of aluminosilicate monolayers in the crystals were unambiguously found

using AFM images and comparing the height the crystal edge (h) with the size of the mica unit cell ($c \approx 10$ Å)[8]. Our analysis also took into account the presence of adsorbed species. Large-area monolayer flakes could be isolated from vermiculite. On the other hand, for muscovite, bilayer crystals were the thinnest that could be isolated, which is consistent with stronger interlayer bonding for muscovite[9].

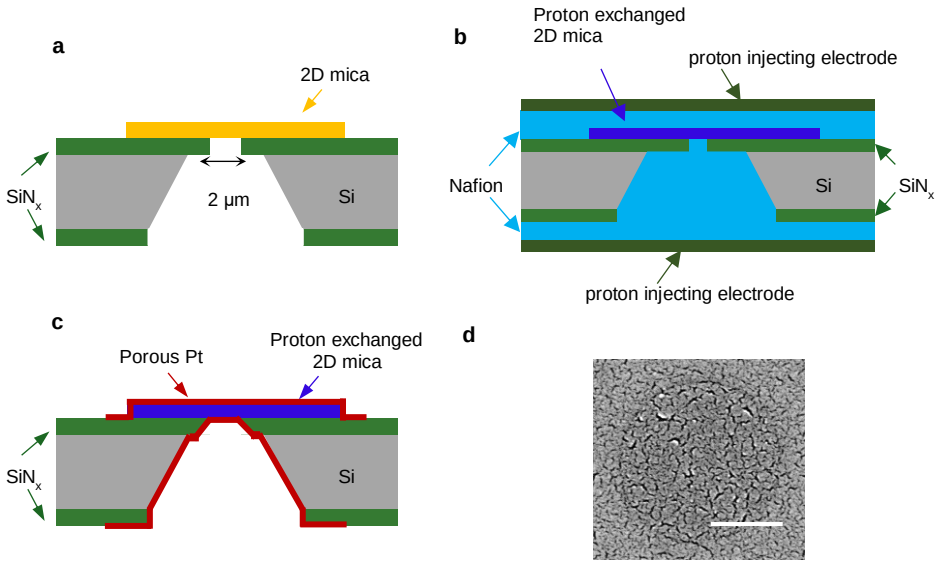

Supplementary Figure 2 | Device fabrication. a, Schematic of suspended mica devices. b, Schematic of Nafion-coated devices. c, Schematic of Pt-coated devices. d, Electron micrograph of one of our Pt- coated mica devices, top view. The darker circle discernible in the image corresponds to the aperture in the SiN_x substrate over which the mica crystal was suspended. Scale bar, 1 µm.

The next step in the fabrication process was to suspend the exfoliated atomically-thin crystals over microfabricated holes etched in free-standing silicon nitride membranes (Supplementary Fig. 2). To this end, we followed the recipe described in the previous report[10]. The devices were then proton-exchanged. They were immersed for ~1 hour in a heated (~80 ˚C) 10 mM acetic acid solution, thoroughly rinsed with deionized water, left to dry in air and then heated at ~150 ˚C to remove remnant moisture. If working with non-exchanged devices, we skipped this step. From this point, the fabrication process differed for Nafion-coated and Pt-coated devices. Nafion-coated devices were fabricated by drop-casting a Nafion solution (5% Nafion; 1100 EW) on both sides of the suspended mica membrane and electrically contacting them with proton-injecting electrodes (PdH_x foil) – see Supplementary Fig. 2b. The whole assembly was then annealed in a humid atmosphere at 130 °C to crosslink the polymer. For Pt-coated devices, instead of coating them with Nafion, thin Pt films (~50 nm) were sputtered directly on both sides of the suspended mica membrane. By controlling the parameters of the sputtering process we obtained porous Pt films (Supplementary Fig. 2d).

Note the similarity of the proton-exchange process with the process involved in fabrication of Nafion-coated devices. In both cases, a heated proton-exchange electrolyte (either acetic acid or Nafion) is in direct contact with the suspended mica membrane. Because of this, all Nafion-coated devices became proton exchanged. To verify this, we fabricated suspended mica devices both proton-

exchanged (with acetic acid) and non-exchanged, as described above. These were assembled into Nafion-coated devices. The measured resistance of both devices was the same, which shows that both were proton-exchanged.

Devices for mass spectrometry were fabricated in essentially the same way as Nafion-coated devices. The mica was suspended over holes etched in SiN_x and proton exchanged. One side of the device was coated with Nafion and a proton injecting electrode as described above. However, the opposite side of the devices was not coated with Nafion but instead a porous Pt film was deposited on top. This Pt layer was required to close the electrical circuit and allowed H_2 to permeate through the porous film. See ref. [11] for further details.

Electrical and mass spectrometry measurements

For electrical measurements, the assembled devices were placed in a chamber with a controlled atmosphere of either H_2 at 100% H_2O relative humidity or, alternatively, ~10% humidity (see below). The *I-V* characteristics were measured with a *Keithley* SourceMeter 2636A at voltages typically varying between ±200 mV and using sweep rates <0.1 V min^{-1}. The resulting *I-V* characteristics were linear, which allowed us to extract the device resistance. It is important to notice that reporting our data in units of areal resistivity (Ω cm^2) rather than bulk resistivity (Ω cm) is central to avoid inconsistencies. The very definition of bulk resistivity (Ω cm) implies that the resistance should scale linearly with the thickness and, hence, cannot be applied to materials like micas, whose resistance scales exponentially with the number of crystal unit cells (*N*). The exponential scaling of proton transport was also observed for other 2D crystals[10].

In control experiments, we measured the resistance of devices with Nafion layers as described above but without a mica membrane. The areal resistivity of these devices was $R \sim 10^{-3}$ Ω cm^2, which is ~100 times smaller than that of our most conductive mica devices. This ensured that the electrical response was dominated by the mica membrane and that the Nafion and proton injecting electrode layers added negligibly little into the series resistance. In another set of control measurements, we checked that there was no leakage along the interface between mica and the SiN_x substrate. To rule this possibility out we measured devices where an SU-8 polymer clamp was used to seal the edges of the mica crystal. The resistance of such devices was found to be the same as those without SU-8 clamps, which shows that there was no interfacial leakage. Note that the found exponential dependence on the crystal thickness also rules out any measurable contribution of leakage currents.

For mass spectrometry measurements, devices were clamped with O-rings to separate two chambers: one filled with a gas mixture (10% H_2 in Ar, 100% humidity) and the other evacuated and connected to a mass spectrometer. The porous Pt layer faced the vacuum chamber whereas the Nafion layer faced the gas chamber. A dc voltage was applied across the mass-spectrometry devices, and both electrical current and hydrogen flow were measured simultaneously. The mass spectrometer used

was an Inficon UL200. As a reference, we measured similar devices prepared as described above but without a mica membrane. For a given voltage bias, both proton and H_2 flows were much larger than those for the mica devices. However, the ratio of the H_2 flux to the proton current remained the same given by Faraday's law of electrolysis, as dictated by 100% charge-to-mass conservation (see ref. [11] for further details).

STEM measurements

Ion exchange in micas was studied using scanning transmission electron microscopy (STEM). Cs was chosen as the exchange ion because it is easily imaged by STEM. Note that ion exchange takes place both in the interlayer space and on the cleaved basal surfaces of mica. To prepare specimens to study interlayer Cs-exchange, we mechanically exfoliated micas on a Si substrate. Two of such substrates were then pressed against each other such that a mica crystal was sandwiched in between them. The Si-mica-Si structure was bound together with epoxy and then mechanically polished using an automatic mechanical polishing instrument (Allied MultiPrep). To perform the Cs exchange, the specimens were immersed in a 0.1 mol L^{-1} $CsNO_3$ for a week and then rinsed in ethanol. On the other hand, to prepare specimens to study surface Cs-exchange, mechanically exfoliated micas were suspended over a hole etched in a free standing SiN_x membrane. The devices were immersed in the same $CsNO_3$ solution for about an hour to perform the Cs-exchange.

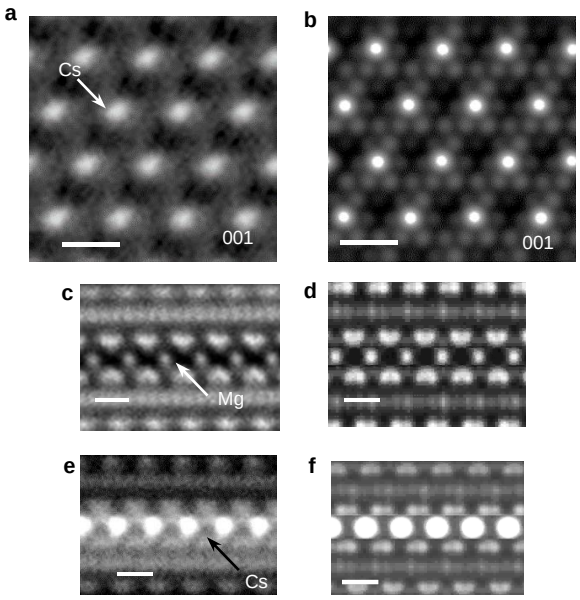

Supplementary Figure 3 | Ion lattices as seen in STEM and DFT simulations. a, High-angle annular bright-field (HAABF) scanning transmission electron microscopy (STEM) plan view image of Cs-exchanged bilayer vermiculite. b, DFT simulation of image in (a). c, Cross-sectional HAABF-STEM image of natural vermiculite. The exchangeable ion is Mg. d, DFT simulation of image in (c). e, Cross-sectional HAABF-STEM image of Cs-exchanged vermiculite. f, DFT simulation of image in (e). All scale bars, 0.5 nm.

STEM imaging was performed using a probe-side aberration-corrected FEI Titan G2 80-200 kV operated at 200 kV. Images were collected using a convergence angle of 21 mrad and a high angle annular dark-field (HAADF) detector with an inner (outer) collection angle of 48(196) mrad, and a probe current of 12 pA. The Cs ions in the devices arranged in the crystalline pattern that agrees with our DFT simulations (Supplementary Fig. 3).

Absence of lattice defects in proton-exchanged micas

Micas are chemically very robust, and all previous studies have found that the proton-exchange process does not damage micas' aluminosilicate layers[12–20]. In our case, no damage was also expected, especially given the mild solution used for proton exchange (acetic acid). Nevertheless, we corroborated the stability of our micas by intentionally trying to dissolve them. If our acetic acid solution was heated to 80 °C, the mica crystals could not be dissolved, regardless of how many days the mica was left inside the solution. We only succeeded in dissolving micas by using an aggressive 1 M nitric acid solution at ~300 °C under reflux conditions for over one day. This result rules out any significant damage to our proton-exchanged mica devices. To further investigate if our mild acetic acid treatment could introduce any microscopic defects in the studied mica membranes, the proton-exchanged membranes were imaged using AFM and TEM. Supplementary Fig. 4a,b show that no defects could be detected with the AFM. The membranes were also inspected with TEM. This allowed atomic-scale resolution images over areas of several nanometers in size (note that Fig. 4c is a TEM rather STEM micrograph). Even with this resolution, no pinholes could be detected. These results are consistent with our mass spectrometry measurements, which ruled out defects of dimensions comparable to hydrogen molecules.

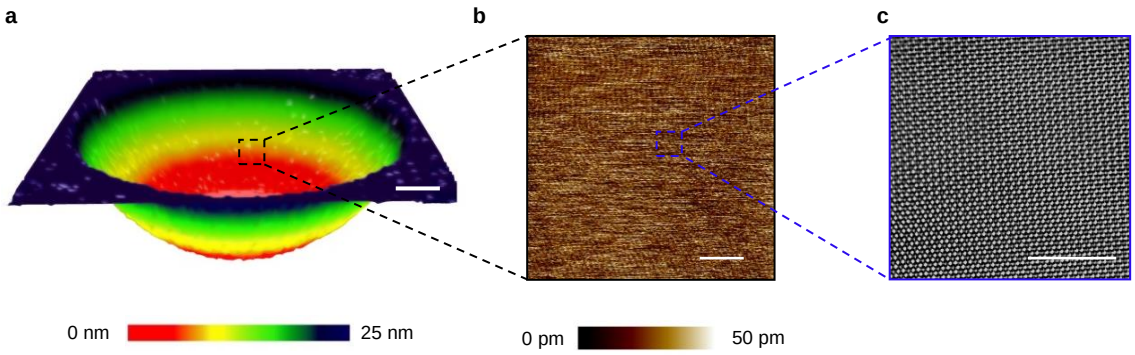

Supplementary Figure 4 | Absence of lattice defects in proton-exchanged micas. a, Atomic force microscopy image of a suspended proton-exchanged mica device. Scale bar, 500 nm b, AFM image zoomed in from the area marked in (a). Scale bar, 100 nm. c, Transmission electron microscopy image of the area in (b). Scale bar, 5 nm.

Dependence of proton transport on humidity and hydrogen pressure

The dependence of proton conductance on hydrogen content and humidity was studied using porous-Pt coated devices. Before discussing the experimental results, it is important to note that the Pt films in these devices are effectively infinite reservoirs of protons. First, Pt films can store large amounts of hydrogen, about one H atom per Pt atom[21]. Second, the Pt films cover an area ~10^7 times larger than the studied mica membranes (~3 μm^2). The latter suggests that, even at very low H_2 pressures, the Pt films would inject enough protons to saturate the mica, acting as infinite proton reservoirs. A similar argument applies for humidity. Despite the expectations, we investigated the dependence of conductance on both hydrogen pressure and humidity.

Let us discuss the humidity dependence first. Pt-coated devices were placed in a chamber with either dry (~10% humidity) or humid (100% humidity) H_2 atmosphere. Supplementary Fig. 5a shows that in humid hydrogen, both G_x and G_n were about 6 times larger than in the dry atmosphere. This increase could be reversed by changing the atmosphere back to dry. Next, the effect of hydrogen pressure was investigated. The devices were placed in a chamber at dry conditions and the H_2 partial pressure was gradually changed. Simultaneously, the proton current was measured as a function of time at a fixed voltage bias. Supplementary Fig. 5b shows that the current across the sample was clearly correlated with the hydrogen pressure. When the hydrogen pressure in the chamber increased from 1 mbar to 1 bar, the current across the sample increased by a factor of about 3. This increase could be reversed by reducing the hydrogen partial pressure to its original low value. These experiments demonstrate that proton conductance through our micrometer-size micas depended on both H_2 pressure and humidity.

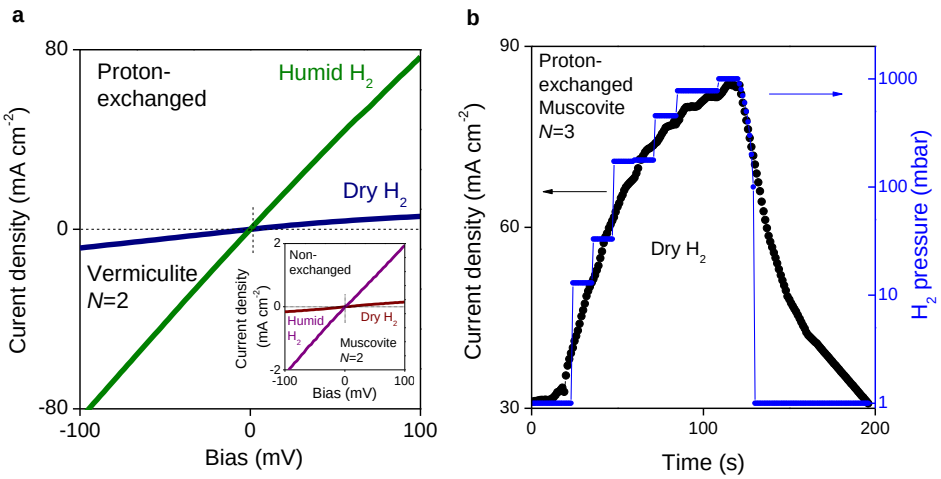

Supplementary Figure 5 | Dependence of proton transport on humidity and hydrogen pressure. a, *I-V* characteristics of a proton-exchanged mica in humid hydrogen (green) and dry hydrogen (blue) atmospheres. Inset: *I-V* characteristics of non-exchanged mica in humid hydrogen (purple) and dry hydrogen (brown) atmospheres. b, Left y-axis: current density recorded as a function of time for a proton-exchanged mica (black symbols). Applied bias, 1 V. Right y-axis: H_2 partial pressure inside the measurement chamber as a function of time (blue). Both data sets were recorded simultaneously.

Reproducibility of Arrhenius plots

Supplementary Fig. 6 shows that the Arrhenius plots $G_x(T)$ were highly reproducible both during heating and cooling cycles and for different devices. The activation energies in $G_x(T)$ were also reproducible for different devices. Below T_p, we found E_p = 0.2±0.05 eV and, above T_p, E_e = 0.83±0.06 eV. The experimental error in these measurements was similar to that in proton-transport measurements made using other 2D crystals[10]. The transition temperature itself was also reasonably reproducible for different devices (see Supplementary Fig. 6b) with T_p = 215±35˚C for muscovite and 170±10˚C for vermiculite.

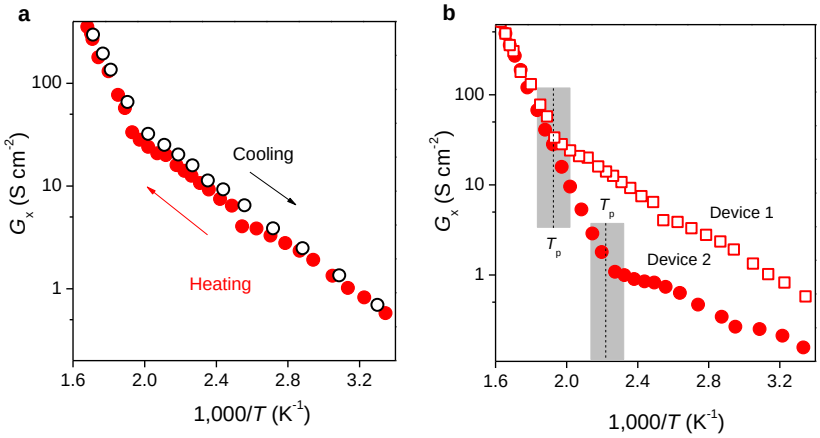

Supplementary Figure 6 | Reproducibility of Arrhenius plots. a, Arrhenius plots of G_x from a bilayer muscovite device (Pt contact) during heating (red) and cooling (black) cycles. b, Arrhenius plots of G_x from two bilayer muscovite devices (Pt contact). The transition temperature (T_p) for both devices is highlighted in grey.

Density functional theory calculations

Proton transport through micas was studied using density functional theory (DFT). The calculations were performed using the projector augmented wave (PAW) method, as implemented in the Vienna *ab-initio* Simulation Package[22–24] (VASP). To describe the electron exchange and correlation, the Perdew-Burke-Ernzerhof form of the generalized gradient approximation was adopted[25]. The van der Waals force, important for the layered materials, was taken into account by using the DFT-D2 method of Grimme[26]. The calculations were performed using the following parameters. The kinetic energy cutoff of the plane-wave basis set was at 500 eV in all calculations. The total energy difference between the sequential steps in the iterations was taken 10^{-5} eV as our convergence criterion. The convergence for the Hellmann-Feynman forces per unit cell was taken to be 10^{-4} eV Å^{-1}. Gaussian smearing of 0.05 eV was used.

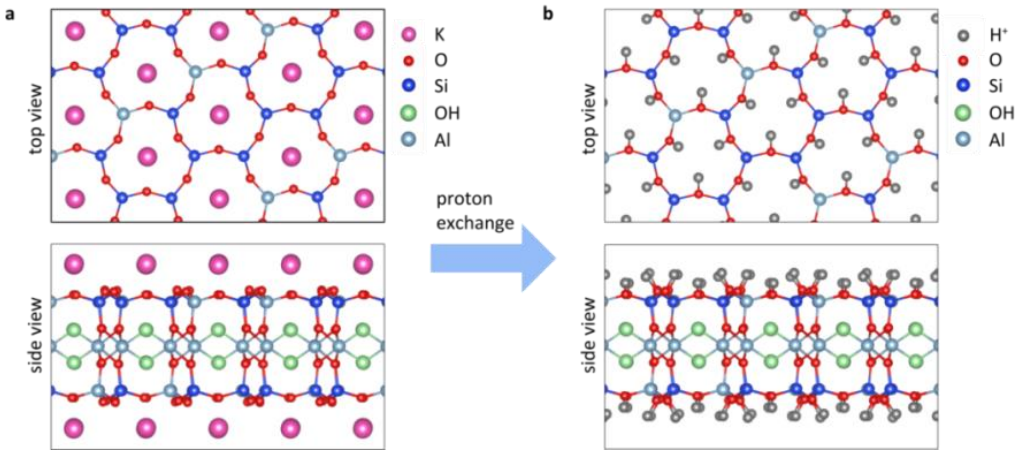

Supplementary Figure 7 | Schematic illustration of proton exchange in muscovite layer. a, Top and side views of non-exchanged muscovite. **b,** Top and side views of proton-exchanged muscovite layer. Each K ion is substituted by 3 protons.

We started by studying the proton exchange process itself. To that end, the energy of a monolayer muscovite crystal was calculated; first with the native ions (assuming K^+ in this case) and then with those K ions exchanged by protons (Supplementary Fig. 7a). We found that each K ion was substituted by 3 protons. Unlike K^+ that bonds to the center of the hexagonal ring in the basal plane, we found that protons bond to all the six oxygen atoms of the hexagonal ring, three for each exchanged K ion (see Supplementary Fig. 7b). The change in energy due to the proton exchange process was calculated using the formula: $\Delta E = E_s + nE_{H^+} - (E_{ex} + E_K)$ where E_s, E_{ex}, E_{H^+}, and E_K are the total energies of the mica slab, the ion-exchanged slab, a single proton, and a single K ion, respectively. This calculation revealed that the proton exchange process was energetically favorable, leading to a gain ΔE=0.92 eV per K ion.

Next, we calculated the minimum energy route for a proton as it transferred through proton-exchanged mica. To that end, a proton was moved in the perpendicular direction (z) to the mica basal plane in steps of ~0.5 Å. Near the minima, we decreased the step further down to ~0.25 Å. At each step, the proton was fixed only in the z-position but allowed to relax freely in the other two directions. This procedure ensured that the minimum energy trajectory was found. Supplementary Fig. 8a shows the proton trajectory (black dots) as found from such calculations. The proton initially moves along the center of the hexagonal ring. Later it moves towards the first of the two hydroxyl (OH^-) groups (green balls) inside the aluminosilicate layer. The proton is then transferred from one hydroxyl group to the next and finally exits through the hexagonal ring on the opposite side of the mica. Supplementary Fig. 8b shows the energy profile associated with this trajectory.

The energy profile is attractive and consists of six local minima. The local minima at both surfaces of the basal plane were found to be physisorption-like with a proton adsorption energy of ~0.37 eV. The second set of minima corresponds to a proton that resides at the interstitial void between the sublayers of Si and Al atoms and is bonded to the hydroxyl group. The corresponding adsorption energy is ~0.51 eV. The lowest energy minima are reached as the proton bonds to the oxygen atoms

at the same sub-plane as the hydroxyl group. It should be pointed out that the energy difference between the lowest and the second lowest configurations is only ~0.06 eV. The existence of local minima inside the mica supports the hypothesis that protons jump along local traps as they transfer along the tubular channels. The calculations also allowed us to determine the activation energy barrier as the largest energy step along the trajectory. This approach leads to E~0.35 eV, which is in reasonable agreement with the experimentally found E_p≈0.2 eV. Even better agreement with the experiment can be expected if we take into account that the initial energy of incoming protons is lifted by zero-point oscillations at oxygen or Pt bonds[11,27].

Having studied proton transport through the mica lattice itself, let us also mention the role of adsorbed water on the surfaces of the aluminosilicate slabs. Water molecules are sterically excluded from the tubular channels of the mica lattice[13,28]. However, atomic force microscopy of water absorbed on proton-exchanged micas showed[29] that protons belonging to surface water molecules are attracted towards the OH groups inside micas' hexagonal rings (green balls in Supplementary Fig. 8). Therefore, protons of surface water slightly penetrate into the tubular channels trying to reach towards the OH groups inside mica[29]. In combination with our study, this result suggests that the first step in the proton transport mechanism for micas should be a proton (H^+) jump from surface H_3O^+ towards the OH^- groups inside.

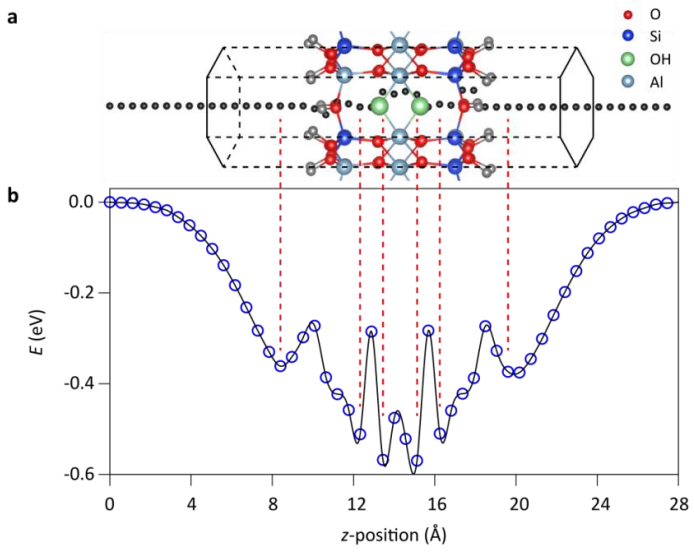

Supplementary Figure 8 | DFT calculation of proton transport through micas. **a**, Minimum energy path for H^+ transport through the basal plane of proton-exchanged muscovite. Localized H^+ after the proton-exchange process are shown by the grey balls to distinguish them from the translocating proton (black dots). **b**, Energy as function of the position of H^+. Local minima in the energy curve are found when H^+ is at the vicinity of hydroxyl groups and oxygen atoms. The red-dotted lines indicate positions of the translocating proton at the energy minima.

Having established the main ingredients of the mechanism of proton permeation through few-layer micas, it would be of interest in the future to consider the role of second-order structural features of aluminosilicate layers. For example, in trioctahedral micas (such as the studied vermiculite) the OH groups are oriented perpendicular to the basal plane whereas in dioctahedral micas (muscovite) they

are leaning out of the plane[30]. This orientation difference was shown to affect the exchange rates of interlayer ions[31] and, therefore, it is possible that this also has repercussions for proton transport (for example, by shortening the distance between proton jumps in vermiculite).

Potential for scaling up

Similar to the industrial techniques developed for graphene, we envisage two potential routes for scaling up mica-based proton membranes. The first one is growth of ultrathin aluminosilicate films on metal or other substrates. For graphene, this approach was shown to produce monolayer films on a true industrial scale[32]. Encouragingly, initial reports show that a similar approach can be implemented for micas[33]. Such few-layer films grown initially on a substrate can then be transferred onto a porous support to form mechanically robust, gas impermeable membranes – similar to those already demonstrated for graphene[32,34,35]. The second route is to produce mica laminates via liquid exfoliation of bulk clay crystals. This approach is capable of producing exceptionally thin laminates (below 10 nm)[36]. Liquid exfoliation of clay minerals has already been reported[37] and with further effort[36], it might be possible to fabricate ultrathin mica laminates that preserve the gas impermeability and proton conducting properties reported in our work.

Supplementary References

1. Christenson, H. K. & Thomson, N. H. The nature of the air-cleaved mica surface. *Surf. Sci. Rep.* **71,** 367–390 (2016).
2. Bailey, S. W. Micas. *Reviews in Mineralogy* **13,** Chapters 1,2 (1984).
3. Arguelles, A., Leoni, M., Blanco, J. A. & Marcos, C. Semi-ordered crystalline structure of the Santa Olalla vermiculite inferred from X-ray powder diffraction. *Am. Mineral.* **95,** 126–134 (2010).
4. Argüelles, A. *et al.* Chemical and physical characterization of iron-intercalated vermiculite compounds. *Phys. Chem. Miner.* **38,** 569–580 (2011).
5. Chambi-Peralta, M. M., Vieira Coelho, A. C., Machado de Souza Carvalho, F. & Toffoli, S. M. Effects of exchanged cation, acid treatment and high shear mechanical treatment on the swelling and the particle size distribution of vermiculite. *Appl. Clay Sci.* **155,** 1–7 (2018).
6. Wada, K., Kakuto, Y., Wilson, M. A. & Hanna, J. V. The chemical composition and structure of a 14 Å intergradient mineral in a Korean Ultisol. *Clay Miner.* **26,** 449–461 (1991).
7. Kretinin, A. V. *et al.* Electronic properties of graphene encapsulated with different two-dimensional atomic crystals. *Nano Lett.* **14,** 3270–3276 (2014).
8. Novoselov, K. S. *et al.* Two-dimensional atomic crystals. *Proc. Natl. Acad. Sci.* **102,** 10451–10453 (2005).
9. Gaines, G. L. The Ion-exchange Properties of Muscovite Mica. *J. Phys. Chem.* **61,** 1408–1413 (1957).
10. Hu, S. *et al.* Proton transport through one-atom-thick crystals. *Nature* **516,** 227–230 (2014).
11. Lozada-Hidalgo, M. *et al.* Sieving hydrogen isotopes through two-dimensional crystals.

Science **351,** 68–70 (2016).

12. Claesson, P. M., Herder, P., Stenius, P., Eriksson, J. C. & Pashley, R. M. An ESCA and AES study of ion-exchange on the basal plane of mica. *J. Colloid Interface Sci.* **109,** 31–39 (1986).
13. Alcantar, N., Israelachvili, J. & Boles, J. Forces and ionic transport between mica surfaces: Implications for pressure solution. *Geochim. Cosmochim. Acta* **67,** 1289–1304 (2003).
14. Schlegel, M. L. *et al.* Cation sorption on the muscovite (0 0 1) surface in chloride solutions using high-resolution X-ray reflectivity. *Geochim. Cosmochim. Acta* **70,** 3549–3565 (2006).
15. Lee, S. S., Fenter, P., Nagy, K. L. & Sturchio, N. C. Monovalent ion adsorption at the muscovite (001)-solution interface: Relationships among ion coverage and speciation, interfacial water structure, and substrate relaxation. *Langmuir* **28,** 8637–8650 (2012).
16. Lee, S. S., Fenter, P., Nagy, K. L. & Sturchio, N. C. Real-time observation of cation exchange kinetics and dynamics at the muscovite-water interface. *Nat. Commun.* **8,** 15826 (2017).
17. Ricci, M., Trewby, W., Cafolla, C. & Voïtchovsky, K. Direct observation of the dynamics of single metal ions at the interface with solids in aqueous solutions. *Sci. Rep.* **7,** 43234 (2017).
18. Bowers, G. M., Bish, D. L. & Kirkpatrick, R. J. Cation exchange at the mineral-water interface: H3O +/K+ competition at the surface of nano-muscovite. *Langmuir* **24,** 10240–10244 (2008).
19. Sides, P. J., Faruqui, D. & Gellman, A. J. Dynamics of charging of muscovite mica: measurement and modeling. *Langmuir* **25,** 1475–1481 (2009).
20. Pashley, R. M. DLVO and hydration forces between mica surfaces in Li+, Na+, K+, and Cs+electrolyte solutions: A correlation of double-layer and hydration forces with surface cation exchange properties. *J. Colloid Interface Sci.* **83,** 531–546 (1981).
21. Candy, J. P., Fouilloux, P. & Renouprez, A. J. Hydrogen adsorption on platinum catalysts: Quantitative determination of the various species population. *J. Chem. Soc. Faraday Trans. 1* **76,** 616–629 (1980).
22. Kresse, G. & Hafner, J. Ab Initio Molecular Dynamics of Liquid Metals. *Phys. Rev. B* **47,** 558 (1993).
23. Kresse, G. & Joubert, D. From ultrasoft pseudopotentials to the projector augmented-wave method. *Phys. Rev. B* **59,** 1758–1775 (1999).
24. Kresse, G. & Furthmüller, J. Efficient iterative schemes for ab initio total-energy calculations using a plane-wave basis set. *Phys. Rev. B* **54,** 11169–11186 (1996).
25. Perdew, J. P., Burke, K. & Ernzerhof, M. Generalized gradient approximation made simple. *Phys. Rev. Lett.* **77,** 3865–3868 (1996).
26. Grimme, S. Semiempirical GGA-type density functional constructed with a long-range dispersion correction. *J. Comput. Chem.* **27,** 1787–1799 (2006).
27. Hu, S. *et al.* Transport of hydrogen isotopes through interlayer spacing in van der Waals crystals. *Nat. Nanotechnol.* **13,** 468–472 (2018).

28. Pashley, R. M. Hydration forces between mica surfaces in aqueous electrolyte solutions. *J. Colloid Interface Sci.* **80,** 153–162 (1981).
29. Fukuma, T., Ueda, Y., Yoshioka, S. & Asakawa, H. Atomic-Scale distribution of water molecules at the mica-Water interface visualized by three-Dimensional scanning force microscopy. *Phys. Rev. Lett.* **104,** 016101 (2010).
30. Giese, R. F. HYDROXYL ORIENTATIONS IN 2:1 PHYLLOSILICATES. *Clays Clay Miner.* **27,** 213–223 (1979).
31. Bassett, W. A. Role of hydroxyl orientation in mica alteration. *Bull. Geol. Soc. Am.* **71,** 449–456 (1960).
32. Bae, S. *et al.* 30 inch Roll-Based Production of High-Quality Graphene Films for Flexible Transparent Electrodes. *Nat. Nanotechnol.* **5,** 574–578 (2010).
33. Boscoboinik, J. A., Yu, X., Shaikhutdinov, S. & Freund, H. J. Preparation of an ordered ultra-thin aluminosilicate framework composed of hexagonal prisms forming a percolated network. *Microporous Mesoporous Mater.* **189,** 91–96 (2014).
34. Wang, L., Williams, C. M., Boutilier, M. S. H., Kidambi, P. R. & Karnik, R. Single-Layer Graphene Membranes Withstand Ultrahigh Applied Pressure. *Nano Lett.* **17,** 3081–3088 (2017).
35. Wang, L. *et al.* Fundamental transport mechanisms, fabrication and potential applications of nanoporous atomically thin membranes. *Nat. Nanotechnol.* **12,** 509–522 (2017).
36. Yang, Q. *et al.* Ultrathin graphene-based membrane with precise molecular sieving and ultrafast solvent permeation. *Nat. Mater.* **16,** 1198–1202 (2017).
37. Nicolosi, V., Chhowalla, M., Kanatzidis, M. G., Strano, M. S. & Coleman, J. N. Liquid exfoliation of layered materials. *Science* **340,** 1226419 (2013).

Chapter 8

Ion-Exchange Properties in Few-Layer Clays

Bulk clay and mica materials are known ion-exchangers, discussed in Chapter 4. Here, in this present chapter, we report the results of a study on the ion-exchange properties of few-layer clays. Isolating selected clay crystals and S/TEM imaging the ion-exchange process in a time 'stepwise' manner is a novel approach. Secondly, we report high-resolution images of the ion distribution on the surface of mica minerals, resolving ion-binding sites as we combine bright and dark-field images. Thirdly, we present restacked mica layers at a twisted angle, creating ion superlattices modulated by the mica moiré. This last observation provides an extra degree of freedom, gaining atomic-scale spatial control of ions at solid-solid interfaces. This was not experimentally explored until now. We believe that the work is of interest in a wide range of disciplines. For example, the observation of ion superlattices will interest academics working on the electronic and optical properties of 2D heterostructures. The electron microscopy and sample fabrication techniques we reported are interesting from a microscopy perspective. The sub-angstrom resolution images of individual ions provide a fresh perspective into as-of-yet-unanswered questions about the layered materials inspired by nature, which remain of great interest to communities (e.g., geologists, geochemists and environmental scientists) beyond those targeted.

The results presented in Chapter 8 are reported in a manuscript submitted to Nature Materials for review, titled: "Ion exchange in atomically thin clays and micas". Y.-C.Z operated the TEM system with L.M in assistance. L.M and G.-P.H fabricated the samples. L.M performed AFM and XRD measurements. L.M and Y,-C.Z carried out data analysis with the help from N.C, Y-.C.W and D.H. F.M.P, C.B and S.M carried out the theoretical modelling. N.C, Y-.C.W and D.H performed TEM image processing. R.G, S.S and K.S.N helped with interpretation. Y.-C.Z, S.J.H and M.L-.H wrote the manuscript. All authors contributed to discussions.

Ion exchange in atomically thin clays and micas

Yi-Chao Zou[1], Lucas Mogg[2,3], Guang-Ping Hao[2,3], Nick Clark[1,2], Cihan Bacaksiz[4], Slavisa Milanovic[4], Yi-Chi Wang[1], David G. Hopkinson[1,2], Roman Gorbachev[2,3], Samuel Shaw[5], Kostya S. Novoselov[2,3], Francois M. Peeters[4], Marcelo Lozada-Hidalgo[2,3]*, Sarah J. Haigh[1,2]*

[1]Department of Materials, The University of Manchester, Manchester M13 9PL, UK

[2]National Graphene Institute, The University of Manchester, Manchester M13 9PL, UK

[3]Department of Physics and Astronomy, The University of Manchester, Manchester M13 9PL, UK

[4]Departement Fysica, Universiteit Antwerpen, Groenenborgerlaan 171, B-2020 Antwerp, Belgium

[5]Research Centre for Radwaste Disposal and Williamson Research Centre, School of Earth and Environmental Science, The University of Manchester, Manchester M13 9PL, UK

Clays and micas are receiving significant attention as materials that, in their atomically thin form, could allow for novel proton conductive[1], ion selective[2-4] or osmotic power generation[5-7] membranes. The interest stems from these materials' ability to exchange ions. However, this property remains largely unexplored in few-layered samples. Here we use atomic-resolution scanning transmission electron microscopy to study the dynamics of the process and reveal the binding sites of individual ions in atomically thin and artificially restacked clays and micas. Imaging ion exchange after different exposure time and for different crystal thicknesses, we find that the ion diffusion constant, *D*, for the interlayer space of atomically thin samples is $\gtrsim 10^5$ times larger than in bulk crystals and approaches its free value in water. *D* can also increase $\gtrsim 10^7$ times if the mica layers are twisted and restacked, yielding periodic cation islands controlled by the moiré superlattice dimensions. We attribute these findings to the modification of interlayer binding energy, which is weaker in both atomically thin and restacked materials. The enhanced ion exchange properties reported here suggest the potential of exfoliation for improving the performance of mica and clay materials used in many applications, including radioactive waste treatment[8] and water decontamination[9,10].

Clays and micas are minerals that consist of aluminosilicate layers with cations both adsorbed on the basal plane surfaces and residing in the space between the layers. The native cations (typically K^+ and Mg^{2+}) can be exchanged for others when the material is exposed to electrolytes *via* a process known as ion exchange[11-15]. The crystals are relatively easy to exfoliate along the basal planes, producing high aspect ratio atomically thin sheets that have been the focus of renewed research interest. Recent experiments demonstrated that exchanging the native cations for protons in atomically thin micas yields highly conductive proton transport membranes that are capable of operation at temperatures where current materials fail[1]. Exfoliated two-dimensional (2D) clay or

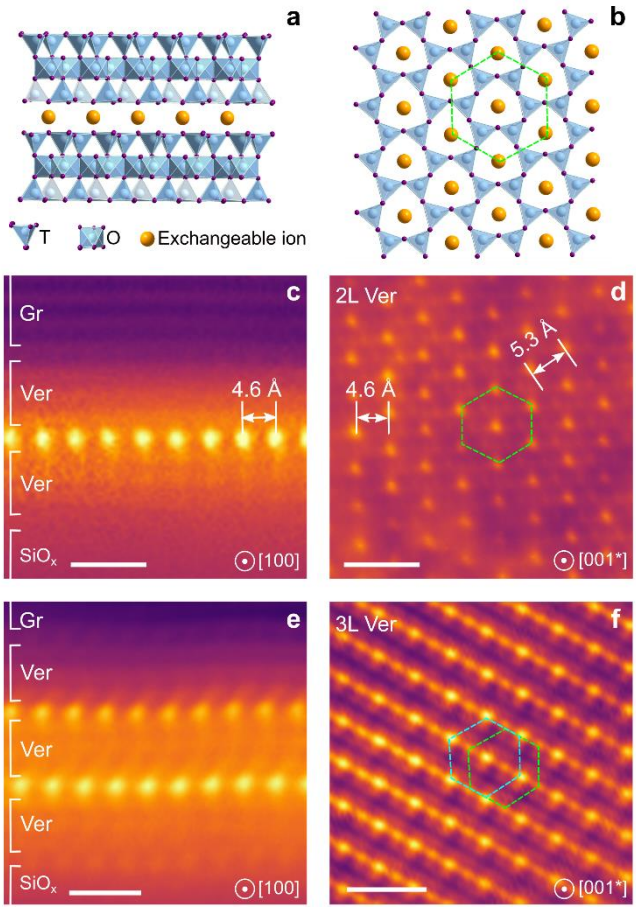

Figure 1| Interlayer cations in exchanged clays and micas. a, Cross-sectional atomic model of a typical pristine bilayer (2L) clay or mica viewed along the layers. The aluminosilicate tetrahedral-octahedral-tetrahedral, (TOT) layers are connected by exchangeable ions (e.g. K^+ and Mg^{2+}). The weakly bonded surface cations have been omitted for clarity. **b**, Plan view atomic model showing the interlayer ions with adjacent top and bottom T layers consisting of aluminosilicate (Al-Si-O) hexagonal rings. The exchangeable interlayer ions form a quasi-hexagonal lattice (marked with the green hexagon), residing in the cavities of both top and bottom Al-Si-O rings which are naturally aligned. **c**, **e** Cross-sectional high-angle annular dark field (HAADF)-STEM images of Cs-exchanged **c,** bilayer and **e**, trilayer (3L) vermiculite (Ver). The interlayer ions are exchanged with Cs^+, visible as rows of bright dots sandwiched by the aluminosilicate layers. The atomically thin vermiculite is encapsulated between graphite (Gr) and SiO_x. **d, f** Plan view HAADF-STEM images of Cs-exchanged **d,** bilayer and **f,** trilayer vermiculite. A single interlayer of Cs^+ ions forms a quasi-hexagonal lattice (marked with the green hexagon in **d**) while the offset between two superimposed planes of interlayer Cs ions creates a linear pattern (**f**). All scale bars, 1 nm.

mica crystallites can also be restacked to produce laminate membranes and composites, *via* similar fabrication methods as those used for graphene oxide[16,17]. The space between the restacked crystallites constitute channels with one of their dimensions comparable or narrower than the Debye length of ions in common electrolytes[3,4]. Water and ion transport through these channels depends critically on the surface charge and ions[10,18]. This allows for the use of clays and micas' ion

exchange properties to influence electro-kinetic phenomena in the channels, such as osmotic power generation[5-7] and ion selective transport[2-4]. However, despite its importance to the application of these materials, ion exchange in atomically thin clays and micas remains largely unexplored. In this Letter, we used advanced aberration corrected scanning transmission electron microscopy (STEM) to study this phenomenon. STEM, unlike the more commonly used techniques of atomic force microscopy or X-ray diffraction[11-14], reveals the local binding environment of exchanged ions with sub-angstrom resolution, enabling understanding of the ion exchange process both between the layers and on the surface of these materials.

Atomic resolution STEM investigations of Cs^+ ion exchange were performed for atomically thin muscovite mica, biotite mica and vermiculite clays. These crystals were chosen because, in the bulk, their ion exchange rates differ by many orders of magnitude[19]. Studying them should allow for the investigation of the dynamics phenomena over a wide timescale in 2D micas and clays. On the other hand, Cs^+ was chosen because its radiocaesium (^{137}Cs) is an environmentally challenging (half-life = 30.2 years) fission product, which has led to wide spread land contamination following nuclear incidents[20]. Its large atomic number also provides bright contrast in high-angle annular dark field (HAADF) STEM and is therefore readily differentiated from the native K^+ and Mg^{2+} ions. To determine three-dimensional lattice information for these atomically thin materials, we have combined both cross-sectional (Fig. 1a) and plan view STEM imaging (Fig. 1b). For cross-sectional imaging, materials were mechanically exfoliated onto oxidized silicon substrates and immersed in a $CsNO_3$ electrolyte for a period from one second to several months to enable ion exchange (Fig. S1). The crystals were then covered by a graphite flake and Pt protective strap, so that thin slices of this assembled stack could be extracted *via* focused ion beam milling[21]. To produce plan view specimens, mechanically exfoliated monolayer, bilayer (2L) and trilayer (3L) crystals were transferred over holes in SiN_x TEM grids and immersed in $CsNO_3$ electrolyte as described above. For further information on sample preparation see SI section 2.1.

Ion exchange can take place both on the outer surface and in the interlayer space of clays. We focus on the interlayer exchange for the next few paragraphs. Fig. 1 shows HAADF-STEM images taken from a typical Cs-exchanged atomically thin clay (vermiculite in this case). Cs^+ ions are visible as rows of bright spots between the aluminosilicate layers. We observe one and two of these rows in bilayer and trilayer cross-sectional specimens, respectively (Fig. 1c,e). Because of the atomic thinness of the samples, these observations can be complemented with plan view imaging, which resolves the lateral distribution of the ions (Fig. 1d,f). These images confirm that the exchanged ions form fully occupied interlayer planes – one in 2L samples, two in 3L – with each layer having quasi-hexagonal symmetry (with an in-plane Cs lattice constant of 5.3 Å). In a pristine trilayer sample, the projected arrangement of the two Cs^+ planes appear as a linear pattern formed by a superposition of two of these quasi-hexagonal Cs^+ lattices (Fig. 1f and SI section 5).

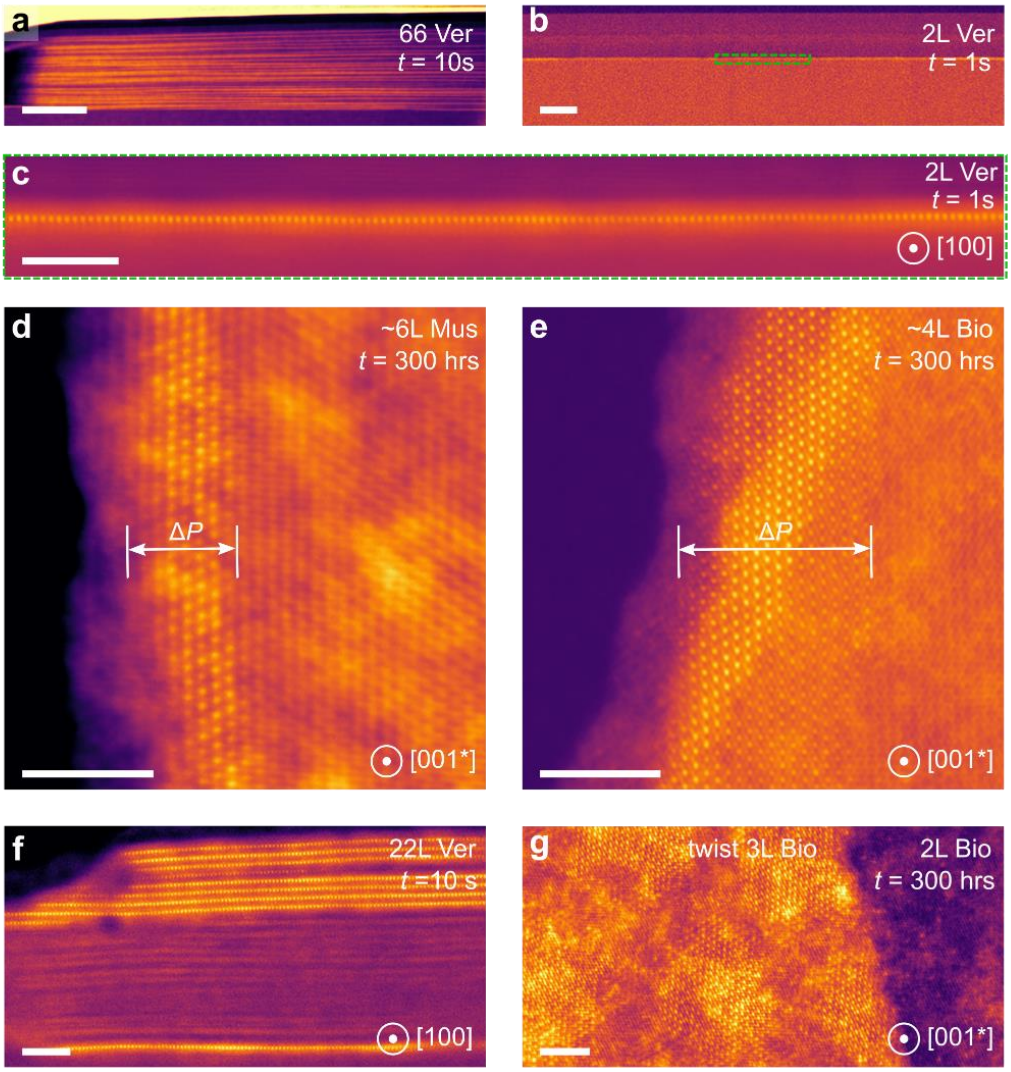

Figure 2| Measuring the interlayer ion exchange penetration distance for flakes of different thickness. **a**, Cross section HAADF-STEM of a multilayer (66L) vermiculite (Ver) exchanged for 10 s. The interlayer spaces exchanged for Cs^+ are visible as bright horizontal lines. $<\Delta P^2>$ is estimated from the average Cs penetration for all interlayer spaces in the crystal (see Fig. S5). Scale bar, 50 nm. **b**, Cross section HAADF-STEM image of 2L vermiculite encapsulated between graphite and the SiO_x substrate. The specimen was Cs-exchanged for 1 s. For this specimen, we found $\Delta P \approx 20$ µm (see Fig. S5d for optical image), which is too long to display in this STEM figure. Scale bar, 50 nm. **c**, Corresponding magnified view for the region marked by a green rectangle in **b,** showing a bright line of Cs ion columns extending the full width of the specimen. Scale bar, 5 nm. **d**, **e** Plan view HAADF-STEM images of **d,** few-layered muscovite (Mus) and **e,** few-layered biotite (Bio), both Cs-exchanged for 300 hrs. Cs^+ ions are visible as bright yellow dots. The largest penetration depth of Cs into the interlayer space in the crystal (ΔP) is indicated, yielding $D_{6L\text{-}Mus} << 10^{-11}$ µm^2 s^{-1}, and $D_{4L\text{-}Bio} << 10^{-11}$ µm^2 s^{-1}. Scale bars, 5 nm. **f**, Cross section HAADF-STEM image taken from a 22L vermiculite (exchanged for 10s) showing greater ion exchange associated with step edges and sub-surface layers. Scale bar, 5 nm. **g**, Plan view HAADF-STEM image taken from a biotite (treated for 300 hours). Right side, 2L region with no interlayer Cs^+ found. Left side, a 3L twisted region (formed by

restacking a monolayer onto the 2L region) with many interlayer Cs^+ ion islands visible. Scale bar, 5 nm.

The speed of ion exchange is a crucial parameter for the applications mentioned in the introduction. However, ion-exchange speeds in the interlayer space of clays are still the subject of debate, even for bulk materials[19,22], and are completely unknown in 2D specimens. To gain quantitative insights into this parameter, we focused on vermiculite – the fastest bulk ion exchanger of the crystals in this study. Cross-section samples with crystals of various thicknesses were subject to $CsNO_3$ solution treatment for different lengths of time (t). STEM images of these samples yielded 'snapshots' of the exchange process. These allow for direct measurement of the penetration distance of Cs^+ into the crystal, ΔP, and estimation of the ion diffusion coefficient, D, as $D \approx \Delta P^2/2t$ (see SI section 6)[12,15,23]. To our surprise, bilayer samples, with large penetration distances of around 20 µm, were fully exchanged after only one second of $CsNO_3$ solution treatment (Fig. 2b,c, SI Fig. S5d). This exceptionally fast exchange yields the ion exchange diffusion constant of bilayer vermiculite $D_{2L\text{-}Ver} \gtrsim 10^2$ µm^2 s^{-1} – only ~10 times slower than the diffusion coefficient of Cs^+ in water[24]. Similar measurements for trilayer vermiculite showed similar interlayer diffusivity values ($D_{3L\text{-}Ver}$>30 µm^2 s^{-1}, see SI Fig. S5d,e). Note that these values are only lower bounds for D, since it is not possible to fabricate atomically thin clay flakes with larger penetration distances nor reduce the duration of $CsNO_3$ solution treatment below one second. Nevertheless, D in these samples reaches close to its limiting value in free water.

We compare these Cs^+ diffusivity values for few-layer vermiculite with that of bulk crystals (>20 layers thick) which gave $D_{ver} \approx 10^{-3}$ µm^2 s^{-1}[11] (e.g. 66L in Fig. 2a, SI section 6) – five orders of magnitude slower. This calculation uses the mean square penetration distance $\langle \Delta P^2 \rangle$, averaged from measurements of all the individual atomic planes, providing a good agreement with previously reported solution based measurements for bulk vermiculite clays[22,23]. Note that averaging was not necessary for bilayer and trilayer samples as the whole interlayer space was fully exchanged. These data reveal that a considerable proportion of individual interlayers in the bulk specimen remain unexchanged (Fig. S5g). We therefore propose a two-step process where ion exchange can be separated into penetration followed by propagation along the interlayer space. We further observe that interlayer planes terminating at a step edge often display greater levels of ion exchange than the rest of the crystal, suggesting that these vicinal steps may offer favourable, low energy entrance sites (Fig. 2f). We also observe that interlayers close to an outer surface are more favourable for ion exchange, suggesting that either the initial penetration or interlayer diffusion is more favourable in proximity to a basal surface. The latter observation can aid our understanding of the measured $\gtrsim 10^5$ times faster Cs^+ diffusion in few-layer vermiculite compared to averaged bulk data, which we attribute to the aluminosilicate layers being effectively more loosely bound in atomically thin crystals. Our density-functional-theory calculations substantiate this interpretation and show

that the energy necessary to expand adjacent aluminosilicate layers is as much as 2 eV smaller in bilayer crystals than in multilayer ones (Fig. S10).

A further degree of freedom for layered structures like clays and micas is that they can restack in such a way that the crystal lattices of two neighbouring aluminosilicate planes are misaligned or 'twisted' with respect to each other (Fig. 2g, Fig. 3a,b). Between the restacked crystals, a 'new' interface is generated. Pristine biotite and muscovite crystals show no measurable ion exchange within a reasonable timescale, except close to edges, even when thinned to few-layer thickness (Fig 2d,e, SI section 6). Nonetheless, the interface between two twisted biotite crystals showed widespread ion exchange (Fig. 2g). Indeed, when exposed to electrolyte for only 1 hour, micrometre-sized twisted biotite samples can be exchanged by Cs^+ ions (Fig. 3, SI Fig. S6-7), translating to $D_{twist\text{-}Bio} > 10^{-4}\ \mu m^2\ s^{-1}$; an increase by a factor of at least 10^7 with respect to the pristine biotite samples (SI, section 6). Here the thickness of the individual biotite crystals is not significant and we observed the same enhancement of Cs exchange at the interface between any two twisted biotite flakes, regardless of the precise twist angle and whether they were monolayers or much thicker ($\gtrsim$10 layer) flakes (see SI Fig. S7).

Perhaps an even more unexpected result is the unusual arrangement of the exchanged ions within a twisted interlayer space when observed at atomic resolution. Fig. 3 shows plan view HAADF STEM data taken from two Cs-exchanged biotite samples, each consisting of two monolayer crystals restacked with a small rotational misorientation. The twist angle between the upper and lower crystals, ϑ, can be measured from the electron diffraction patterns (Fig. 2c,d) determined as $\vartheta \approx 9.5^o$ and 2.6^o for specimens shown in the top and bottom panels of Fig. 3 respectively. We find that the Cs^+ ions (bright dots shown in Fig. 3e-h) exchanged at the interface between these twisted bilayers arrange with the same in-plane interionic separation of 5.3 Å seen in the aligned bilayer samples. However, unlike in the uniform and continuous arrangement seen in the aligned samples (Fig. 1b,d), these Cs^+ ions form groups of 7±2 and 130±15 atoms per island for $\vartheta \approx 9.5^o$ and 2.6^o, respectively (Fig. 3g,h). Outside these islands, Cs^+ is rarely observed. The islands occur periodically with periods of L = 3.1±0.2 nm for $\vartheta \approx 9.5^o$ and 11.7±0.7nm for $\vartheta \approx 2.6^o$ (Fig. 3e,f). Interestingly, the found L corresponds to the moiré periodicity of the underlying twisted aluminosilicate bilayers, L_M. This latter periodicity is given by $L_M = a/[2\sin(\vartheta/2)]$, where a is the aluminosilicate lattice constant. For biotite, the known a = 0.53 nm yields L_M = 3.2 nm for $\vartheta \approx 9.5^o$ and 11.7 nm for $\vartheta \approx 2.6^o$ in excellent agreement with the measured periodicities, indicating that the Cs^+ ion islands are commensurate with the biotite moiré 'template'.

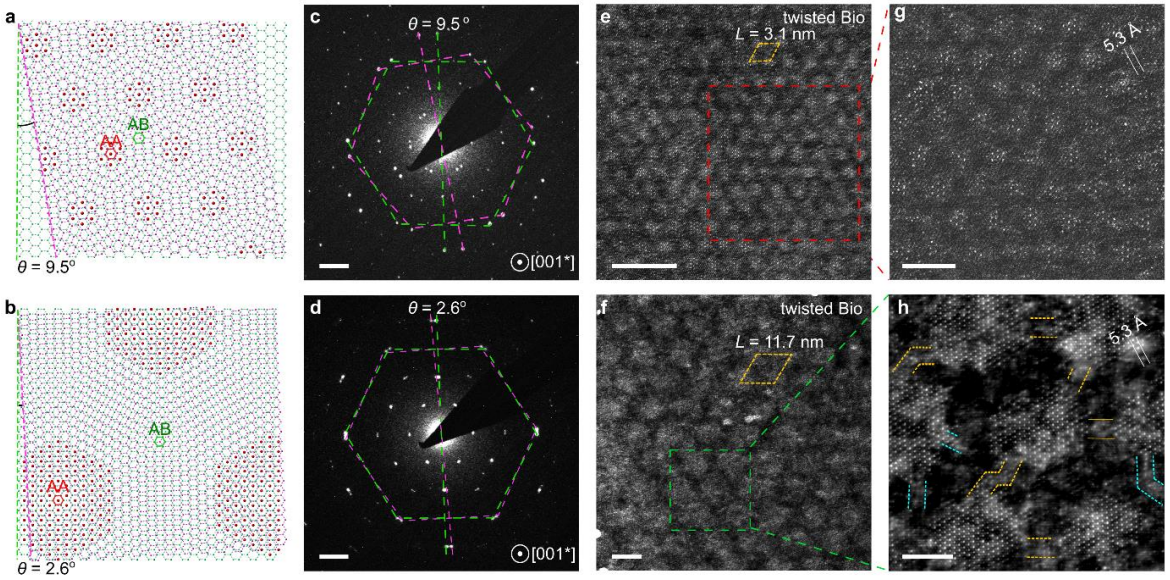

Figure 3|Interlayer Cs islands in twisted biotite bilayers. a,**b** Schematic atomic models showing the formation of a moiré pattern by a twist between two biotite monolayers, in which the interlayer ions commensurate with the moiré superlattice, for twist angles of $\vartheta \approx 9.5^{o}$ and $\vartheta \approx 2.6^{o}$ respectively. The two twisted aluminosilicate layers are shown in green and magenta respectively, with red balls showing the location of interlayer Cs. The high-symmetry sites in this rigid lattice model are labelled as AA and AB according to the stacking sequence of aluminosilicate rings that are adjacent to interlayer ions, with AA being the same stacking type as pristine bilayer biotite. **c,d,** Experimental selected area electron diffraction (SAED) patterns from twisted biotite bilayer samples, showing that the twist angles between the two biotite monolayers are 9.5^{o} and 2.6^{o} respectively. Scale bars, 2 nm^{-1}. **e,f,** Plan view HAADF-STEM images taken from the Cs-exchanged twisted bilayer samples for $\vartheta \approx 9.5^{o}$ and $\vartheta \approx 2.6^{o}$, respectively. The Cs^{+} ions form islands visible as brighter regions in the micrographs. The moiré unit cell is marked by the orange dashed oblique and the periodicity, *L,* is indicated. Scale bars, 10 nm. **g**,**h**, Magnified views from panels **e** and **f**, respectively. Interionic separation marked with white lines. Ion bridges between islands are marked by orange and blue dashed lines respectively, depending on their lattice orientation alignment. Scale bars, 5 nm.

To understand the formation mechanism behind the periodic clustering of Cs^{+} ions, we investigate their local binding environment, related to the stacking sequence of the neighbouring aluminosilicate (Al-Si-O) hexagonal rings. In general, ions bind into the local minima in the potential energy surface provided by the aluminosilicate layer. In a pristine bilayer mica (Fig. 1b), the top and bottom Al-Si-O hexagonal rings are aligned (AA stacking), resulting in a periodic array of energetically favourable hexagonal centre sites to host for interlayer cations. At the interface in a twisted biotite sample, two potential energy surfaces superpose to form a new energy landscape with the larger period of the aluminosilicate moiré superlattice (Fig. S11). The moiré supercell contains various stacking sequences including high-symmetry AA and AB sites, as well as low-symmetry incommensurate bridging sites (Fig. 3a,b). The Cs^{+} islands are aligned with the regions of

AA stacking, equivalent to that present in perfect biotite and correlated with the favourable low energy regions in the potential energy landscape. Our calculations agree with this interpretation and reproduce both the periodicity of the ion superlattice and the number of ions per island as a function of twist angle (Fig. S11, SI section 9.3). Notably, no Cs is observed at AB regions, while occasional Cs^+ bridges link the islands *via* the incommensurate boundary regions (Fig. 3h), suggesting that these are the route for Cs^+ propagation between the islands. As for the 'fast' ion exchange in twisted biotite mica, our calculation found that the interlayer interactions are weaker in the twisted interlayer compared to the pristine interlayer (See SI, Fig. S11). The weaker interlayer interaction facilitates interlayer expansion, which is proposed to reduce the energy barriers for both ion penetration and propagation.

We now consider ion exchange on the outer basal plane surfaces, as this constitutes a large fraction of the total ion exchange potential in atomically thin specimens. Characterizing surface ions by STEM is experimentally more demanding and such studies have remained conspicuously absent in the literature. Nonetheless, we found that the weakly bound surface ions can be preserved by use of a protective graphene layer or by fast transfer of plan view specimens to the TEM after removal from the electrolyte. Employing low dose imaging conditions allows images to be acquired before electron beam induced degradation of the structure. We focus our surface analysis on muscovite because this mica displays negligible interlayer ion exchange, even after several months' exposure to electrolyte (Fig. S5f). We can therefore be sure that Cs ions observable far from the edges of plan view specimens are adsorbed on the basal surface. HAADF-STEM of our cross-sectional samples revealed that the out-of-plane distance for native and exchanged ions differed by ~1 Å (Fig. 4a,b), consistent with previous reports from bulk x-ray measurements[25,26]. Note that in the particular sample shown in Fig. 4b, Cs^+ ions are only present on one surface of the muscovite, while K^+ ions remained on the other (bottom and top muscovite surface in Fig. 4b, respectively) – an asymmetry that was sometimes observed in our samples (Fig. S8). Complementary plan view STEM imaging allows us to characterise with sub-angstrom resolution the in-plane ordering of surface Cs^+ ions and, crucially, the ions relative position with respect to the aluminosilicate lattice. To achieve this, we employ simultaneous dark-field (HAADF)-STEM and annular bright-field (ABF)-STEM imaging[27]. The HAADF image captures the heavy Cs^+ ions while the ABF image captures the lighter cations and the atoms in the aluminosilicate layer. Fig. 4e shows that surface Cs^+ ions, visible as bright spots in HAADF, form a quasi-hexagonal lattice. The ABF image of the same area is shown in Fig. 4f, and here atomic positions are visible as dark spots, rather than bright ones. This image shows that Al-O and Si-O form ring structures, known in the literature as hexagonal or ditrigonal rings[12] (coloured blue and magenta in Fig. 4d). Correlation of the HAADF and ABF-STEM images reveals that K^+ and Cs^+ ions are adsorbed on different sites within these rings and, in this sample, on opposite surfaces. K^+ ions adsorb in the centre of the hexagonal rings (Type I site) on the top surface (T^1); whereas Cs^+ ions overwhelmingly (76%, see Fig. S9) adsorb on the vertex of the hexagonal rings (Type II site on

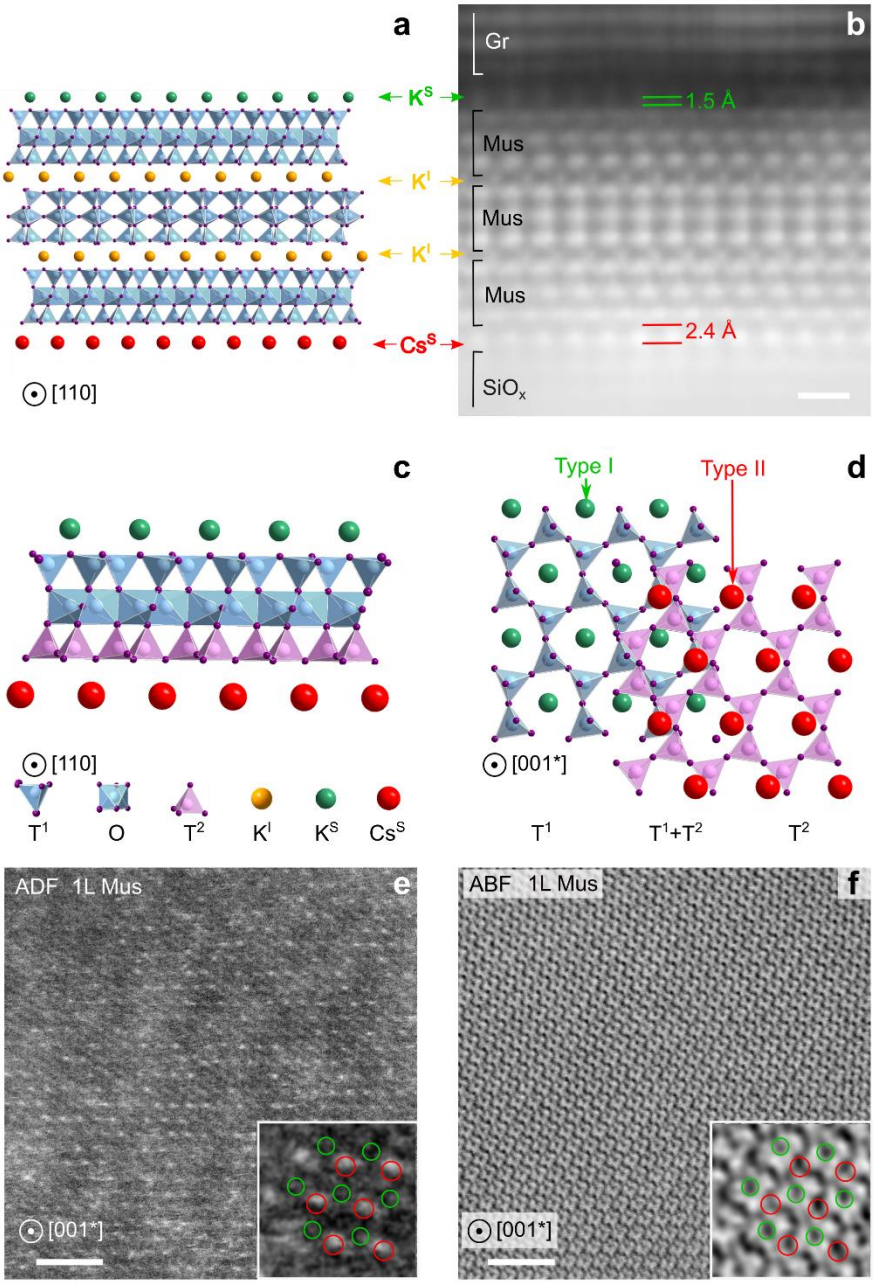

Figure 4| Cations adsorbed on the surface basal plane of muscovite. a,b, Schematic and corresponding cross-sectional HAADF-STEM image of a 3L muscovite sample. The sample was encapsulated between graphite (Gr) and SiO_x. Distance between the surface ions and the outer aluminosilicate layer is marked with horizontal lines. Superscripts 'S' and 'I' refer to surface and interlayer ions, respectively. Scale bar, 5 Å. **c**, Cross-sectional schematic of a monolayer muscovite with K^+ and Cs^+ ions adsorbed on opposite surfaces. The aluminosilicate TOT layers are indicated with the top (T^1) and bottom (T^2) tetrahedral sheets in the aluminosilicate layer coloured blue and magenta, respectively, to emphasize that the layers are not vertically aligned. **d**, Plan view schematic of the monolayer muscovite in panel **c**. For clarity, only the T sheets are shown (octahedral sheet is not shown). Type I and Type II refer to the different adsorption sites of K^+ and Cs^+ ions with respect to the neighbouring T-layer. For clarity, each of the two T sheets in the aluminosilicate monolayer is presented separately and then overlapped (T^1 +T^2). **e**, HAADF-STEM image of Cs-exchanged monolayer muscovite. Cs ions are visible as bright spots. **f**, Annular bright

field (ABF)-STEM image of the same area imaged in panel **e**. Atomic positions are visible as dark spots. For both **e** and **f** higher magnification images are inset with red and green circles indicating the positions of Cs^+ and K^+ ions, respectively. Note that the K^+ ions are not identifiable in HAADF STEM due to their low atomic number, so their position was obtained from the ABF image. In panel **f** the schematic of the T^1 lattice and K^+ ion position is superimposed top left as a guide to the eye. Scale bars, 2 nm.

T^2). The difference in in-plane and out-of-plane coordinates observed here for Cs compared to the native K^+ cations is attributed to the Cs^+ being adsorbed as a hydrated ion species. The presence of a minority of Cs^+ at a different lattice site and the related variation in out-of-plane distance is attributed to the presence of different hydration complexes[10,26,28], which could stabilise at different lattice sites (see Fig. S9 and SI section 8).

Our results provide an atomic-scale description of surface ion adsorption and interlayer ion diffusion dynamics in atomically thin micas and clays, of relevance to their use as catalytic supports and membrane materials, and for understanding the intercalation process in 2D materials. Applications such as water treatment[9,10] and radioactive effluent decontamination[8] have long used bulk micas and clays as ion exchangers. We have shown that ion uptake in 2D clay is ultimately fast – probably as fast as free diffusion in water – which could be used to enhance the effectiveness of materials for these applications. On the other hand, our results also provide a fresh perspective on ion exchange in natural environments, indicating a potential two-step mechanism for interlayer incorporation of Cs^+ into clays/micas, which may result in the limited movement of heavy metal ions in contaminated land[20]. Beyond this, given the interest in the electronic and optical properties of 2D micas[29], 2D metals[30], and twisted 2D materials heterostructures[31], our observations suggest opportunities for fabricating mica-encapsulated 2D metal ion superlattices[32], demonstrating a new route towards designing 2D lattices at van der Waals interfaces with atomic precision - enticingly, the materials discussed here are only some of the many where this should be possible.

Acknowledgments

The work was supported by EPSRC grants EP/M010619/1 and EP/P009050/1, the European Research Council (ERC) under the European Union's Horizon 2020 research and innovation programme (Grant ERC-2016-STG-EvoluTEM-715502 and the ERC Synergy Hetero2D project 319277). L.M. acknowledges the EPSRC NOWNano programme for funding.

References

1 Mogg, L. *et al.* Atomically thin micas as proton-conducting membranes. *Nat. Nanotechnol.* **14**, 962-966 (2019).

2 Liu, M.-L. *et al.* Two-Dimensional Nanochannel Arrays Based on Flexible Montmorillonite Membranes. *ACS Appl. Mater. Interfaces* **10**, 44915-44923 (2018).

3 Shao, J.-J., Raidongia, K., Koltonow, A. R. & Huang, J. Self-assembled two-dimensional nanofluidic proton channels with high thermal stability. *Nat. Commun.* **6**, 7602 (2015).

4 Gao, J. *et al.* Kirigami nanofluidics. *Mater. Chem. Fron.* **2**, 475-482 (2018).

5 Cheng, H. *et al.* Electrokinetic Energy Conversion in Self-Assembled 2D Nanofluidic Channels with Janus Nanobuilding Blocks. *Adv. Mater.* **29**, 1700177 (2017).

6 Zhang, Z. *et al.* Emerging hydrovoltaic technology. *Nat. Nanotechnol.* **13**, 1109-1119 (2018).

7 Gao, J., Feng, Y., Guo, W. & Jiang, L. Nanofluidics in two-dimensional layered materials: inspirations from nature. *Chem. Soc. Rev.* **46**, 5400-5424 (2017).

8 *Application of Ion Exchange Processes for Treatment of Radioactive Waste and Management of Spent Ion Exchangers*. (INTERNATIONAL ATOMIC ENERGY AGENCY, 2002).

9 Beall, G. W. The use of organo-clays in water treatment. *Appl. Clay Sci.* **24**, 11-20 (2003).

10 Huang, K. *et al.* Cation-controlled wetting properties of vermiculite membranes and its promise for fouling resistant oil–water separation. *Nat. Commun.* **11**, 1097 (2020).

11 Alcantar, N., Israelachvili, J. & Boles, J. Forces and ionic transport between mica surfaces: implications for pressure solution. *Geochim. Cosmochim. Acta* **67**, 1289-1304 (2003).

12 Cheng, L., Fenter, P., Nagy, K. L., Schlegel, M. L. & Sturchio, N. C. Molecular-Scale Density Oscillations in Water Adjacent to a Mica Surface. *Phys. Rev. Lett.* **87**, 156103 (2001).

13 Fukuma, T., Ueda, Y., Yoshioka, S. & Asakawa, H. Atomic-Scale Distribution of Water Molecules at the Mica-Water Interface Visualized by Three-Dimensional Scanning Force Microscopy. *Phys. Rev. Lett.* **104**, 016101 (2010).

14 Martin-Jimenez, D., Chacon, E., Tarazona, P. & Garcia, R. Atomically resolved three-dimensional structures of electrolyte aqueous solutions near a solid surface. *Nat. Commun.* **7**, 12164 (2016).

15 Helfferich, F. *Ion Exchange*. (McGraw Hill, 1962).

16 Nair, R. R., Wu, H. A., Jayaram, P. N., Grigorieva, I. V. & Geim, A. K. Unimpeded Permeation of Water Through Helium-Leak–Tight Graphene-Based Membranes. *Science* **335**, 442-444 (2012).

17 Nicolosi, V., Chhowalla, M., Kanatzidis, M. G., Strano, M. S. & Coleman, J. N. Liquid Exfoliation of Layered Materials. *Science* **340**, 1226419 (2013).

18 Stein, D., Kruithof, M. & Dekker, C. Surface-Charge-Governed Ion Transport in Nanofluidic Channels. *Phys. Rev. Lett.* **93**, 035901 (2004).

19 Fuller, A. J. *et al.* Caesium incorporation and retention in illite interlayers. *Appl. Clay Sci.* **108**, 128-134 (2015).

20 Taniguchi, K. *et al.* Transport and Redistribution of Radiocesium in Fukushima Fallout through Rivers. *Environ. Sci. Technol.* **53**, 12339-12347 (2019).

21 Haigh, S. J. *et al.* Cross-sectional imaging of individual layers and buried interfaces of graphene-based heterostructures and superlattices. *Nat. Mater.* **11**, 764-767 (2012).

22 Sánchez-Pastor, N., Aldushin, K., Jordan, G. & Schmahl, W. W. K^+–Na^+ exchange in phlogopite on the scale of a single layer. *Geochim. Cosmochim. Acta* **74**, 1954-1962 (2010).

23 Walker, G. F. Diffusion of Exchangeable Cations in Vermiculite. *Nature* **184**, 1392-1393 (1959).

24 Sato, H., Yui, M. & Yoshikawa, H. Ionic Diffusion Coefficients of Cs^+ , Pb^{2+} , Sm^{3+} , Ni^{2+} , SeO_4^{2-} and TcO_4^- in Free Water Determined from Conductivity Measurements. *J. Nucl. Sci. Technol.* **33**, 950-955 (1996).

25 Lee, S. S., Fenter, P., Nagy, K. L. & Sturchio, N. C. Monovalent Ion Adsorption at the Muscovite (001)–Solution Interface: Relationships among Ion Coverage and Speciation, Interfacial Water Structure, and Substrate Relaxation. *Langmuir* **28**, 8637-8650 (2012).

26 Sakuma, H. & Kawamura, K. Structure and dynamics of water on Li^+-, Na^+-, K^+-, Cs^+-, H_3O^+-exchanged muscovite surfaces: A molecular dynamics study. *Geochim. Cosmochim. Acta* **75**, 63-81 (2011).

27 Ishikawa, R. *et al.* Direct imaging of hydrogen-atom columns in a crystal by annular bright-field electron microscopy. *Nat. Mater.* **10**, 278-281 (2011).

28 Lee, S. S., Fenter, P., Nagy, K. L. & Sturchio, N. C. Real-time observation of cation exchange kinetics and dynamics at the muscovite-water interface. *Nat. Commun.* **8**, 15826 (2017).

29 Kim, S. S. *et al.* Tunable Bandgap Narrowing Induced by Controlled Molecular Thickness in 2D Mica Nanosheets. *Chem. Mater.* **27**, 4222-4228 (2015).

30 Briggs, N. *et al.* Atomically thin half-van der Waals metals enabled by confinement heteroepitaxy. *Nat. Mater.* **19**, 637-643 (2020).

31 Alexeev, E. M. *et al.* Resonantly hybridized excitons in moiré superlattices in van der Waals heterostructures. *Nature* **567**, 81-86 (2019).

32 Roger, M. *et al.* Patterning of sodium ions and the control of electrons in sodium cobaltate. *Nature* **445**, 631-634 (2007).

Ion exchange in atomically thin clays and micas

Supplementary Information

Yi-Chao Zou[1], Lucas Mogg[2,3], Guang-Ping Hao[2,3], Nick Clark[1,2], Cihan Bacaksiz[4], Slavisa Milanovic[4], Yi-Chi Wang[1], David G. Hopkinson[1,2], Roman Gorbachev[2,3], Samuel Shaw[5], Kostya S. Novoselov[2,3], Francois M. Peeters[4], Marcelo Lozada-Hidalgo[2,3]*, Sarah J. Haigh[1,2]*

[1]Department of Materials, The University of Manchester, Manchester M13 9PL, UK

[2]National Graphene Institute, The University of Manchester, Manchester M13 9PL, UK

[3]Department of Physics and Astronomy, The University of Manchester, Manchester M13 9PL, UK

[4]Departement Fysica, Universiteit Antwerpen, Groenenborgerlaan 171, B-2020 Antwerp, Belgium

[5]Research Centre for Radwaste Disposal and Williamson Research Centre, School of Earth and Environmental Science, The University of Manchester, Manchester M13 9PL, UK

1. Source Materials

The materials studied in this work were: two natural mica minerals; ruby muscovite, purchased from Agar Scientific, and natural biotite, sourced from Lanark, Ontario (Canada); and a natural vermiculite clay sourced from Gorainas, Minas Gerais (Brazil). The chemical composition of the three materials was provided by the suppliers (Table S1). The simplified crystal structure and approximate unit cell dimensions for the materials are given neglecting partial occupancies of interlayer cations, or the associated water molecules, –OH bonding, and minor chemical impurities (Table S2).

Table S1| Material composition (wt. %), excluding trace elements

Material	**SiO_2**	**Al_2O_3**	**K_2O**	**MgO**	**Fe_2O_3**	**water**
muscovite	45.57	33.10	9.87	0.38	2.48	2.99
Biotite	50.79	18.45	3.72	12.28	3.21	4.9
vermiculite	40.4	11.1	0.01	26.9	7.85	11.43

Table S2| Indicative crystal structure and unit cell dimensions of the source materials[1-3]. Chemical formulas are expressed in the form **interlayer cation (IC) and (tetrahedral-octahedral-tetrahedral, TOT) layer.**

Crystal	**a(Å)**	**b(Å)**	**c (Å)**	**α (°)**	**β(°)**	**γ(°)**	**Space group**	**Chemical formula, IC (TOT)**
muscovite	5.2	9.0	20.0	90.0	95.2	90.0	C12/c1 (15)	$K(Al_2Si_4O_{11})$
Biotite	5.3	9.2	20.1	90.0	95.1	90.0	C12/c1 (15)	$K_3(Mg_8Al_7Si_9O_{36})$
vermiculite	5.3	9.1	28.9	90.0	97.1	90.0	C12/c1 (15)	$Mg_2(Mg_6AlSi_3O_{10})$

2. Transmission electron microscopy (TEM) and specimen preparation

2.1 Specimen preparation

For cross-sectional TEM imaging, we prepared samples by two different methods: mechanical polishing and focussed ion beam milling (FIB). The mechanical polishing method was mainly used to image relatively thick ($\gtrsim$ 20 layer) clay or mica flakes. In this approach, the source materials were mechanically exfoliated onto a Si substrate[4], which is then covered with another Si substrate. The Si-flake-Si sandwich structure was glued together by epoxy and mechanically polished down to electron-transparent thickness using an automatic polishing instrument (Allied MultiPrep). The polished structure was glued onto a 3 mm molybdenum slot TEM support grid, followed by cleaning in an Argon milling system (Gatan PIPS II) operated at 0.5 kV for 10 min. To perform the Cs exchange, the prepared specimens were immersed in a 0.1 M $CsNO_3$ water solution for time scales ranging from 1 s to 9 months. The specimens were cleaned by washing in de-ionized (DI) water and in acetone (for 20 s each) and drying in a nitrogen atmosphere at 90 ^{o}C for 5 min.

The FIB method was used to prepare cross-sectional TEM samples, and allows investigation of flakes with known thicknesses, even down to a single monolayer. The mica and clay flakes were mechanically exfoliated onto SiO_x/Si substrates and the thickness of the thin regions is identified by optical contrast together with atomic force microscopy (AFM) measurements (Fig. S1). The substrate with the flake was immersed in 0.1 M $CsNO_3$ solution for the desired amount of time and then cleaned in DI water and acetone. To avoid surface damage during FIB sample preparation, the flake of interest was protected by transferring a graphite flake (5-200 layers thick) over it. The SiO_x-flake-graphite assembly was further protected by depositing a narrow Pt strip (2 µm thick, 1 µm wide and 15 µm long) inside the FIB scanning electron microscope (FIB SEM, FEI Helios 660). Standard milling protocols were used to cut the lamella free from the substrate and transfer it to a pillar of a specialist OmniProbe™ Cu TEM support grid, followed by 30 kV, 16 kV, 5 kV and 2 kV ion beam milling and polishing to electron transparency.

For plan-view specimens, preparation is performed by first identifying mechanically exfoliated atomically thin mica/clay regions at the top of polyvinyl alcohol and polypropylene carbonate stacks, *via* the 'dry peel' transfer method[4]. Sample thickness can be confirmed by optical contrast and AFM. These flakes were then transferred over holes in SiN_x membrane supported TEM grids and cleaned using acetone, isopropyl alcohol and DI water several times, until the suspended flakes are optically free from contamination. The samples were then ion exchanged by immersing the whole TEM grid assembly into a 0.1 M $CsNO_3$ solution for the desired time length and then cleaned using ethanol, dried and stored in N_2 atmosphere prior to TEM analysis.

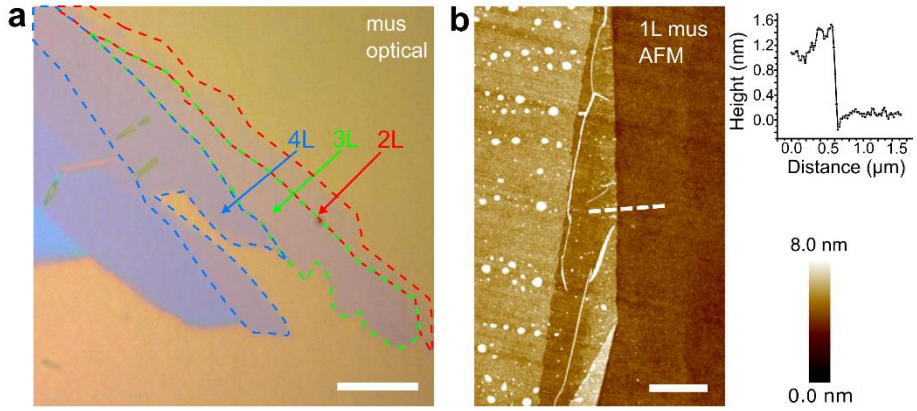

Supplementary Figure S1 | Identifying atomically-thin crystals. a, A typical optical image taken from a mechanically exfoliated muscovite flake on a SiO_x/Si substrate. Scale bar, 10 μm. **b,** AFM image showing a monolayer region in a $CsNO_3$ electrolyte treated muscovite flake. Right-top insert is the line height profile taken from the white dashed line marked in **b**, confirming that the height of the monolayer region is ~1 nm. Scale bar, 1 μm.

2.2 S/TEM imaging

A probe-side aberration-corrected FEI Titan G2 80-200 S/TEM "ChemiSTEM" microscope was used for annular dark field (ADF) scanning transmission electron microscopy (STEM). This microscope was operated at 200kV with a probe current of 8-15 pA, a convergence angle of 21 mrad and a high-angle ADF (HAADF) detector with an inner (outer) collection angle of 48(196) mrad. Selected area electron diffraction (SAED) patterns were obtained using the same microscope operated in TEM mode.

A JEOL ARM300CF double aberration corrected microscope was used to acquire HAADF- and annular bright field (ABF)-STEM images simultaneously. This instrument has a cold FEG electron source, was operated at 80kV with a probe current of ~6 pA and a convergence angle of 24.8 mrad. Images were acquired with a HAADF detector having a collection angle of ~50-150 mrad and an ABF detector having a ~12-24 mrad collection angle. Multi-slice image simulation for high resolution STEM images was conducted using atomic models created under the Atomic Simulation Environment[5], and the QSTEM software[6] with the above experimental parameters, and a source size of 0.8-1 Å.

3. XRD, TEM and STEM Characterization of bulk source crystals

The as received bulk crystals were characterized in house using cross-sectional STEM imaging, SAED and X-ray diffraction (XRD) (Fig. S2). XRD measurements (Fig. S2j) reveal the expected differences in (002) interlayer separations for the three source crystals. Pristine bulk specimens were found to have interlayer spacings of 9.8, 9.9 and 14.4 Å for muscovite, biotite and vermiculite respectively, when measured under ambient environmental conditions, consistent with expected literature values[1-3]. The differences in these interlayer spacings can be related to the ability of the crystals to hold interlayer water, which is closely related to their composition and interlayer ion species (section 1, Table S1). The exchangeable ions in all three materials are typically K^+ or Mg^{2+}. From Table S1 and S2, it can be seen that the interlayer cation is dominated by Mg^{2+} in vermiculite, by K^+ in muscovite, and by K^+ in biotite (referred to Table S1, S2). Compared to K^+, Mg^{2+} has a much lower hydration enthalpy[7], and hence vermiculite has a higher capacity to hold interlayer water than muscovite or biotite and a correspondingly larger interlayer spacing. Indeed, the difference in interlayer ion species is visible from our HAADF-STEM images (Fig. S2) where the presence of the native interlayer K^+ cations is directly observed for muscovite and biotite, but the interlayer ions are not visible for the lighter Mg^{2+} ions in vermiculite (see Fig. S2, the positions of the interlayer cations are indicated by yellow arrows). This difference is a natural consequence of the atomic-number sensitivity of the HAADF STEM imaging mode. The lower atomic number of Mg compared to K results in a lower HAADF intensity, and the hydration of Mg^{2+} also creates additional disorder and a consequent blurring of image contrast.

After cross-sectional sample preparation and transfer to the S/TEM ultra-high vacuum environment, we measured local interlayer spacing of 9.8 to 9.9 Å for muscovite and biotite (Fig. S2b,e), consistent with our XRD values and showing little variability across each of the specimens. In contrast, for vermiculite we observe interlayer distances in the S/TEM ranging from ~9.8 Å to ~14.3 Å (Fig. S2h). Vermiculite is known to contain 0-3 molecular layers of water associated with its interlayer cations between the aluminosilicate layers, with the precise number of water molecular layers depending on the humidity of the surrounding environment[8,9]. Dehydration of the crystal can cause collapse of the interlayer distance, and the variability of interlayer separation visible by TEM is therefore attributed to partial loss of water during sample preparation or in the TEM vacuum. Nonetheless, the presence of local regions with the fully hydrated vermiculite lattice structure suggests that some water remains trapped at the interlayer space even after TEM sample preparation.

In addition to the differences in interlayer separation, HAADF STEM imaging also reveals differences in the octahedral (O) layers for the three materials. Substitution of Al^{3+} in the O layer by other cations with lower valence charge (e.g. Mg^{2+}) changes the local co-ordination environment from a

dioctahedral to a trioctahedral structure[10]. In our samples, the O layer of muscovite is dioctahedral, whereas vermiculite and biotite are trioctahedral. This difference is visible in the cross-sectional HAADF-STEM images (Fig. S2b,e,h), where the sparser atomic arrangement in dioctahedral muscovite produces a lower HAADF intensity within the O layer compared with that observed in trioctahedral vermiculite and biotite.

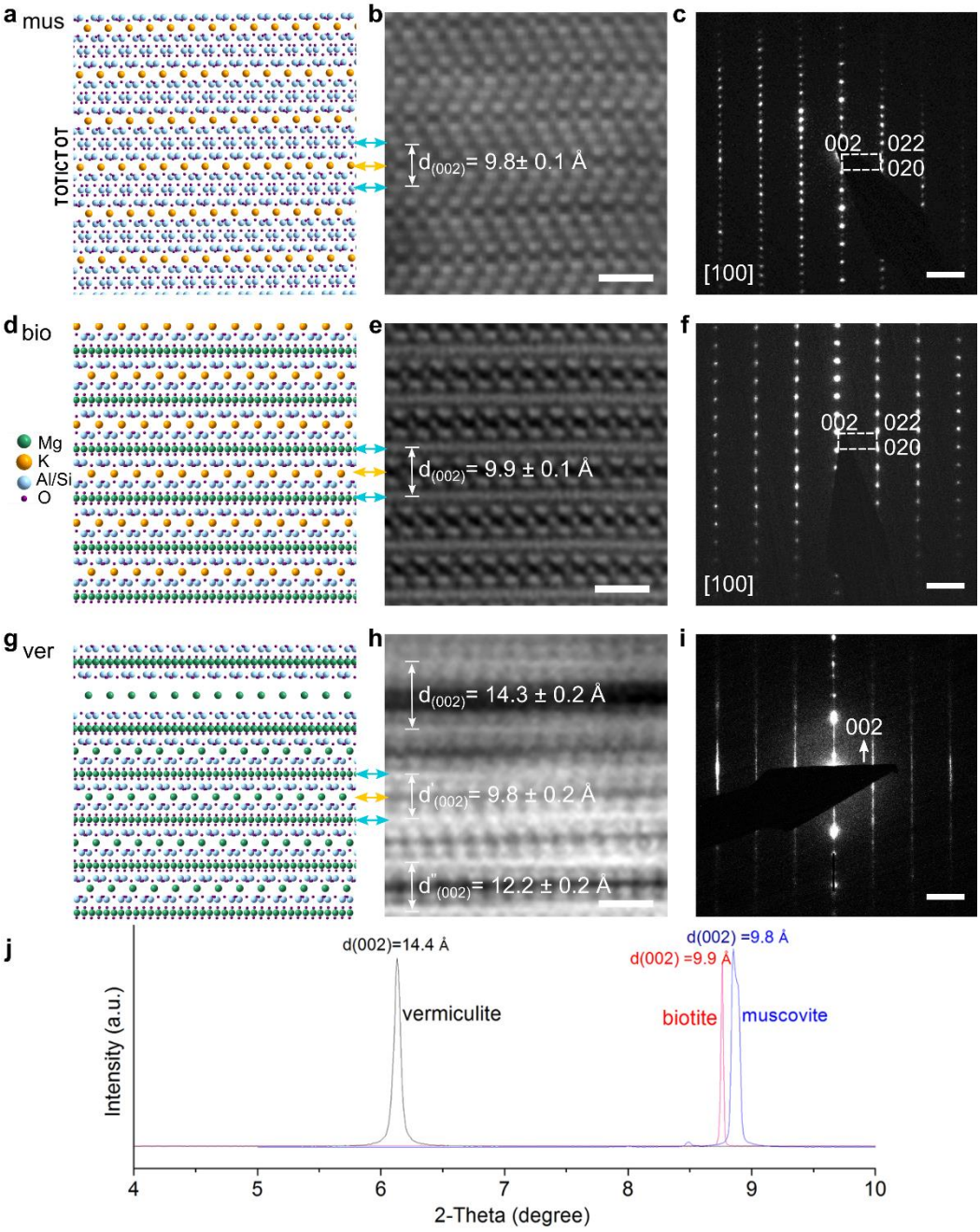

Supplementary Figure S2|S/TEM and XRD characterization of bulk crystals. Here we study exfoliated products from three materials: **a-c,** muscovite; **d-f,** biotite; and **g-i,** vermiculite. **a,d,g,** Schematic atomic models showing the crystal structures of the source materials. **b,e,h,** Cross-sectional high-angle annular dark field (HAADF) STEM images. Scale bars, 1 nm. All materials consist of alternating layers of aluminosilicate (TOT) and interlayer cations (IC) when viewed along the [100] direction. The atomic models have been aligned to the experimental images with some

octahedral 'O' layers and 'IC' layers highlighted by blue and orange arrows, respectively. **c,f,i,** Selected area electron diffraction (SAED) patterns, for the materials viewed along [100]. Scale bars, 2 nm^{-1}. **j,** Powder X-ray diffraction (XRD) spectra taken from the source crystals, showing that each pristine crystal has uniform interlayer spacing under ambient environmental conditions.

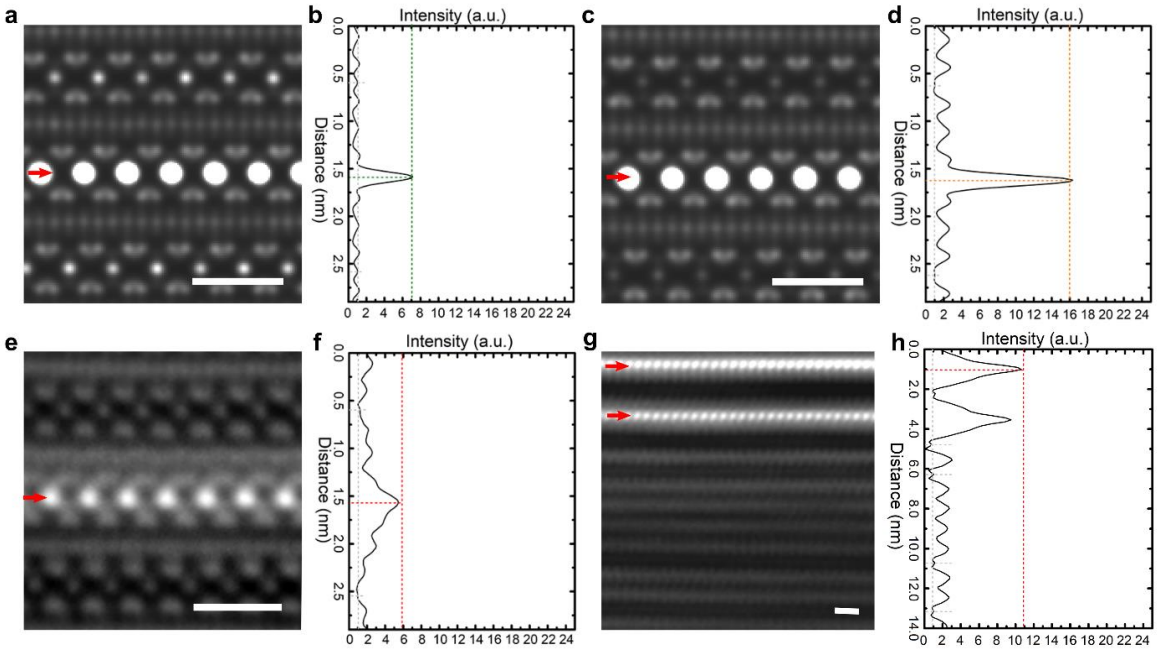

Supplementary Figure S3| Quantifying Cs occupancy in the interlayer cation sites from cross-sectional images. a,c, Simulated HAADF-STEM images for K-biotite (**a**) and dehydrated Mg-vermiculite (**c**) respectively. In the simulated structures, each only has one atomic plane that is fully exchanged for Cs^+, highlighted by the red arrows. **b,d,** Corresponding line intensity profiles summed horizontally across the whole image, normalized to the native interlayer cation column intensity. The intensity ratios between the exchanged layer and the native interlayer cation is found to be $I_{Cs}/I_K \approx 7$ for biotite and $I_{Cs}/I_{Mg} \approx 15$ for vermiculite, using simulation parameters given in section 2.2. **e,g,** Experimental HAADF-STEM images for Cs exchanged biotite (**e**) and vermiculite (**g**) respectively. Red arrows denote the Cs-exchanged atomic layer. **f,h,** Corresponding line intensity summed horizontally across the whole image and normalized to the native ion column intensity. These show $I_{Cs}/I_K \approx 6$ for biotite and $I_{Cs}/I_{Mg} \approx 11$ for vermiculite. All scale bars, 1 nm.

4 Evaluating local Cs content from cross-sectional HAADF imaging

The atomic-number sensitivity of the HAADF STEM imaging mode can be used to quantify atomic occupancies for individual columns. For full ion exchange, the HAADF intensity of ion columns in an exchanged interlayer should have increased by a factor of 7 for Cs^+ substituting K^+ (as in K-biotite) and by a factor of 15 for Cs^+ substituting Mg^{2+}(as in Mg-vermiculite) as demonstrated by the simulations in Fig. S3a-d. Partial ion exchange will result in a correspondingly smaller increase in HAADF intensity. Fig. S3e shows an experimental HAADF-STEM image taken from a Cs exchanged biotite, where a single layer of bright dots can be seen, corresponding to a single exchanged

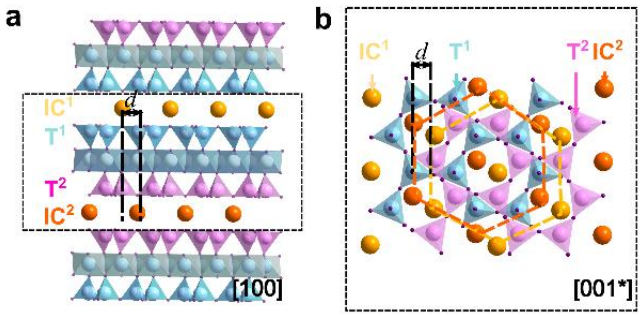

Supplementary Figure S4| Stacking of interlayer cations in a perfect mica/clay. a, Cross-sectional atomic model of a trilayer biotite. Tetrahedral (T) sublayers that are adjacent to a given interlayer cation plane are horizontally aligned with each other. This is illustrated by marking aligned T sub layers with the same colour (magenta, blue). The cations in adjacent interlayer spaces are marked in different colours (yellow, orange). **b**, Atomic model showing a plan view projection of clay. Only the T^1, T^2, IC^1 and IC^2 layers are shown for clarity. interlayer. From the image and line scan intensity profile (Fig.3f), the intensity of the exchanged layer relative to an apparently pristine interlayer region, I_{Cs}/I_{K}, is measured to be around 6, very close to the theoretical $I_{Cs}/I_K \approx 7$, suggesting that Cs has completely replaced K at the exchanged interlayer. Lower I_{Cs}/I_K values were measured in other data demonstrating that partial exchange is also possible.

For vermiculite with Mg^{2+} interlayer cations, experimentally determining the interlayer occupancy is much more challenging due to the relatively weak HAADF signals of light Mg, and the necessity for low dose imaging of these beam sensitive minerals (total fluence below $5x10^3$ $e{\cdot}A^{-2}$) giving relatively large experimental errors[11]. Our analysis revealed a highest $I_{Cs}/I_{Mg} \approx 11$ from dozens of samples examined, as illustrated in Fig. S3g-h. This is smaller than the theoretical $I_{Cs}/I_{Mg} \approx 16$ and may suggest only partial occupancy of Cs^+ was observed. Nonetheless, we find that a full analysis of interlayer ion occupancies requires complementary plan view imaging as discussed in the main text.

5 Stacking of interlayer cations

In this section, we discuss the observed projected lateral arrangement for interlayer cations, as seen in Fig. 1f. Fig. S4a,b show cross-sectional and plan view atomic models for trilayer clay, to illustrate the expected interlayer-cation stacking behaviour. It can be seen that, within each single TOT layer, the 'T' sublayers (T^1, T^2) are horizontally displaced with respect to each other, which results in a lateral displacement, *d,* between the cations (IC^1, IC^2) in nearest-neighbouring interlayers. As shown in Fig. S4b, the projected linear patterns formed by IC^1, IC^2 matches the linear arrangement of interlayer ions observed in Fig. 1f (main text).

6 Estimation of diffusion content from ion-exchanged samples

Here we consider the measurement of ion exchange speed for mica and clays in more detail. In general, ion exchange is considered to be purely a diffusion based phenomenon[12]: that is the ion exchange speed is dominated by diffusion of ions in and out of the ion exchange site, rather than by a chemical reaction between the ions and the matrix[12]. Considering a one-dimensional model for interlayer ion diffusion[13], after time t, the penetration distance $\Delta P = (2Dt)^{0.5}$, and the diffusion constant, D can be calculated as $<\Delta P^2>/2t$.

Previously, the diffusion constant, D, for different micas and clays has been estimated experimentally using crushed bulk powders[12,14], often by immersing the material in electrolyte and monitoring the chemical composition of the solution as a function of time. Note that such estimates provide an average over the entire crushed powder, which cannot distinguish the effects of crystal thickness, particle sizes and orientations in powder samples. In contrast, our plan view and cross-sectional STEM image 'snapshots' obtained for different time points during the exchange process can be used to determine diffusivities as a function of crystal thickness and also gain insights into the influence of vicinal surface on ion exchange. STEM mages such as those in Fig. 2a,g (Fig. S5a,b) allow direct observation of the penetration distance, ΔP, of Cs^+ ions into the crystal. Averaging over all the visible penetration distances for different interlayers (Fig. S5g) allows estimation of the mean penetration distance, $<\Delta P>$ for a particular exposure time and hence D can be calculated.

It is of interest to compare our observed diffusivity values for our thick samples with bulk literature data. Let us start with vermiculite, because its relatively fast interlayer ion exchange makes it a promising candidate for many functional applications described in main text. Depending on the particular type of vermiculite studied, and the type of ion being exchanged (heavy ions diffuse more slowly), the literature reports D values varying from 10^{-5} up to 10^{1} $\mu m^2\ s^{-1}$ in vermiculite bulk powders, with some specimens displaying diffusivity values too slow to be measured in a realistic time frame[14,15]. The diffusion constant we measured for Cs^+ ions in our multilayer (66L, 22L) vermiculite specimens is ~10^{-3} $\mu m^2\ s^{-1}$ calculated using t = 10s, and the measured mean penetration distance ΔP shown in Fig. 5g. This is consistent with the literature values measured in bulk powder experiments for vermiculite clays, especially given that slow Cs^+ ions were used in our experiments[14]. We note that the largest amount of ion exchange has occurred on the layers close to the top or bottom surfaces, or those layers terminating at step edges, suggesting that the ion entry probability can be enhanced by step edges or by proximity to free surfaces.

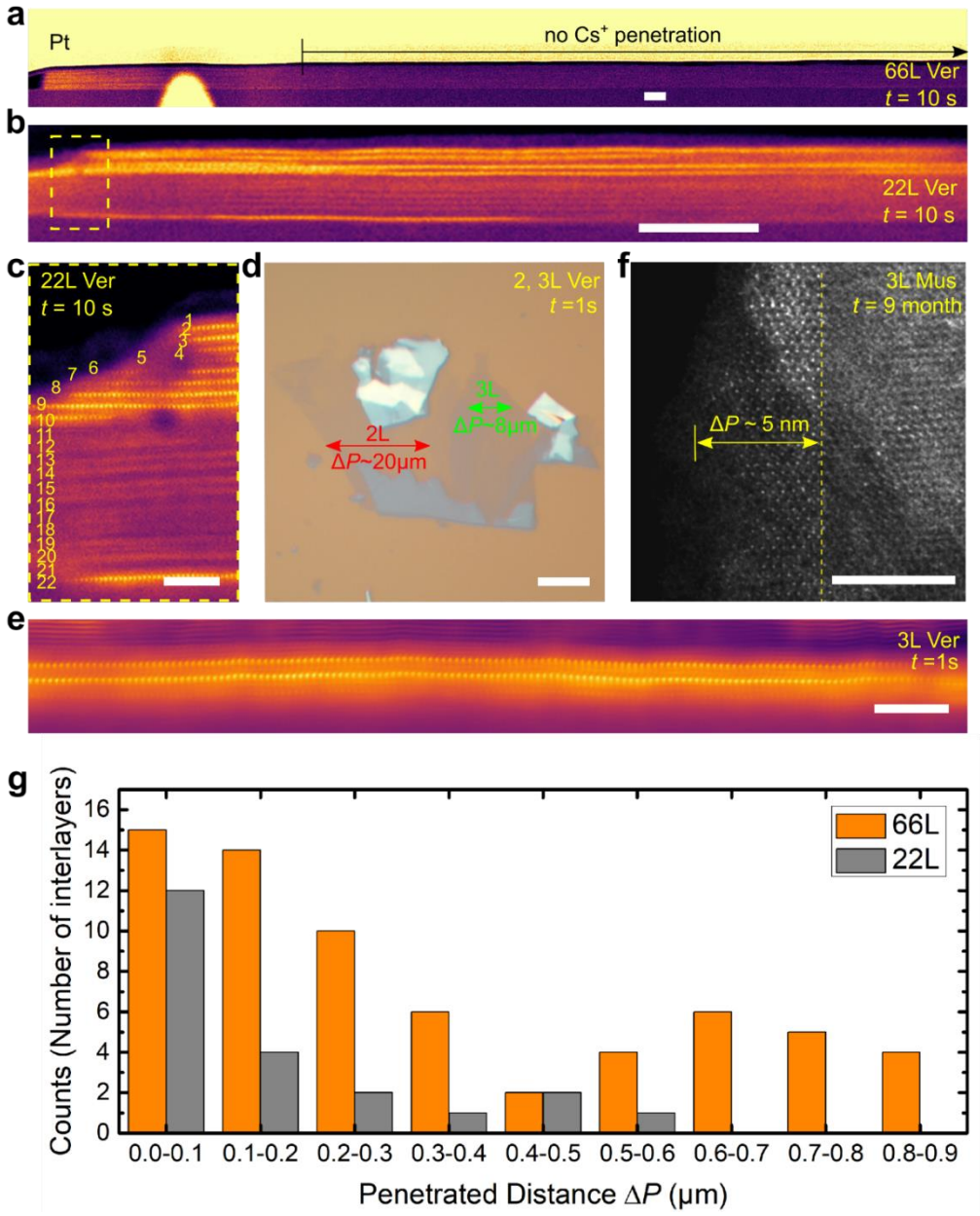

Supplementary Figure S5| Interlayer exchange speed in clays. a, Low-magnification cross-sectional HAADF-STEM images taken from the edge of a 66-layer (66L) vermiculite crystal exposed to electrolyte for 10s, showing a full view of the Cs^+ penetration depth from the edge (left side), and the interior non-exchanged area (right side), corresponding magnified view also shown in Fig. 2a (main text). Scale bar, 50 nm. **b,** Low-magnification cross-sectional HAADF-STEM images taken from a 22-layer (22L) vermiculite crystal exposed to electrolyte for 10s, corresponding magnified view shown in Fig. 2f (main text). Scale bar, 50 nm. **c,** Magnified region from **b** with total number of layers labelled. More exchange is seen at the top or bottom of the flake or where the interlayer terminates at a step edge. Scale bar, 5 nm. **d,** Optical image taken from a 1s Cs-exchanged vermiculite flake, with the Cs penetration length in 2L and 3L regions labelled. Scale bar, 10μm. **e,** Corresponding atomic-resolution HAADF-STEM image taken from the 3L region in **d**, showing a full exchange. Scale bar, 5 nm. **f,** HAADF-STEM plan view image of a few-layer muscovite flake exposed to Cs^+ electrolyte for >9 months. Dotted line marks the distance of deepest penetration of Cs ions

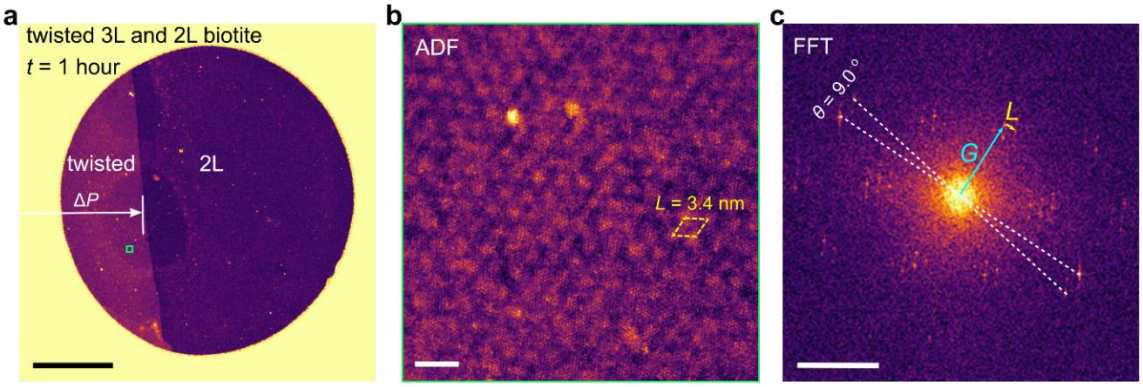

Supplementary Figure S6| Plan view characterization for ion exchange at the interface of twisted few-layer biotite flakes. a, Low-mag HAADF image taken from a Cs-biotite sample. The right-side is a 2L region where no Cs^+ was observed, whereas left side is a 9.0° twisted region, found to have been exchanged by Cs^+ in a micro-sized scale (ΔP>2µm). Scale bar, 2 µm. **b**, Representative zoom-in HAADF image taken from the local region marked by square in **a**, showing the formation of Cs^+ islands with a periodicity of ~3.4 nm. Scale bar, 5 nm. **c**, Fast Fourier transform (FFT) of **b**, where the Cs^+ lattice/biotite matrix spots (*G* corresponding to lattice vector of 5.3 Å), are surrounded by satellites caused by the periodic occurring of Cs^+ islands (*L* corresponding to Cs^+ superlattice vector of 3.4 nm), showing the exchanged Cs^+ ions are spatially modulated by the twist angle. Scale bar, 2 nm^{-1}.

into the crystal. Scale bar, 5 nm. **g,** Histograms of measured Cs^+ penetration distances for individual layers in 66L and 22L crystals shown in **a** and **b.**

The case of ion-exchange speed in muscovite is also of interest. Most studies have reported extremely slow interlayer ion exchange in muscovite; below what is measurable in a realistic time frame [14,16]. Our observation of exchanged interlayer Cs^+ diffusion only reaching several nanometres from the muscovite edges is consistent with these reports. We measured STEM images for a few layered muscovite specimen Cs exchanged for 300 hrs (12.5 days, Fig. 2d, main text) and for >9 months, (Fig. S5f). Despite the large difference in time, negligible additional interlayer exchange was observed after 9 months. For both samples Cs^+ ions can be identified only within several nanometres from the crystal edges of which gives the upper bound for the estimated interlayer ion diffusivity in muscovite as $D_{6L\text{-}Mus}$<<10^{-11} µm^2 s^{-1}, showing that only the surface basal plane of muscovite is believed to allow for ion exchange. Indeed, our density-functional-theory (DFT) calculation found that removing one K^+ ion at the surface of a bilayer muscovite increases the energy of the system by ~1.3 eV, while at the interlayer space the energy cost is ~2.2 eV. Therefore, ion exchange at the surface of muscovite is much more favourable compared to interlayer ion exchange, in agreement with the experimental results.

Diffusivity measurements were also performed on few layer specimens of biotite for various thickness. timescale considered in this work (up to 9 months)[14]. Again, only the few nanometers

close to the edges of the crystal were ever found to have interlayer exchange providing maximum diffusivity values for few layer biotite, $D_{4L\text{-}Bio}$, only ~3 times larger than for muscovite (Fig. 2e, main text).

7 Observing fast ion exchange at the interfaces of restacked flakes

To the best of our knowledge no previous work has considered the speed of ion exchange for the interlayer space between restacked clay and mica crystals. Note that restacked flakes are always misaligned, due to the negligibly small probability of restacking two flakes in the perfect crystallographic orientation. Indeed we find that the flakes are misaligned even if we intentionally try to align the two crystals[17]. Fig. S6a shows plan-view characterization results for a biotite flake that consists of both a restacked region and a bilayer region. The restacked region (ΔP > 2 μm, see Fig. S6a) was found to have been fully exchanged by Cs^+ after exposed to for t= 1 hour, which gives $D_{twist\text{-}Bio} > 10^{-4}$ μm^2 s^{-1}, whereas 2L region shows no Cs exchange. Fig. S6a is a high-resolution HAADF-STEM image taken from the exchanged twisted region and periodic contrast showing Cs^+ islands were observed, consistent with the example shown in main text. Corresponding fast Fourier transform pattern (Fig. S6c) show satellites peaks that can be assigned to the superlattice vector. Such satellite peaks are a signature of periodic Cs^+ islands and can only be observed in the Cs-exchanged twisted biotite region.

Fig. S7 show cross-sectional characterization for two restacked multilayer biotite flakes, that were exposed to the Cs-exchange procedure for t= 1 hour after being restacked. Fig. S7c,d show high-resolution images indicating that the interlayer space between the two misaligned crystals indeed hosts only one plane of Cs^+ ions, visible as a row of bright dots. In contrast, the interlayer spaces in each of the original flakes show no Cs exchange at all. From performing many similar STEM studies of interlayer ion exchange for the interface between twisted mica crystals, we find that ion exchange in the interlayer space between two twisted biotite flakes takes place ~8 orders of magnitude faster than in the interlayer space of perfect biotite crystals. This is the case even if the two twisted flakes are relatively thick (≳10 layers thick). We also note that the interlayer distance at the interface between the two flakes is just ~1.0 nm. This rules out the presence of contamination, like hydrocarbons, at the interface as a contributor to fast ion exchange. Instead, it is consistent with our explanation outlined in the main text, which attributes the fast ion exchange to the weaker interlayer binding energy between the misaligned flakes.

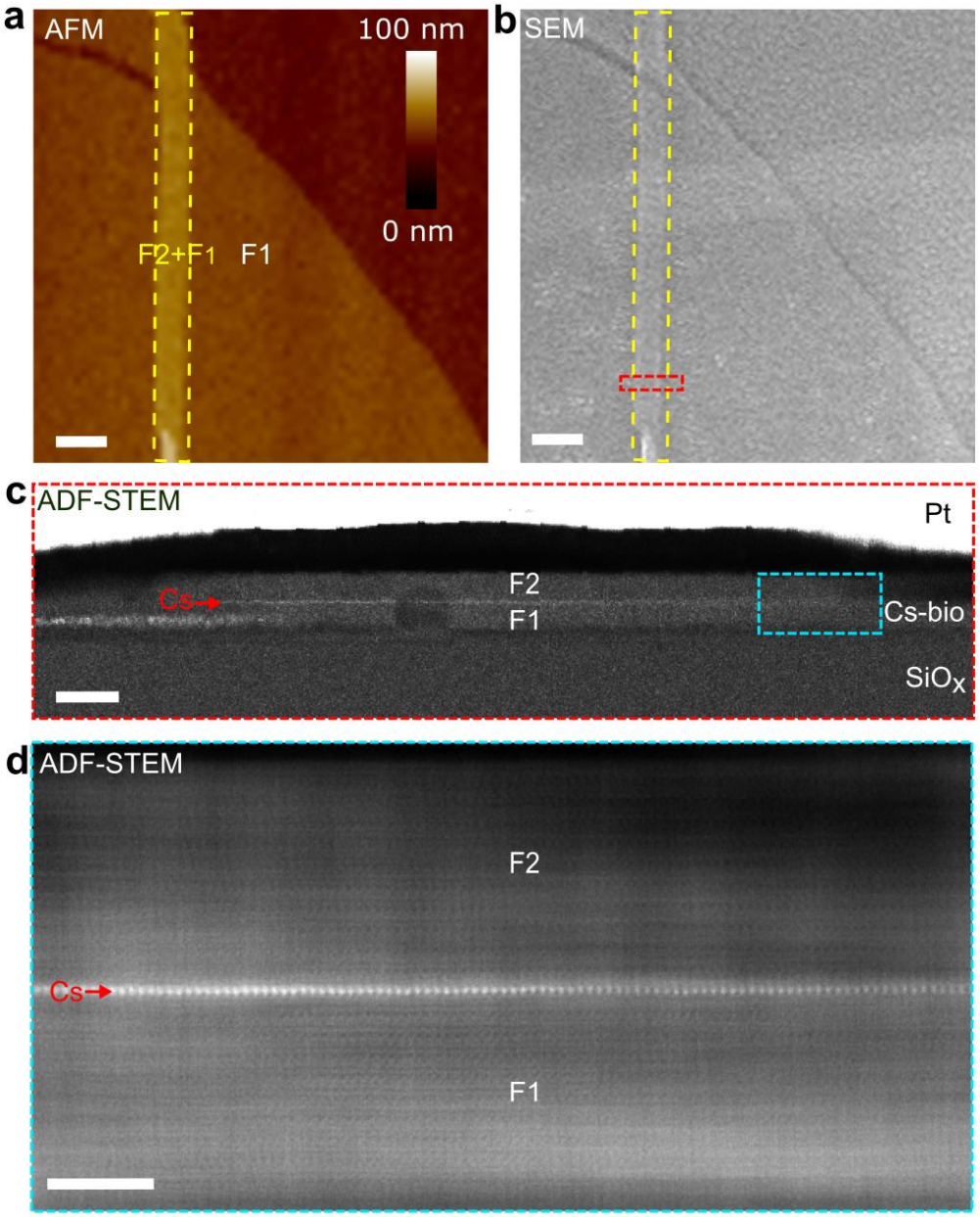

Supplementary Figure S7| Ion exchange at the interface of twisted multilayer biotite flakes. a, AFM topography image taken from a biotite sample consisting of two restacked flakes. The bright-contrast region shows the area where the two biotite flakes (labelled as F1, and F2) are restacked. Scale bar, 500 nm**. b,** Scanning electron micrograph of the sample in **a**. The red marker shows the region that was lifted out for FIB TEM cross-sectioning. Scale bar, 500 nm. **c,** Corresponding HAADF-STEM image taken from the as-prepared TEM cross-sectional specimen. Scale bar, 20 nm. **d,** Magnified HAADF-STEM image taken from the area marked by the blue rectangle in **b**. Scale bar, 5 nm.

8 Measuring the binding sites of adsorbed Cs ions on mica and clay surfaces

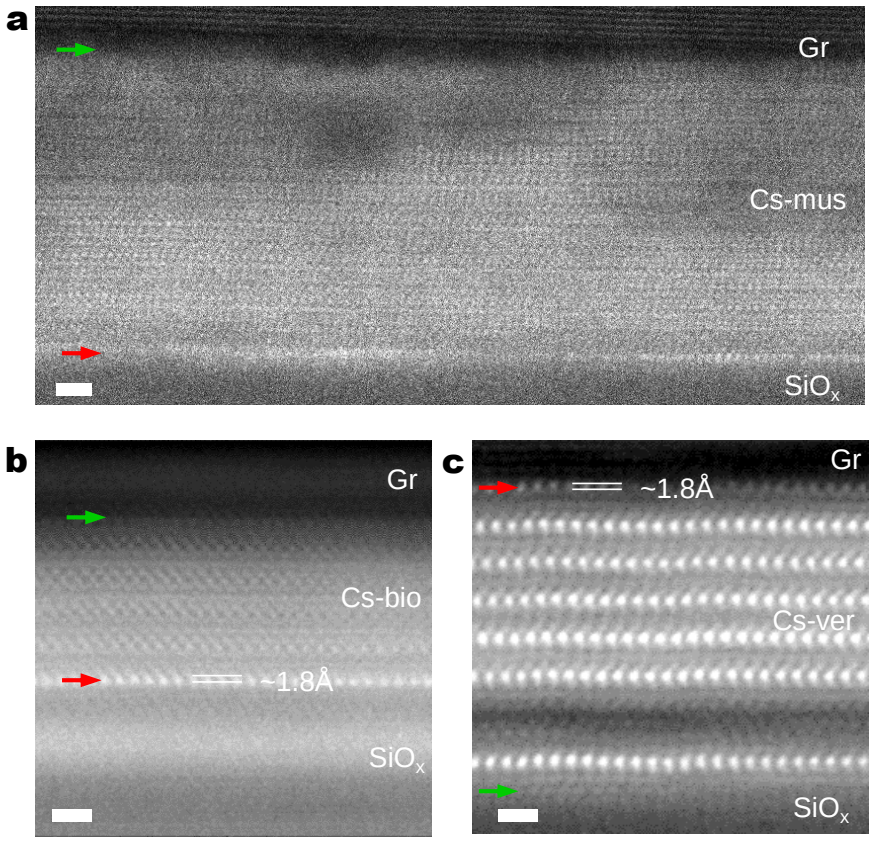

Supplementary Figure S8|Out-of-plane distribution of surface ions on clay and mica. a,b,c HAADF-STEM cross-sectional image of a muscovite (**a**), biotite (**b**) and vermiculite (**c**) specimens. Red (green) arrows indicate the Cs^+ (native) ion dominated surface layer. Scale bars, 1 nm.

By encapsulating the mica and clay flakes between graphite and a Si substrate, we find it is possible to perform cross-sectional STEM imaging in order to probe the position of adsorbed surface ions (Fig. S8). Analysis of these images allows measurement of the projected out-of-plane separation, *z*, between the surface-ion plane, and the outmost edge of the 'T' aluminosilicate layer at the basal surface[18,19]. We find that the *z* values for native ions, are the same for all materials within our experimental measurement error: $z \approx 1.4 \pm 0.2$ Å. On the other hand, we find a relatively large variability in *z* for surface adsorbed Cs^+ ions. We observe $z \approx 1.8 \pm 0.2$ Å for Cs for the biotite and vermiculite specimens in Fig. S8b and 8c, respectively which is notably smaller than the $z \approx 2.5 \pm 0.2$ Å for the muscovite specimen in the main text (Fig. 4). We speculate that the larger variability in *z* for Cs adsorption compared to the native ion location is due to the more complex hydration structures possible for surface adsorbed Cs. Cs^+ ions on mica and clay surfaces have been reported

to exist in both 'inner-sphere' and 'outer-sphere' hydration states[18-22]. Although to our best knowledge, STEM imaging has not previously been demonstrated for adsorbed surface ions, such

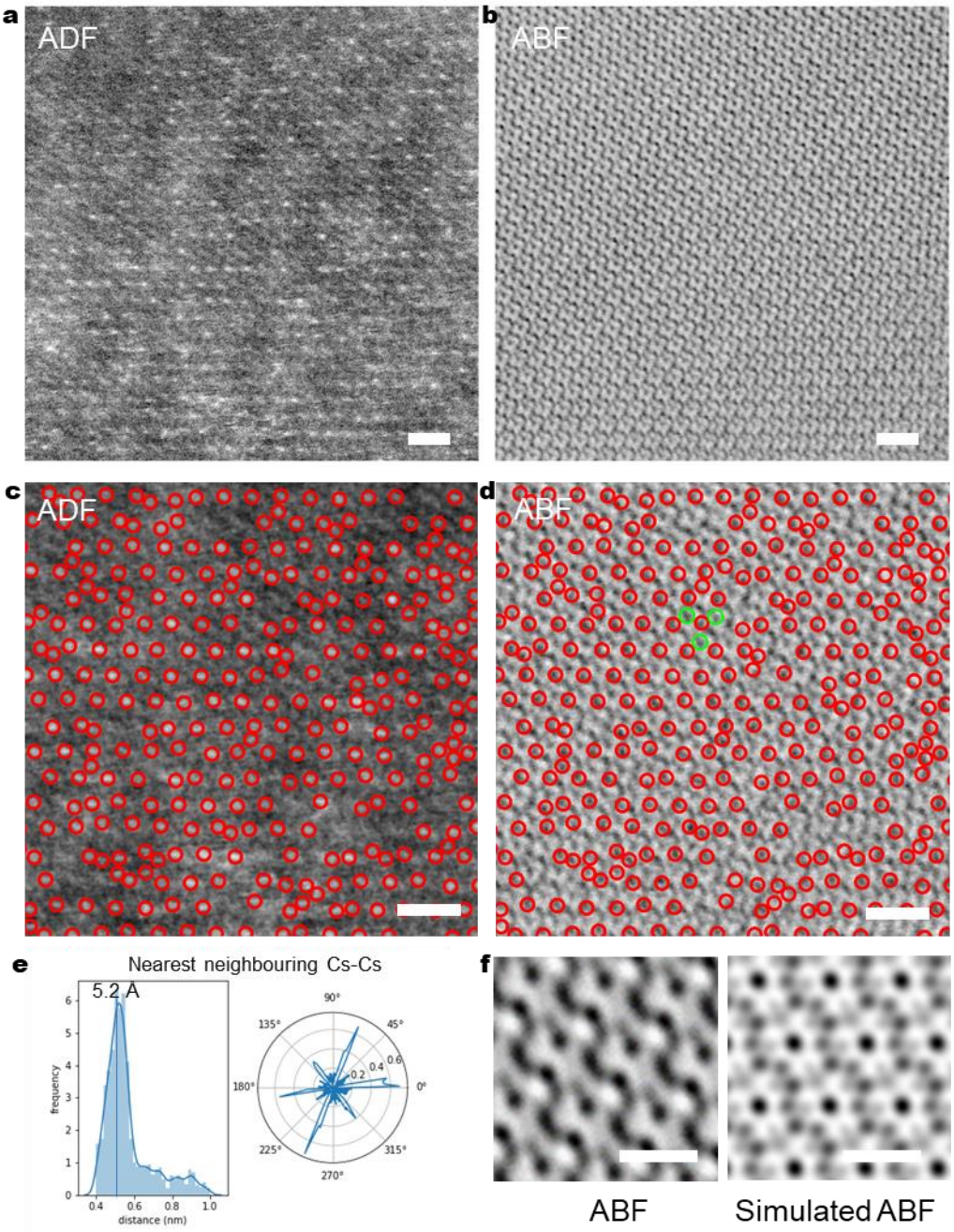

Supplementary Figure S9|Local ordering of surface adsorbed Cs^+ ions on monolayer muscovite. **a,** HAADF-STEM plan view image of monolayer muscovite. Cs^+ ions are visible as bright dots. **b,** ABF-STEM image of the same area imaged in **a**. **c,** HAADF image with Cs^+ ion positions marked with red circles. **d,** Corresponding ABF-STEM image with Cs ion positions identified from the HAADF image marked by red circles. Green circles mark the position of selected K^+ ions. **e,** Histogram of nearest neighbour Cs-Cs interion distance. Right panel shows the relative orientations between the neighbouring Cs^+ ions, demonstrating a quasi-hexagonal symmetry and local ordering of adsorbed ions aligned to the underlying aluminosilicate lattice. **f,** Left, magnified averaged experimental ABF-

STEM image. Right, simulated ABF-STEM image for monolayer muscovite. **a-d,** Scale bars, 1 nm. **f,** Scale bars, 5 Å.

differences in hydration complexes are known to yield different z[18,19,21], which explains the z variability we observe experimentally.

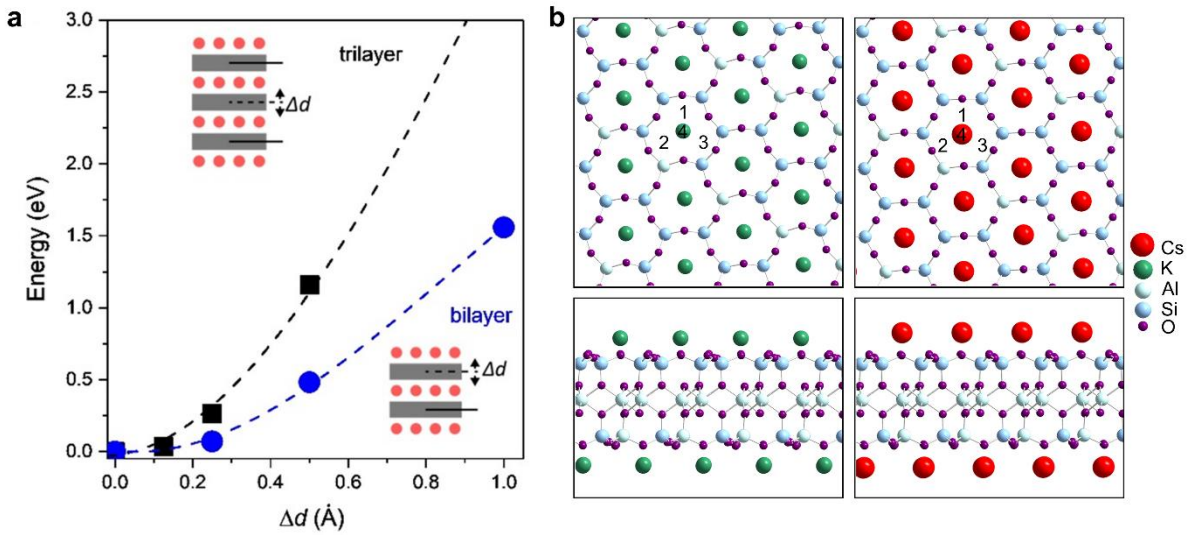

Figure S10| DFT calculation of energies involved in the ion exchange process. a, Interlayer binding energy for dehydrated vermiculite clay as function of layer displacement (Δd) from its equilibrium position. Data for trilayer vermiculite, black symbols; data for bilayer vermiculite, blue symbols. Dotted lines, guide to the eye. Top inset, schematic of trilayer clay indicating that the middle layer is displaced by Δd. Bottom inset, schematic of bilayer clay. Grey rectangles, aluminosilicate layers; red balls, exchangeable ions. Solid horizontal lines indicate that the aluminosilicate layers are fixed in the z-direction. Dotted horizontal lines indicate the layer being displaced. **b**, Top left, plan view DFT relaxed atomic model of the muscovite basal plane with K^+ ions adsorbed. The adsorption sites at which the adsorption energy of ions was calculated is marked with black dots labelled 1,2 and 3 (Type II), 4 (Type I). Bottom left, cross-sectional projection of top left panel. Top and bottom right, corresponding images for Cs^+ exchanged muscovite.

Cross-sectional images only provide information on the out of plane location of surface ions. In order to analyse the location of exchanged ions with respect to the underlying aluminosilicate lattice we have obtained simultaneously acquired HAADF- and annular bright field (ABF)-STEM plan view images of a Cs exchanged muscovite monolayer flake (exchange time 24 hours, Fig. S9). The positions of Cs ions were identified from bright dots in the HAADF image (shown as the red circles in Fig. S9) and this was related to the aluminosilicate lattice structure observable from the simultaneously acquired ABF image. A statistical analysis was conducted on the Cs^+ ion positions in order to understand their surface distribution. Fig. S9e shows the calculated histogram from the nearest neighbour Cs-Cs distances as a function of relative orientation, revealing that Cs^+ ions form a semi-ordered hexagonal lattice with a mean inter-ion separation of ~5.2 Å. To identify the location

of the Cs^+ ions with respect to the aluminosilicate support and confirm the expected monolayer structure, we compared the experimental images to simulations. This revealed that 228 out of 300 Cs^+ positions (76%) can be identified as Type II binding sites, i.e. adsorption on the vertex between three oxygen atoms in ditrigonal rings. On the other hand, nearly all K^+ ions were found to adsorb at the centre of the ditrigonal rings (Type I sites, see Fig. 4 in maintext). The location of selected K^+ ions are marked by the green circles in Fig. S9d. Only a few are indicated for clarity, but nearly all K ions were found to be located in Type I sites.

9. Theoretical Modelling

9.1 Methods

DFT calculations were performed using the projector augmented wave (PAW) method implemented in the Vienna *ab-initio* Simulation Package (VASP)[23-25]. The electron exchange and correlation is described by adopting the Perdew-Burke-Ernzerhof (PBE) form of the generalized gradient approximation (GGA)[26]. The van der Waals force – important for layered materials – was introduced by using DFT-D2 method of Grimme[27]. The following parameters were used in our calculations. The kinetic energy cut-off of the plane-wave basis set was 500 eV in all calculations Convergence was assumed if the energy difference between sequential steps in the iterations was below 10^{-5} eV. Gaussian smearing of 0.05 eV was used.

9.2 Calculating interlayer binding energies and surface sites

To gain insight into the experimentally observed fast ion exchange for the interlayer of bilayer vermiculite clays, we calculated the energy necessary to expand the interlayer space in bilayer and multilayer clays using DFT. To that end, we calculated the interlayer binding energy of the clay layers as a function of separation in the perpendicular direction to the plane (*z*-direction). For a given *z*, this energy was calculated using the formula $E_b = (nE_{1L}-E_{nL}) / (n-1)$; where *n* is number of layers, and E_{1L} and E_{nL} are the total energies of single layer and n-layer systems, respectively. To model the expansion in bilayer clays, one of the layers was fixed in the *z*-direction and the other layer was displaced by a distance, Δd, from its equilibrium position. The expansion in multilayer clays was modelled using a trilayer clay structure where both surface layers are fixed in the *z*-direction and the middle layer was displaced by a distance Δd from its equilibrium position. Fig. S10a shows that expanding the interlayer space in multilayer clays requires significantly higher energy for any Δd. Even for a modest expansion of $\Delta d \approx 0.5$ Å, the energy necessary for the expansion is ~1 eV higher for multilayer than for bilayer clays. For $\Delta d \approx 1$ Å, this difference is ~2 eV. This energy difference is due to the resistance to expansion placed by the outermost layer in the multilayer model, which is not present in bilayers. This large energy difference is consistent with the experimental observation that *D* for bilayer clays is over 6 orders of magnitude larger than for multilayer clays.

DFT was also used to study the adsorption site of ions (K^+ or Cs^+) on the basal surface plane of thin muscovite; in particular, to understand the different binding sites found for K^+ and Cs^+ in the experiment. To that end, un-hydrated ions were placed at different sites on the basal plane (see Fig. S10b) and the structure was allowed to relax. We found that in the dehydrated relaxed structures, both ions adsorbed at the centre of the hexagonal rings, regardless of their initial position. For K^+ ions this finding is consistent with our STEM images. As for Cs^+, the finding suggests that the hydration shell of Cs plays a crucial role in its adsorption, which is hardly surprising. As mentioned in section 8, Cs^+ ions on micas' surfaces can form various hydration states[28,29]. Such differences in hydration states should lead to different lateral binding sites for surface ions in the lattice[28,29], as we observed in the experimental data.

9.3 Ion superlattices

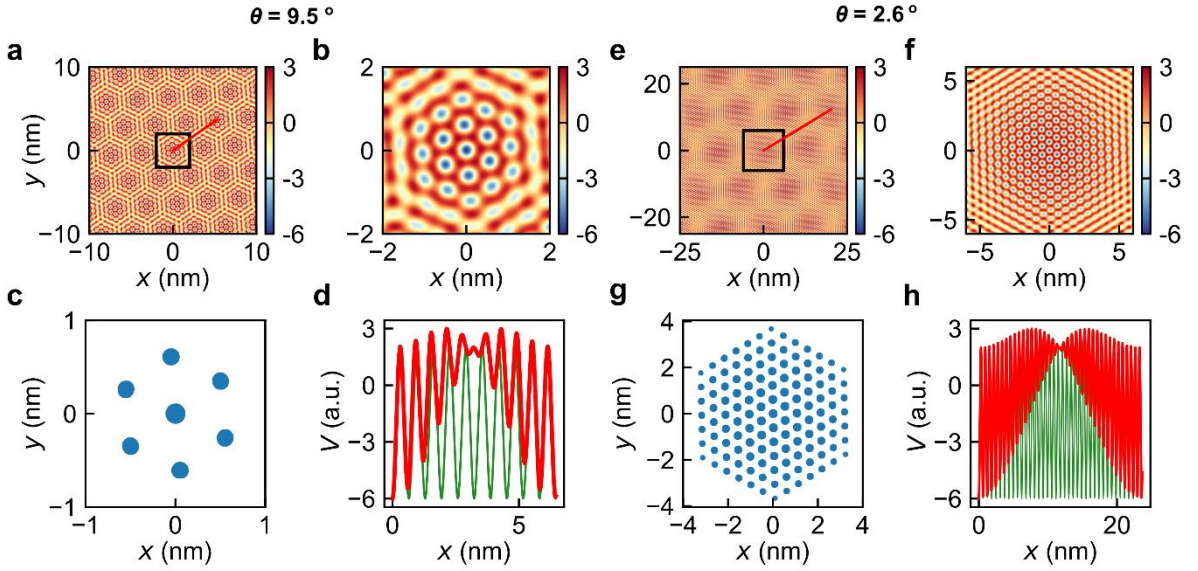

Figure S11| Model of interlayer potential energy landscape in twisted biotite. a, Potential energy map resulting from the superposition of two hexagonal periodic potentials with a twist angle of ϑ = 9.5°, each with a period of 0.53 nm. The resulting moiré potential has a period of 3.1 nm. Energy scale in arbitrary units. **b**, Magnified region of the potential energy map from the high-symmetry area marked by the black square in panel **a**. **c**, Potential energy map with blue dots marking the areas where the energy minima is 77% as deep or deeper than the minima of the pristine single-layer potential. **d**, Red line is the potential energy profile taken along the red line in panel **a** (drawn from one AA site to a neighbouring one) compared to the equivalent line profile taken from a perfectly aligned (untwisted) bilayer system (green line). **e,f,g,h**, Corresponding results for a smaller twist angle, ϑ = 2.6°.

To gain insight into the moiré patterns observed in twisted biotite micas, we modelled the potential energy landscape in their interlayer space. Each of the biotite layers was modelled using a periodic hexagonal potential (same period as in the mica lattice) and these were then superposed at a twist

angle ϑ ($V(\vartheta)+V(0^o)$). Fig. S11 shows our results for twist angles of $\vartheta = 9.5^o$ and $\vartheta = 2.6^o$. We found that the superposed potential consists of minima (blue dots in Fig. S11c,g) at the AA stacked high-symmetry areas of the moiré unit cell, which cluster in groups of 7 and 127 for $\vartheta = 9.5^o$ and $\vartheta = 2.6^o$, respectively. Outside of these clusters, the potential becomes repulsive (red and orange areas in Fig. S11a,b,e,f). Note that the number of minima per cluster is in good agreement with the number of Cs^+ ions per island observed in the experiment (~7 and ~130 for $\vartheta = 9.5^o$ and $\vartheta = 2.6^o$, respectively). This indicates that the energy necessary to trap ions is 77% of the single-layer potential minima. Furthermore, we find that these clusters occur periodically and with the same periodicity found experimentally for the Cs^+ superlattices. These results therefore validate the use of this model, which attributes the Cs^+ superlattice islands to moiré potential 'wells'.

The model also helps to explain the large enhancement in ion exchange speed found in twisted biotite compared to the pristine aligned interlayers. Fig. S11d,h show that in a twisted system (red curves), for sites outside the high-symmetry AA region of the moiré unit cell, the interlayer potential energy is higher (more positive/repulsive) than that in the aligned bilayer system (green curves). This results in a less favourable interlayer binding in twisted materials compared to that in pristine untwisted one, which in turn facilitates enhanced ion entry probability and diffusion.

10. Liquid AFM Measurement of Vermiculite Swelling and Exchange

To gain insight into vermiculite layer swelling when immersed in an ion exchanging solution, AFM measurements of few-layer vermiculite in dry ambient conditions, as well as imaging after immersion in a 0.1 M NaCl and CsCl solution were performed.

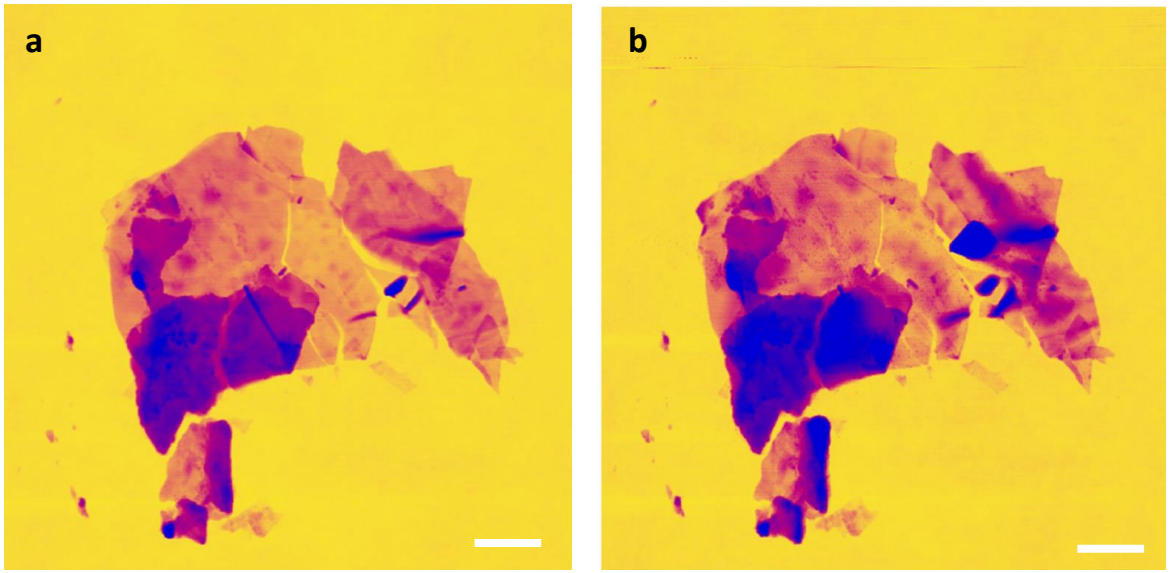

Figure S12| Few layer vermiculite before and after immersion in 0.1 M NaCl. a, *AFM image of Vermiculite sample in dry ambient conditions and* ***b****, an AFM image of the same sample in 0.1 M NaCl aqueous solution. Scale bar 1 µm.*

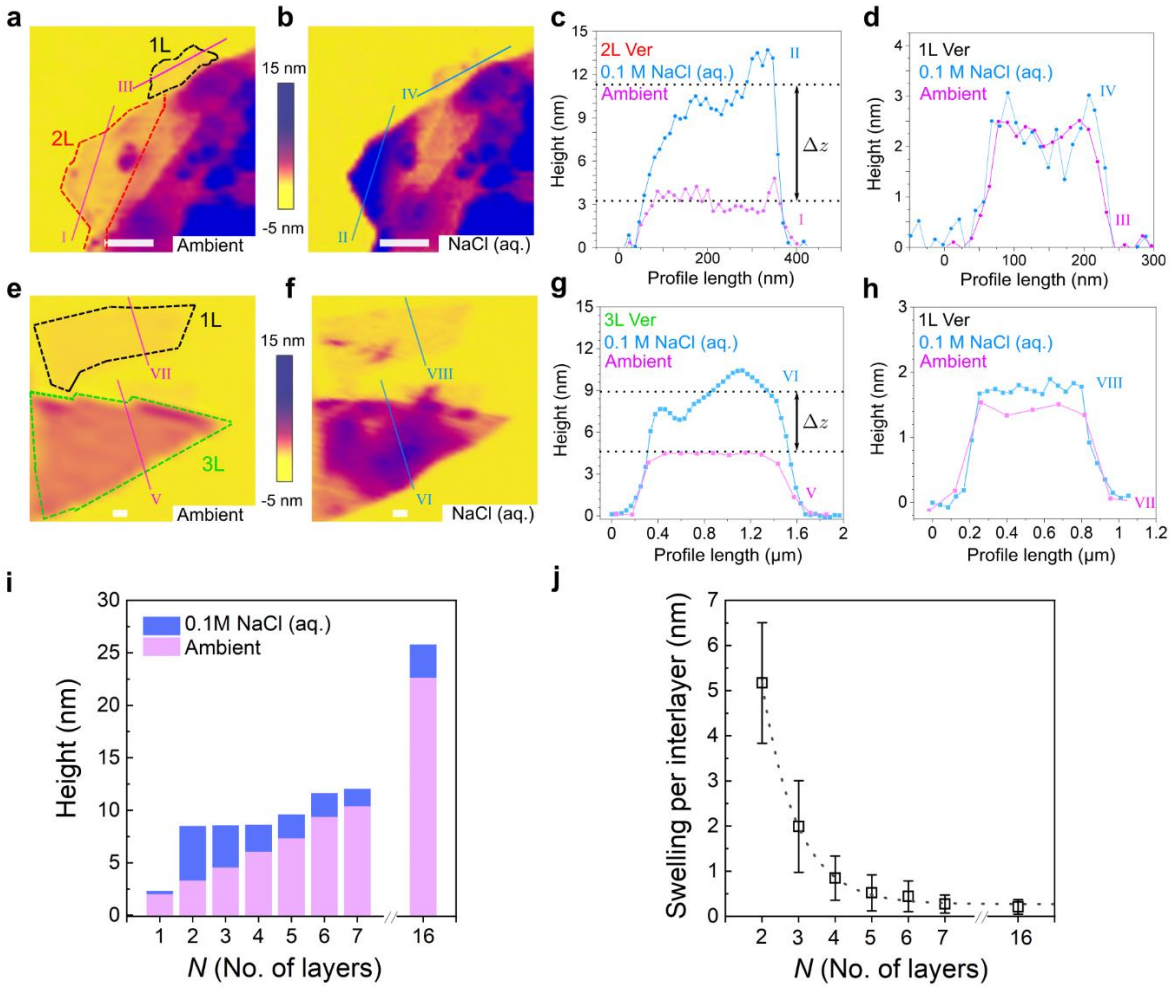

Supplementary Figure S13| Measurements comparing swelling behaviour of vermiculite with different thicknesses in NaCl solution. a-d, AFM results for a 2L vermiculite region (outlined by red dashed lines) and a local 1L region (outlined by black dashed lines). **a, b,** AFM height image taken **a,** in ambient air and **b,** in aqueous 0.1 M NaCl. **c,d,** Corresponding height profiles in air and liquid extracted from the positions of the lines (I, II, III, IV) for **c,** 2L region and **b,** 1L region. **e-h,** AFM results for a 3L vermiculite (green dashed lines) containing a local 1L region (black dashed lines). **e, f,** AFM height image taken **e,** in ambient air, and **f,** in aqueous 0.1 M NaCl. **g,h,** Corresponding height profiles extracted from the positions of the lines (V, VI, VII, VIII) for **g,** 3L region, and **h,** 1L region. **i,** Statistical results showing the AFM measured height (*z*) values for vermiculite as a function of *N*, in ambient air (magenta) and liquid NaCl (blue). Swelling values (Δ*z*) are extracted as height difference in liquid and ambient, with the standard deviation extracted from at least three different measurements. **j,** Mean swelling values per interlayer as a function of *N*, calculated as Δz x $(N\text{-}1)^{-1}$ using Δz values shown in **i**. Dotted line, guide to the eye. Scale bars, 200 nm.

To investigate the possible effect of crystal thickness on interlayer expandability, we measured the height profile of vermiculite flakes in ambient conditions and in liquid using AFM. Swelling values for a certain flake are extracted from the difference in height measured in ambient air and in liquid environment. To ensure that the difference in height is not due to water intercalation between the vermiculite flake and the substrate, the SiO_x/Si substrates were coated with an adhesion layer of

SU8 3005 epoxy and then photo-cured under a UV source. Vermiculite samples were then mechanically exfoliated onto the as-prepared substrates. The samples are 'hard

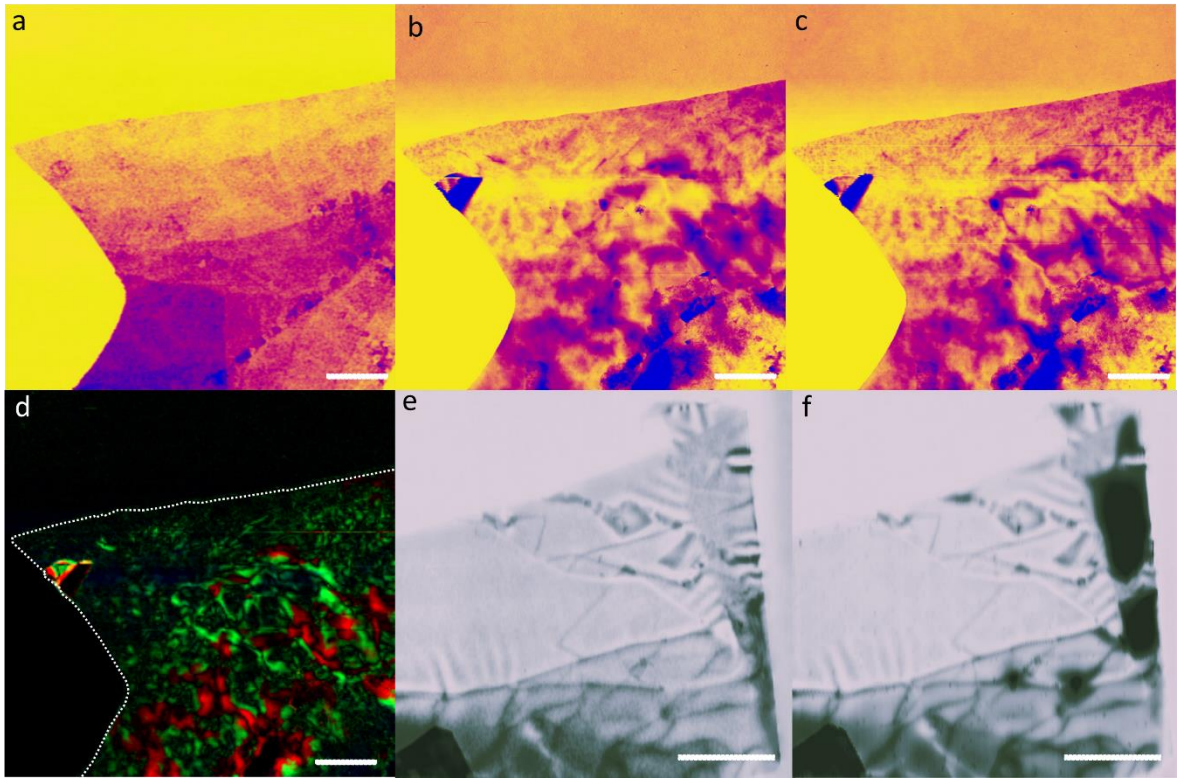

Supplementary Figure S14| Liquid AFM measurements of the ion exchange and swelling effects of few-layer vermiculite. a) few layer (8-15L) sample in ambient air conditions prior to ion exchange solution. b) Scan after immersion in 0.1 M NaCl solution. c) Scan in 0.1 M CsCl solution. d) Subtraction of b and c height profiles. e) an overlapped vermiculite particle in dry ambient conditions and then f) scanned in DI water. Scale bars a-f 4 µm**.**

baked', typically at 60 °C for 10 minutes, to further promote polymer/clay adhesion. For measurements in ambient air, AFM scans were taken in ambient conditions in a 1000 class clean room environment at ~50% relative humidity and ~21 °C. For measurement of flakes immersed in liquid, we used a 0.1M NaCl and CsCl aqueous solution.

Such measurements are presented in figures S12, S13 and S14. The clay height profiles can be observed dynamically as solution is imbibed within the lattice. We can assume that this process accompanies the ion exchange process within the interlayer space. Three major observations are made. The first is that single layer vermiculite (consisting of no interlayer space) undergoes negligible swelling, which is to be expected if occurring within the clay interlayer. Secondly, bilayer vermiculite clay swells to a larger degree relative to its thickness than thicker clays, as presented in figure S13 i). Thirdly, overlapped (or restacked) clay layers swell considerably more than intact layers. These observations support the proposed mechanism of enhanced exchange rates arising from decreased layer adhesion as the number of layers of vermiculite is decreased.

This technique, more generally, offers the exciting possibility to observe the morphology/swelling of clays as ion exchange occurs, something experimentally challenging to undertake. To illustrate this, an experiment was performed where a sample of few-layer vermiculite is scanned via AFM and then immersed in NaCl and then subsequently CsCl 0.1 M solutions as it is scanned in solution. As already discussed, caesium cations are known to exchange preferentially over sodium cations and as our TEM images have shown, collapse the interlayer space. This effect manifests in changes in height profile of the vermiculite particle in figure S14 a-d. Finally, the reduced layer-layer bonding of twisted layer vermiculite is evidenced in the swelling observed in S14 e and f as the regions overlapping undergo expansion in water to a greater degree than non-overlapping regions.

References

1 Liang, J.-J. & Hawthorne, F. C. Rietveld refinement of micaceous materials; muscovite-2M 1 , a comparison with single-crystal structure refinement. *Can. Mineral.* **34**, 115-122 (1996).

2 Takeda, H. & Ross, M. Mica polytypism: Dissimilarities in the crystal structures of coexisting 1M and 2M1 biotite. *Am. Mineral.* **60**, 1030-1040 (1975).

3 Shirozu, H. & Bailey, S. W. Crystal structure of a two-layer Mg-vermiculite. *Am. Mineral.* **51**, 1124-1143 (1966).

4 Kretinin, A. V. *et al.* Electronic Properties of Graphene Encapsulated with Different Two-Dimensional Atomic Crystals. *Nano Lett.* **14**, 3270-3276 (2014).

5 Hjorth Larsen, A. *et al.* The atomic simulation environment—a Python library for working with atoms. *J. Phys.: Condens. Matter* **29**, 273002 (2017).

6 Koch, C. T. *Determination of core structure periodicity and point defect density along dislocations*. (2002).

7 Smith, D. W. Ionic hydration enthalpies. *J. Chem. Educ.* **54**, 540 (1977).

8 Collins, D. R., Fitch, A. N. & Catlow, C. R. A. Dehydration of vermiculites and montmorillonites: a time-resolved powder neutron diffraction study. *J. Mater. Chem.* **2**, 865-873 (1992).

9 Ma, L. *et al.* The structural change of vermiculite during dehydration processes: A real-time in-situ XRD method. *Appl. Clay Sci.* **183**, 105332 (2019).

10 Dymek, R. F. Titanium, aluminum and interlayer cation substitutions in biotite from high-grade gneisses, West Greenland. *Am. Mineral.* **68**, 880-899 (1983).

11 Egerton, R. F. Radiation damage to organic and inorganic specimens in the TEM. *Micron* **119**, 72-87 (2019).

12 Helfferich, F. *Ion Exchange*. (McGraw Hill, 1962).

13 Jost, W. *Diffusion in solids, liquids, gases*. 3rd printing with addendum. edn, (Academic, 1960).

14 Nye, P. H. in *Advances in Agronomy* Vol. 31 (ed N. C. Brady) 225-272 (Academic Press, 1980).

15 Lai, T. M. & Mortland, M. M. Cationic Diffusion in Clay Minerals: II. Orientation Effects. *Clays Clay Miner.* **16**, 129-136 (1968).

16 Gaines, G. L. The Ion-exchange Properties of Muscovite Mica. *The Journal of Physical Chemistry* **61**, 1408-1413 (1957).

17 Ponomarenko, L. A. *et al.* Cloning of Dirac fermions in graphene superlattices. *Nature* **497**, 594-597 (2013).

18 Bostick, B. C., Vairavamurthy, M. A., Karthikeyan, K. G. & Chorover, J. Cesium Adsorption on Clay Minerals: An EXAFS Spectroscopic Investigation. *Environ. Sci. Technol.* **36**, 2670-2676 (2002).

19 Schlegel, M. L. *et al.* Cation sorption on the muscovite (001) surface in chloride solutions using high-resolution X-ray reflectivity. *Geochim. Cosmochim. Acta* **70**, 3549-3565 (2006).

20 Cheng, L., Fenter, P., Nagy, K. L., Schlegel, M. L. & Sturchio, N. C. Molecular-Scale Density Oscillations in Water Adjacent to a Mica Surface. *Phys. Rev. Lett.* **87**, 156103 (2001).

21 Lee, S. S., Fenter, P., Nagy, K. L. & Sturchio, N. C. Real-time observation of cation exchange kinetics and dynamics at the muscovite-water interface. *Nature Comm.* **8**, 15826 (2017).

22 Xu, L. & Salmeron, M. An XPS and Scanning Polarization Force Microscopy Study of the Exchange and Mobility of Surface Ions on Mica. *Langmuir* **14**, 5841-5844 (1998).

23 Kresse, G. Ab initio molecular dynamics for liquid metals. *J. Non-Cryst. Solids* **192-193**, 222-229 (1995).

24 Kresse, G. & Furthmüller, J. Efficient iterative schemes for ab initio total-energy calculations using a plane-wave basis set. *Phys. Rev. B* **54**, 11169-11186 (1996).

25 Kresse, G. & Joubert, D. From ultrasoft pseudopotentials to the projector augmented-wave method. *Phys. Rev. B* **59**, 1758-1775 (1999).

26 Perdew, J. P., Burke, K. & Ernzerhof, M. Generalized Gradient Approximation Made Simple. *Phys. Rev. Lett.* **77**, 3865-3868 (1996).

27 Grimme, S. Semiempirical GGA-type density functional constructed with a long-range dispersion correction. *J. Comput. Chem.* **27**, 1787-1799 (2006).

28 Sakuma, H. & Kawamura, K. Structure and dynamics of water on Li^+-, Na^+-, K^+-, Cs^+-, H_3O^+-exchanged muscovite surfaces: A molecular dynamics study. *Geochim. Cosmochim. Acta* **75**, 63-81 (2011).

29 Huang, K. *et al.* Cation-controlled wetting properties of vermiculite membranes and its promise for fouling resistant oil–water separation. *Nature Commun.* **11**, 1097 (2020).

Chapter 9

Conclusions and Outlook

In this work, we have presented ion transport phenomena of 2D materials such as graphene, hexagonal boron nitride, micas and clays. Specifically, the objective was to contribute to the fundamental understanding of the ion-selective nature of 2D material membranes, expand the knowledge of proton transport for a wide range of 2D materials, and explore the process of ion-exchange for few-atomic-layer-thick clays and micas. To these ends, we have presented work to each of those topics respectively in chapters 6, 7 and 8.

To shed further light on the proton transport mechanisms through 2D materials, we studied proton over chloride selectivity using two reservoirs of HCl separated by a 2D material and measured the membrane potential. As discussed, the membrane potential is established from selective transport, and in this study, we measure a potential reflective to that of a perfectly selective membrane (possessing a transport number t_+=1). The observation of negligible chloride ion transport lends support to the proposed mechanism for non-defect mediated transport. However, as we have seen, cation-selective nanopores can still display selectivity.

Few-atomic-layer-thick micas were reported to be highly proton conductive, even at temperatures beyond 200 °C. This came as a surprise, given the impermeability of the three-atom thick MoS_2. This conductivity was shown to be facilitated by proton exchange of the mica lattice where the transport process is assumed to be rather different from that of the proposed mechanism for monolayer graphene and hBN. We attribute mica proton permeation to 5 Å wide tubular channels that perforate micas' crystal structure, which, after ion-exchange, contain only hydroxyl groups within. It is worth noting that for bilayer proton exchanged muscovite, we ascribed a change in thermally-activated electrical measurements to a switch from proton- to electron-dominated transport at around 220 °C. We demonstrated the ion-exchangeable nature of the surfaces of bilayer mica, byway of S/TEM imaging exchanged caesium ions.

In the last study, we aimed to further investigate ion-exchange effects in atomically-thin mica and clays. To achieve this, we exfoliated and targeted few-layer clay minerals to study ion-exchange rates, by measurement of the diffusion coefficient directly, using the S/TEM snapshot method. We observed close to bulk aqueous ion diffusion rate exchange in few-layer clay minerals. In this work, we also showed ion distribution on the surface of mica and clay minerals in very high detail using HAADF-S/TEM. We isolated monolayer muscovite and were able to resolve the binding sites of caesium ions using a combination of bright-field

and dark-field S/TEM imaging.

Let us now finally discusses the future outlook and work that could ensue from the work presented in this thesis. Atomically-thin crystals as ion conductive membranes are a fascinating system to explore and present desirable properties from a fundamental proton transport, selective and ion-exchange perspective. They offer us bench-top scale systems to probe as well as the exciting possibility to fabricate at scale. For example, if we can fabricate large-scale mica membranes, we could use them as highly-conductive elevated temperature fuel cell separation membranes, with a desirable set of qualities. Demonstrating that micas are highly permeable to protons opens the door to many other 2D oxide minerals as candidate proton-conductors, a whole new area of study to explore.

The proton selective nature of 2D materials such as graphene and hBN offer the exciting possibility to use these materials as barriers in selective technologies, such as in hydrogen fuel cells, reducing detrimental effects such as fuel cross over. From a fundamental perspective, we can use 2D material membranes to study systems in which reservoirs are separated by membranes whose length-scales are smaller or comparable to the Debeye length. Exploring the fast ion-exchanging properties of few-atomic-layer-thick clays is a new area of research. Given the large application range for ion-exchangers, these materials may offer ion-exchange and storage solutions, such as the fast adsorption and entrapment of dangerous radionuclides. Being able to study the ion-exchange properties of clays at such a high level of resolution and in a targeted fashion is a new experimental capability that affords new ways to study these systems. Further, the work undertaken here may be applied to other few-atomic-layer exchangers such as layered double hydroxides, zeolites, metal-organic-frameworks and perovskites. The surface S/TEM imaging of the ion distribution of mica and clay has hitherto proven to be a significant experimental challenge, we may now be able to explore selectivity and kinetics at unprecedented levels of detail. Further work beyond this thesis could involve investigating how ion-exchange may enhance other properties of 2D materials, and perhaps gain further insight into how clay/mica compositional changes may also enhance proton-conducting properties. Finally, AFM measurements of vermiculite clays within ion exchanging solutions, offers a method to map and measure swelling/shrinkage effects as processes such as ion exchange and/or intercalation unfold. This may well be useful for studying hydrophillic layered materials that have hitherto proved challenging to measure in such a way.

Appendices

Appendix A

Migration and Diffusion Currents

Equation 2.1 can be expressed, by encompassing further terms of the electrochemical potential, standard chemical potential (μ_i^0) and the convective term, due to ion velocity ($\bar{\mathbf{v}}_\mathbf{i}$) [1] as

$$\boldsymbol{J_i} = \frac{C_i D_i}{RT} \nabla \left(\mu_{i^0} + RTln(a_i) + (P - P_0)V_i + z_i F\psi \right) + C_i \bar{\mathbf{v}}_\mathbf{i} \tag{A.1}$$

where v_i is the ion velocity . Equation A.1 could also contain further contributions, such as those from van der Waals interactions between ions [2]. Returning to also consider the electrical potential, where an ion has charge valance z_i, the flux J_i is equivalent to (molar) current density I_i

$$J_i(x) = \frac{-I_i(x)}{z_i F A} \tag{A.2}$$

where A is the cross-sectional area of the system. Direct current electrochemical measurements allow us to measure and apply known voltages (ϕ) and currents (I_i) to our system of study. Hence, we can obtain measurements of I_i in equation A.2 and relating this to equation 2.3 we can quantify properties of the system. Further, set concentration gradients can be applied to better limit the unknowns in this equation. By combining equation 2.3 and A.2, We have arrived at an expression for ionic current due to migration and diffusion

$$I(x) = \frac{F^2 A}{RT} \cdot \frac{\partial \phi}{\partial x} \sum_i z_i^2 D_i C_i + FA \sum_i z_i D_i \frac{\partial C_i}{\partial x} \tag{A.3}$$

Measurement of the diffusion coefficients allow us to begin to determine and characterise underlying ion transport mechanisms. Now, the diffusion coefficient is related to the mobility (in bulk solution) μ_i of ions by the Einstein-Smoluchowski equation [3] as

$$\mu_i = \frac{z_i F}{RT} D_i \tag{A.4}$$

Which, by incorporation into equation A.3 one can extract, from bulk[1] current-voltage measurements, the ionic mobility of a given ion

$$I_i(x) = z_i F A \mu_i C_i \cdot \frac{\partial \phi}{\partial x} \tag{A.5}$$

[1] Where concentration gradients are negligible

To determine the velocity profile of ions we can solve the Navier-Stokes equations. This profile can then be included in equation 2.10, allowing a more comprehensive picture of ionic transport. The Navier-Stokes equations are

$$\text{Momentum equations} \tag{A.6}$$

$$\rho\left(\frac{\partial \boldsymbol{v}}{\partial t} + (\boldsymbol{v}\cdot\nabla)\boldsymbol{v}\right) = -\nabla P + \eta_s \nabla^2 \boldsymbol{v} + \rho \boldsymbol{f} \tag{A.7}$$

$$\text{Continuity equation} \tag{A.8}$$

$$\nabla \cdot \boldsymbol{v} = 0 \tag{A.9}$$

Where d_s is the density, P pressure, η_s kinematic viscosity and f represents body accelerations.

Appendix B

Membrane Potential

Where we have a single monovalent ($z = 1$) cation and anion in solution, as will be for this work, we can express equation2.14 as

$$(\phi_\beta - \phi_\alpha) = E_m = -\frac{RT}{F}\int_\alpha^\beta \sum_i t_i, dln(a_i) \tag{B.1}$$

$$= -t_+\frac{RT}{F}ln(\frac{a_{+\beta}}{a_{+\alpha}}) + t_-\frac{RT}{F}ln(\frac{a_{-\beta}}{a_{-\alpha}}) \tag{B.2}$$

The ratio of concentration (a_i) for each ion across the two phases α and β satisfies

$$\frac{a_{+\beta}}{a_{+\alpha}} = \frac{a_{-\beta}}{a_{-\alpha}} \tag{B.3}$$

resulting in equation B.1 becoming a form of the Nernst equation

$$E_m = -(t_+ - t_-)\frac{RT}{F}ln\frac{a_\beta}{a_\alpha} \tag{B.4}$$

where $t_+ + t_- = 1$ being the condition that the sum total of all transport numbers are equal to unity. The membrane potential arising from cation selectivity is therefore given as

$$E_m = -(2t_+ - 1)\frac{RT}{F}ln\frac{a_\beta}{a_\alpha} \tag{B.5}$$

which is the potential established across a cation selective membrane where a concentration gradient $\frac{a_\beta}{a_\alpha}$ exists. The potential can be measured, hence we can readily extract the apparent transport number t_+ from such measurements. If we measure an ion selective membrane using non reference electrodes, immersed in two reservoirs with differing concentration, we must also include the contribution for the electrode redox potential difference E_{redox} from the anode to cathode. Consequently, the measured potential E_{cell} is then the sum

$$E_{cell} = E_m + E_{redox} \tag{B.6}$$

$$= -(2t_+ - 1)\frac{RT}{F}ln\frac{a_\beta}{a_\alpha} + E_{redox} \tag{B.7}$$

For Ag/AgCl electrodes, used extensively in this study, the electrode potential for a given chloride concentration is [1], [2]

$$E_{redox}^{Ag/AgCl} = E_0^{Ag/AgCl} - \frac{RT}{F} ln(a_{Cl^-}) \tag{B.8}$$

Where $E_0^{Ag/AgCl}$ is the potential against the standard hydrogen electrode (SHE). When we consider both electrode potentials for the high concentration and low concentration reservoirs, the redox potential becomes

$$E_{redox,H}^{Ag/AgCl} - E_{redox,L}^{Ag/AgCl} = -\frac{RT}{F} \left(-ln(a_H) + ln(a_L)\right) = -\frac{RT}{F} ln \frac{a_H}{a_L} \tag{B.9}$$

Therefore equation B.7 becomes

$$E_{cell} = -2t_+ \frac{RT}{F} ln \frac{a_H}{a_L} \tag{B.10}$$

The result presented in equation 2.12 is what can be measured using a Ag/AgCl anode and cathode, so long as the solution is compatible with AgCl (typically containing a chloride ion) and voltages and/or currents applied are small enough to neglect any side reactions occurring at each of the electrodes.

Appendix C

Donnan Potential Derivation

Donnan equilibrium theory rests upon equating the electrochemical potential (see equation 2.1), in membrane and electrolyte phases. Once we equate the electrochemical potential for both phases, solution (x) and membrane ($\bar{x}$), we arrive at the expressions

$$RT\ln\left(\frac{a_+}{\bar{a}_+}\right) - (\bar{P} - P)V_+ - z_I F(\bar{\psi} - \psi) = 0 \tag{C.1}$$

$$RT\ln\left(\frac{a_-}{\bar{a}_-}\right) - (\bar{P} - P)V_- - z_I F(\bar{\psi} - \psi) = 0 \tag{C.2}$$

$$RT\ln\left(\frac{a_w}{\bar{a}_w}\right) - (\bar{P} - P)V_w = 0 \tag{C.3}$$

where the $+$, $-$, and w indices are the cation, anion and water molecule respectively. The From equations C.1 - C.3, we obtain an expression for the Donnan potential, for an arbitrary species (i)

$$E_{Don} = \bar{\psi} - \psi = \left(\frac{RT}{z_i F}\right)\left(\ln\left(\frac{a_i}{\bar{a}_i}\right) - \pi V_i\right) \tag{C.4}$$

Where π is the pressure difference between both phases ($\bar{P} - P$), equivalent to the osmotic (swelling) pressure, an expression we can readily extract from equation C.3. Now, using $E^+_{Don} - E^-_{Don}$, the osmotic swelling pressure π from equation C.3 and for $v_i z_i$ moles of each cation and anion, we have

$$\ln\left[\left(\frac{a_+}{\bar{a}_+}\right)^{v_+}\left(\frac{a_-}{\bar{a}_-}\right)^{v_-}\right] = \frac{v_{+,-}}{v_w}\ln\left(\frac{a_w}{\bar{a}_w}\right) \tag{C.5}$$

where $v_{+,-}$ is the partial molar volume of the electrolyte (containing both anions and cations). From equation C.5, and let $r = \frac{v_{+,-}}{v_w}$, it follows that

$$\frac{a_+^{v_+}a_-^{v_-}}{a_w^r} = \frac{\bar{a}_+^{v_+}\bar{a}_-^{v_-}}{\bar{a}_w^r} \tag{C.6}$$

Now, if the activity of water is approximately the same as in the membrane phase ($a_w^r \approx \bar{a}_w^r$) and the activity coefficient, defined as $a_i = \gamma_i C_i$, being set to unity, we arrive at the Donnan equilibrium phenomena

$$C_+^{v_+}C_-^{v_-} = \overline{C}_+^{v_+}\overline{C}_-^{v_-} \tag{C.7}$$

Now, charge neutrality is required within the membrane. This is satisfied (for a cation exchange membrane) when

$$\overline{C}_+ = \overline{C}_- + \overline{C}_R \tag{C.8}$$

where $\overline{C}_R$ is the concentration of fixed charge sites within the lattice. Substituting equation C.8 into C.7 gives expressions for concentrations within a cation exchange membrane as

$$\overline{C}_- = \frac{1}{2}\sqrt{\overline{C}_R^2 - 4C_-C_+} - \overline{C}_R \tag{C.9}$$

$$\overline{C}_+ = \frac{1}{2}\sqrt{\overline{C}_R^2 - 4C_-C_+} + \overline{C}_R \tag{C.10}$$

From equations C.9 and C.10, assuming that the activity of water $\bar{a}_w = a_w$, the concentration of anions and cations are the same in the bulk ($C_- = C_+$) and using equations B.1 and B.2, we arrive at an expression for both of the Donnan potentials from either side of the membrane

$$E_{Don2} - E_{Don1} = -\frac{RT}{F}\ln\left(\frac{C2}{C_1}\frac{\sqrt{\overline{C}_R^2 - 4C_1^2} + \overline{C}_R}{\sqrt{\overline{C}_R^2 - 4C_2^2} + \overline{C}_R}\right) \tag{C.11}$$

Where C_1 is the concentration one side of the membrane and C_2 is the concentration on the other side. Now, the total potential which will be established across the membrane must also include the diffusion potential across the entire membrane. Teorell derived [1] an expression for this as

$$E_{Diff} = -\frac{RT}{F}\bar{\mu}\ln\left(\frac{C2}{C_1}\frac{\sqrt{\overline{C}_R^2 - 4C_1^2} + \bar{\mu}\overline{C}_R}{\sqrt{\overline{C}_R^2 - 4C_2^2} + \bar{\mu}\overline{C}_R}\right) \tag{C.12}$$

where

$$\bar{\mu} = \frac{\bar{\mu}_+ - \bar{\mu}_-}{\bar{\mu}_+ + \bar{\mu}_-} \tag{C.13}$$

Appendix D

Poisson-Boltzmann Equations

For a surface at equilibrium, we can set the chemical potential (equation 2.1) to be zero and unchanging. This gives the expression

$$k_B T \ln(\rho_i) = z_i e \psi \tag{D.1}$$

where ρ_i is the ionic concentration. By constraining ρ_i that where $\psi = 0$, $\rho_i = \rho_0$ gives

$$\rho_i = \rho_{0,i} \exp\left(-\frac{z_i e \psi}{k_B T}\right) \tag{D.2}$$

and from Poisson's equation

$$\nabla^2 = \frac{ze\rho}{\epsilon_0 \epsilon_r} \tag{D.3}$$

where ϵ_0 and ϵ_r are the permittivity of vacuum and relative permittivity respectively. At the surface, with co-ion concentration (σ), we can determine, from Gauss' Law, that the electric field, shall be:

$$E_s = \frac{\sigma}{\epsilon_0 \epsilon_r} \tag{D.4}$$

By differentiating D.2 and incorporating this derivative into D.3, we can arrive at an expression for the surface ion density, as a function of the bulk value

$$\rho_s = \frac{\sigma^2}{\epsilon_0 \epsilon_r k_B T} + \rho_0 \tag{D.5}$$

Further, we can solve the Poission Boltzmann equation D.6 (found by combining D.2 and D.3) for the potential

$$-\frac{ze\rho_o}{\epsilon_0 \epsilon_r} \exp\left(-\frac{ze\psi}{k_B T}\right) = \nabla^2 \psi \tag{D.6}$$

solving, gives

$$\psi = \frac{k_B T}{ze} \ln\left(cos(Kx)\right) \tag{D.7}$$

where

$$K^2 = \frac{(ze)^2 \rho_0}{2\epsilon_0 \epsilon_r k_B T}$$

By taking the derivative of equation D.7 and equating this electric field to equation D.4, we can extract the value ρ_0.

Appendix E

Gibbs-Duhem and Van 't Hoff Equation

Gibbs-Duhem equation

$$\sum_{i=1}^{I} N_i d\mu_i \; = \; -SdT \; + \; VdP \tag{E.1}$$

van't Hoff equation

$$\frac{dln(K_{ex})}{dT} = \frac{\Delta H^0_{ex}}{RT^2} \tag{E.2}$$

where K_{ex} is the exchange equilibrium constant and ΔH^0_{ex} is the standard enthalpy of exchange.

Appendix F

Ion-Exchange Kinetics

$$\boldsymbol{J_i} = -D_i \nabla C_i - \frac{z_i F}{RT} D_i C_i \nabla \psi + C_i \boldsymbol{v_i} \tag{F.1}$$

$$\overline{D} = \overline{D}_A \overline{D}_B (z_A^2 \overline{C}_A + z_B^2 \overline{C}_B) / (z_A^2 \overline{C}_A \overline{D}_A + z_B^2 \overline{C}_B \overline{D}_B) \tag{F.2}$$

$$|z_A| \overline{C}_A + |z_B| \overline{C}_B = \overline{C} \tag{F.3}$$

where $\overline{C}$ is the total counter-ion concentration in the exchanger and the second condition

$$z_A \overline{J}_A + z_B \overline{J}_B = 0. \tag{F.4}$$

Appendix G

Mica Composition

$I_2M_{4\text{-}6}X_{2\text{-}0}T_8O_{20}A_4$

where:

I is often K or Na, but can be Cs NH_4, Rb, Ca, Ba as well as other cations.

M is typically Mg, Fe^{2+},Fe^{3+}, Al, Li, Ti, Mn, Zn, Cr, V and other cations

X is a vacant site

T is usually Si, Al and occasionally Fe^{3+}

A is most often either OH or F, but can be Cl, O and S

Appendix H

Raman Spectra (OH stretching) of Bulk Mica and Vermiculite

Using a Renishaw inVia confocal Raman microscope, with a 532 nm laser.

a

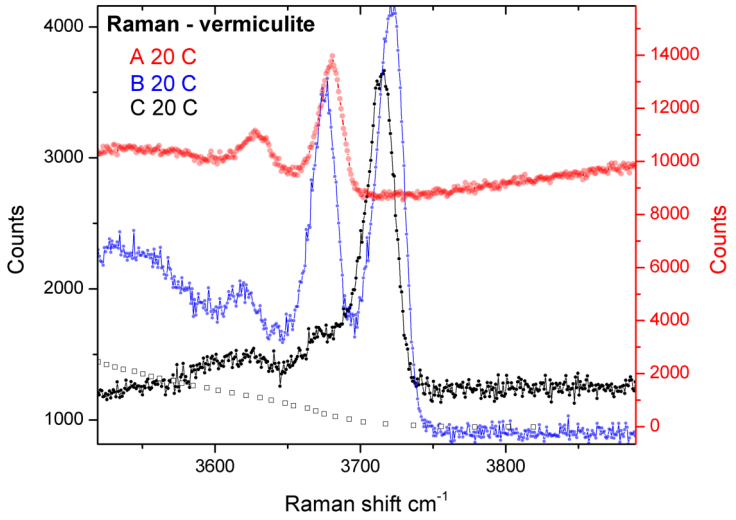

b

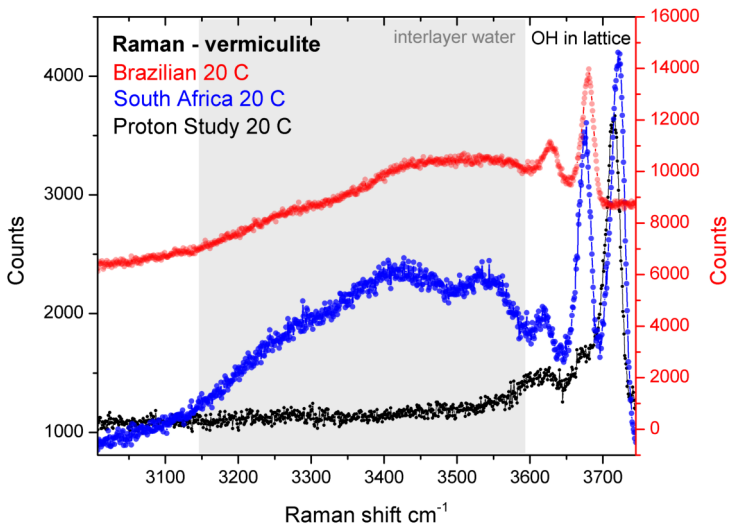

Appendix I

XRD of Vermiculite

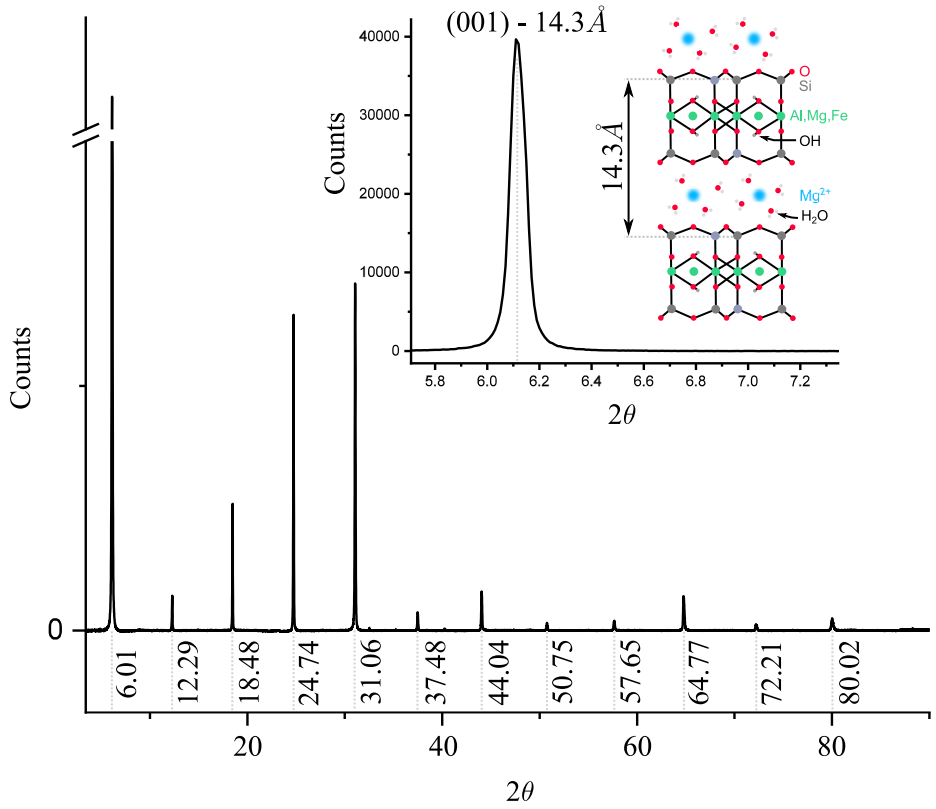

Appendix J

Micro-Manipulator Stage

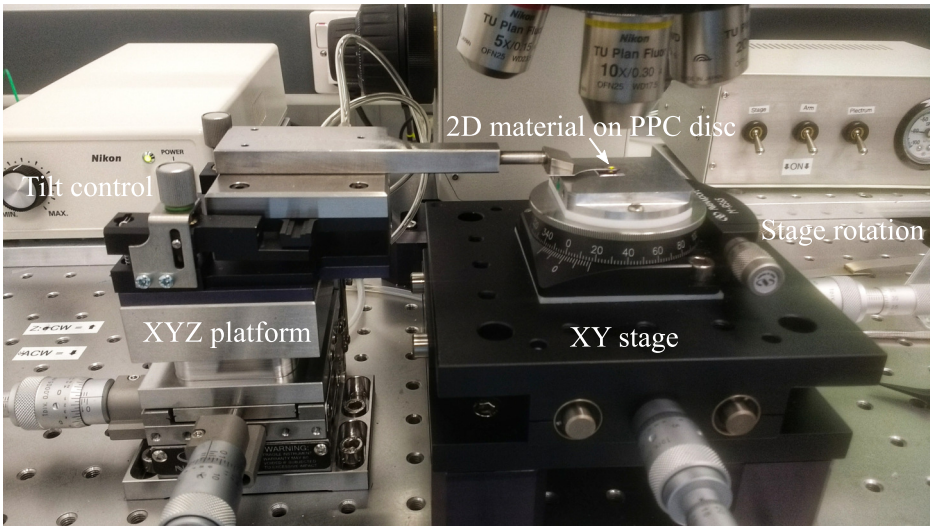

Micro-manipulator stage with XYZ control and the suspended 2D material is suspended at the end of the vacuum held arm.

Appendix K

Hydrogen Mass Spectrometry

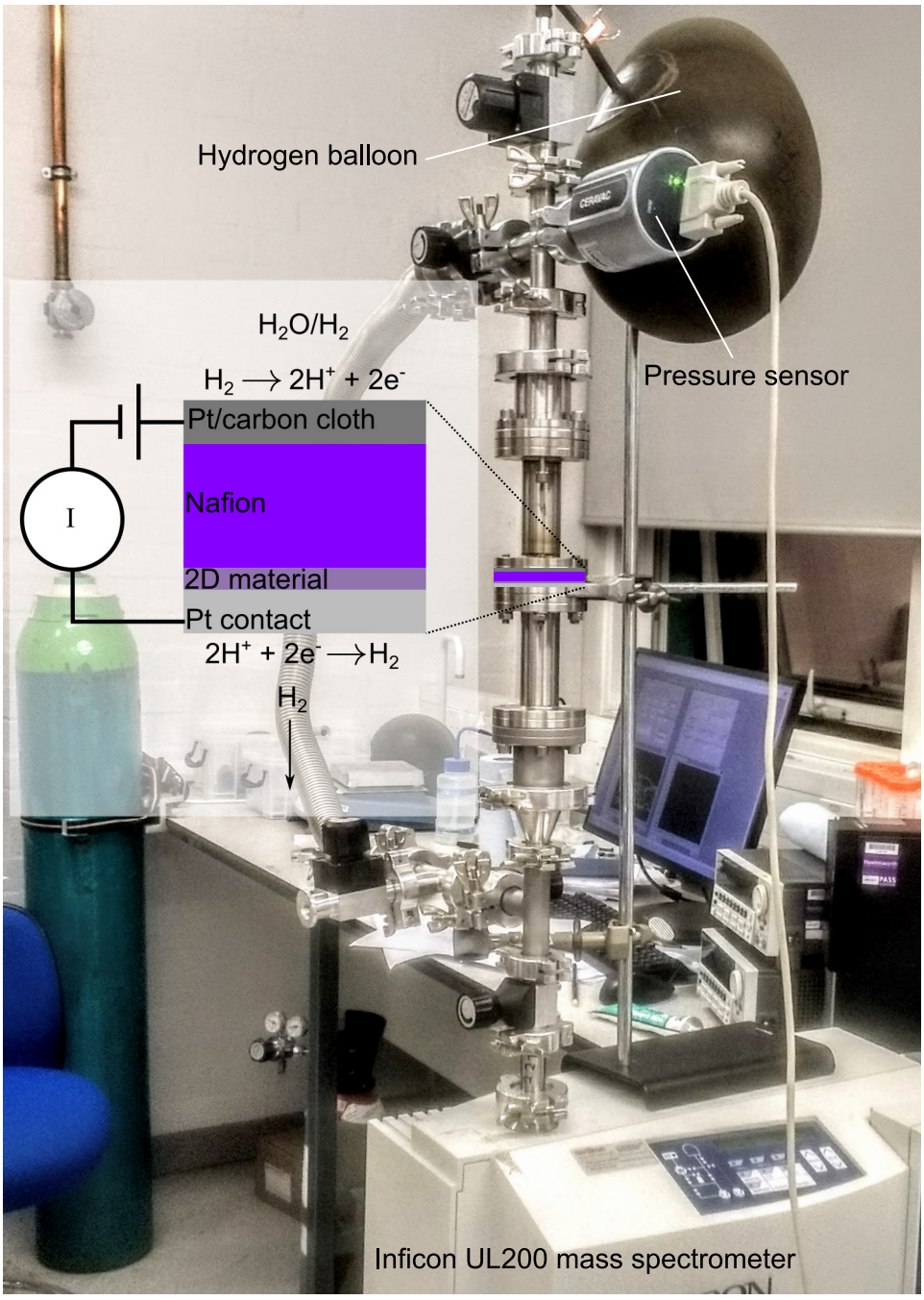

Appendix L

Graphene Liquid Cell Measurement

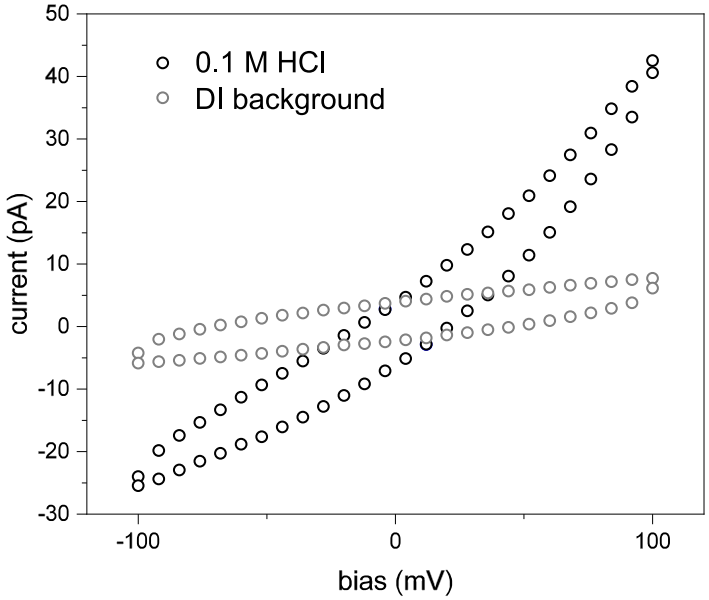

Appendix M

Vermiculite Chemical Analysis

SGS GEOSOL LABORATÓRIOS LTDA.

CERTIFICADO DE ANÁLISES
GY1902105

Dados do Cliente

Nome: BRASIL MINERIOS S/A
Attn.: Eduardo Hiromu
Endereço: ROD GO - 164 SAO LUIZ DE MONTES A SANCLERLANDIA KM 16 S/N FAZENDA BOM JESUS ZONA RURAL POVOADO BRASILANDIA 76100000 GO SAO LUIS DE MONTES BELOS

Referência do Lote de Amostras

Ref. Cliente: Pedido 01/10/2019
Produto: CONCENTRADO
Projeto: Prod. BM. 09.2019
Número de Amostras: 1
Data do Recebimento: 07/10/2019
Data de Envio: 22/10/2019
Completado Em: 22/10/2019

Referência Analítica

PHY01E: LOI (Loss on ignition) - Perda ao fogo por calcinação da amostra a 405ºC e/ou 1000ºC
XRF79C: Fusão com tetraborato de lítio e quantificação por XRF

Legenda

L.D.= Limite de Detecção	**BLK =** Branco	**REP =** Replicata	**DUP =** Duplicata
L.N.R. = Listado e não Recebido	**I.S. =** Amostra Insuficiente	**N.A. =** Não Analisado	**STD =** Padrão
I.N.F. = Não reportado devido a interferentes		**OVR =** Não Analisado devido ao alto teor	

Marcos Filipe Gonçalves Silva
CRQ II 02202046
Responsável Técnico

SGS GEOSOL LABORATÓRIOS LTDA.

CERTIFICADO DE ANÁLISES
GY1902105

Análises	SiO2	Al2O3	Fe2O3	CaO	MgO	TiO2	P2O5	Na2O	K2O
Método	XRF79C	XRF79C	XRF79C	XRF79C	XRF79C	XRF79C	XRF79C	XRF79C	XRF79C
Unidade	%	%	%	%	%	%	%	%	%
Limite Detecção	0,10	0,10	0,01	0,01	0,10	0,01	0,01	0,10	0,01
BRANCO_PREP	98,1	<0,1	0,71	0,01	<0,1	<0,01	<0,01	0,10	0,01
Conentrado de Vermiculita	40,6	11,1	7,93	0,31	26,9	1,00	0,01	<0,1	0,18
* REP Conentrado de Vermiculita	40,4	11,1	7,85	0,30	26,9	0,98	0,01	<0,1	0,19
* STD SG_100	40,8	1,28	9,82	1,02	35,8	0,02	<0,01	<0,1	<0,01

Análises	MnO	LOI
Método	XRF79C	PHY01E
Unidade	%	%
Limite Detecção	0,01	-45,00
BRANCO_PREP	<0,01	0,15
Conentrado de Vermiculita	0,06	11,34
* REP Conentrado de Vermiculita		11,43
* STD SG_241		12,01
* REP Conentrado de Vermiculita	0,06	
* STD SG_100	0,14	